Structure and Bonding 138

Series Editor: D.M.P. Mingos

Angel Vegas *Editor*

Inorganic 3D Structures

Springer

138

Structure and Bonding

Series Editor: D. M. P. Mingos

For further volumes:
http://www.springer.com/series/430

Structure and Bonding

Series Editor: D. M. P. Mingos

Recently Published and Forthcoming Volumes

Zintl Ions
Principles and Recent Developments
Volume Editor: Thomas F. Fässler
Vol. 140, 2011

Zintl Phases
Principles and Recent Developments
Volume Editor: Thomas F. Fässler
Vol. 139, 2011

Inorganic 3D Structures
Volume Editor: Angel Vegas
Vol. 138, 2011

Molecular Catalysis of Rare-Earth Elements
Volume Editor: Peter W. Roesky
Vol. 137, 2010

Metal-Metal Bonding
Volume Editor: Gerard Parkin
Vol. 136, 2010

Functional Phthalocyanine Molecular Materials
Volume Editor: Jianzhuang Jiang
Vol. 135, 2010

Data Mining in Crystallography
Volume Editors: Hofmann, D. W. M.,
Kuleshova, L. N.
Vol. 134, 2010

Controlled Assembly and Modification of Inorganic Systems
Volume Editor: Wu, X.- T.
Vol. 133, 2009

Molecular Networks
Volume Editor: Hosseini, M. W.
Vol. 132, 2009

Molecular Thermodynamics of Complex Systems
Volume Editors: Lu, X., Hu, Y.
Vol. 131, 2009

Contemporary Metal Boron Chemistry I
Volume Editors: Marder, T. B., Lin, Z.
Vol. 130, 2008

Recognition of Anions
Volume Editor: Vilar, R.
Vol. 129, 2008

Liquid Crystalline Functional Assemblies and Their Supramolecular Structures
Volume Editor: Kato, T.
Vol. 128, 2008

Organometallic and Coordination Chemistry of the Actinides
Volume Editor: Albrecht-Schmitt, T. E.
Vol. 127, 2008

Halogen Bonding
Fundamentals and Applications
Volume Editors: Metrangolo, P., Resnati, G.
Vol. 126, 2008

High Energy Density Materials
Volume Editor: Klapötke, T. H.
Vol. 125, 2007

Ferro- and Antiferroelectricity
Volume Editors: Dalal, N. S.,
Bussmann-Holder, A.
Vol. 124, 2007

Photofunctional Transition Metal Complexes
Volume Editor: V. W.W. Yam
Vol. 123, 2007

Single-Molecule Magnets and Related Phenomena
Volume Editor: Winpenny, R.
Vol. 122, 2006

Inorganic 3D Structures

Volume Editor: Angel Vegas

With contributions by

D.J.M. Bevan · V.A. Blatov · F. Liebau · R.L. Martin ·
D. Santamaría-Pérez · A. Vegas

Springer

Editor
Angel Vegas
Instituto de Química Física "Rocasolano"
CSIC, C/ Serrano 119
28006 Madrid
Spain
avegas@iqfr.csic.es

ISSN 0081-5993 e-ISSN 1616-8550
ISBN 978-3-642-20340-4 e-ISBN 978-3-642-20341-1
DOI 10.1007/978-3-642-20341-1
Springer Heidelberg Dordrecht London New York

Library of Congress Control Number: 2011929693

Cover design: eStudio Calamar, Berlin/Figueres, Spain

Printed on acid-free paper

Springer is part of Springer Science+Business Media (www.springer.com)

Series Editor

Volume Editor

Editorial Board

Structure and Bonding
Also Available Electronically

Structure and Bonding is included in Springer's eBook package *Chemistry and Materials Science*. If a library does not opt for the whole package the book series may be bought on a subscription basis. Also, all back volumes are available electronically.

For all customers who have a standing order to the print version of *Structure and Bonding*, we offer the electronic version via SpringerLink free of charge.

If you do not have access, you can still view the table of contents of each volume and the abstract of each article by going to the SpringerLink homepage, clicking on "Chemistry and Materials Science," under Subject Collection, then "Book Series," under Content Type and finally by selecting *Structure and Bonding*.

You will find information about the

- Editorial Board
- Aims and Scope
- Instructions for Authors
- Sample Contribution

at springer.com using the search function by typing in *Structure and Bonding*.

Color figures are published in full color in the electronic version on SpringerLink.

Aims and Scope

The series *Structure and Bonding* publishes critical reviews on topics of research concerned with chemical structure and bonding. The scope of the series spans the entire Periodic Table and addresses structure and bonding issues associated with all of the elements. It also focuses attention on new and developing areas of modern structural and theoretical chemistry such as nanostructures, molecular electronics, designed molecular solids, surfaces, metal clusters and supramolecular structures. Physical and spectroscopic techniques used to determine, examine and model structures fall within the purview of *Structure and Bonding* to the extent that the focus is on the scientific results obtained and not on specialist information concerning the techniques themselves. Issues associated with the development of bonding models and generalizations that illuminate the reactivity pathways and rates of chemical processes are also relevant.

The individual volumes in the series are thematic. The goal of each volume is to give the reader, whether at a university or in industry, a comprehensive overview of an area where new insights are emerging that are of interest to a larger scientific audience. Thus each review within the volume critically surveys one aspect of that topic and places it within the context of the volume as a whole. The most significant developments of the last 5 to 10 years should be presented using selected examples to illustrate the principles discussed. A description of the physical basis of the experimental techniques that have been used to provide the primary data may also be appropriate, if it has not been covered in detail elsewhere. The coverage need not be exhaustive in data, but should rather be conceptual, concentrating on the new principles being developed that will allow the reader, who is not a specialist in the area covered, to understand the data presented. Discussion of possible future research directions in the area is welcomed.

Review articles for the individual volumes are invited by the volume editors.

In references *Structure and Bonding* is abbreviated *Struct Bond* and is cited as a journal.

Impact Factor in 2009: 4.152; Section “Chemistry, Inorganic & Nuclear”:
Rank 2 of 43; Section “Chemistry, Physical”: Rank 7 of 113

Preface

The classical ionic model is widely accepted as the basic framework for describing the crystal structures of three-dimensional inorganic structures. However, it has been shown to be incapable of explaining the underlying principles governing all the relevant crystal structures. This limitation also highlights a second, more important constraint – its lack of predictive power. In other words, if the main principles are ill-defined, how can we predict the structure of a given compound? Can we find any novel governing principles to predict inorganic structures beyond the ionic model?

In 1964, Wondratschek, Merker, and Schubert (WMS) highlighted a structural analogy between Fe_5Si_3 and the Ca_5P_3-subarray of apatite, $Ca_5(PO_4)_3Cl$, and proposed that it may well be the result of an underlying general principle, which they were not able to formulate completely, but they recognized that it deviated significantly from the commonly accepted paradigms for three-dimensional infinite inorganic structures. Since then, several authors, including Adams, Lebedev, Göttlicher, Huheey, Dunitz, Slater, O'Keeffe, and Hyde, have drawn attention to the weaknesses of the classical ionic model, launching severe criticisms of the way in which inorganic structures are presented, in some cases even questioning the existence of ions in crystals. Their arguments are founded not only in the limitations of the ionic model in describing simple structures but also in the impossibility of determining whether an iconic compound such as NaCl is really formed from ions. Structure factor calculations as well as the experimental determination of the electron density distribution undermined the commonly accepted ionic model. Furthermore, a model which considers the O atoms, in oxides, as big anions, whereas the neighboring C and N atoms are considered as small spheres in interstitial carbides and nitrides seem to embody internal inconsistencies.

The observation that the cation arrays in oxides bear a strong relationship to the structures of the metal ions observed in Zintl phases leads to interesting insights into the structures of many oxides. Indeed in many of the oxides, the cation array is identical to the corresponding alloy, for example $Ca_5(AsO_4)_3$ and Ca_5As_3. In other cases, the cation array adopts the structure of HP/HT phases of the alloy, that is HT-Na_2SO_4 and HP-Na_2S. These features have been explained by assuming a relationship between oxidation and pressure. This pressure can be released by increasing T as it occurs in $ZnSO_4$ at HT where the ZnS subarray recovers the zincblende structure.

The p-block elements sometimes preserve a memory of the structures of the element in their oxides, for example P_4 and $P_4O_{6\text{-}10}$, Si and SiO_2-cristobalite. This was remarked on in many undergraduate textbooks, but first generalised in the work of Santamaría-Pérez et al. in 2003 and extended to the structures of aluminates and silicates by Vegas et al. in 2003–2007. Specifically, if in the silicate, $Rb[AlSiO_4]$, the O atoms are removed, the remaining atoms behave as the Zintl phase Rb[AlSi] and the [AlSi] subarray (Ψ-Si) form the same structure as the Al atoms (also Ψ-Si) in the $SrAl_2$ Zintl phase. The cation arrays in aluminates, silicates, etc., adopt the same three-dimensional arrangement as the cations in the Zintl phase and the skeletons of the aluminate and silicate polyanions reproduce the structures of Zintl polyanions.

Although, the resulting skeletons have much expanded dimensions, because the extensive bonding between the p block elements, which is such a characteristic feature of the Zintl structures, is no longer strong because the element–element bonds are replaced by oxide bridges. This relationship has been described as either the “Extended Zintl–Klemm Concept” or the “Generalized Zintl–Klemm Concept”, and has also been used by other authors (Hoffmann 2000; Nesper 2003) to describe nonclassical electron-rich polyanionic networks. This same term has also been used in a different context to describe the extension of the Zintl–Klemm model to those Zintl phases containing deltahedral structures identical to those observed in polyhedral boranes and encompassed by the Wade–Mingos rules. Clearly, the multiplicity of meanings associated with this phrase may result in some confusion, but leaves no doubt that the central concept is sufficiently robust for the ideas to survive the expansion into new areas as new compounds and structures are discovered. In time clearer definitions will crystallize which will facilitate the transmission of these ideas to future generations of chemists.

Coincidentally, this volume appears at the same time as two volumes (Volumes 139 and 140), edited by Prof. T.F. Fässler, which provide a comprehensive review of recent developments in the Zintl area. The chapters within these volumes summarize the structures of these interesting compounds, which contain extensive metal–metal bonding and novel three-dimensional structures, which have been interpreted using a range of theoretical models. The occurrence of the three volumes simultaneously represents a good opportunity to fully appreciate the wide ranging ramifications of the area, which has come to be associated with the names of Zintl and Klemm.

In this volume, the reader will find a topical account of examples illustrating WMS’s conjecture (Fe_5Si_3/Ca_5P_3) which when taken together define a General Principle which has considerable predictive utility. In Chap. 1, Santamaría-Pérez and Liebau report the elegant relationships between intermetallic clathrates, porous tectosilicates, and clathrate hydrates, thus completing the huge task of putting the structures of the whole silicate family under a common basis, which was initiated some years ago. The reader is also directed to the chapter on Zintl Clathrates by

Andrei V. Shevelkov and Kirill Kovnir in Volume 139 of Structure and Bonding edited by T.F. Fässler, which gives a complementary analysis of related Zintl structures.

In Chap. 2, Blatov illustrates how a topological analysis of the structures is possible using the Periodic-Graph Approach (TOPOS package). It serves to establish the universal applicability of the WMS conjecture. Blatov's work will simplify and enrich our knowledge of the structural types displayed by the cation subarrays in oxide structures.

In the remaining chapters, the development of new insights based on the equivalent effects of oxidation and the application of external pressure are presented in a didactic manner. This has led to a better understanding of oxide structures. The study of these variables has led to a proposed connection between the structures of oxides and the real high pressure phases of the corresponding alloys.

In Chap. 5, Bevan and Martin have made use of this concept, and used "Bärnighausen Trees" very effectively. They analyze all the structures derived from the parent $Fm\overline{3}m$ space group in fluorite that can be identified as partial substructures in the three phases of Li_7VN_4, a compound with an anti-fluorite stoichiometry M_8N_4. They also develop the possibility of charge transfer between atoms, even if they are of the same kind. This application invokes the resonance concept in this class of inorganic solid, and suggests how alloys and oxides may follow concurrent pathways in their respective phase transitions, as developed in Chaps. 3 and 4.

We are aware that, although most of these alternative approaches have been proposed in the last 25 years, the majority of publications in crystallography remain tied to the past and, in general, interpret the observed structures in the light of Pauling's rules and overlook these newer concepts. We hope that this volume will encourage chemists to explore the new pathways outlined in this volume and thereby discover a deeper understanding of the laws that govern inorganic structures.

Madrid *Angel Vegas*
March 2011

Obituary

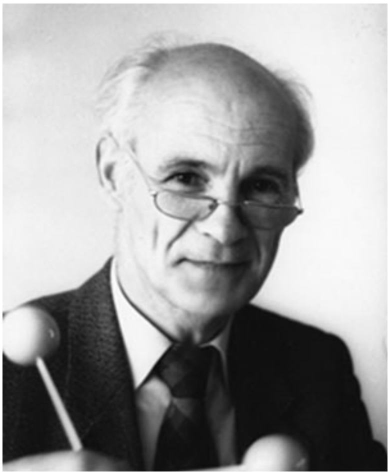

*Friedrich Karl Franz Liebau (*Berlin 1926, † Kiel 2011)*

When writing this Preface, Prof. Wulf Depmeier (University of Kiel) communicated us the sad news that Professor Friedrich Liebau had passed away last Friday (11 March 2011).

As Editor of this volume, and with the unanimous wish of all co-authors, I would like to express our condolences and send our love to his wife, Waltrude, and their children.

As scientists we must say that, with the loss of Friedrich Liebau, an important page on the crystal chemistry of silicates, a field to which he devoted most of his life, is closed. His huge work condensed in his classical book "*Structural Chemistry of Silicates: Structure, Bonding and Classification,* Springer-Verlag (1985) became a reference for all crystalchemists over the world.

He was an open-minded scientist with a keen interest in the new concepts that we were developing. We humbly recognize his valuable contribution to our common paper concerning the application of the Zintl–Klemm concept to the structures of silicates, completed in the first chapter of this volume. Since we met for the first time at the IUCr Congress in Glasgow (1999), until our meeting in Kiel, in 2005, we could appreciate his permanent interest in Science and how much he appreciated novel concepts. He always explained the difficulties found by many scientists to introduce new ideas into our community, based on examples charged with a touch of benevolent humour. For instance, he spoke about the resistance exhibited by many chemists against the reality of the crystal structure of NaCl (Bragg and Bragg, 1913), when they claimed: *this structure (arrangement) cannot be true, because the compound is NaCl!*

It is quite probable that Chap. 1 of this volume will be the last work of Friedrich. We will always keep in mind his scientific rigor, his support, his hospitality, and his sincere friendship.

Contents

Structural Relationships Between Intermetallic Clathrates, Porous Tectosilicates and Clathrate Hydrates 1
D. Santamaría-Pérez and F. Liebau

Crystal Structures of Inorganic Oxoacid Salts Perceived as Cation Arrays: A Periodic-Graph Approach 31
Vladislav A. Blatov

FeLi[PO_4]: Dissection of a Crystal Structure 67
Angel Vegas

Rationalization of the Substructures Derived from the Three Fluorite-Related [$Li_6(M^VLi)N_4$] Polymorphs: An Analysis in Terms of the "Bärnighausen Trees" and of the "Extended Zintl–Klemm Concept" 93
D.J.M. Bevan, R.L. Martin, and Ángel Vegas

Concurrent Pathways in the Phase Transitions of Alloys and Oxides: Towards an Unified Vision of Inorganic Solids 133
Ángel Vegas

Index 199

Struct Bond (2011) 138: 1–29
DOI: 10.1007/430_2010_27

Structural Relationships Between Intermetallic Clathrates, Porous Tectosilicates and Clathrate Hydrates

D. Santamaría-Pérez and F. Liebau

Abstract Intermetallic clathrate-type compounds, such as $|Eu_8|[Ga_{16}Ge_{30}]$, are Zintl phases in which a formal charge transfer from the more electropositive guest atoms (Eu) to the more electronegative host atoms (Ga or Ge) allows the latter to form skeletons with strong directed covalent bonds (polyanions $[Ga_{16}Ge_{30}]^{16-}$). On the other hand, in clathrasils, porous silica polymorphs, such as melanophlogite $|(CH_4, N_2, CO_2, \ldots)_8|$ $[Si_{46}{}^{[4]}O_{92}{}^{[2]}]$ the Si atoms form skeletons which are related to those of Zintl phases, if oxygen atoms are neglected. As in other silicates, in clathrasils the oxygen atoms are located near to hypothetical Si(Al)–Si(Al) bonds, thus producing the tetrahedral coordination around the Si(Al) atoms. The similarities between the structures of intermetallic clathrates and clathrasils can be understood in the light of both the extended Zintl–Klemm concept and the Pearson's generalised octet rule. It is recalled that these principles were successfully applied to describe the structures of other ternary and quaternary aluminates and silicates. In this article, we report a comprehensive and comparative study of both clathrate-like and zeolite-like porous tectosilicate structures to show that their skeletons obey the same general principles. Clathrate hydrates, which also adopt similar skeletons to clathrasils, are also discussed in detail.

Keywords Clathrates · Hydrates · Tectosilicates · Zintl–Klemm concept

---

In memoriam Prof. Friedrich Liebau. Excellent scientist and extraordinary person.

D. Santamaría-Pérez (✉)
Departamento de Química-Física I, Universidad Complutense de Madrid, Avda. Complutense s/n, 28040, Madrid, Spain
e-mail: dsantamaria@quim.ucm.es
F. Liebau
Institut für Geowissenschaften, Kristallographie, Christian-Albrechts-Universität zu Kiel, Olshausenstrasse 40, 24098 Kiel, Germany

Contents

1 Introduction 2
2 Nomenclature and Importance of Clathrate-Type Compounds 4
3 Similarities Between Clathrasils, Intermetallic Clathrates and Clathrate Hydrates 6
  3.1 Group A Clathrates 8
  3.2 Group B Clathrates 13
  3.3 Group C Clathrates 18
4 Similarities Between Zeolites and Intermetallic Clathrates 21
  4.1 ABW-Type Zeolites 21
  4.2 BCT-Type Zeolites 23
5 Considerations on the Stability of Intermetallic Clathrates and Clathrasils 24
6 Conclusions 25
References 26

Abbreviations

EZKC	Extended Zintl–Klemm concept
FD	Framework density
s	Connectedness
SBU	Secondary building unit
vec	Valence electron concentration

1 Introduction

Tectoaluminosilicates contain three-dimensional frameworks built from [$\mathbf{T}O_4$] tetrahedra, where **T** is Al or Si. Some of them are structurally rather complex. Usually, these compounds contain networks of corner-sharing [$\mathbf{T}O_4$] tetrahedra, where all the corners are shared between two tetrahedra (connectedness $s = 4$), although some cases with lower connectedness are also known (some tetrahedra in the structure share less than four corners). To this day, richly illustrated monographs have described and classified the structures of crystalline tectosilicates [1–3]. The structures of aluminates and silicates have often been described as more or less distorted dense packings of oxygen anions O^{2-} in which Al^{3+} and Si^{4+} cations occupy part of the interstitial tetrahedral voids, and more electropositive cations, such as alkaline, alkaline-earth or rare-earth, are placed in larger voids [1, 2]. Thus, this descriptive model considers that tectosilicates are formed by the condensation of [SiO_4] tetrahedra, but no explanation on the rich variety of polyanions is given. Although this type of compounds has been widely studied, the reasons why they adopt a particular structure are still not well known.

To understand the structures of oxides, Vegas and coworkers have analysed hundreds of structures within the last 20 years, focusing on their cation subarrays [3–14]. They based their studies on the assumption that *the global structure of the oxide is determined by that of the parent metal or the corresponding alloy* [5, 8]. Some striking structural coincidences between elements and alloys, on the one hand, and the cation subarray in different oxides, on the other, have been reported by Wondratschek (Mn_5Si_3 alloy and apatite, $Ca_5(PO_4)_3Cl$) [15], Addison (elemental phosphorus and corresponding oxides) [16], Wells (γ-Ge and SiO_2 keatite, see Fig. 1) [17] and O'Keeffe and Hyde (the reader is referred to their article to see the complete list of structural similarities) [18]. These coincidences have motivated Vegas et al. to study in a systematic way the cation subnets of binary, ternary and quaternary oxides. According to the initial hypothesis, they confirmed the surprising fact that cations do not arrange in an arbitrary way, but try to reproduce the structure of the corresponding elements and alloys in spite of being embedded in an oxygen matrix. This led the authors to establish the concept of "real stuffed alloy" for those oxides whose cation arrays maintain the structure of the corresponding alloy [5].

Another step forward in understanding the structures of ternary and quaternary aluminosilicates was taken by Santamaría-Pérez et al. [3, 6, 19], who reinterpreted

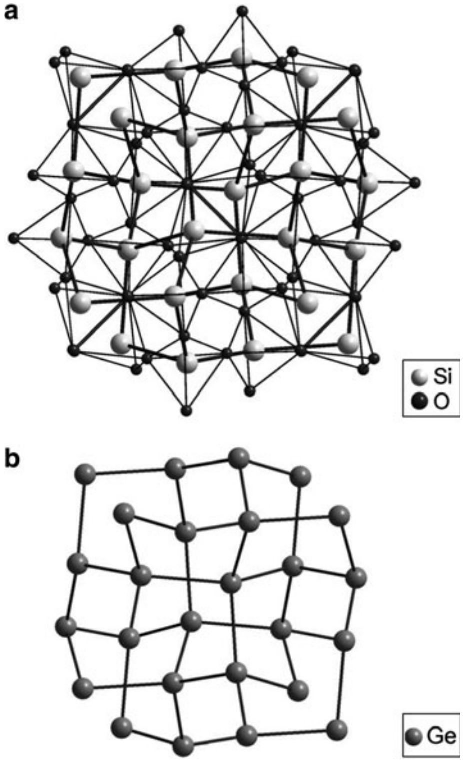

Fig. 1 (**a**) Projection of the keatite structure in which the Si–Si "links" have been drawn with *thick lines* to show its similarity with (**b**) the structure of γ-Ge

these structures in the light of both the extended Zintl–Klemm concept (EZKC) [3, 6, 20, 21] and Pearson's generalised octet rule [22]. In aluminosilicates of highly electropositive metals, the Si and Al atoms form three-dimensional skeletons which can be interpreted as if *Si*(*Al*) *atoms were behaving as Zintl polyanions*, adopting the structure of either main-group elements or isoelectronic Zintl polyanions, showing the same connectivity [3, 6]. That is, the more electropositive cations seem to transfer their valence electrons to the tetrahedral atoms, converting them into pseudo-atoms, such as pseudo-Si (Ψ-Si), pseudo-phosphorus (Ψ-P) or pseudo-sulphur (Ψ-S). The oxygen atoms are then located close to both the hypothetical two-electron bonds and the lone pairs of the cations, giving rise to the tetrahedral coordination of silicon or aluminium. From this, it was concluded that the coordination sphere of Si and Al and the global three-dimensional structure of the aluminosilicates depend on the nature of the other cations accompanying Si and Al in the structure [3, 6].

In this report, we describe a comprehensive and comparative study of the structures of both, the intermetallic clathrates and porous tectosilicates (clathrasils and some zeolites), to show that their skeletons obey the same general principles. The structures of porous tectosilicates will be discussed in terms of the EZKC and Pearson's octet rule, showing that oxides adopt structures similar to those of the corresponding intermetallic compounds. Hydrates, which adopt similar skeletons to clathrasils, will be studied in detail also. Before discussing the clathrate structures, it will be useful to review information concerning the nomenclature and the importance of this family of compounds. These aspects will be covered in Sect. 2. Subsequently, the different structures will be described and discussed, and the comparison of both, the clathrasil and zeolite compounds with the intermetallic–clathrate compounds will be presented in Sects. 3 and 4, respectively. Finally, we will present some considerations on the stability of this type of compounds.

2 Nomenclature and Importance of Clathrate-Type Compounds

Clathrate-type compounds have attracted the attention of scientists since they were discovered. At the beginning of the nineteenth century, Sir Humphry Davy first showed that water was the main component of a solid substance that was previously considered as solid chlorine [23]. Subsequent experiments showed that this new phase has an approximate composition $Cl_2 \cdot 10H_2O$ and is the first crystalline clathrate hydrate known. From this moment, clathrate hydrates of many substances, including rare gases and hydrocarbons, have been found [24].

Clathrate hydrates belong to a large group of compounds, which consist of three-dimensional frameworks (host structures) trapping different molecules or atoms (guest species). The term "clathrate" was coined in 1948 by Powell [25], who discovered an inclusion compound, where guest atoms were enclosed in cavities formed by the host structure and where the distances between the guest and the host atoms were of the order of typical van der Waals forces, that is, there was an absence of conventional chemical bonds between both types of atoms. To describe this compound, he used the term “clathrate”, from the Greek *klethra*, which means encaged.

Throughout this article, several terms related to cage-like compounds are used and it is necessary to be familiar with the differences between them.

Clathrates are inclusion compounds in which certain atoms or molecules (guest species) are completely enclosed in cavities formed by the crystal structure of another substance (host structure). The unit cells of these compounds are usually quite symmetric and have rather large lattice parameters. Generally, there are only relatively weak interactions between the atoms of the host structure and the guest atoms or molecules. However, it should be pointed out that the presence of guest species in the cavities of the clathrate is not fortuitous. The guest species act as templates during the condensation process and condition the type of cage formed. The thermodynamics of these compounds makes clear that the host–guest interactions (either ionic or intermolecular) are very important, and give rise to the formation of the different kinds of cavities, which combine to form the crystalline structure.

Clathrates can be divided into two groups according to the type of interactions between the atoms and molecules of the host structure:

(a) The three-dimensional host framework is formed by water molecules interconnected by means of hydrogen bonds. These compounds are usually formed at enhanced pressures and low temperatures in the presence of the guest substance. In this way, the weak hydrogen bonds form open structures with non-polar molecules in their cavities. These clathrates are known as clathrate hydrates.

(b) The three-dimensional host framework is formed by atoms that are covalently bonded. In the cavities of these structures with strong directional bonds, either neutral molecules or ions, usually cations of very electropositive elements, are lodged. Clathrates of the elements of Group IV of the Periodic System of Elements and clathrasils/clathralites are included in this group. On the one hand, Group-IV clathrates are characterised by an extended 3D framework of Si and/or other elements of Groups III and IV with large voids usually filled with atoms of electropositive elements (Zintl phases). On the other hand, clathrasils and clathralites are tectosilicates or tectoaluminosilicates, respectively, with polyhedral cavities having windows too small to let pass the encaged ions or molecules [2, 26]. Another term in widespread use is zeolite. In the narrow sense of the word, it refers to tectosilicates containing systems of polyhedral cavities interconnected by large channels such that the enclosed ions or molecules can readily diffuse through the crystal [2, 26]. In a wider sense, the term zeolite is also applied to non-siliceous materials with channel-like pores, such as the so-called AlPOs included in the Database of Zeolite Structures [http://www.iza-structure.org/databases/].

Clathrate-like materials do not comprise an easily definable family of crystalline solids and tectosilicates and tectoaluminosilicates, in particular, are very difficult to classify. Whether or not a molecule or ion passes from one polyhedral void to the next depends on the size of the windows formed by the oxygen atoms of the shared faces [2, 26, 27]. If the number of tetrahedra forming a common face between polyhedra is less than six, only small ions such as Li^+ can pass through. If the size of the common face increases, larger species can move from one cavity to the adjacent one. This could give rise to the formation of open channels, like those in zeolite structures.

Therefore, a criterion is needed to distinguish porous from denser tectosilicates. Usually, tetrahedral frameworks are classified according to their framework density (FD) [28], which is the number of tetrahedra per 1,000 $Å^3$. Looking at the density values of all the 4-connected tectosilicates whose structures are well established, a gap is clearly recognised above 21 **T**-atoms per 1,000 $Å^3$. Dense frameworks with $FD > 21$ have rather small voids that are either empty, as in cristobalite, or contain barely or non-exchangeable cations, as in feldspars. Silicates with $FD < 21$, have larger cavities and channels and are classified as microporous.

The particular structure of these compounds leads to interesting physical properties such as cation exchange or molecule confinement and makes them useful for industrial applications. Hydrates, for example, are denser than their typical fluid hydrocarbons so that the gas molecules they contain are effectively compressed, which offers a potential way to energy storage and transportation. Zeolites have a wide range of utilities based on their selective cation-exchange ability (i.e. molecular sieves, raw materials, etc.) and catalytic properties. They are used in different fields such as oil industry, construction industry, water treatment or storage of nuclear waste.

3 Similarities Between Clathrasils, Intermetallic Clathrates and Clathrate Hydrates

This section provides structural descriptions of both intermetallic clathrates and clathrasils, as well as similarities between them. The three-dimensional structures of these compounds, particularly silicates, are usually difficult to describe. Hereafter, to simplify their description, they will be presented as formed by secondary building units (SBUs). Rings of different sizes that are repeated along the structure are considered as the most common SBUs. The sides of these polygonal rings can be represented by the straight lines between neighbouring Si atoms, and the O atoms would be placed near to the midpoints of these Si–Si lines. The SBUs give rise to polyhedral building units that are the common constituents of clathrasil frameworks.

The known types of clathrate structures are collected in Table 1. In the fifth column of the table, only the general formulas of the intermetallic clathrates (Zintl phases) are given. Corresponding general formulas for the clathrasils, AlPOs

Table 1 Structure types of the known clathrates

Group	Clathrate type	Code IZA	Aristo type	General formula	Pearson symbol	Hydrates	Oxides	Zintl phases
A	I	MEP	$Pm\bar{3}n$	$\vert\mathbf{A}_8\vert[\mathbf{E}_{46}{}^{[4]}]$	$cP54$	+	+	+
	II	MTN	$Fd\bar{3}m$	$\vert\mathbf{A}_{24}\vert[\mathbf{E}_{136}{}^{[4]}]$	$cF160$	+	+	+
B	H	DOH	$P6/mmm$	$\vert\mathbf{A}_6\vert[\mathbf{E}_{34}{}^{[4]}]$		+	+	
		DDR	$R\bar{3}m$	$\vert\mathbf{A}_{15}\vert[\mathbf{E}_{120}{}^{[4]}]$			+	
		NON	$Fmmm$	$\vert\mathbf{A}_4\vert[\mathbf{E}_{88}{}^{[4]}]$			+	
		SGT	$I4_1/amd$	$\vert\mathbf{A}_4\vert[\mathbf{E}_{64}{}^{[4]}]$			+	
		SOD	$Im\bar{3}m$	$\vert\mathbf{A}_2\vert[\mathbf{E}_{12}{}^{[4]}]$		+	+	
		AST	$Fm\bar{3}m$	$\vert\mathbf{A}_{20}\vert[\mathbf{E}_{40}{}^{[4]}]$			+	
C	III		$P4_2/mnm$	$\vert\mathbf{A}_{33}\vert[\mathbf{E}_{129}{}^{[4]}\mathbf{E}_{33}{}^{[3]}]$	$tP195$	+		+
	VIII		$I\bar{4}3m$	$\vert\mathbf{A}_8\vert[\mathbf{E}_{46}{}^{[4]}]$	$cI54$			+
	IX		$P4_132$	$\vert\mathbf{A}_{24}\vert[\mathbf{E}_{68}{}^{[4]}\mathbf{E}_{32}{}^{[3]}]$	$cP124$			+

The three columns at the right-hand side indicate, by means of *cross marks*, whether these clathrates exist as clathrate hydrates, oxides, or as Zintl phases

(aluminium phosphates) and related compounds (oxides) are given in the paragraphs for the particular clathrate types. In these general formulas, the number of oxygen atoms is not indicated. Only the relations between guest atoms or molecules (**A** and **M**) and the usually tetra-connected atoms that correspond to the host framework (**E** and **T**), respectively, are shown. The term **A** corresponds to guest atoms in Zintl phases, whereas **M** corresponds to guest atoms in clathrasils. **E** and **T** denote the atoms of the host framework in Zintl phases and tectosilicates, respectively.

As in other aluminates and silicates, several structural coincidences between the cation subarrays in oxides and corresponding Zintl phases have been observed. This is the case for the Group A clathrates, where the structure of the tetra-connected atoms in silicides and germanides (Zintl phases) is maintained in the related clathrasils and clathrate hydrates. The structural similarities between the type I and II intermetallic clathrates, on the one hand, and the oxides melanophlogite and dodecasil 3C, respectively, on the other, were already pointed out by O'Keeffe and Hyde [18], whereas Wells, in his book "Structural inorganic chemistry", showed the similarity between the structures of melanophlogite and clathrate hydrate I [17]. Despite the fact that the Group B clathrates, with the exception of the SOD clathrate hydrate and the DOH clathrasils, do not show any coincidences, the group of structures formed by the tetrahedral atoms of clathrasils of Group B may be found as structures for Zintl-clathrates, and the structures of Zintl-clathrates of group C may be metastable phases of the $\mathbf{A}_x\mathbf{T}_y$ framework of clathrate oxides.

The structural analogy between clathrate hydrates and clathrasils (oxides) deserves further discussion. Like all the crystalline phases of ice, the water molecules of clathrate hydrates are hydrogen bonded to four neighbouring water molecules in such a way that a H_2O molecule has two additional hydrogen atoms linked with each oxygen by hydrogen bonds. These hydrogen bonds are generated by the difference in electronegativity between H and O atoms, which make water molecules polar. The four hydrogen atoms around each oxygen atom have a pseudo-tetrahedral configuration and their H–O–H bonds are arranged in a similar way as the O–**T**–O bonds in the oxides of elements of Group 14 of the Periodic System of

Elements. Thus, the structures of phases I_h, I_c and III of ice are similar to those of three silica polymorphs: tridymite, cristobalite and keatite, respectively. Therefore, it is not a surprise to find structural coincidences among clathrate hydrates and silica clathrates, as we will see in the following section.

Next, the structures of different clathrates will be described, giving some examples of each structural type. The descriptions are given in terms of the net of tetra-connected atoms (**E**) which, in oxides, is the so-called "cation subarray" (**T**). In addition to this, an analysis of the different cavities or cages and the number of rings per unit cell is given. The cages are defined by the number of rings (faces) of different size forming them, such that $[5^{12}]$ is the symbol for a cavity formed by 12 pentagons (pentagonal dodecahedron) and $[5^{12}6^2]$ stands for a cavity having 12 pentagons and two hexagons.

3.1 Group A Clathrates

3.1.1 Type I Clathrates

The general composition of these clathrates is $|\mathbf{M}_2\mathbf{M}'_6|[(\mathbf{T}_{24}\mathbf{T}'_{16}\mathbf{T}''_6)_{\sum 46}{}^{[4]}\mathrm{O}_{92}{}^{[2]}]$ for oxides and $|\mathbf{A}_2\mathbf{A}'_6|[(\mathbf{E}_{24}\mathbf{E}'_{16}\mathbf{E}''_6)_{\sum 46}{}^{[4]}]$ for Zintl phases. Here, **M** and **M′** and **A** and **A′** are guest species enclosed in the cages of the structural framework. This framework is formed by a basic building block called pentagonal dodecahedron $\mathbf{E}_{20}$, which is usually described as $[5^{12}]$. Two of these dodecahedra occupy the origin and the centre of the unit cell and create interstices that are filled with other polyhedral cavities that consist of 12 pentagons and two hexagons (tetrakaidecahedra, $[5^{12}6^2]$). The structure of this type of clathrate is presented in Fig. 2 and shows

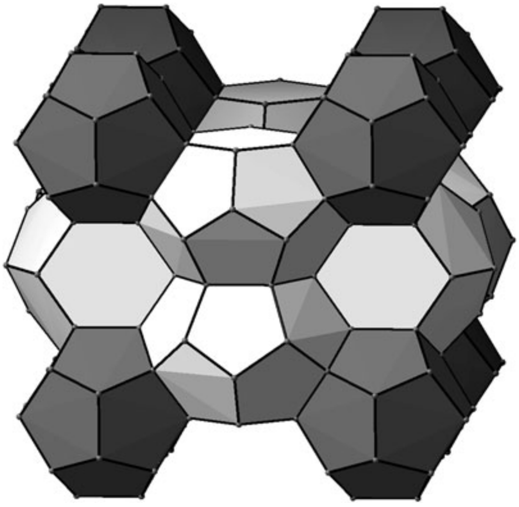

Fig. 2 Packing of polyhedra formed by the host Si framework in Na_8Si_{46} [32]. Pentagonal dodecahedra $[5^{12}]$ and tetrakaidecahedra $[5^{12}6^2]$ are depicted in *dark* and *light grey*, respectively

the two different building units, pentagonal dodecahedra and tetrakaidecahedra, in dark and light grey shading, respectively. In this complex, three-dimensional skeleton, all the **E** atoms of the Zintl phases and **T** atoms in the case of the oxides have fourfold connectivity.

Cages per unit cell: $2 \times [5^{12}] + 6 \times [5^{12}6^{2}]$.
Rings per unit cell: $(48 \times 5R) + (6 \times 6R)$.
Examples of this type of clathrate are:

(a) Hydrates:	Clathrate-hydrates I	$\vert\mathbf{M}_{8-x}\vert[O_{46}{}^{[4]}H_{92}{}^{[2]}]$ $\mathbf{M} = CH_4, N_2, H_2S, Ar \ldots Xe, \ldots$	[29]
(b) Oxides:	Melanophlogite	$\vert\mathbf{M}_{8-x}\vert[Si_{46}{}^{[4]}O_{92}{}^{[2]}]$ $\mathbf{M} = CH_4, N_2, CO_2, CH_3NH_2, Kr, \ldots$	[30]
(c) Zintl phases:		$\vert(K,Rb,Cs)_8\vert[(Al,Ga,In)_8(Si, Ge, Sn)_{38}]$	[31]
		$\vert(Na,K)_8\vert[Si_{46}]$	[32]
		$\vert Eu_8\vert[Ga_{16}Ge_{30}]$	[33]
		$\vert(Sr, Ba)_8\vert[(Al, Ga)_{16}(Si, Ge, Sn)_{30}]$	[34]
		$\vert Ba_8\vert[Cu_4Si_{42}]$	[35]
		$\vert Ba_8\vert[(Zn, Cd)_8Ge_{38}]$	[36]
		$\vert I_8\vert[Sn_{10}In_{14}P_{22}]$, $\vert I_8\vert[Sn_{14}In_{10}P_{21.2}\square_{0.8}]$	[37]
		$\vert I_8Br_8\vert[Sn_{17}Zn_7P_{22}]$, $\vert I_8Br_8\vert[Sn_{20}Zn_4P_{22}]$	[38]
		$\vert I_8\vert[Sb_8Ge_{38}]$	[39]
		$\vert Br_8\vert[Ge_{38}As_8]$	[40]
		$\vert Te_8\vert[Si_{38}Te_8]$	[41]
		$\vert K_8\vert[Ge_{44}\square_2]$	[42]
		$\vert(Rb, Cs)_8\vert[Sn_{44}\square_2]$	[43]

In the Zintl phases $|(K, Rb, Cs)_8|[(Al, Ga, In)_8(Si, Ge, Sn)_{38}]$, $|(Sr, Ba)_8|[(Al, Ga)_{16}(Si, Ge, Sn)_{30}]$, $|Eu_8|[Ga_{16}Ge_{30}]$, $|Ba_8|[Cu_4Ga_4Si_{38}]$ and $|Ba_8|[(Zn, Cd)_8Ge_{38}]$, the electropositive atoms – alkaline, alkaline-earth and rare-earth atoms – transfer their valence electrons to the more electronegative atoms belonging to Groups 11, 12 and 13 of the Periodic Table (Cu, Zn, Cd, Al, Ga and In), converting them into Ψ-Si, Ψ-Ge or Ψ-Sn atoms. In this way, the Zintl–Klemm (ZK) concept explains the fourfold connectivity of these atoms that, together with the Group 14 atoms, form the three-dimensional host framework of the clathrates. In fact, the charge must be considered to be transferred from the donor cations to the skeleton as a whole, not specifically to an individual atom, giving rise in any case to a fourfold connected skeleton. The electropositive atoms are placed in centres of both, the pentagonal dodecahedra and the tetrakaidecahedra, constituting a subarray that is similar to the structure of the intermetallic phases A15 (Cr_3Si-type). This amazing correspondence between structures of completely different atoms as Cr and Si in Cr_3Si and the electropositive atoms in these clathrates was first observed by Kasper et al. [32].

The compounds $|I_8|[Ge_{38}Sb_8]$ and $|Br_8|[Ge_{38}As_8]$ can be called "inverse Zintl phases" [44, 45]. In these cases, there are no electropositive atoms transferring electrons, but very electronegative atoms (Br and I atoms) that receive electrons from the **E** framework. Thus, the eight halogen atoms would accept one electron each (a total of eight e^-) to complete their electron valence shell and convert the As and Sb atoms into Ψ-Ge and Ψ-Sn atoms, respectively. In this way, the tetra-connected skeleton of the type I clathrate is formed. The same interpretation can be applied to the compound $|Te_8|[Si_{38}Te_8]$.

The composition of the compounds described as $|I_8|[Sn_{10}In_{14}P_{22}]$ and $|I_8|[Sn_{14}In_{10}P_{21.2}]$ also complies with the Zintl–Klemm formalism. These two compounds differ by the Sn:In atomic ratio. In the first case, the iodine atoms would receive eight electrons from the skeleton, giving rise to a polyanion $[Sn_{10}In_{14}P_{22}]^{8+}$, which has a valence electron concentration (*vec*) of four electrons per atom, typical of a 4-connected framework. $|I_8|[Sn_{14}In_{10}P_{21.2}]$ can also be analysed as an inverse Zintl phase but this compound contains a partially vacant phosphorus site in the covalent Sn–In–P framework. The formula should, therefore, be written as $|I_8|[Sn_{14}In_{10}P_{21.2}\square_{0.8}]$. These vacancies in the structure of the polyanion $[Sn_{14}In_{10}P_{21.2}\square_{0.8}]^{8+}$ can be justified with the ZK concept in such a way that 42 atoms of the framework would have four valence electrons per atom, whereas 3.2 P atoms would maintain the phosphorus configuration (five valence electrons). The existence of these 3.2 phosphorus atoms is responsible for the formation of 0.8 vacancies in the **E** skeleton, since the 3.2 tri-connected atoms are necessary to remove 0.8 "original" atoms from the clathrate I framework.

The Zintl phases $|(Na, K)_8|[Si_{46}]$ are of particular interest. These compounds also have a tetra-connected skeleton in spite of having eight electrons more than expected (valence electron concentration $vec > 4$). The authors that reported these compounds justified this fact by assuming that these extra electrons were delocalised over the whole framework, generating bond orders slightly higher than one. However, the average experimental Si–Si distance in $|Na_8|[Si_{46}]$ (2.37 Å) is slightly longer than that of elemental silicon (diamond-type, 2.35 Å), in contrast to what is expected for a higher bond order. In any case, these compounds show some metallic behaviour, in comparison with the semiconducting behaviour of the previous compounds, indicating some delocalisation of charge over the framework.

On the other hand, there exist other Zintl phases, such as the compounds $|K_8|[Ge_{44}\square_2]$ and $|(Rb, Cs)_8|[Sn_{44}\square_2]$, which have a structure with two vacant positions per formula unit, so that some of the Ge and Sn atoms are only 3-connected. This can be understood in the light of the ZK concept by assuming that the alkaline metals donate eight electrons to the **E** skeleton, giving rise to a $[Ge(Sn)_{44}\square_2]^{8-}$ polyanion (Ψ-$Ge(Sn)_{36}As(Sb)_8$ skeleton). In fact, to generate eight tri-connected atoms in this type of clathrate framework, it is necessary to have two vacant **E** positions, as found experimentally. Therefore, the number of vacant positions in an **E** skeleton seems to be determined by the number of electrons received from the more electropositive atoms.

The existence or not of such vacancies is currently a matter of controversy. It is still not clear whether these compounds are $\mathbf{M}_8\mathbf{E}_{46}$, $\mathbf{M}_8\mathbf{E}_{44}\square_2$, $\mathbf{M}_{8-x}\mathbf{E}_{46}$ or an intermediate structure.

It has been previously mentioned that this type of clathrates also exists in oxides such as the clathrasils, AlPOs and related compounds. Thus, the cation arrangement in the Zintl phases $|\mathbf{A}_8|[\mathbf{E}_{46}{}^{[4]}]$ is similar to that of the atoms in the $|\mathbf{M}_8|[\mathbf{T}_{46}]$ skeleton of the rare natural "polymorph" of silica, melanophlogite $|(CH_4, N_2, CO_2, \ldots)_8|[Si_{46}{}^{[4]}O_{92}{}^{[2]}]$. The framework density of this oxide is only 19 tetrahedra per 1,000 Å^3, in comparison with that of 23 and 26.6 for cristobalite and quartz, respectively. This density decrease entails that the framework becomes less stable. In fact, the tetrahedral frameworks of clathrasils are thermodynamically stable only in aqueous solution during synthesis when the concentration of suitable template molecules is sufficiently high and when, at least, a certain fraction of their cages are occupied by those template molecules. As it occurs in all the aluminates and silicates [3, 6, 19], in melanophlogite, the oxygen atoms elongate the Si–Si distances (around 3.10 Å) with respect to those in the Zintl phases. However, the same four-connected network is preserved. These structures are further examples of how "cations", in oxides, recognise themselves in spite of being surrounded by "anions". The oxygen atoms, located near to the midpoints of all the hypothetical Si–Si bonds, produce the tetrahedral coordination of the Si atoms.

It is also worth mentioning the structural coincidence between the skeleton of the water molecules in the hydrates I, $|\mathbf{M}_{8-x}|[\mathrm{O}_{46}{}^{[4]}\mathrm{H}_{92}{}^{[2]}]$, and that of the silica "polymorph" melanophlogite, $|(\mathrm{CH}_4, \mathrm{N}_2, \mathrm{CO}_2, \ldots)_8|[\mathrm{Si}_{46}{}^{[4]}\mathrm{O}_{92}{}^{[2]}]$. More examples of this kind of similarity will be given in the next subsections.

3.1.2 Type II Clathrates

With formula $|\mathbf{M}_{16}\mathbf{M}'_8|[(\mathbf{T}_{96}\mathbf{T}'_{32}\mathbf{T}''_8)_{\sum 136}{}^{[4]}\mathrm{O}_{272}{}^{[2]}]$ for oxides and $|\mathbf{A}_{16}\mathbf{A}'_8|[(\mathbf{E}_{96}\mathbf{E}'_{32}\mathbf{E}''_8)_{\sum 136}{}^{[4]}]$ for Zintl phases, this type of clathrates is also cubic. Its structure consists of a compact packing of [5^{12}] pentagonal dodecahedra and [$5^{12}6^4$] hexakaidecahedra (polyhedra of 16 faces, 12 pentagons and 4 hexagons) in a ratio 2:1 (see Fig. 3). The framework contains hexagonal layers of face-sharing pentagonal dodecahedron cages that are stacked in an ABCABC sequence, where

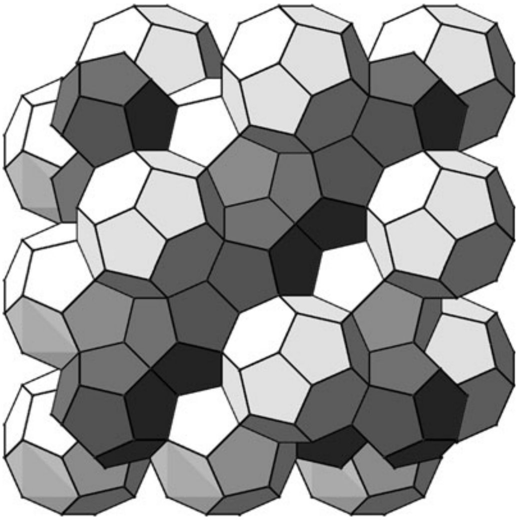

Fig. 3 Type-II clathrate framework of the compound $|\mathrm{Cs}_8\mathrm{Na}_{16}|[\mathrm{Si}_{136}]$ [50]. The shading of the different types of polyhedra (pentagonal dodecahedra and hexakaidecahedra) indicates their occupation by different guest species at their centres (*light grey* for Cs, *dark grey* for Na, respectively)

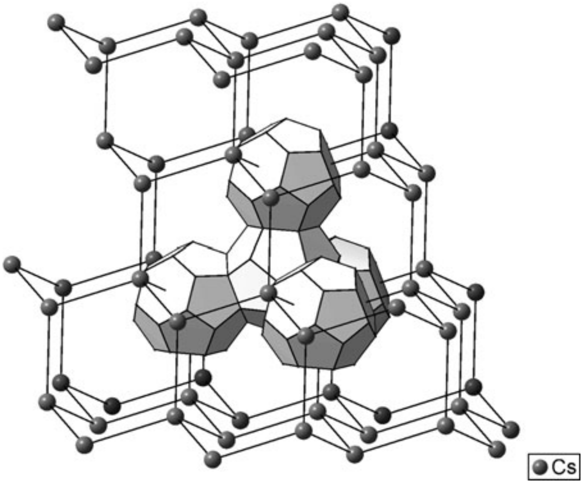

Fig. 4 Cs subarray in the type-II clathrate compound $|Cs_8Na_{16}|[Si_{136}]$ [50]. In this structure, the $[5^{12}6^4]$ hexakaidecahedra share hexagonal faces forming a diamond-type skeleton

the $[5^{12}6^4]$ polyhedra are the interstices of the compact packing. All the **E** and **T** atoms are tetra-connected. An alternative description to the ordering of the $[5^{12}6^4]$ polyhedra in this structure was proposed by Higgins [46], who pointed out that these polyhedra form a diamond-like lattice connected through six-ring faces (Fig. 4).

Cages per unit cell: $16 \times [5^{12}] + 8 \times [5^{12}6^4]$.
Rings per unit cell: $(144 \times 5R) + (16 \times 6R)$.
Examples of this type of clathrate are:

(a) Hydrates:	Clathrate-hydrates II	$\vert\mathbf{M}_{16-x}\mathbf{M'}_{8-x}\vert[O_{136}{}^{[4]}H_{272}{}^{[2]}]$	[47]
(b) Oxides:	Dodecasils 3C	$\vert(N_2)_{16-x}(C_6H_{11}N)_{8-y}\vert[Si_{136}{}^{[4]}O_{272}{}^{[2]}]$	[48]
(c) Zintl phases:		$\vert Ba_{16}\square_8\vert[Ga_{32}Sn_{104}]$	[49]
		$\vert Cs_8Na_{16}\vert[(Si, Ge)_{136}]$	[50]

Clathrates of Type II are new examples of structural similarity between the substructures of oxides (Dodecasil 3C) and the structures of related Zintl phases. With regard to the Zintl phases presented in this section, they have the same behaviour as those described in the previous one. In the compound $|Ba_{16}\square_8|[Ga_{32}Sn_{104}]$, the tetraconnectivity of the **E** framework can be explained by means of the ZK concept, since the valence electrons of the Ba atoms would convert the Ga atoms into Ψ-Ge. Nevertheless, in the compounds $|Cs_8Na_{16}|[(Si, Ge)_{136}]$ there exists an excess of electrons. This fact can be related, as it was mentioned before, either to a delocalisation of these electrons over the bonds of the skeleton or to the existence of vacant **E** positions. An experimental evidence that supports the first hypothesis is the metallic behaviour of these compounds, compared to the semi-conducting behaviour of $|Ba_{16}\square_8|[Ga_{32}Sn_{104}]$. The structure of the compound $|Cs_8Na_{16}|[Si_{136}]$ is represented in Fig. 3.

It is important to mention that this framework of 136 **E** atoms per unit cell can accommodate up to 24 **A** atoms in its cavities, 16 of them located at the centres of the small pentagonal dodecahedra and eight atoms at the centres of the larger hexakaidecahedra. A feature not yet explained is that these 16:8 **A** atoms are forming a Laves $MgCu_2$-type skeleton (C15 type).

3.2 Group B Clathrates

The six types of clathrates described in this subscription have only been found in oxides. Two types, DOH and SOD, have been observed as hydrates. No Zintl polyanion with this structure is known. All clathrates of this group have four-connected **T** networks.

3.2.1 DOH-Type Clathrates

Oxides of this type have the formula $|\mathbf{M}_3\mathbf{M}'_2\mathbf{M}''|[(\mathbf{T}_{12}\mathbf{T}'_{12}\mathbf{T}''_6\mathbf{T}'''_4)_{\sum 34}{}^{[4]}\mathrm{O}_{68}{}^{[2]}]$, and $|\mathbf{A}_3\mathbf{A}'_2\mathbf{A}''|[(\mathbf{E}_{12}\mathbf{E}'_{12}\mathbf{E}''_6\mathbf{E}'''_4)_{\sum 34}{}^{[4]}]$ would be the formula of the hypothetical Zintl phases that could be derived from them. This structure can be described as Kagomé layers of face-sharing $[5^{12}]$ dodecahedral cages that are stacked in an AA sequence (Fig. 5). These layers alternate with other layers of more complicated polyhedra (see the types of cages in the unit cell).

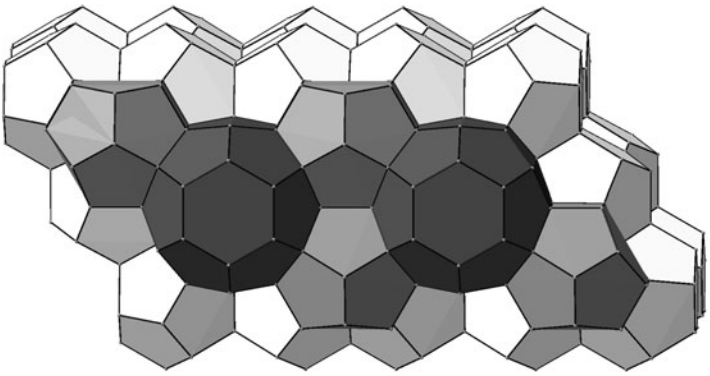

Fig. 5 The ratio between the different kind of polyhedra in dodecasil $|(N_2)_{5-x}(C_5H_{11}N)_{1-x}|$ $[Si_{34}O_{68}]$ [52] is 1:2:3 for $[5^{12}6^8]$:$[4^35^66^3]$:$[5^{12}]$, respectively (*dark grey*, *medium grey* and *white cages*, respectively). The arrangement of the cavities is similar to the structure of some AB_2X_3 compounds, such as UNi_2Al_3, with a $CaCu_5$-type structure. The oxygen atoms (omitted for clarity) would be placed near to the midpoints of the polyhedron edges

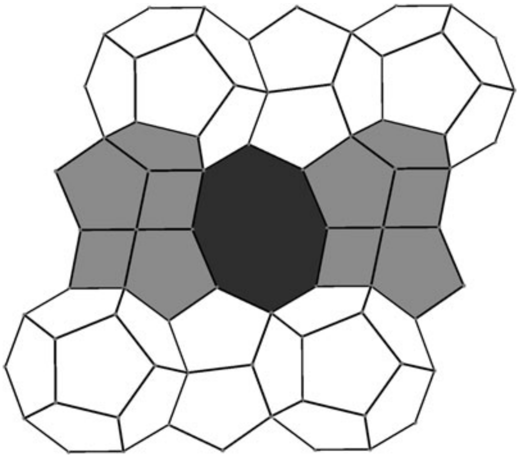

Fig. 6 View of the tetrahedral framework of the DDR-type clathrasil along the axis [110]. Different shadings represent the different types of polyhedra existing in the DDR structure, i.e.: *White*, *light grey* and *dark grey* for $[5^{12}]$, $[4^35^66^1]$ and $[4^35^{12}6^18^3]$ cages, respectively

Cages per unit cell: $3 \times [5^{12}] + 2 \times [4^35^66^3] + 1 \times [5^{12}6^8]$.
Rings per unit cell: $(3 \times 4R) + (30 \times 5R) + (6 \times 6R)$.
Examples of this type of clathrate are:

(a) Hydrates:	Clathrate-hydrate H	$\vert Xe_{5-x}(C_7H_{14})_{1-x}\vert [O_{34}{}^{[4]}H_{68}{}^{[2]}]$	[51]
(b) Oxides:	Dodecasil 1H	$\vert (N_2)_{5-x}(C_5H_{11}N)_{1-x}\vert [Si_{34}{}^{[4]}O_{68}{}^{[2]}]$	[52]

3.2.2 DDR-Type Clathrates

With formula $|\mathbf{M}_9\mathbf{M}'_6\mathbf{M}''_6|[(\mathbf{T}_{36}\mathbf{T}'_{18}\mathbf{T}''_{18}\mathbf{T}'''_{18}\mathbf{T}_{18}{}^{4'}\mathbf{T}_6{}^{5'}\mathbf{T}_6{}^{6'})_{\sum 120}{}^{[4]}O_{240}{}^{[2]}]$, these oxides have a structure based on $[SiO_4]$ tetrahedra, which are connected in such a way that they form layers of face-sharing $[5^{12}]$ pentagonal dodecahedra. Like in the type II clathrates, the layers are stacked in an ABCABC sequence. However, in this case, the layers are interconnected via additional $[SiO_4]$ tetrahedra that form six-membered rings between the layers. Thus, two new types of cavities are generated: a $[4^35^66^1]$ decahedron and a polyhedron with 19 faces ($[4^35^{12}6^18^3]$). This configuration produces a rhombohedral framework (see Table 1 and Fig. 6), with zeolitic properties.

Cages per unit cell: $6 \times [4^35^66^1] + 9 \times [5^{12}] + 6 \times [4^35^{12}6^18^3]$.
Rings per unit cell: $(18 \times 4R) + (108 \times 5R) + (6 \times 6R) + (9 \times 8R)$.
An example of this type of clathrate is:

(a) Oxides:	Dodecasil 3R	$\vert (N_2)_9(C_{10}H_{17}N)_6\vert [Si_{120}{}^{[4]}O_{240}{}^{[2]}]$	[53]

No clathrate hydrates and Zintl phases of this structure type are known.

3.2.3 NON-Type Clathrates

These clathrasils, with formula $|\mathbf{M}_8\mathbf{M}'_8\mathbf{M}''_4|[(\mathbf{T}_{32}\mathbf{T}'_{16}\mathbf{T}''_{16}\mathbf{T}'''_{16}\mathbf{T}_8{}^{4'})_{\sum 88}{}^{[4]}O_{176}{}^{[2]}]$, have a very complex structure (Fig. 7). The framework is generated joining small

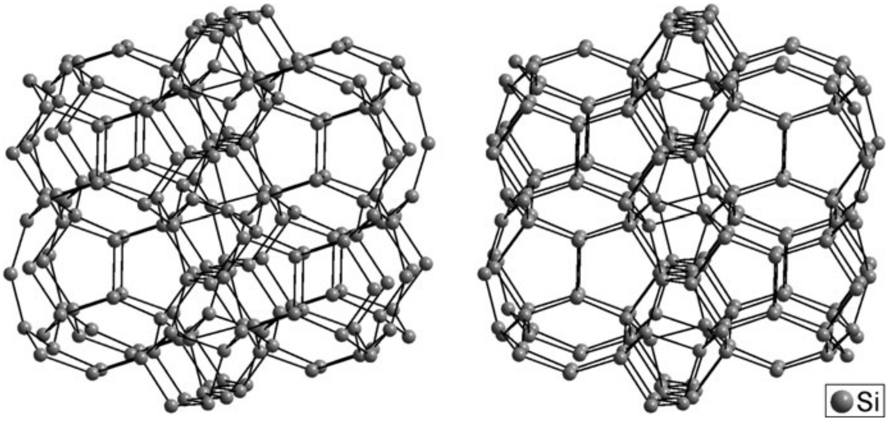

Fig. 7 Stereopair showing the tetrahedral framework of the NON-type clathrasils

nonahedron $[4^1 5^8]$ and octahedron $[5^4 6^4]$ cages, producing larger $[5^8 6^{12}]$ 20-hedron cavities (see Fig. 8). These polyhedra have an atypical non-convex shape; the latter one occludes different types of organic molecules used as templates during the clathrate synthesis.

Cages per unit cell: $8 \times [5^4 6^4] + 8 \times [4^1 5^8] + 4 \times [5^8 6^{12}]$.
Rings per unit cell: $(4 \times 4R) + (64 \times 5R) + (48 \times 6R)$.
Examples of this type of clathrate are:

(a) Oxides:	$\|(C_5H_{13}N)_4\|[Si_{88}{}^{[4]}O_{176}{}^{[2]}]$	[54]
	$\|(Co(C_5H_5)_2)_4F_4\|[Si_{88}{}^{[4]}O_{176}{}^{[2]}]$	[55]

Neither clathrate hydrates nor Zintl phases are known for this structure type.

3.2.4 SGT-Type Clathrates

With formula $|\mathbf{M}_8\mathbf{M}'_4|[(\mathbf{T}_{16}\mathbf{T}'_{16}\mathbf{T}''_{16}\mathbf{T}'''_{16})_{\sum 64}{}^{[4]}\mathrm{O}_{128}{}^{[2]}]$, this clathrate has a skeleton formed by two different types of cavities, $[4^3 5^6]$ nonahedra and larger polyhedra $[5^{12} 6^8]$ of 20 faces, consisting of five- and six-membered rings in a 3:2 ratio. It is interesting to note that each small $[4^3 5^6]$ cavity shares its three four-ring faces with three neighbouring nonahedron cavities, adopting a structure similar to that of the compound $SrSi_2$ at high pressure (see Fig. 9).

Cages per unit cell: $8 \times [4^3 5^6] + 4 \times [5^{12} 6^8]$.

Rings per unit cell: $(12 \times 4R) + (48 \times 5R) + (16 \times 6R)$.

An example of this type of clathrate is:

(a) Oxides:	Sigma-2	$\|(C_{10}H_{17}N)_4\|[Si_{64}{}^{[4]}O_{128}{}^{[2]}]$	[56]

Neither clathrate-hydrates nor Zintl phases of this type are known.

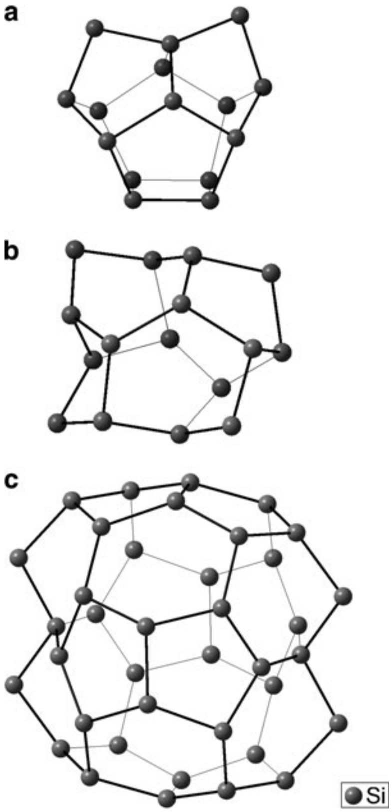

Fig. 8 The polyhedral cavities observed in NON-type clathrasils. (**a**) $[4^1 5^8]$ nonahedron, (**b**) $[5^4 6^4]$ octahedron and (**c**) $[5^8 6^{12}]$ 20-hedron. Oxygen atoms are placed near by the midpoints of the lines connecting neighbouring Si atoms

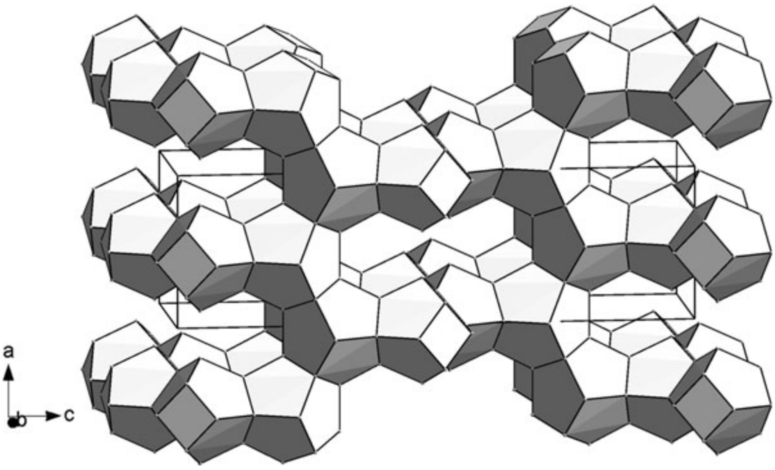

Fig. 9 Host framework of SGT-type clathrates. In this structure, the $[4^3 5^6]$ nonahedra share square faces giving rise to a polyhedron distribution similar to that in the structure of $SrSi_2$ at high pressure

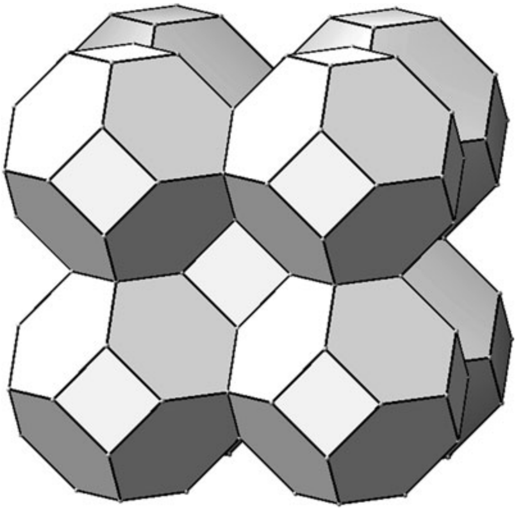

Fig. 10 The space-filling packing of $[4^6 6^8]$ cubo-octahedra in the SOD framework

3.2.5 SOD-Type Clathrates

The aluminosilicate mineral sodalite $|\mathbf{M}_2|[\mathbf{T}_{12}{}^{[4]}\mathrm{O}_{24}{}^{[2]}]$ usually has an Al:Si ratio close to 1, but silica- and alumina-rich sodalites have also been synthesised. The structure (Fig. 10) is one of the simplest tetrahedral frameworks with a space-filling packing of $[4^6 6^8]$ cubooctahedral cages in a bcc-like configuration. These regular truncated octahedra are relatively large cavities with rather small windows, which prevent the guest molecules from migration from one cavity to the next.

Cages per unit cell: $2 \times [4^6 6^8]$.
Rings per unit cell: $(6 \times 4\mathrm{R}) + (8 \times 6\mathrm{R})$.
Examples of this type of clathrate are:

(a) Hydrates:	Clathrate-hydrate SOD	$\|(\mathrm{HPF}_6)_2\|[\mathrm{O}_{12}{}^{[4]}\mathrm{H}_{24}{}^{[2]}]$	[57]
(b) Oxides:	Sodalites	$\|(\mathrm{ClNa}_4)_2\|[\mathrm{Al}_6{}^{[4]}\mathrm{Si}_6{}^{[4]}\mathrm{O}_{24}{}^{[2]}]$	[58]
		$\|(\mathrm{C}_2\mathrm{H}_4(\mathrm{OH})_2)_2\|[\mathrm{Si}_{12}{}^{[4]}\mathrm{O}_{24}{}^{[2]}]$	[59]

No SOD-type Zintl phases have been reported so far.

More examples of sodalite-type compounds can be found in an extensive review on this family of crystalline microporous solids written by Depmeier [60].

3.2.6 AST-Type Clathrates

The framework of the AST-type clathrate, $|\mathbf{M}_4\mathbf{M}'_4|[(\mathbf{T}_{32}\mathbf{T}'_8)_{\sum 40}{}^{[4]}\mathrm{O}_{80}{}^{[2]}]$, consists of a three-dimensional assemblage of $[4^6 6^{12}]$ octadecahedral cages that share all their hexagonal faces, thus forming additional small $[4^6]$ cube-like cages (see Fig. 11).

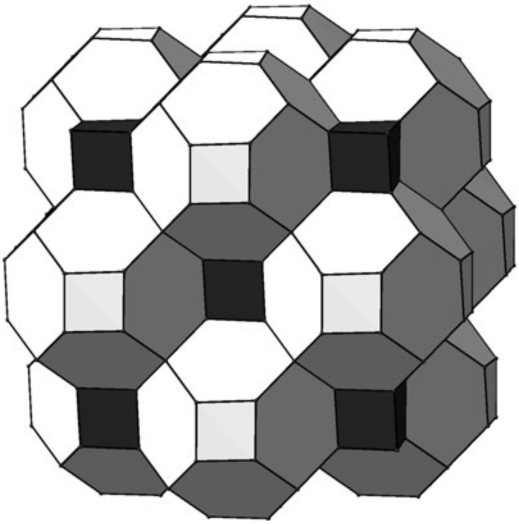

Fig. 11 Host framework of AST-type clathrates. In this structure, the *lightly shaded* $[4^6 6^{12}]$ *cages* share the hexagonal faces giving rise to the formation of additional cubic cages (*darkly shaded ones*). The polyhedra distribution is similar to the structure of NaCl

These two types of cavities are arranged in the same way as the cations and anions in the NaCl-type structure.

Cages per unit cell: 4 × $[4^6]$ + 4 × $[4^6 6^{12}]$.
Rings per unit cell: (24 × 4R) + (24 × 6R).
Examples of this type of clathrate are:

(a) Oxides:	AlPO-16	$|(C_7H_{13}N)_4(H_2O)_{16}|[Al_{20}{}^{[4]}P_{20}{}^{[4]}O_{80}{}^{[2]}]$	[61]
	Octadecasil	$|(C_7H_{12}N)_2F|[Si_{40}{}^{[4]}O_{80}{}^{[2]}]$	[62]

Clathrate hydrates and Zintl phases of this type are unknown.

3.3 Group C Clathrates

These clathrates have only been found as hydrates and as Zintl phases. No oxide with a similar **T** framework is known.

3.3.1 Type III Clathrates

This clathrate type, with ideal formula $|\mathbf{A}_{20}\mathbf{A}'_{10}|[\mathbf{E}_{172}{}^{[4]}]$, has a tetragonal unit cell with 172 framework sites, which form pentagonal dodecahedra $[5^{12}]$, tetrakaidecahedra $[5^{12}6^2]$ and pentakaidecahedra $[5^{12}6^3]$ (see Fig. 12).

Cages per unit cell: 10 × $[5^{12}]$ + 16 × $[5^{12}6^2]$ + 4 × $[5^{12}6^3]$.
Rings per unit cell: (180 × 5R) + (22 × 6R).

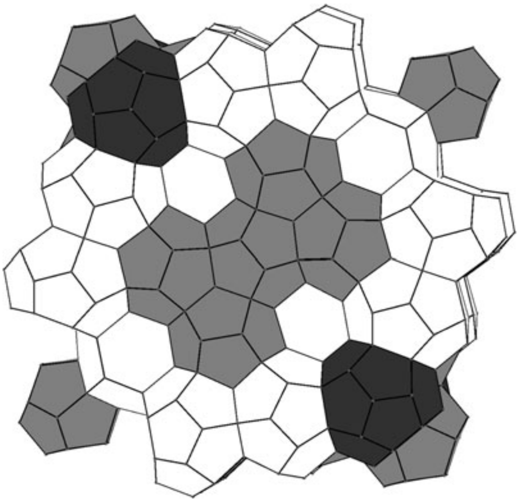

Fig. 12 Polyhedral host framework of the Zintl phase $|Cs_{30}Na_{2.8}|[Sn_{162.4}\square_{9.6}]$ [64]. The different shading indicates the different types of polyhedra present in the structure (*medium grey* for $[5^{12}]$ pentagonal dodecahedra, *dark grey* for $[5^{12}6^{3}]$ pentakaidecahedra and *unshaded* for $[5^{12}6^{2}]$ tetrakaidecahedra). Six percent of the Sn positions are vacant in the structure, as explained in the text

Examples of this type of clathrate are:

(a) Hydrates:	Clathrate-hydrate III	$|((C_4H_9)_4N{\cdot}C_6H_5COO)_4|[O_{172}{}^{[4]}H_{344}{}^{[2]}]$	[63]
(b) Oxides:		Unknown	
(c) Zintl phase:		$|Cs_{30}Na_{2.8}|[Sn_{129.6}{}^{[4]}Sn_{32.8}{}^{[3]}\square_{9.6}]$	[64]

In this Zintl phase, the electrons transferred from the Cs and Na atoms produce a framework with a valence electron concentration higher than 4 e^-/atom. This excess of electrons in the **E** framework gives rise to an underlinked structure. Thus, the Cs and Na atoms transfer almost 33 electrons to an equal number of Sn atoms, transforming them into Ψ-Sb atoms. As a result, these Ψ-Sb atoms are tri-connected and 9.6 vacancies are generated in the idealised fourfold connected framework, $Cs_{30}Na_{2.8}|[Sn_{162.4}\square_{9.6}]$. Note that, in this compound, the number of electropositive atoms slightly exceeds the number of available cavities of the ideal $|\mathbf{A}_{20}\mathbf{A}'_{10}|[\mathbf{E}_{172}]$ compound.

3.3.2 Type VIII Clathrates

This clathrate type is known only as Zintl phase with the general formula $|\mathbf{A}_8|[(\mathbf{E}_{24}\mathbf{E}'_{12}\mathbf{E}''_{8}\mathbf{E}'''_{2})_{\sum 46}{}^{[4]}]$. It has a complex structure in which the more electronegative atoms (**E**) have a fourfold connectivity. This is easily deducible from the Zintl–Klemm concept. The structure consists of a spatial assemblage of $[5^{6}6^{6}]$ dodecahedra (see Fig. 13), but can also be described in terms of two characteristic building units: clusters $\mathbf{E}_8$ and stuffed tetrahedra $\mathbf{E}@(\mathbf{E}_4)$.

Cages per unit cell: 8 × $[5^{6}6^{6}]$.
Rings per unit cell: (24 × 5R) + (24 × 6R).

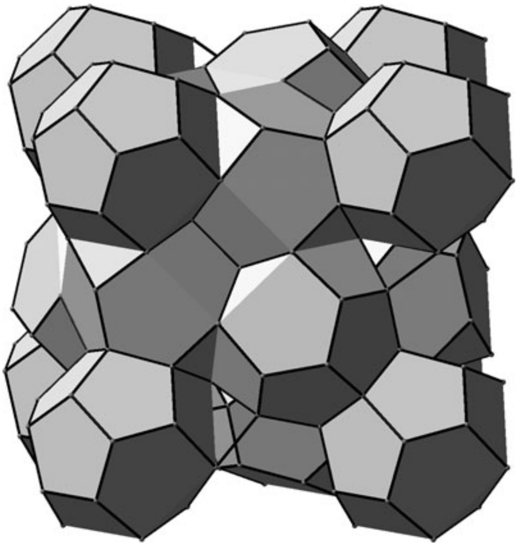

Fig. 13 Structure of the clathrate VIII compound $|Ba_8|[Ga_{16}Sn_{30}]$ [34]. It is formed by $[5^66^6]$ cages of Sn and Ga atoms at the polyhedron vertices and the Ba atoms in the centres of the cavities

Examples of this type of clathrate are:

(a) Zintl phases:	$\|Ba_8\|[Ga_{16}Sn_{30}]$	[34]
	$\|Eu_8\|[Ga_{16}Ge_{30}]$	[33]

Hydrates and oxides of type VIII are unknown.

3.3.3 Type IX Clathrates

Zintl phases of this clathrate type have a general formula $|\mathbf{A}_{12}\mathbf{A}'_8\mathbf{A}''_4|[(\mathbf{E}_{24}\mathbf{E}'_{24}\mathbf{E}''_{12}\mathbf{E}'''_8)_{\sum 68}{}^{[4]}(\mathbf{E}_{24}\mathbf{E}'_8)_{\sum 32}{}^{[3]}]$ and a tetragonal structure characterised by a three-dimensional framework of condensated $\mathbf{E}_{20}$ pentagonal dodecahedra (Fig. 14). The electropositive **A** atoms are located in a narrow 3D channel labyrinth.

Cages per unit cell: 8 × $[5^{12}]$ and big cavities formed by 5R, 11R and 12 R.
Rings per unit cell: (84 × 5R) + (24 × 11R) + (24 × 12R).
Examples of this type of clathrate are:

(a) Zintl phases:	$\|K_{24}[Sn_{92}Bi_8]$	[65]
	$\|Ba_{24}\|[Ge_{84}In_{16}]$	[66]
	$\|K_{32}\|[Sn_{100}]$	[67]
	$\|Ba_{29-x}Eu_x\|[Ge_{100}]$	[68]

Clathrate hydrates and oxides of type IX are unknown.

All the Zintl phases of this type, except the last one, have polyanions with pseudo-stoichiometry Ψ-$Si_{68}P_{32}$ (ratio of tetra-/tri-connected atoms = 17:8), the formation of which is explained by the formal transference of electrons from the more electropositive atoms. The last example, however, has an excess of electrons

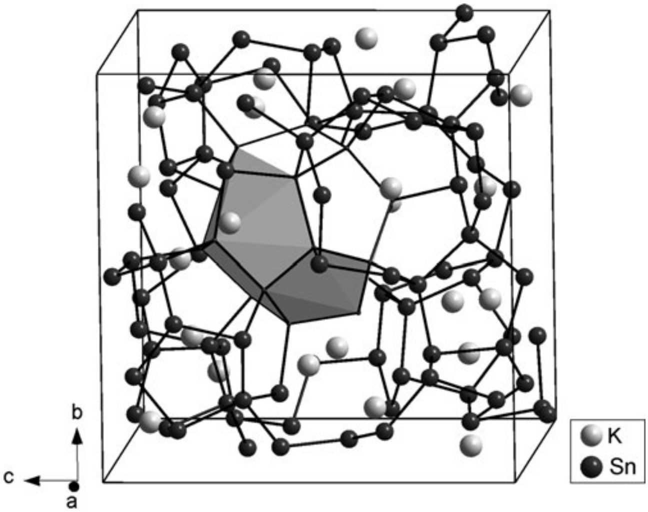

Fig. 14 Structure of the intermetallic clathrate $|K_{32}|[Sn_{100}]$ [67]. The Sn atoms form a polyanion with pseudo-stoichiometry Ψ-$Si_{68}P_{32}$ (Ψ-$Si_{17}P_8$), where Ψ-P atoms are only tri-connected. A pentagonal dodecahedron cavity is also accentuated

per formula unit. These excess electrons were considered by the authors as conduction electrons. Electrical resistivity measurements above 230 K seem to confirm its slight metallic character.

4 Similarities Between Zeolites and Intermetallic Clathrates

Compounds of the zeolite family are characterised by polyhedral cavities interconnected in such a way that they form infinite channels in which the guest atoms or molecules can migrate. In this section, we will see that the structures of some of these zeolites are also similar to certain Zintl phases. These similarities occur when the framework density FD of zeolites is higher than 18.5 **T**/1,000 Å^3. For lower FD values, the structure of the Zintl phases should be very open, becoming unstable.

4.1 ABW-Type Zeolites

Compounds belonging to this group form 3D tetrahedral frameworks consisting of four-, six- and eight-membered rings. The oxygen atoms are located near the midpoints of all the **T**–**T** lines, producing the tetrahedral coordination of these atoms. This structure is represented in Fig. 15.

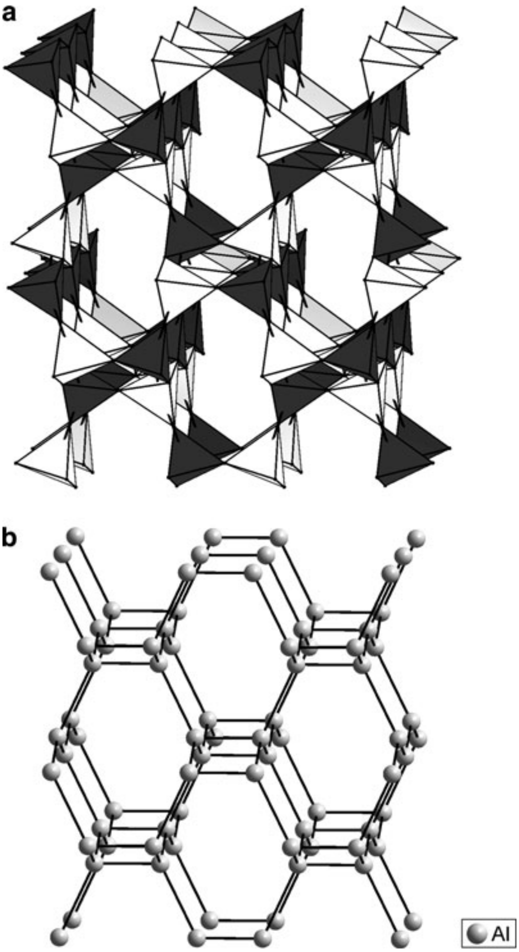

Fig. 15 (**a**) Tetrahedral structure of the aluminosilicate $|Rb_4|[Al_4^{[4]}Si_4^{[4]}O_{16}^{[2]}]$ [70], to compare with the Ψ-Si framework of $SrAl_2$ [71] (**b**). $[AlO_4]$ and $[SiO_4]$ are depicted as *unshaded* and *shaded tetrahedra*, respectively

Cages per unit cell: 4 × $[4^2 6^2 8^2]$.
Rings per unit cell: (4 × 4R) + (4 × 6R) + (4 × 8R).
Examples of this type of zeolite are:

(a) Oxides:	ABW	$|Li_4(H_2O)_4|[Al_4^{[4]}Si_4^{[4]}O_{16}^{[2]}]$	[69]
		$|Rb_4|[Al_4^{[4]}Si_4^{[4]}O_{16}^{[2]}]$	[70]
(b) Zintl phases:		$|Sr_4|[Al_8]$	[71] (=$SrAl_2$)

Clathrate hydrates with ABW structure are unknown.

It is remarkable that this structure is identical to that adopted by the Al (Ψ-Si) atoms in the Zintl phase $SrAl_2$. The structural similarity between the Zintl phase and the tectosilicate is shown in Fig. 15. This similarity is consistent with the EZKC: In $|Rb_4|[Al_4Si_4O_{16}]$, the Rb atoms would donate $4e^-$ to the $[Al_4Si_4]$ skeleton, which is formally converted into a $[Al_4Si_4]^{4-}$ polyanion, that is, a Ψ-Si framework. The oxygen atoms are then situated near the bonding electron pairs, thus giving rise to the tetrahedral coordination. Once more, the cation subarray in an oxide behaves as a Zintl polyanion.

4.2 BCT-Type Zeolites

The structure of the mineral metavariscite, $AlPO_4 \cdot 2H_2O$ [72] belongs to the framework type BCT. Its subarray of aluminium and phosphorus atoms forms a three-dimensional framework in which each Al atom is connected to four P atoms and vice versa [6, 19]. This skeleton, represented in Fig. 16, is formed by four-, six- and

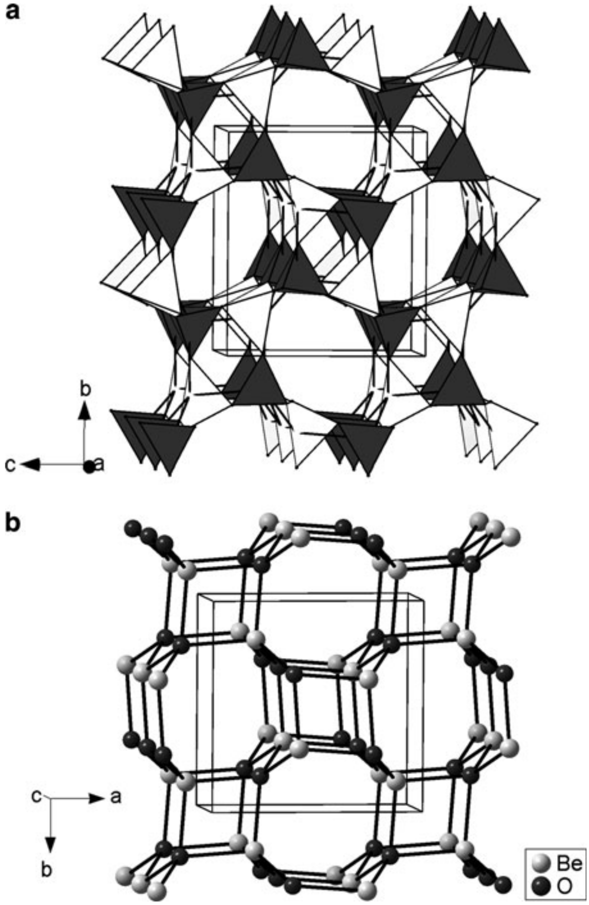

Fig. 16 (**a**) Tetrahedral skeleton in metavariscite $AlPO_4 \cdot 2H_2O$ [72]. [AlO_4] and [PO_4] tetrahedra are depicted as *unshaded* and *shaded tetrahedra*, respectively. [**T**O_4] tetrahedra share all their corners with adjacent tetrahedra and give rise to a **T** substructure similar to that of the II–VI compound β-BeO [75] (**b**)

eight-membered rings in the ratio 2:8:4. The framework presents octagonal channels along the [001] direction with a pore diameter of approximately 2.4 Å.

Cages per unit cell: 2 × $[4^2 6^4]$ + 4 × $[6^2 8^2]$.
Rings per unit cell: (2 × 4R) + (8 × 6R) + (4 × 8R).
Examples of this type of zeolite are:

(a) Oxides:	Metavariscite	$AlPO_4{\cdot}2H_2O$	[72]
	BCT-type zeolite	$|K_{4.56}|[Mg_{2.28}{}^{[4]}Si_{5.72}{}^{[4]}O_{16}{}^{[2]}]$	[73]
(b) Binary compounds:		CrB_4	[74]
		β-BeO	[75]

No clathrate hydrate with BCT framework has been observed.

The framework of $|K_{4.56}|[Mg_{2.28}{}^{[4]}Si_{5.72}{}^{[4]}O_{16}{}^{[2]}]$ is also consistent with the EZKC. This means that a Ψ-Si array is formed when potassium atoms donate their valence electrons to the [Mg–Si] skeleton. In this way, its structure is similar to the AlP array in metavariscite, a Ψ-Si skeleton formed by an equal amount of atoms of the Groups III and V.

The tetrahedral framework of these zeolite-like compounds is strongly related to potential structures of the Group 14 elements. Thus, this array is similar to the boron network in the intermetallic compound CrB_4 and to the structure of the binary oxide β-BeO, a II–VI compound. Although no element of Group 14 with this type of structure is known, it is remarkable that a Zintl phase such as CrB_4, where the boron atoms could be converted into Ψ-C, and a II–VI compound can adopt this same type of structure.

5 Considerations on the Stability of Intermetallic Clathrates and Clathrasils

An analysis of the SBUs (rings) that form the different polyhedra of the structures of intermetallic clathrates and clathrasils can give us some insight into the stability of these compounds. Most of the rings of these skeletons are quasi-planar. This fact becomes evident by analysing the torsion angles of all the five- and six-membered rings present in these structures. Moreover, the angles ∠**E-E-E** in the intermetallic clathrates and ∠**T-T-T** in the clathrasils are close to those of the different regular polygons: 60° for the triangle, 90° for the square, 108° for the pentagon and 120° for the hexagon. The exception is the NON-type clathrasil, whose rings deviate considerably from regular polygons (see Figs. 7 and 8).

Consider now the **E** frameworks in intermetallic clathrates. They mainly consist of Group 14 or pseudo-Group 14 elements that are tetra-connected. Si atoms in these clathrates, for instance, have a strong hybridisation of the 3*s* orbital with the three 3*p* orbitals to form four equivalent lobes of a sp^3 hybrid orbital, all pointing towards the corners of a regular tetrahedron. In this case, the Si atoms form directed bonds with angles close to the tetrahedral value of 109.5° (the ideal

sp^3 hybridisation). Among the regular polygons, the angles of the pentagon are the closest to those of a tetrahedron. This suggests that the existence of a large portion of five-membered rings in the structure might be connected to a higher thermodynamic stability of a compound. If this is correct, it would imply that type I and type II clathrates would show a higher stability as a consequence of its higher proportion of 5R in their structures (89 and 90%, respectively). This could explain why these types of clathrates exist not only as Zintl phases but as oxides as well.

Another fact that seems to support the hypothesis of the stability of structures rich in 5R is the observed high-temperature phase transition in $|Eu_8|[Ga_{16}Ge_{30}]$ [33]. When this compound is annealed below 687°C, a type VIII clathrate structure appears, whereas above this temperature, this phase transforms into a type I clathrate structure, increasing the portion of five-membered rings from 50 to 89%.

On the other hand, in clathrasils and zeolites, **T** atoms are directly bonded to four oxygen atoms, each one bridging two **T** atoms (**T**–O–**T**). The presence of oxygen atoms in the structure implies that the angles ∠**E–E–E** of the intermetallic clathrates are replaced by angles ∠**T–O–T** what would add a certain degree of flexibility to the angles between **T** atoms. Thus, the structures of intermetallic clathrates of Group B, which have a higher ratio of four- and six-membered rings, would be more stable as the corresponding oxides. In spite of the fact that all their rings are 4R, 6R or 8R, the zeolites analysed in the previous section present structural coincidences with related Zintl phases and some binary compounds with a Ψ-Si framework.

It is worth mentioning here that mean values of ∠**T–O–T** angles, as determined in crystal-structure analyses with diffraction methods, are considerably larger than corresponding values in dense frameworks, such as pyroxenes, feldspars and quartz. This is particularly true for clathrasils (oxides) of high crystallographic symmetry, where the average angle is close to 180° (in contrast with the mean angle of 140° in denser silicates). Such almost straight Si–O–Si bonds are feigned by dynamic or static disorder of the oxygen atoms. In most cases, the true angles are in fact considerably smaller ([2], p. 24ff). Nevertheless, it can be concluded that the O atoms seem to play a similar role as a bonding electron pair [3, 6, 19].

6 Conclusions

In this work, we have reported a comprehensive and comparative study of the structures of both, the intermetallic clathrates and porous tectosilicates (clathrasils and some zeolites). The skeletons of the former have been explained in terms of the Zintl concept and Pearson's octet rule. It has been shown that oxides tend to adopt structures similar to those of the corresponding intermetallic compounds. The structures of oxides seem to be determined by a combination of two factors: (a) the cation recognition: Cations seem to recognise themselves in spite of being embedded in an oxygen matrix. The nature and physical meaning of this "interaction" is at present a challenge for theoretical chemistry. (b) The oxygen behaviour:

Oxygen atoms seek to complete their outer valence-electron shells with two electrons. These would be provided by the bonding electron pairs. This is the main reason why oxides tend to adopt structures similar to those of isoelectronic Zintl polyanions.

Another interesting aspect is the existence of a correspondence between the metal atom sites in some compounds and the location of the cage centres in clathrates. Frank and Kasper were the first to recognise that type I and type II clathrates were dual to the structures of Cr_3Si and $MgCu_2$ alloys. In this work, we have seen that there are more similarities of this kind, i.e.: DOH-type clathrates and the structure of $CaCu_5$ or SGT-type clathrates and the high pressure modification of $SrSi_2$. One might assume that these similarities were just mere coincidences, but nature does not usually act at random. The challenge of giving insight into these resemblances remains open.

Acknowledgements Thanks are due to Dr. Olga Prieto and Dr. Raquel Chulia for valuable suggestions. Financial support from Spanish MICCIN under project CTQ2009-14596-C02-01 as well as from Comunidad de Madrid and European Social Fund: S2009/PPQ-1551 4161893 (QUIMAPRES) is gratefully acknowledged.

References

1. Klein HJ, Liebau F (2008) Computerized crystal-chemical classification of silicates and related materials with CRYSTANA and formula notation for classified structures. J Solid State Chem 181:2412–2417
2. Liebau F (1985) Structural chemistry of silicates. Structure, bonding and classification. Springer, Berlin
3. Santamaria-Perez D, Vegas A, Liebau F (2005) The Zintl–Klemm concept applied to cations in oxides. II. The structure of silicates. Struct Bond 118:121–177
4. Grzechnik A, Vegas A, Syassen K et al (2000) Reversible antifluorite to anticotunnite phase transition in Li_2S at high pressures. J Solid State Chem 154:603
5. Martinez-Cruz LA, Ramos-Gallardo A, Vegas A (1994) MSn and $MSnO_3$ ($M = Ca, Sr, Ba$): new examples of oxygen-stuffed alloys. J Solid State Chem 110:397–398
6. Santamaria-Perez D, Vegas A (2003) The Zintl–Klemm concept applied to cation in oxides. I. The structures of ternary aluminates. Acta Crystallogr B 59:305–323
7. Santamaria-Perez D, Vegas A, Müller U (2005) A new description of the crystal structures of tin oxide fluorides. Solid State Sci 7:479–485
8. Vegas A (2000) Cations in inorganic solids. Crystallogr Rev 7:189–283
9. Vegas A, Grzechnik A, Hanfland M et al (2002) Antifluorite to Ni_2In-type phase transition in K_2S at high pressures. Solid State Sci 4:1077–1081
10. Vegas A, Grzechnik A, Syassen K et al (2001) Reversible phase transitions in Na_2S under pressure: a comparison with the cation array in Na_2SO_4. Acta Crystallogr B 57:151–156
11. Vegas A, Jansen M (2002) Structural relationships between cations and alloys: an equivalence between oxidation and pressure. Acta Crystallogr B 58:38–51
12. Vegas A, Mejía-López J, Romero AH et al (2004) Structural similarities between Ti metal and titanium oxides: implications on the high-pressure behavior of oxygen in metallic matrices. Solid State Sci 6:809–814
13. Vegas A, Santamaria-Perez D, Marques M et al (2006) Anions in metallic matrices model: application to the aluminium crystal chemistry. Acta Crystallogr B 62:220–227

14. Marques M, Florez M, Recio JM et al (2006) Structure, metastability and electron density of Al matrices in the light of the model of anions in metallic matrices. J Chem Phys B 110:18609–18618
15. Wondratchek H, Merker L, Schubert K (1964) Beziehungen zwischen der Apatit-Struktur und der Struktur der Verbindungen vom Mn_5Si_3-(D88)Typ. Z Kristallogr 120:393–395
16. Addison WE (1965) Structural principles in inorganic compounds. Longmans, London
17. Wells AF (1975) Structural inorganic chemistry. Clarendon, Oxford
18. O'Keeffe M, Hyde BG (1985) An alternative approach to non-molecular crystal structures. With emphasis on the arrangement of cations. Struct Bond 61:77–144
19. Santamaria-Perez D (2006) Reinterpretación de las estructuras de aluminatos y silicates. Equivalencia entre oxidación y presión. PhD thesis, University Carlos III, Madrid
20. Klemm W (1958) Centenary-lecture – metalloids and their compounds with the alkali metals. Proc Chem Soc Lond 12:329–341
21. Zintl E (1939) Intermetallische Verbindungen. Angew Chem 52:1–100
22. Pearson WB (1964) Crystal structures of semiconductors and a general valence rule. Acta Crystallogr 17:1–15
23. Davy H (1811) Philos Trans R Soc Lond 101:1
24. Sloan ED, Koh CA (2007) Clathrate hydrates of natural gases, 3rd edn. CRC, Taylor and Francis Group, Boca Raton
25. Powell HM (1948) The structure of molecular compounds. 4. Clathrate compounds. J Chem Soc: 61–73
26. Liebau F (1983) Zeolites and clathrasils – two distinct classes of framework silicates. Zeolites 3:191–193
27. Baerlocher C, McCusker LB, Olson DH (2007) Atlas of zeolite framework types, sixth revised edition. Elsevier, Amsterdam
28. Brunner GO, Meier WM (1989) Framework density distribution of zeolite-type tetrahedral nets. Nature 337:146–147
29. von Stackelberg M, Müller HR (1954) Feste Gashydrate: II. Struktur und Raumchemie. Z. Elektrochem 58:25–39
30. Gies H (1983) Studies on clathrasils. 3. Crystal-structure of melanophlogite, a natural clathrate compound of silica. Z Kristallogr 164:247–257
31. von Schnering HG, Menke H, Kröner R et al (1998) Crystal structure of the clathrates $Rb_8In_8Ge_{38}$ and $K_8In_8Ge_{38}$. Z Kristallogr NCS 213:673–674
32. Kasper JS, Hagenmuller P, Ponchard RM et al (1965) Clathrate structure of silicon and Na_xSi_{136}. Science 150:1713–1714
33. Paschen S, Carrillo-Cabrera W, Bentien A et al (2001) Structural, transport, magnetic and thermal properties of $Eu_8Ga_{16}Ge_{30}$. Phys Rev B 64:214404
34. Eisenmann B, Schäfer H, Zagler R (1986) $A_8B_{16}B'_{30}$ compounds (A=Sr, Ba; B=Al, Ga; B′=Si, Ge, Sn) and their cage structures. J Less Common Metals 118:43–55
35. Yang L, Wang Y, Liu T et al (2005) Copper position in type-I $Ba_8Cu_4Si_{42}$ clathrate. J Solid State Chem 118:1773–1777
36. Kuhl B, Czybulka A, Schuster HU (1995) New ternary clathrate compounds in the system Ba-In/Zn/Cd-Ge: Zintl compounds with phase width? Z Anorg Allg Chem 621:1–6
37. Shatruk MM, Kovnir KA, Lindsjö M et al (2001) Novel compounds $Sn_{10}In_{14}P_{22}I_8$ and $Sn_{14}In_{10}P_{21.2}I_8$ with clathrate I structure: synthesis and crystal and electronic structure. J Solid State Chem 161:233–242
38. Kovnir KA, Shatruk MM, Reshetova LN et al (2005) Novel compounds $Sn_{20}Zn_4P_{20.8}I_8$, $Sn_{17}Zn_7P_{22}I_8$, and$Sn_{17}Zn_7P_{22}Br_8$: synthesis, properties, and special features of their clathrate-like crystal structures. Solid State Sci 7:957–968
39. Mudryk Y, Rogl P, Paul C et al (2002) Thermoelectricity of clathrate I Si and Ge phases. J Phys Condens Matter 14:7991–8004
40. Corbett JD (1996) Zintl phases of the early p-block elements. In: Kauzlarich SM (ed) Structure and bonding of Zintl phases and ions. VCH, Weinheim

41. Jaussand N, Toulemonde P, Pouchard M et al (2004) High-pressure synthesis and crystal structure of two forms of a new tellurium–silicon clathrate related to the classical type-I. Solid State Sci 6:401–411
42. von Schnering HG (1985) Zintl-phases: Prinzipien von Struktur und Bindung. Nova Acta Leopoldina Halle 59:168–182
43. von Schnering HG, Kröner R, Baitinger M et al (2000) Crystal structure of the defect clathrate Cs_8Sn_{44} square (2). Z Kristallogr NCS 215:205–206
44. Shevelkov AV, Shatruk MM (2001) Mercury and cadmium pnictidehalides: the inverted Zintl phases. Russ Chem Bull 50:337–352
45. Vegas A, Santamaria-Perez D (2003) The structures of ZrNCl, TiOCl and AlOCl in the light of the Zintl–Klemm concept. Z Kristallogr 218:466–469
46. Higgins JB (1994) Silica zeolites and clathrasils. Rev Miner Geochem 29:507–543
47. Hondoh T, Anzai H, Goto A et al (1990) The crystallographic structure of the natural air-hydrate in Greenland Dye-3 deep ice core. J Inclus Phenom 8:17–24
48. Gies H (1984) Studies on clathrasils. 6. Crystal-structure of dodecasil-3C, another synthetic clathrate compound of silica. Z Kristallogr 167:73–82
49. Kröner R, Peters K, von Schnering HG (1998) Crystal structure of the clathrate-II, $Ba_{16}Ga_{32}Sn_{104}$. Z Kristallogr NCS 213:664
50. Bobev S, Sevov SC (1999) Synthesis and characterization of stable stoichiometric clathrates of silicon and germanium: $Cs_8Na_{16}Si_{136}$ and $Cs_8Na_{16}Ge_{136}$. J Am Chem Soc 121:3795–3796
51. Ripmeester JA, Tse JS, Ratcliffe CI et al (1987) A new clathrate hydrate structure. Nature 325:135–136
52. Gerke H, Gies H (1984) Studies on clathrasils. 4. Crystal structure of dodecasil-1H, a synthetic clathrate compound of silica. Z Kristallogr 166:11–22
53. Gies H (1986) Studies on clathrasils. 9. Crystal structure of decadodecasil 3R, the missing link between zeolites and clathrasils. Z Kristallogr 175:93–104
54. Marler B, Dehnbostel N, Eulert HH et al (1986) Studies on clathrasils. 8. Nonasils-$[4^1 5^8]$, $88SiO_2{\cdot}8M^8{\cdot}8M^9{\cdot}4M^{20}$ – Synthesis, thermal-properties, and crystal-structure. J Inclus Phenom 4:339–349
55. van der Goor G, Freyhardt CC, Behrens P (1995) The cobalticinium cation $[Co^{III}(eta(5)\text{-}C_5H_5)_2]^+$. A metal organic complex as a novel template for the synthesis of clathrasils. Z Anorg Allg Chem 621:311–322
56. McCusker LB (1988) The ab initio structure of sigma-2 (a new clathrasil phase) from synchrotron powder diffraction data. J Appl Cryst 21:305–310
57. Bode H, Teufer G (1955) Die Kristallstrktur der Hexafluorophisphorsaeure. Acta Crystallogr 8:611–614
58. Wartchow R (1997) Redetermination of the crystal structure of hexaaluminium hexasilicon octasodium dichloride tetracosaoxide (sodalite), $Na_8(Al_6Si_6O_{24})Cl_2$. Z Kristallogr NCS 212:80
59. Richardson JW, Pluth JJ, Smith JV et al (1988) Conformation of ethylene-glycol and phase-change in silica sodalite. J Phys Chem 92:243–247
60. Depmeier W (2005) The sodalite family. A simple but versatile framework structure. Rev Miner Geochem 57:203–240
61. Bennett JM, Kirchner RM (1991) The structure of As-synthesized $AlPO_4$-16 determined by a new framework modelling method and Rietveld refinement of synchrotron powder diffraction data. Zeolites 11:502–506
62. Caullet P, Guth JL, Hazm J et al (1991) Synthesis, characterization and crystal-structure of the new clathrasil phase octadecasil. Eur J Solid State Inorg Chem 28:345–361
63. Bonamico M, McMullan RK, Jeffrey GA (1962) Polyhedral clathrate hydrates. III. Structure of tetra n-butyl ammonium benzoate hydrate. J Chem Phys 37:2219–2231
64. Bovev S, Sevov SC (2001) Clathrate III of group 14 exists after all. J Am Chem Soc 123:3389–3390

65. Fässler TF (1998) Lone pair interactions in Zintl phases: Band structure and real space analysis of the cP124 clathrate structure type. Z Anorg Allg Chem 624:569–577
66. von Schnering HG, Kröner R, Carrillo-Cabrera W et al (1998) Crystal structure of the novel chiral clathrate, $Ba_6In_4Ge_{21}$. Z Kristallogr NCS 213:665–666
67. Zhao JT, Corbett JD (1994) Zintl phases in alkali-metal-tin systems – K_8Sn_{25} with condensed pentagonal dodecahedra of tin – 2 A(8)Sn(44) phases with a defect clathrate structure. Inorg Chem 33:5721–5726
68. Carrillo-Cabrera W, Cardoso Gil R, Paschen S (2003) Crystal structure of barium europium germanide, $Ba_{6-x}Eu_xGe_{25}$ ($x = 0.6$), a chiral clathrate. Z Kristallogr NCS 218:397–398
69. Kerr IS (1974) Crystal-structure of a synthetic lithium zeolite. Z Kristallogr 139:186–195
70. Klaska R, Jarchow O (1975) Die Kristallstruktur und die Verzwillingung von $RbAlSiO_4$. Z Kristallogr 142:225–238
71. Cordier G, Czech E, Schäfer H (1982) On a high-pressure modification of $SrAl_2$. Z Naturforsch B37:1442–1445
72. Kniep R, Mootz D (1973) Metavariscite – redetermination of its crystal-structure. Acta Crystallogr B 29:2292–2294
73. Dollase WA, Ross CR (1993) Crystal structures of the body-centered tetragonal tectosilicates – $K_{1.14}Mg_{0.57}Si_{1.43}O_4$, $K_{1.1}Zn_{0.55}Si_{1.45}O_4$ and $K_{1.11}Fe_{1.11}Si_{0.89}O_4$. Am Miner 78:627–632
74. Andersson S, Lundström T (1968) The crystal structure of CrB_4. Acta Chem Scand 22: 3103–3110
75. Smith DK, Cline CF, Austerman SB (1965) Crystal structure of beta-beryllia. Acta Crystallogr 18:393–397

Struct Bond (2011) 138: 31–66
DOI: 10.1007/430_2010_34

Crystal Structures of Inorganic Oxoacid Salts Perceived as Cation Arrays: A Periodic-Graph Approach

Vladislav A. Blatov

Abstract A total of 569 crystal structures of anhydrous simple salts $M_y(LO_3)_z$ (L = B, C, N, S, Se, Te, Cl, Br, I) and $M_y(XO_4)_z$ (X = Si, Ge, P, As, S, Se, Cl, Br, I) are considered as three-periodic nets of $M_y(L/X)_z$, where M are cations derived from metal atoms whereas (L/X) are conventional cations derived from nonmetal atoms. Both L and X cations are located in the centers of triangular/trigonal-pyramidal LO_3 and tetrahedral XO_4 oxoanions, respectively. The cation arrays (M+L/X) are proved to be the elements determining and governing the topology of the respective crystal structures, whereas the oxygens seem to play a secondary role as links between the cations. The preponderant role of cations in determining the crystal structures is founded on a greater uniformity (regularity) of their arrays when compared with those of anions or, even, with mixed cation–anion arrangements. In about three-fourth of the crystal structures analyzed in this work, the cation arrays appear to be topologically equivalent to some binary compounds, such as NaCl, NiAs, FeB, and α-Al_2O_3. The influence of both charge and size on the resulting array topology is also studied in detail. A quasi-binary representation $M_y[L/X]_z$ is proposed as a general model for the crystal structures of these anhydrous oxoacid salts.

Keywords Cation arrays, Ionic packings, Oxoacid salts, Periodic graph, Software and databases

Contents

1 Introduction 32
2 Periodic-Graph Approach in Crystal Chemistry 33
  2.1 Terminology 33
  2.2 The Concepts of Structure Representation, Underlying Net, and Packing Net 37
  2.3 Computer Tools to Study Periodic Graphs 40

V.A. Blatov
Samara State University, Ac. Pavlov St. 1, Samara 443011, Russia
e-mail: blatov@ssu.samara.ru

3 Underlying Nets and Cation Arrays in Inorganic Oxoacid Salts 41
3.1 Oxoacid Salts with Triangular Anions 41
3.2 Oxoacid Salts with Trigonal-Pyramidal Anions 48
3.3 Oxoacid Salts with Tetragonal Anions 52
3.4 Uniformity of Cation Arrays in Inorganic Oxoacid Salts 59
4 General Regularities in the Cation Arrays 60
5 Concluding Remarks 62
References 63

1 Introduction

Those crystal structures with a pronounced ionic bonding have represented a good field for exploring crystallochemical models and theories. Since the very beginning, two of these models have become widely used and commonly accepted. Usually, ions are considered to have well-defined sizes of approximate spherical shape that can be described within a simple geometrical *model of sphere packing*. Since the Coulomb forces are nondirectional, one can apply a *model of point charges* being in equilibrium.

Both models postulate that one ionic component (cations or anions) determines the structure pattern, while the other component plays a subordinate role following the structure-forming component and introducing only slight modifications in the "ideal" skeleton. However, the roles of the components can be quite different in the two models. In most tables of ionic radii, anions are larger than cations, so that the first model ordinarily represents the ionic crystal as packing of anions with cations occupying the packing holes. In contrast, the second model considers cations as the structure-forming component since they usually have larger effective charges than anions. The model of sphere packing is the oldest one in crystal chemistry and is commonly used for description of inorganic ionic compounds even nowadays.

In 1972, Lebedev [1] stressed the priority of connections between cations, in particular, in the rutile crystal structure. Then, O'Keeffe and Hyde, in a series of publications [2–4], drew attention to the fact that many ionic crystals can be considered as regular arrays of cations, while anions play a subordinate role (oxygen-stuffed alloys). The regular arrangement of cations was called *eutactic* [2] to emphasize that although the centers of cations often occupy the positions of a regular packing, the cations do not touch each other. Borisov [5] showed that the structure types of heavy-cation oxides, fluorides, and sulfides are determined by the cation arrays densely packed into almost planar layers.

In many cases, the cation array in complex oxides reproduces the structure of simple intermetallic or ionic compounds with the same stoichiometry. In both cases, however, oxygens are considered as a medium and the complex oxide can be treated as an "anion-stuffed alloy" [4]. For instance, the cation array Ca_2Si in larnite (β-Ca_2SiO_4) is arranged like δ-Ni_2Si where a main metallic bonding is assumed [4]. On the contrary, the sodium and sulfur cations in Na_2SO_4 adopt the structure of an ionic compound like the high-pressure phase of Na_2S [6].

Many other examples of such similarities are collected in [7] and a brief consideration of inorganic oxysalts as cation arrays can be found in [8].

O'Keeffe and Hyde [3, 4] illustrated the eutaxy by many examples and considered this phenomenon as a result of mutual repulsion of cations. Further attempts to interpret these experimental facts were undertaken by Vegas et al. [6, 7, 9–12], by extending the Zintl–Klemm concept to the cation arrays in oxides. It should be recalled that the original Zintl concept [13] was conceived to explain the crystal structures of compounds formed between highly electropositive atoms (A) and main-group atoms (X). The resulting structure consists of an X-skeleton in which the X atoms are bonded by directed covalent bonds, whose connectivity obey the 8-N rule (where N is the number of valence electrons of X). In this type of compounds (the so-called Zintl-phases), it is assumed that all valence electrons of the A atoms are formally transferred to the X atoms, forming so a negatively charged X-skeletons known as Zintl polyanions. Because the X-skeletons adopt the structure of the element, whose number of electrons is equal to N plus the electrons transferred from A, Klemm [14] named the X atoms as pseudo-atoms. Vegas [7] extended the Zintl–Klemm concept to oxides with complex oxoanions $[XO_n]$ and rationalized the structures of many ionic compounds.

The cation array model was then developed in [15–17] by applying the concept of an infinite graph (net), which allows one to formally describe the cation arrays and to analyze their geometrical-topological properties with strict computer algorithms. Using the program package TOPOS [18], we studied topological motifs in all known crystal structures of inorganic salts of formulae $M_y[LO_3]_z$ or $M_y[XO_4]_z$. In them, the $[LO_3]$ groups have either trigonal or trigonal-pyramidal geometry, and the $[XO_4]$ oxoanions are tetrahedral. The study revealed that more than 50% of the structures followed the motifs of binary compounds A_yX_z. The *eutaxy* of those arrays was evaluated by numerical criteria of uniformity, based on the Voronoi partition of the crystal space.

Our aim, in this chapter, is to extend the analysis of the cation arrays, using novel methods of crystal structure taxonomy. These methods are based on the concept of underlying net derived from the periodic-graph approach and have been initially developed to explore metal-organic frameworks [19]. We will show the general applicability of these new tools that can be easily adjusted to describe the crystal structures of any composition and bonding type.

2 Periodic-Graph Approach in Crystal Chemistry

2.1 Terminology

The term "topology" is often used in chemistry rather ambiguously [20]. Although in most cases the crystal chemists admit that topology describes the properties of connectivity of the crystal space, even the assertion that "the structures are topologically equal (similar, different) to…" is usually drawn after a visual analysis, comparing only a few local topological properties of the structures, while the overall structure topology is the natural crystallochemical subject. In short, crystal chemistry begins when the crystal structure topology is taken into consideration.

Below, we briefly consider the simplest formalization of the crystal space topology perceived as a periodic graph. A more detailed terminology on this topic can be found in [21].

Graph is a set of vertices (points); each ordered pair of the vertices determines an edge of the graph. The set of all edges is called the *topology* of the graph. Since in crystal chemistry the graph vertices and edges correspond to atoms and interatomic bonds, respectively, the chemical term "topology" means merely the set of all interatomic bonds in the crystal structure.

Net is a kind of *infinite* graph that is *simple* (it has no loops, multiple or directed edges) and *connected* (any pair of vertices in the graph is connected by a chain of edges); vertices of the graph are often called *nodes* of the net. The *degree n* of a node is the number of edges incident to the node; it is equivalent to coordination number of the corresponding atom, so that the node (atom) is called *n*-coordinated. A *subnet* (*supernet*) of the net *A* is a net whose sets of nodes and edges are subsets (supersets) of corresponding sets of *A*. Two nets are called *isomorphic* if there is one-to-one mapping between the sets of their nodes and edges. The symmetry of the net is described by an *automorphism group* that enumerates all possible permutations of nodes giving rise to isomorphic nets; this symmetry does not involve any geometrical realization of the net and, hence, can be considered as "topological" symmetry of the corresponding chemical structure. Net is *n-periodic* if its automorphism group contains a subgroup being isomorphic to a group of *n*-independent translations. When we consider some arrangement of the net nodes in the space, we speak about an *embedding* of the net. The symmetry of the net embedding can be lower (but not higher) than the symmetry of the net. *Coordination figure* of the node is the solid formed by nodes incident to this node; if the coordination figure has a polyhedral form, it corresponds to the coordination polyhedron of the corresponding atom. The net is *uninodal* (*bi*-, *tri*-,…, *polynodal*) if all its nodes are equivalent by symmetry (or there are two, three,…, many nonequivalent nodes).

If the crystal structures have isomorphic nets, they are called (topologically) *isotypic* belonging so to the same *topological type* [22]. Since the notion of isomorphism is strictly determined, the concept of topological type is a way to an objective taxonomy (independent of the visual analysis) of crystal structures. Note that the oldest primary classification taxon in crystal chemistry, *structure type*, arranges crystal structures according to their geometrical properties (unit cell dimensions, space group, atomic positions). In contrast, topological type includes all structures with the same system of chemical bonds irrespective of their embeddings. To designate the topological type, we can use the name of one of its representatives as well as the symbol of the net corresponding to the type. In this chapter, we will use three kinds of nomenclature for net symbols: (1) three-letter symbols from the RCSR database, (2) *sqc*XXX EPINET codes (see Sect. 2.3), and

(3) **s**-*d*-*G*-*n* symbols proposed in [23] for the subnets derived from the most important crystallochemical nets. For example, the RCSR symbols **dia** (the corresponding EPINET code *sqc*6) and **dia-b** are assigned to both the diamond net and the isotypic binary compound (sphalerite, ZnS), with the same topology, but with two chemically and crystallographically nonequivalent atoms. The **s**-*d*-*G*-*n* symbol **nia**-5,5-$Pna2_1$ designates the subnet derived from the RCSR **nia** (NiAs) net with two topologically different 5-coordinated atoms, and the maximum-symmetry embedding of the net has the space group $Pna2_1$. If a net does not fall in any topological classification, we designate it by the Cambridge Structural Database Reference Code or by the chemical formula of the corresponding compound.

When performing the topological taxonomy, the problem that emerges is how to compare two infinite objects that are periodic nets. The representation of a periodic net as a finite object is achieved by means of the concept of *labeled quotient graph* [24]. The labeled quotient graph is a graph whose vertices and edges correspond to infinite sets of both translation-equivalent nodes and edges of the net; the corresponding atoms and bonds occupy the same primitive cell of the crystal structure. Hence, the labeled quotient graph is finite, but it stores all the information about the net topology. It is extremely important to develop the theory of labeled quotient graphs; this theory could play the same role for crystal chemistry as space-group theory did for crystallography. Such attempts have been undertaken in recent years [25–27].

Topological index of a net is a set of numbers that is related to the net topology. The net topology is completely described by the *adjacency matrix* of the labeled quotient graph; the adjacency matrix contains the information about all edges (chemical bonds) of the net. Thus, the adjacency matrix can be used as the strictest topological index to check the isomorphism of the nets [28] and also to relate the crystal structures to the same topological type. For a quick comparison of the net topologies or to find non-strict topological similarities, one can use other kinds of topological indices [23, 29]. *Coordination sequence* $\{N_k\}$ is a set of numbers N_1, $N_2, \ldots$ representing the atoms in the first, second, etc., coordination shells around a given atom of the net (Fig. 1). The first ten coordination shells are usually considered for the topological classification. The cumulative number of atoms in the first ten coordination shells averaged over all nonequivalent atoms (TD_{10}) is defined as the *topological density* of the net; the larger TD_{10}, the denser the net, i.e., the more neighbors are in a local area of the net node. *Point symbol* lists the shortest circuits (closed chains of connected atoms) meeting at all bond angles of each nonequivalent atom in the net. *Extended* point symbol gives the information on circuits in more detail, while *net* point symbol summarizes the point symbols for all nonequivalent atoms with the corresponding stoichiometric coefficients. *Vertex symbol* gives the information similar to extended point symbol but for rings (circuits without shortcuts). If the nets have equal sets of all these indices, they are assumed to be topologically isotypic [23]. If the sets of indices are different, but close to each other, the nets can be considered topologically similar. The same can be said of different atoms in the same structure: if their indices are identical, the atoms are topologically equivalent even if they are not related by a space-group operation.

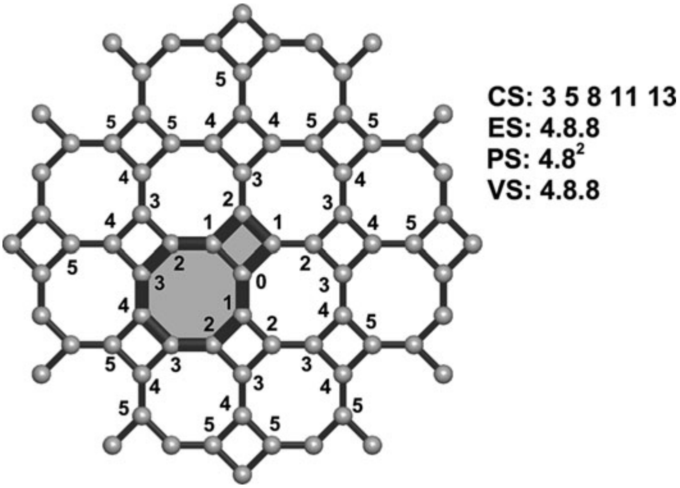

Fig. 1 Coordination sequence (CS), extended point symbol (ES), point symbol (PS), and vertex symbol (VS) for the uninodal 2-periodic net **fes**. A 10-circuit is selected that is not a ring (it has a shortcut and composed of two smaller 4- and 8-rings). The nodes of the first five coordination shells are marked by the ordinal number of shell; the initial atom of the sequence formally corresponds to the zero coordination shell

Table 1 Topological indices in **pcu-b**, **nia**, and related 6-coordinated nets

Net (representative)	Net point symbol	Coordination sequence N_{1-5}
pcu-b (NaCl)	$\{4^{12}.6^3\}$	Na, Cl: 6 18 38 66 102
nia (NiAs)	$\{4^{12}.6^3\}\{4^9.6^6\}$	Ni: 6 20 42 74 114
		As: 6 18 42 74 114
sev-6-*C*2/*m* (β-$HgSeO_3$)	$\{4^{10}.6^5\}$	Hg, Se: 6 19 42 74 115
HIYXUJ ($CaSeO_3$)	$\{4^{10}.6^5\}\{4^{11}.6^4\}$	Ca: 6 18 40 70 108
		Se: 6 19 40 70 108
FEQWOO ($NaIO_3$)	$\{4^8.6^6.8\}\{4^{13}.6^2\}$	Na: 6 16 42 72 114
		I: 6 20 42 74 114

For example, in the NaCl structure (topological type **pcu-b**) there are two chemically and crystallographically different atoms, but both Na and Cl are topologically identical since they possess the same set of topological indices (the net point symbol coincides with the point symbols of Na and Cl; Table 1).

On the contrary, in NiAs (topological type **nia**) Ni and As atoms are topologically different, in spite of having similar indices, also close to those of NaCl. In particular, the point symbols of Ni and Na(Cl) are the same $\{4^{12}.6^3\}$, i.e., in both cases the minimal circuits of bonds are the same (12 fourfold and 3 sixfold circuits). Other nets collected in Table 1 can also be considered as similar to either **pcu-b** or **nia**, as it will be discussed below.

2.2 The Concepts of Structure Representation, Underlying Net, and Packing Net

While the set of the net nodes is usually predetermined by the chemical composition of the crystal (we do not consider here disordered, incommensurate structures or quasicrystals), the net topology can be established in different ways. The problem of determination of chemical bonding is one of the crucial points of crystallochemical analysis. Depending on strength and type of bonding, different sets of bonds can be assigned to the same crystal structure that will have different topologies on the same set of nodes. Moreover, some atoms can be excluded from the analysis if they do not form part of the structure under consideration.

2.2.1 The Concept of Structure Representation

One can introduce the concept of (crystal) structure representation as a subset of atoms of the crystal structure as well as some topology specified on the subset, i.e., any structure representation is a net. Although an infinite number of representations can be ascribed to the same crystal structure, the number of those with crystallochemical sense is always finite and small. For example, one can consider the following representations for the crystal structure of an $M_y(XO_4)_z \cdot nH_2O$ oxoacid salt hydrate: (1) the whole structure including H-bonded water molecules, (2) valence-bonded $M_y(XO_4)_z$ framework or packing of oxygens with interstitial cations; water molecules as well as H-bonds are ignored, (3) M_yX_z cation array with direct contacts between first-neighbor cations. Note that in this last case, oxygens and their bonds are excluded. The question about which of the several representations is “the best” is meaningless because the goodness depends on the goals of the investigation.

All chemically reasonable structure representations can be derived from the so-called *complete representation* where all atoms and interatomic interactions, even the weakest ones, are taken into account [22]. Any other representation can be obtained from the complete one by some *simplification procedure*. A *primary* simplified net can be derived from the complete one by applying the following procedures: (1) removing the edges corresponding to the bonds to be ignored; (2) removing some nodes (atoms) together with their edges (bonds); and (3) contracting some multiatomic groups to their centroids or central atoms but maintaining the structure connectivity. In case (3), all atoms of a multiatomic group are fused in the center of the group giving their bonds to the center; we call this procedure *contraction*. For instance, the crystal structure of $Lu(ClO_4)_3$ (Fig. 2a, see Sect. 3.3.4) can be considered as a net of the Lu atoms and perchlorate anions that are represented by only the Cl atoms after contracting oxygens (Fig. 2b). Thus, the nodes of the primary simplified net (Lu and Cl) correspond to *structural groups* of a given chemical compound (the Lu^{3+} cations and ClO_4^- anions), while the nodes of the complete representation always correspond to *atoms*. Usually the

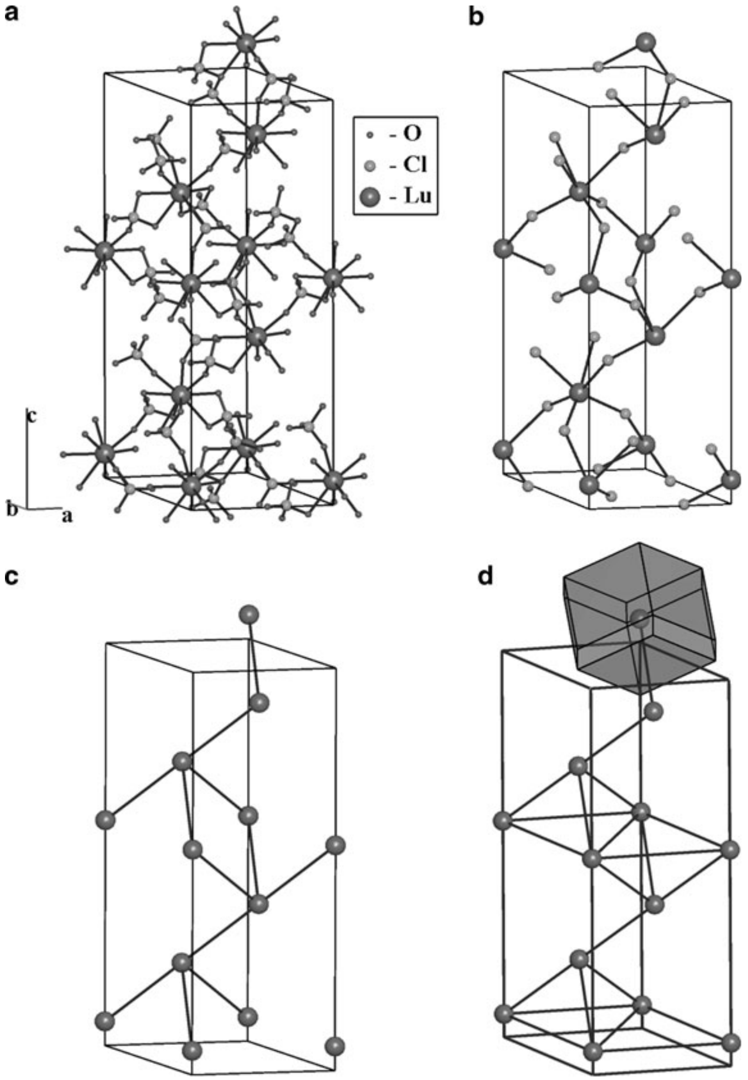

Fig. 2 Different representations of the Lu(ClO_4)$_3$ crystal structure: (**a**) all valence bonds are considered; (**b**) primary simplified net (standard representation); (**c**) secondary simplified net (underlying net); (**d**) packing net. The Voronoi polyhedron is shown for one of the Lu atoms

primary simplified net coincides with the so-called *standard representation* [30], where the structural groups are selected according to a conventional view of the structure. For instance, it is natural to consider the crystal structure of an inorganic oxoacid salt as a framework of metal cations and oxoanions (Fig. 2a). The *secondary* simplification procedure is used if the primary simplified net contains 0-coordinated (isolated), 1-coordinated (terminal), or 2-coordinated (bridge) nodes; the procedure removes isolated and terminal nodes and contracted bridge nodes converting them into edges as shown in Fig. 2c.

2.2.2 The Concept of Underlying Net

After the simplification, we obtain an *underlying net* of the crystal structure [31], i.e., the net that describes the method of connection of the structural groups. If all crystal structures under consideration were simplified in the same way, their underlying nets can be used to find resemblances in their topological organization irrespective of chemical composition, geometrical and topological features of the structural groups.

2.2.3 The Concept of Packing Net

The underlying net is derived from the complete representation; so it is always based on the topology of the crystal structure as a whole. This means that edges in this net corresponds to chains of the bonds involving contracted atoms; for instance, the bonds Lu–Lu in Fig. 2b conform to the chains Lu–O–Cl–O–Lu. However, it could be insufficient if the eutaxy of the cation array should be studied since some first-neighbor cations in the array could not be linked by such chains. To resolve this problem, we can consider a *packing net* (cf. [32]), where the edges between the cations are assigned by geometrical, not topological reasons. The assignment criteria could be some range of interatomic distances, or, more precisely, the shape of the Voronoi polyhedra of the cations [32]. In particular, in the Lu cation array of $Lu(ClO_4)_3$, there are six additional long (8.11 Å) Lu–Lu contacts (the Voronoi polyhedron of any Lu atom has $6 + 6 = 12$ faces), and the corresponding packing net is f.c.c. (**fcu**) that allows one to treat the array as a distorted cubic close packing (Fig. 2d).

Thus, cation array can be considered as an underlying or packing net; in most cases these nets coincide with each other and, more rarely, the underlying net is a subnet of the packing net. The opposite case (the packing net is a subnet of the underlying net) can occur only in structures with prolonged, not spherical polyatomic ions [16]. Studying both kinds of net gives the comprehensive and objective information about the topology of the cation array.

The approach described above has an important advantage over the traditional visual analysis: it can be made into an algorithm and implemented in a computer program that makes the crystallochemical analysis universal, objective, and fast. With such a program one does not need even to look at the crystal structure; the conclusions about the structure topology, its taxonomy, and comparison with other compounds can be made in an automatic mode.

2.3 Computer Tools to Study Periodic Graphs

Although the concept of a periodic graph began as far back as the classic series of Wells' publications [33], the relating computer methods began to develop just in the 1990s. Now there are the following crystallochemical program packages that are based on the periodic-graph approach and distributed free of charge:

Gavrog[1] consists of two programs: *Systre* (*Symmetry*, *Structure Recognition*, and *Refinement*) [28] is intended to find the net embedding with maximal symmetry and to test nets for isomorphism by comparing their adjacency matrices; *3dt* (*3D tiler*) works with 3D space tilings based on periodic nets [34].

TOPOS[2] [18] contains a lot of routines to study geometrical and topological properties of crystal structures; it includes the procedures to build various structure representations, underlying and packing nets.

Gavrog Systre and TOPOS were used to create a new type of electronic databases that can be called *crystallochemical* since they describe the topology of periodic nets as contrasted to *crystallographic* databases like the Cambridge Structural Database or Inorganic Crystal Structure Database that contain the information on atomic positions, perhaps on some bonds, but not on the overall topology of crystal structures. Currently, the following free crystallochemical databases are available:

RCSR[3] [35] accumulates about 1,800 two- and three-periodic nets of importance for crystal chemistry and selected by hand. Most of them were revealed as underlying nets in crystal structures, and the remaining nets can be useful for crystal design. The three-letter nomenclature for net topologies used in this chapter was originally elaborated for RCSR.

EPINET[4] project [36] currently collects 14,532 nets (*epinets*) generated by special mathematical procedures. Although the epinets do not originate in crystal structures, some of them have been found out as underlying nets. The epinets are denoted by *sqc*XXX symbols where XXX is an ordinal number, for instance, *sqc*1964.

TTD and *TTO* collections[5] [37] are an integrated part of TOPOS; the TTD collection contains the information on topological indices of more than 71,000 topological types including RCSR and EPINET, while the TTO collection links the data on underlying nets with the structural data stored in crystallographic databases.

Below we use the periodic-graph approach together with the TOPOS program package and TTD collection to perform the systematic analysis of topology of cation arrays in inorganic oxoacid salts and to reveal the relations in their structure organization.

---

[1] *Generation, Analysis and Visualization of Reticular Ornaments using Gavrog*; http://www.gavrog.org.

[2] http://www.topos.ssu.samara.ru.

[3] *Reticular Chemistry Structure Resource*, http://rcsr.anu.edu.au/.

[4] *Euclidean Patterns in Non-Euclidean Tilings*, http://epinet.anu.edu.au/.

[5] *TOPOS Topological Databases* and Topological Types Observed, http://www.topos.ssu.samara.ru.

3 Underlying Nets and Cation Arrays in Inorganic Oxoacid Salts

Inorganic oxoacid salts $M_y[LO_3]_z$ or $M_y[XO_4]_z$ with triangular, trigonal-pyramidal, and tetrahedral anions is a good starting point to demonstrate the advantages of the periodic-graph approach and the concept of underlying net since this class of ionic compounds is numerous (more than 600 crystal structures according to Inorganic Crystal Structure Database, release 2010/1), and the standard representation of their crystal structures is conventional, clear, and simple. The structure units are the cations M and oxoanions $[LO_3]$ or $[XO_4]$, i.e., oxygens are contracted to L or X cations that represent the anions in the resulting underlying net. Thus, the composition of the underlying net is M_yL_z or M_yX_z, i.e., it naturally describes the cation array; the stoichiometric ratio $\gamma = y{:}z$ is unambiguously determined by charges of the ions. This *quasi-binary* representation assumes that ionic forces play the most significant role in the formation of the periodic structure; the essentially covalent bonding within the anions is considered local and their internal structure is ignored. If the strength of bonds M–O is similar to that of bonds L(X)–O, one can consider the crystal structure of an oxoacid salt as a whole; no simplification is applied in this case. The relation to a binary compound can be found if the cations M and L(X) are topologically equivalent; this is so-called *grey isomorphism* [15]. Vice versa, the existence of "grey isomorphism" could be considered as an implicit indication of similarity of bonding between cations and oxygens in an oxoacid salt; however, this emerges rarely [15–17]. Note that in most cases the authors of original structural investigations do not recognize the relations to binary compounds.

We have analyzed 569 crystal structures of oxoacid salts $M_y(LO_3)_z$ (L = B, C, N, S, Se, Te, Cl, Br, I) and $M_y(XO_4)_z$ (X = Si, Ge, P, As, S, Se, Cl, Br, I), where the underlying nets are 3-periodic. For all of them, the *quasi-binary* representation was built and the resulting nets were classified with the TOPOS TTD collection. To characterize the method of coordination of the oxoanion, we use the notation $X^{mbtk...}$ [38], where the letter *X* shows the ligand *denticity* (M, B, T, or K for mono-, bi-, tri-, or tetradentate ligands, respectively), the integers *mbtk...* are equal to the numbers of the M atoms connected to one, two, three, or four atoms of the oxoanion.

3.1 Oxoacid Salts with Triangular Anions

3.1.1 Carbonates

Carbonates are the most investigated group of the oxoacid salts with triangular anions owing to their significance as minerals. They show rather strong relations between chemical composition, synthesis conditions, and the topology of the underlying nets (Table 2).

Table 2 Underlying nets in carbonates

Underlying net	Carbonate	Correspondence[a]	CO_3 coordination type
pcu-b (NaCl)	MCO_3 (M = Mg, Ca, Sr, Ba, Mn, Fe, Co, Ni, Zn, Cd)	Normal	T^6; T^{33}; T^{51}
nia (NiAs)	MCO_3 (M = Ca, Sr, Ba, Pb, Eu)	Anti	T^{33}
		Normal (vaterite)	T^6
bcu (CsCl)	$CaCO_3$-HP	Normal	T^{44}
sqp (SnP)	$CuCO_3$	Normal	T^{32}
flu (CaF_2)	Li_2CO_3	Anti	T^8
alb (AlB_2)	Li_2CO_3-HP	Anti	$T^{(12)}$
Ni_2In (BaF_2-HP)	M_2CO_3 (M = Na, K, Rb, Cs)	Anti	T^{74}; T^{83}
fit ($MoSi_2$)	Ag_2CO_3-LT	Anti	$T^{(10)}$

[a] Hereafter two kinds of correspondences of M cations and XO_n anions to the atoms of a binary compound A_yX_z (if any) are given in tables: *normal* or *anti* if the M cations match the electropositive atoms A or electronegative atoms X, respectively

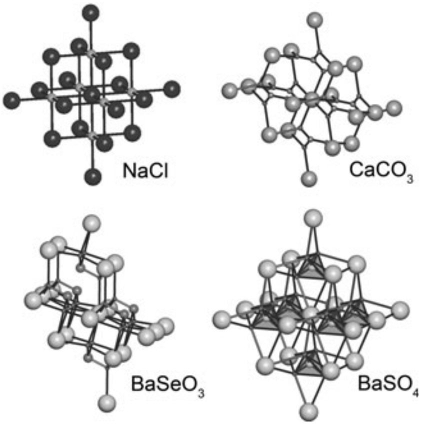

Fig. 3 The NaCl net ($Fm\bar{3}m$) and some related nets of oxoacid salts: $CaCO_3$ (calcite) and isostructural MBO_3, MNO_3 ($R\bar{3}c$); $BaSeO_3$ and isostructural $PbSO_3$, $MSeO_3$, $KClO_3$ ($P2_1/m$); $BaSO_4$-HT and isostructural MSO_4, $MClO_4$ ($F\bar{4}3m$). Hereafter by default an M atom is placed in the center of the net fragment for any oxoacid salt. Only one representative of each isostructural series is shown

$\gamma = 1{:}1$. This group of carbonates contains the most abundant $CaCO_3$ minerals (calcite and aragonite) as well as the related magnesite ($MgCO_3$), strontianite ($SrCO_3$), witherite ($BaCO_3$), and cerussite ($PbCO_3$). The calcite and aragonite structure types can be described as oxygen-stuffed NaCl (**pcu-b**) and *anti*-NiAs (**nia**), respectively; M^{2+} and CO_3^{2-} ions in the aragonite type correspond to As and Ni, respectively [39] (Figs. 3 and 4). There is a strong dependence between the size of M^{2+} cation and the topological motif: large cations stabilize the aragonite type.

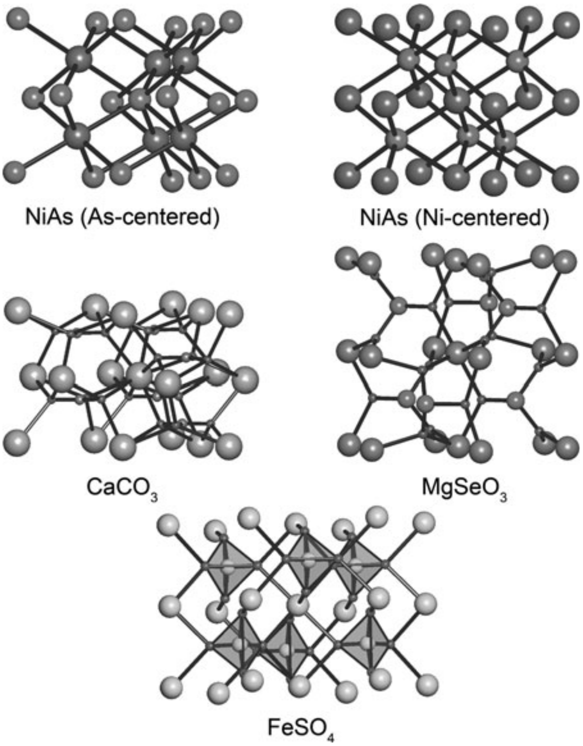

Fig. 4 The NiAs net ($P6_3/mmc$) and some related structures of oxoacid salts. *Anti*-NiAs: $CaCO_3$ (aragonite) and isostructural MCO_3, MBO_3 (*Pnma*); normal NiAs: $MgSeO_3$ and isostructural $MSeO_3$, $NaIO_3$ (*Pnma*); $FeSO_4$ and isostructural MPO_4, MSO_4, $MSeO_4$ (*Cmcm*)

Thus, $MgCO_3$ exists only in the calcite form; for $CaCO_3$ this form is stable at ambient conditions, while MCO_3 (M = Sr, Ba, Pb) crystallize in the aragonite type. This tendency is kept for carbonates of *d*- and *f*-metals: MCO_3 (M = Mn, Fe, Co, Ni, Zn) belong to the calcite type, while $EuCO_3$ has the aragonite-like structure. Calcite-like disordered high-temperature phases are known for $SrCO_3$ and $BaCO_3$ but they are not quenchable [40]. High-pressure phases of $CaCO_3$ (post-aragonite [41]) and $BaCO_3$ [42] have topologically denser 8,8-coordinated CsCl (**bcu**) and a novel binodal 9,9-coordinated underlying net, respectively. One more metastable phase of $CaCO_3$, the mineral vaterite [43], represents an antitype to aragonite, i.e., M^{2+} and CO_3^{2-} ions are topologically equivalent to Ni and As atoms in the NiAs-like underlying net.

The differences in topologies of the calcite and aragonite underlying nets are reflected by different coordination types of carbonate ions: T^6 and T^{33}, respectively (Fig. 5). In both cases, the carbonate ion is connected to six M cations but forms different numbers of M–O bonds: 6 and 9, respectively. As a result, the coordination numbers of cations are larger in the latter case that conforms to large sizes of the cations in the aragonite type. Since the oxoanion has very flexible coordination, it can fit any coordination numbers of cations. An example is the crystal structure of $CuCO_3$, where Cu atoms have CN = 7 but the resulting topology is 5-coordinated

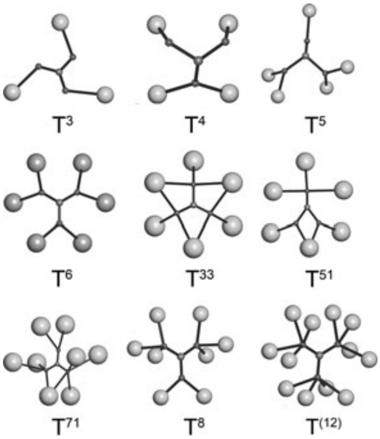

Fig. 5 Most typical coordination types of triangular and trigonal-pyramidal oxoanions

Table 3 Space-group symmetries for M_2CO_3 polymorphs

M atom	α-phase	β-phase	γ-phase
Na	$P6_3/mmc$	$C2/m$	$C2/m$
K	$P6_3/mmc$	$C2/c$	$P2_1/c$
Rb	$P6_3/mmc$	$Pnma$	$P2_1/c$
Cs	$P6_3/mmc$	$Pnma$	$P2_1/c$

sqp (SnP) net; both Cu and carbonate ions are topologically equivalent in the underlying net.

$\gamma = 2{:}1$. The thermal polymorphism gives three phases for M_2CO_3 (M = Na, K, Rb, Cs) with a great variety in space-group symmetries [44, 45] (Table 3). Strictly speaking, these structures cannot be considered as oxygen-stuffed: owing to the large γ ratio and large size of the alkali atoms, not all cations are shielded by the oxygens. This leads to abnormal coordination numbers of some alkali atoms and to an essential distortion of their environment. As a result, in all phases there is a large room around the abnormally coordinated alkali atoms; different size of this room gives rise to the structural differences of the polymorphs.

However, all these phases can be described in terms of the same underlying net of the Ni_2In structure type (Fig. 6), a net of great importance for this stoichiometric γ ratio (see [7] and more examples below). For the ionic model, it is important that there is a binary ionic compound, the high-pressure phase of BaF_2, which has the same topological motif [46]. Thus, all varieties of these polymorphs are caused by different distortions of the same cation array.

The Li_2CO_3 polymorphs show the typical trend for baric polymorphism: the underlying net becomes topologically denser in the high-pressure phase. Thus, at ambient conditions the cation array Li_2C follows the anti-fluorite (Li_2O) 4,8-coordinated motif, but above 10 GPa it transforms to the 5,10-coordinated AlB_2-like net.

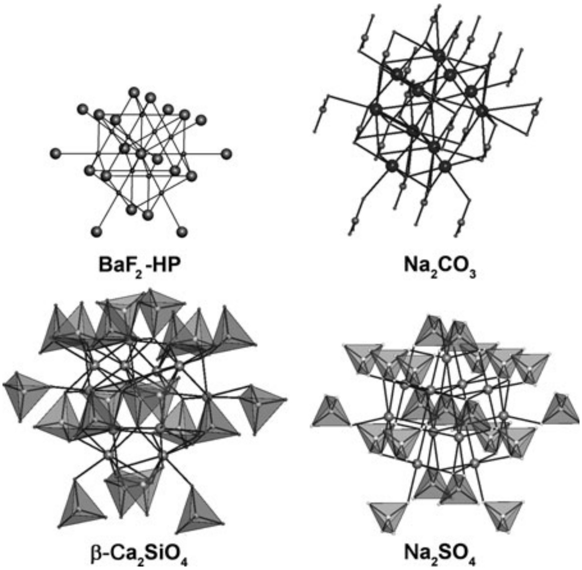

Fig. 6 The Ni_2In (BaF_2-HP, *Pnma*) net and some related structures of oxoacid salts: Na_2CO_3 (*C*2/*m*); β-Ca_2SiO_4 (larnite) and isostructural M_2SiO_4, Sr_2GeO_4 ($P2_1/n$); Na_2SO_4 and isostructural M_2SO_4 (*Cmcm*)

Table 4 Underlying nets in orthoborates

Underlying net	Orthoborate	Correspondence	BO_3 coordination type
pcu-b (NaCl)	MBO_3 (M = Al, Ti, V, Cr, Fe, Sc, In, Bi, La, Ce, Nd, Dy, Sm, Eu, Yb, Lu)	Normal	T^6; T^{33}; T^{42}
nia (NiAs)	MBO_3 (M = La, Ce, Nd)	Anti	T^{33}
cor (α-Al_2O_3)	$M_3(BO_3)_2$ (M = Ca, Sr, Hg, Eu)	Anti	T^6
K_2Te_3	$M_3(BO_3)_2$ (M = Mg, Mn, Ni, Cd)	Anti	T^{71}
gfy (UCl_3)	Tl_3BO_3	Anti	T^9
*sqc*908	Ag_3BO_3		$T^{(12)}$

The low-temperature phase of Ag_2CO_3 also has the 5,10-coordinated underlying net, but of the $MoSi_2$ structure type.

3.1.2 Orthoborates

$\gamma = 1{:}1$. This is the most numerous group of orthoborates that is topologically closely related to carbonates. Since all these orthoborates are obtained at a high temperature and/or pressure, it is not easy to determine which phase is the most stable at ambient conditions [47]. However, the general trend is similar to carbonates: smaller M^{3+} cations provide the **pcu-b** cation array (Fig. 3), while larger rare-earth M^{3+} cations give rise to a **nia** aragonite-like underlying net (Fig. 4; Table 4).

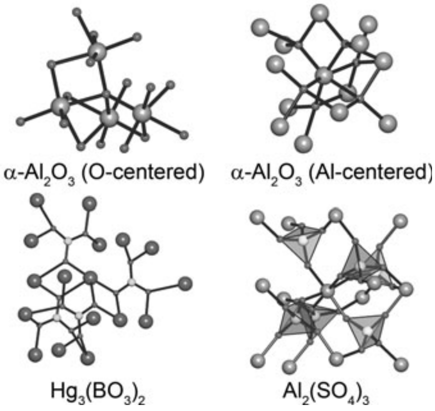

Fig. 7 The corundum (α-Al_2O_3) net ($R\bar{3}c$) and some related structures of oxoacid salts. *Anti*-Corundum: $Hg_3(BO_3)_2$ and isostructural $M_3(BO_3)_2$ ($R\bar{3}c$); normal corundum: $Al_2(SO_4)_3$ and isostructural $M_2(SO_4)_3$ ($R\bar{3}$)

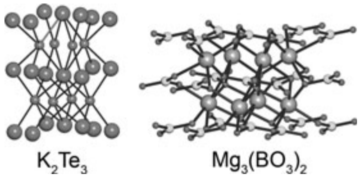

Fig. 8 Topological resemblance between K_2Te_3 and $Mg_3(BO_3)_2$ crystal structures

$\gamma = 3{:}2$. The orthoborates of the $Ca_3(BO_3)_2$ family can be considered as based on a distorted anti-corundum (**cor**) motif M_3B_2 if one takes into account the four strongest M–O bonds out of eight oxygens surrounding the M^{2+} cation (Fig. 7) [48]. The four remaining M–O contacts give rise to additional connections M–B in the cation array and to a new 6,9-coordinated underlying net derived from **cor**. The series $M_3(BO_3)_2$ (M = Mg, Mn, Ni, Cd) with octahedrally coordinated M atoms is related to the K_2Te_3 crystal structure [49] if one ignores Te–Te bonds (Fig. 8). The α, β-$Zn_3(BO_3)_2$ polymorphs [50], being unique structure types, are topologically close to the **cor** net since their topological indices are similar (Table 5). One can conclude that the differences are caused by the appearance of eight-cycles in the underlying nets of the polymorphs compared to the **cor** net.

$\gamma = 3{:}1$. These cation-rich structures of M_3BO_3 compounds are also tend to have antitypes as underlying nets; thus, the cation array Tl_3B in Tl_3BO_3 have the topology of 3,9-coordinated UCl_3 net (Fig. 9). The Ag_3B arrays in two Ag_3BO_3 phases (obtained at ambient and high pressure) are the first examples of 4,12-coordinated epinet *sqc*908.

3.1.3 Nitrates

$\gamma = 1{:}1$. At ambient conditions the MNO_3 nitrates also show a strong dependence of the underlying net topology on the size of the M^+ cation. Like carbonates

Table 5 Topological indices in the underlying nets of α, β-$Zn_3(BO_3)_2$ polymorphs and some related binary compounds[a]

Compound	Net point symbol	Coordination sequence
α-Al_2O_3	$\mathbf{\{4^6.6^9\}}_2\{4^3.6^3\}_3$	**Al: 6 13 39 46 105** O: 4 16 26 66 70
Rh_2O_3-HP	$\mathbf{\{4^5.6^9.8\}}_2\{4^2.6^4\}_2\{4^3.6^3\}$	**Rh: 6 14 42 50 114** O: 4 16–17 28 70–72 76
α-$Zn_3(BO_3)_2$	$\mathbf{\{4^5.6^8.8^2\}\{4^6.6^8.8\}}\{4^3.6^3\}\{4^4.6^2\}_2$	**B(1–4): 6 12–13 37–41 45–49 107–111** Zn(1–6): 4 16–17 25–27 66–69 71–76
β-$Zn_3(BO_3)_2$	$\mathbf{\{4^5.6^9.8\}}_2\{4^2.6^4\}\{4^4.6^2\}_2$	**B(1–2): 6 13 40 48 111–112** Zn(1–3): 4 16–18 26–27 65–74 74–75

[a] The indices of metal atoms and the corresponding orthoborate anions are bold; the ranges of terms of the coordination sequences are given for crystallographically nonequivalent atoms

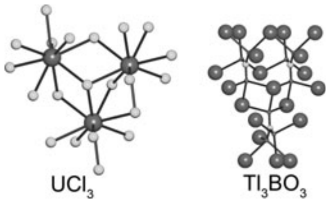

Fig. 9 Topological resemblance between UCl_3 and Tl_3BO_3 crystal structures

Table 6 Underlying nets in nitrates

Underlying net	Nitrate	Correspondence	NO_3 coordination type
pcu-b (NaCl)	MNO_3 (M = Li, Na, K, Ag)	Normal	T^6; T^{33}
nia (NiAs)	α-KNO_3	Anti	T^{33}
FeB	KNO_3-IV	Anti	T^{34}
bcu (CsCl)	MNO_3 (M = Rb, Cs, Tl)	Normal	T^{44}; T^{62}; T^{71}; T^8
pyr (FeS_2)	$M(NO_3)_2$ (M = Ca, Sr, Ba, Mn, Co, Ni, Cd)	Normal	T^3; T^{21}; T^{03}
mog (SiO_2, moganite)	β-$Cu(NO_3)_2$	Normal	B^2

and orthoborates, small cations (Li and Na) provide the **pcu-b** motif (Fig. 3), while α-KNO_3 possesses anti-NiAs (aragonite) underlying topology (Fig. 4; Table 6). In contrast to other compounds with triangular anions, nitrates containing the largest M^+ cations (Rb, Cs, Tl) follow the denser 8,8-coordinated CsCl motif that was elucidated in [51]. High-pressure phases have the same ($RbNO_3$-V, $CsNO_3$-III, IV) or denser (KNO_3-IV; 7,7-coordinated FeB; Fig. 10) underlying nets compared to phases at ambient conditions. In the former case, the high pressure gives rise to increase in the coordination of anions (from T^8, T^{71} to T^{62}, T^{44} for $RbNO_3$ or $CsNO_3$). The trend is reversed for the high-temperature phase KNO_3-III that has

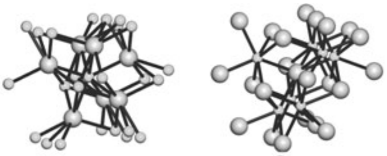

FeB (B-centered) FeB (Fe-centered)

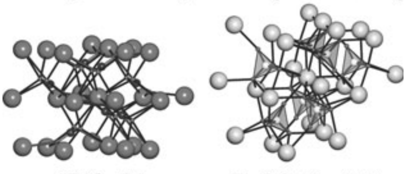

KNO_3-IV $BaSO_4$ (barite)

Fig. 10 The FeB net (B–B contacts are ignored) and some related structures of oxoacid salts. *Anti*-FeB: KNO_3-IV; normal FeB: $BaSO_4$ (barite) and isostructural MSO_4, $BaSeO_4$, $MClO_4$, and $MBrO_4$

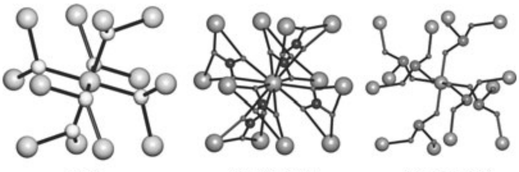

FeS_2 $Ca(NO_3)_2$ α-$Sn(SeO_3)_2$

Fig. 11 The pyrite-like net ($Pa\bar{3}$, S–S contacts are ignored) and some related structures of oxoacid salts: $Ca(NO_3)_2$ and isostructural $M(NO_3)_2$ ($Pa\bar{3}$); α-$Sn(SeO_3)_2$

topologically less dense underlying net (**pcu-b**, topological density $TD_{10} = 1{,}561$) than α-KNO_3 (**nia**, $TD_{10} = 1{,}748$).

$\gamma = 1{:}2$. Almost all nitrates $M(NO_3)_2$ investigated by X-rays have the same pyrite-like (**pyr**) 3,6-coordinated underlying net (Fig. 11); however, the space-group symmetries vary from orthorhombic ($Pca2_1$, M = Cd) to rhombohedral ($R\bar{3}$, M = Co) and cubic ($Pa\bar{3}$, M = Ca, Sr, Ba, Mn, Ni); the highest symmetry coincides with the maximal-symmetry embedding of the **pyr** net. The coordination numbers of the M atoms also change from 6 (M = Mn, Co, Ni) to 7 (M = Cd) and 12 (M = Ca, Sr, Ba), which results in the corresponding change in coordination type of the nitrate groups: from T^3 for CN = 6 to T^{03} for CN = 12. A special (square) coordination of copper atoms in β-$Cu(NO_3)_2$ gives rise to the moganite (**mog**) motif that is nontypical for cation arrays.

3.2 Oxoacid Salts with Trigonal-Pyramidal Anions

This group of ionic compounds is characterized by an asymmetric environment of anions owing to stereochemically active lone electron pair (E-pair). This distortion, being rather strong, often does not allow one to recognize the topological motif of the underlying net just with a visual analysis of the crystal structure. Indeed, the number of correspondences to binary compounds is less compared to the oxoacid salts considered in the previous part; however, the periodic-graph approach reveals non-strict resemblances in many cases [17].

3.2.1 Sulfites, Selenites, and Tellurites

Sulfites, selenites, and tellurites present some examples of nontrivial topological relationships. According to [17], the β and γ phases of $HgSeO_3$ are the first example of formally isostructural compounds that have similar geometrical parameters (space group and unit cell dimensions) but different topologies, and hence are related to different topological types. Indeed, both phases belong to the same space group ($P2_1/c$) with very close unit cell volumes (309.5 and 306.2 $Å^3$) and equal coordination numbers of corresponding atoms. This allowed the author [52] to put them into the same structure type. However, the coordination sequences for β- and γ-$HgSeO_3$ differ even in the second coordination shell: in β-$HgSeO_3$ each SeO_3^{2-} anion is bonded to 6 Hg atoms via oxygens, while for γ-$HgSeO_3$ the number of Hg atoms in the second coordination shell is 5; the same concerns the numbers of Se atoms in the second coordination shell of Hg atoms. As a result, the underlying nets in these polymorphs have the topologies of 6-coordinated uninodal and 5,5-coordinated binodal nets, derived in [23, 37] from 7-coordinated **sev** and 6,6-coordinated **nia** nets, respectively (Table 7). At the same time, the quasi-binary representation allows one to discover similarities between geometrically and topologically nonequivalent crystal structures. According to [17], there are three such cases: between Na_2SO_3, K_2SO_3, K_2TeO_3, and Cs_2TeO_3; between two phases of $PbSO_3$, $PbSeO_3$, and $BaSeO_3$; between $CdSO_3$-II, $CdSeO_3$, and β-$MnSO_3$. In fact, the similarity of topological types in the quasi-binary representation means a topological equivalence of cation arrays or packings of cations and structureless anions. In particular, when comparing the underlying nets, the different coordination types of anions are ignored in Na_2SO_3 (T^{901}) and K_2SO_3 (T^{631}); only the total

Table 7 Underlying nets in sulfites and selenites

Underlying net	Sulfite/selenite	Correspondence	LO_3 coordination type
pcu-b (NaCl)	$PbSO_3$, $MSeO_3$ (M = Sr, Ba, Pb)	Normal	T^{33}
nia (NiAs)	$MSeO_3$ (M = Mg, Mn, Co, Ni, Cu, Zn, Cd, Hg)	Normal	T^{6}
sev-6-*C*2/*m*	β-$HgSeO_3$		T^{51}
HIYXUJ	$CaSeO_3$		T^{51}
nia-5,5-$P2_1/c$	$CdSO_3$, γ-$HgSeO_3$		T^{32}
bnn (BN)	$MSeO_3$ (M = Cu, Zn)	Normal	T^{5}
Ni_2Al	Na_2SO_3		T^{901}
NASTEH	$M_2(SeO_3)_3$ (M = Bi, Er)		T^{31}, T^{22}
stp	$Sc_2(SeO_3)_3$		T^{4}
rtl (TiO_2, rutile)	$M(SeO_3)_2$ (M = Ti, Mn, Sn, Pb)	Normal	T^{3}
pyr (FeS_2)	α-$Sn(SeO_3)_2$	Normal	T^{3}

number of coordinated cations ($9 + 0 + 1 = 6 + 3 + 1$) is important for the comparison.

$\gamma = 1{:}1$. The topological types **pcu-b** and **nia** play the key role in the cation arrays of selenites $MSeO_3$; however, the dependence on the size of the M^{2+} cation is inverted compared to the oxoacid salts with triangular anions: large cations provide the **pcu-b** motif with the T^{33} coordination type of the anions (Fig. 3), while smaller cations facilitate the formation of the NiAs (**nia**) array of vaterite type (not *anti*-NiAs as for most structures considered in Sect. 3.1). Note that the NiAs-like selenites (Fig. 4) are described as distorted perovskite-like structures [53]; these descriptions, however, do not elucidate the relations to other $MSeO_3$ structure types. The coordination types of the LO_3^{2-} anions (T^{33} and T^6) correlate with the size of the M^{2+} cations. It seems reasonable to correlate the inversion with the E-pair. However, the mechanism of this effect remains unexplained so far.

This effect gives rise to the appearance of other 6-coordinated underlying nets (**sev**-6-*C*2/*m* and HIYXUJ) that are unique for this group of compounds. **sev**-6-*C*2/*m* was generated ab initio [23] and has not been found in crystal structures so far. The HIYXUJ underlying topology was revealed quite recently in the lead-organic compound (μ_6-3,4-dihydro-3-thioxo-1,2,4-triazin-5(2*H*)-onate)Pb(II) [54] (CSD Reference code HIYXUJ). Both topological types can be considered as intermediate between **pcu-b** and **nia** because the topological indices of **sev**-6-*C*2/*m* and HIYXUJ lie between those of **pcu-b** and **nia** (Table 1). The same concerns the pair of 5-coordinated underlying nets **bnn** and **nia**-5,5-$P2_1/c$; the latter one can be considered as a topological distortion of **bnn** that has a higher symmetry.

$\gamma = 2{:}1$. The relations between the cation array Na_2S in Na_2SO_3 and the Ni_2Al structure type are discussed in detail in this volume [55].

$\gamma = 2{:}3$. The topological types of the underlying nets in $M_2(LO_3)_3$ are predetermined by pyramidal (ψ^1-tetrahedral) form of the coordination figures of the cations with the stereochemically active E-pair. The corundum motif (**cor**) is not preferred in this case since the tetrahedral coordination of the 4-coordinated atom in **cor** does not fit the ψ^1-tetrahedral form [56]. Therefore, two other 4,6-coordinated nets, **stp** and NASTEH, appear; they contain square-planar coordination figures in the most symmetrical embedding (Fig. 12). Both of them were revealed only in metal-organic compounds [57]; **stp** is quite common (16 examples), NASTEH was found only in (ethane-1,2-diammonium)((μ_6-ethylenediphosphonato)$_2$Zn$_3$) [58] (CSD Reference code NASTEH).

$\gamma = 1{:}2$. Two well-known topological types of AB_2 ionic compounds, rutile (**rtl**) and pyrite (**pyr**), lie in the base of the $M(SeO_3)_2$ compounds (Figs. 11 and 13;

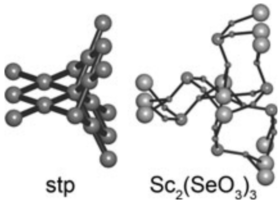

Fig. 12 Topological resemblance between the **stp** net (*P*6/*mmm*) and $Sc_2(SeO_3)_3$

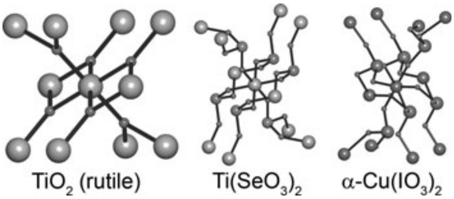

Fig. 13 The TiO_2 (rutile) net ($P4_2/mnm$) and some related structures of oxoacid salts: $Ti(SeO_3)_2$; α-$Cu(IO_3)_2$ and isotypic $M(IO_3)_2$ ($P2_1$)

Table 8 Underlying nets in chlorates, bromates, and iodates

Underlying net	Chlorate/bromate/iodate	Correspondence	LO_3 coordination type
pcu-b (NaCl)	$MClO_3$; $MBrO_3$ (M = Na, K, Rb, Tl); MIO_3 (M = K, Tl)	Normal	T^{33}, T^6, T^{42}
nia (NiAs)	MIO_3 (M = Li, Na)	Normal	T^6
crb (CrB_4)	β-$LiIO_3$	Normal	T^4
nia-5,5-*Pna*2$_1$	γ-$LiIO_3$		T^5
FEQWOO	$NaIO_3$		T^6
Tl_2S_2	$AgClO_3$	Normal	T^6
kwh	$CsBrO_3$; MIO_3 (M = K, Rb)		T^{331}, T^{61}, T^{52}
bcu-7-*Pnnm*	$CsIO_3$		T^{331}
rtl (TiO_2, rutile)	$M(IO_3)_2$ (M = Mg, Mn, Co, Cu)	Normal	T^3
scu ($BaTe_2$)	$Ba(LO_3)_2$ (L = Br, I)	Normal	T^{31}
*sqc*1964	$M(ClO_3)_2$ (M = Sr, Ba, Pb); $Ba(BrO_3)_2$		T^{31}, T^4
acs (WC)	$M(IO_3)_3$ (M = Al, Fe, Ga, In)	Normal	B^2

Table 7); they emerge in α and β modifications of $Sn(SeO_3)_2$, respectively. The pyrite cation array was also revealed for the $M(NO_3)_2$ compounds (Fig. 11; Table 6); the relation between β-$Sn(SeO_3)_2$ and $M(NO_3)_2$ was reported in [59].

3.2.2 Chlorates, Bromates, and Iodates

The relations of chlorates, bromates, and iodates to binodal nets are quite similar to sulfites and selenites owing to the like geometry and coordination capability of their oxoanions; the differences are mainly caused by a smaller charge of the chlorate-, bromate, or iodate oxoanions compared to sulfite or selenite ones and, hence, other possible γ ratios (Table 8).

$\gamma = 1{:}1$. The general trend in the cation array topology follows the features described in the previous part. Large alkali cations promote the **pcu-b** underlying net, while smaller ones tend to form the NiAs-like underlying net. In both cases, the underlying nets are geometrically distorted in comparison with the ideal **pcu-b** and

Fig. 14 Topological resemblance between the **scu** ($BaTe_2$) net ($P4/mmm$, Te–Te contacts are ignored) and the $Ba(IO_3)_2$ crystal structure

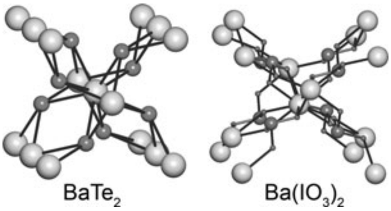

nia nets, thanks to existence of E-pairs (cf. Figs. 3 and 4). Further increase in the size of the M^+ cation gives rise to 7-coordinated **kwh** and **bcu**-7-*Pnnm* underlying nets that have not yet been found in binary inorganic compounds. In the high-temperature phases of $LiIO_3$, the coordination of the structure units decreases yielding the 4- and 5-coordinated cation arrays with the **crb** (boron subnet in CrB_4 or the silicon framework in the tectosilicates of the BCT family) and NiAs-related **nia**-5,5-$Pna2_1$ topologies, respectively. A $NaIO_3$ modification [60] contains the 6-coordinated underlying net FEQWOO topologically close to **nia** (Table 1) that was found in [4,4′-bipyridinium](μ_6-benzene-1,2,4,5-tetracarboxylato)$_2$Pr(III)$_2$ hydrate (CSD Reference code FEQWOO) as well as in 13 other metal-organic frameworks [57].

$\gamma = 1{:}2$. There are two main groups of $M(LO_3)_2$ compounds: small M^{2+} cations together with iodine cations form the 3,6-coordinated rutile array as in the corresponding selenites (Table 7), while large alkaline-earth cations and Pb^{2+} provide topologically denser 4,8-coordinated *sqc*1964 or **scu** underlying nets. The **scu** topological type is related to barium ditelluride ($BaTe_2$) [61] if one ignores Te–Te bonds in the Te_2^{2-} anions (Fig. 14).

$\gamma = 1{:}3$. A large group of $M(IO_3)_3$ iodates contains M^{3+} cations bridged by iodate anions; the resulting 6-coordinated WC (**acs**) underlying net does not include the iodine atoms because they transform to edges at the second step of the simplification procedure (Fig. 2). Among binary compounds, AgF_3 and AuF_3 [62] have the same topology as MI_3 array in $M(IO_3)_3$. According to [63], there is a close relation between MIO_3, $M(IO_3)_2$, and $M(IO_3)_3$ crystal structures: the iodate anions form a pseudo-hexagonal close packing, where M cations occupy all, one half or one third of the octahedral holes, respectively. This reflects in more detail the relations between **nia**, **rtl**, and **acs** nets.

3.3 Oxoacid Salts with Tetragonal Anions

Tetragonal coordination of a nonmetal cation provides its good shielding; hence, the model of the oxygen-stuffed alloy seems even more valid in this case. The coordination types of XO_4 anions are rather diverse (Fig. 15) and provide the topologies with quite different coordination of the nodes. Indeed, many examples of correspondences between this class of oxoacid salts and binary compounds were reported in [4, 7, 16]. Below these results are summarized and updated.

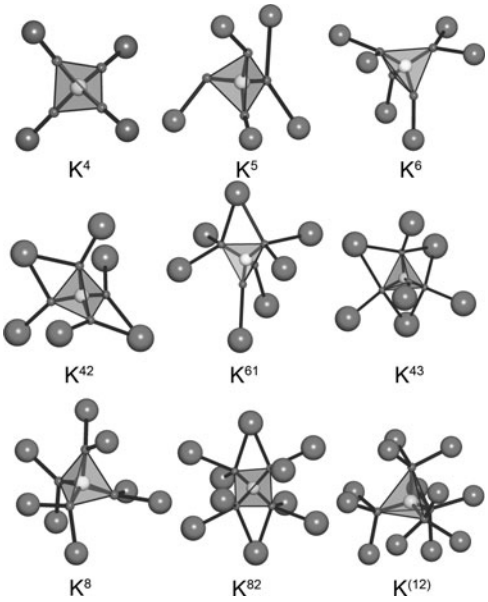

Fig. 15 Most typical coordination types of tetrahedral oxoanions

3.3.1 Orthosilicates and Orthogermanates

$\gamma = 1{:}1$. **pcu-b** and **nia** topological types, being quite common for most classes of oxoacid salts, have not been found in orthosilicates or orthogermanates; the higher-coordinated underlying nets are more typical for them. The crystal structure of $ZrSiO_4$ (zircon) illustrates a rare case of contradictions in the topology of the underlying net and cation array [16]. O'Keeffe and Hyde [4] found the topological similarity between the ZrSi cation array and the 10-coordinated array of metal atoms in rutile or β-Hg. However, the orthosilicate groups are not condensed in zircon, and the contacts Si–Si existing in the array disappear in the underlying net that has the 6-coordinated uninodal **msw** topology (Fig. 16a; Table 9). The underlying net in $ThSiO_4$ (huttonite) is 7-coordinated **bcu**-7-$P2_1/c$ (Fig. 16b); it occurs in monoclinic RhSi [64] and in the monazite-type orthophosphates (see below), while the orthosilicates and orthogermanates of the scheelite type contain topologically dense 8-coordinated **lsz** underlying net (Fig. 16c).

$\gamma = 2{:}1$. In [4, 7], the olivine (γ-Ca_2SiO_4) structure type was related to $PbCl_2$ (cotunnite) or Ni_2In-type cation arrays. In a later review [16], it was shown that the Ca_2Si trinodal underlying net in olivine has the same 4,5,9-coordination as the cotunnite net, but starting from the second coordination shell the coordination sequences are different. This is a good illustration of the advantages of the computer approach: in most cases, it is impossible to recognize the differences in outer coordination shells by visual analysis. Instead of olivine, the β-Ca_2SiO_4 (larnite) structure type has the Ni_2In-type underlying net [16] (Fig. 6).

Fig. 16 Topological resemblances between (**a**) the **msw** net ($P4_2/nnm$) and $ZrSiO_4$ (zircon); (**b**) the **bcu**-7-$P2_1/c$ (RhSi) net and $ThSiO_4$ (huttonite); (**c**) the **lsz** net ($P4_2/nnm$) and $ZrSiO_4$ (scheelite)

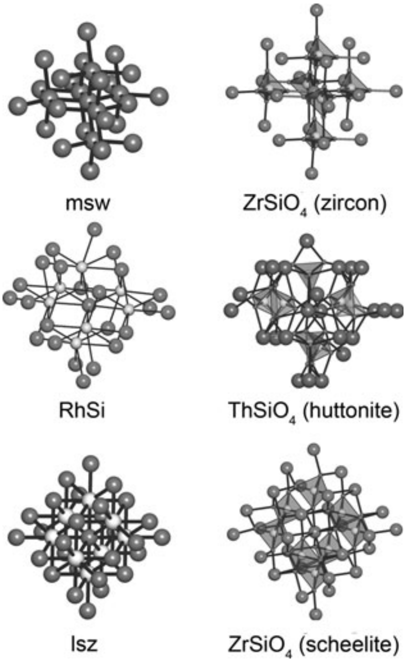

Table 9 Underlying nets in orthosilicates and orthogermanates

Underlying net	Orthosilicate/orthogermanate	Correspondence	XO_4 coordination type
lsz	$ZrSiO_4$; $MGeO_4$ (M = Zr, Hf, Th, U) (scheelite type)	Normal	K^8
bcu-7-$P2_1/c$ (RhSi)	$ThSiO_4$	Normal	K^{52}
msw	$MSiO_4$ (M = Zr, Hf, Ce, Th) (zircon type)		K^{42}
mgc ($MgCu_2$)	M_2SiO_4 (M = Mg, Fe, Co, Ni, Zn, Cd); M_2GeO_4 (M = Mg, Fe, Co, Ni, Cu) (spinel type)	Anti	$K^{(12)}$
Ni_2In (BaF_2-HP)	M_2SiO_4 (M = Ca, Sr, Ba, Eu); Sr_2GeO_4	Anti	K^{74}, K^{83}, K^{92}, K^{461}, K^{641}
$TiSi_2$	M_2SiO_4 (M = Cr, Cd); Hg_2GeO_4	Anti	K^{82}
*sqc*1964	Zn_2SiO_4-II		K^8
tph; Th_3P_4	$Bi_4(XO_4)_3$ (X = Si, Ge)	Anti	K^8

The oxoanion has its maximal coordination in the spinel-type orthosilicates and orthogermanates; the 6,12-coordinated cation array has the topology of the Laves phase $MgCu_2$, where the contacts Cu–Cu are ignored. The high-pressure chromium and cadmium orthosilicates as well as Hg_2GeO_4 are characterized by a 5,10-coordinated underlying net of the $TiSi_2$ type [65], where the contacts Si–Si are omitted. Note that this topology differs from other 5,10-coordinated nets (**alb** and **fit**) revealed in cation arrays in carbonates (Table 2). One more high-pressure phase, Zn_2SiO_4-II, has a 4,8-coordinated *sqc*1964 underlying net that we saw in chlorates (Table 8).

$\gamma = 4:3$. $Bi_4(SiO_4)_3$ (eulitite) and isostructural $Bi_4(GeO_4)_3$ have a Th_3P_4-like cation array [4].

3.3.2 Orthophosphates and Orthoarsenates

$\gamma = 1:1$. In this group of oxoacid salts, the **pcu-b** and **nia** underlying nets are again observed (Table 10). Orthophosphates and orthoarsenates with small trivalent cations belonging to the $CrVO_4$ structure type [66] are based on the **nia** motif (Fig. 4), while **pcu-b** is realized only in a high-temperature modification of $BiPO_4$ [67]. The underlying nets **lsz** (scheelite type), **bcu**-7-$P2_1/c$ (monazite type), and **msw** (zircon/xenotime type) found in orthosilicates and orthogermanates (Fig. 15; Table 9) are quite common for orthophosphates and orthoarsenates, which reflects well-known relations between these groups of compounds [68].

Orthophosphates and orthoarsenates with tetrahedrally coordinated M^{3+} cations represent a large group of silica-like structures most of which are microporous

Table 10 Underlying nets in orthophosphates and orthoarsenates

Underlying net	Orthophosphate/orthoarsenate	Correspondence	XO_4 coordination type
pcu-b (NaCl)	$BiPO_4$-HT	Normal	K^{42}
nia (NiAs)	MPO_4 (M = Al, In, Ti, V, Cr, Fe, Tl); $MAsO_4$ (M = Cr, Mn)	Normal	K^6
lsz	MPO_4 (M = Yb, Lu); $MAsO_4$ (M = Bi, Sm)	Normal	K^8
bcu-7-$P2_1/c$ (RhSi)	MPO_4 (M = Bi, La, Ce, Pr, Nd, Sm, Eu, Gd); $MAsO_4$ (M = Bi, La, Ce, Nd) (monazite type)	Normal	K^{61}, K^{52}
msw	MPO_4 (M = Sc, Y, Tb, Dy, Ho, Er, Tm, Lu); $MAsO_4$ (M = Sc, Y, Sm, Eu, Tb, Dy, Ho, Yb, Lu)		K^{42}
sma	MPO_4 (M = La, Ce, Nd)		K^{42}
nia-5,5-$P2_1/c$	$FeXO_4$ (X = P, As)		K^5
dia-b (ZnS, sphalerite)	MPO_4 (M = Al, Ga); $AlAsO_4$	Normal	K^4
qtz (α-HgS)	MPO_4 (M = Al, Fe, Ga); $MAsO_4$ (M = Al, Ga)	Normal	K^4
lon (ZnS, wurtzite)	$AlPO_4$	Normal	K^4
alw (Rh_2O_3-HP)	$Sb_2(PO_4)_3$	Normal	K^4
cor (α-Al_2O_3)	$Nb_2(PO_4)_3$	Normal	K^4
XEBHOB	$M_3(PO_4)_2$ (M = Mg, Co, Zn); $Zn_3(AsO_4)_2$		K^{61}
Cu_3Sb	Li_3XO_4 (X = P, As)	Normal	$K^{(12)}$
ith (Cr_3Si)	Ag_3XO_4 (X = P, As)	Normal	$K^{(12)}$
wzz	K_3AsO_4		K^{68}

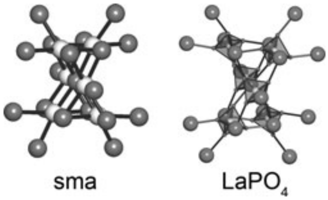

Fig. 17 Topological resemblance between the **sma** net ($P6_222$) and the $LaPO_4$ crystal structure

zeolite-like [69] and can hardly be considered within the cation array model. Three “dense” structure types are “grey-isomorphic” to quartz (**qtz**), cristobalite, or tridymite [70]; in the quasi-binary representation they correspond to α-HgS, sphalerite (**dia-b**), and wurtzite (**lon**), respectively.

The underlying nets of other orthophosphates correspond to the phases metastable at ambient conditions. Hexagonal modifications of lanthanum, cerium, and neodymium phosphates are based on the 6,6-coordinated **sma** topology (Fig. 17). $FePO_4$ obtained by the “soft” chemistry method [71] has the **nia**-5,5-$P2_1/c$ cation array that was also revealed in sulfites and selenites (Table 7). Alternative descriptions of both $FeLiPO_4$ and $FePO_4$, in terms of the extended Zintl–Klemm concept, can be found in this volume [72]

$\gamma = 2{:}3$. Two orthophosphates with this γ ratio have similar, but not equivalent topologies: $Nb_2(PO_4)_3$ has the topology of the Nasicon framework with the corundum-like underlying net (Fig. 7), while $Sb_2(PO_4)_3$ adopts the motif of a high-pressure modification of Rh_2O_3 [73] to be topologically close to corundum (Table 5). This is one more example of resemblance between the oxygen-stuffed alloys and high-pressure forms of the corresponding binary compounds (cf. [7]).

$\gamma = 3{:}2$. Most of the orthophosphates and orthoarsenates of this γ ratio have complex polynodal underlying nets with a unique topology; the relations to known topologies of nets are occasional. Thus, the structure type of farringtonite, $Mg_3(PO_4)_2$, has the trinodal 4,6,7-coordinated underlying net that was found in Mn_3(μ$_7$-phosphonopropionato)$_2$ (CSD Reference code XEBHOB) [74].

$\gamma = 3{:}1$. According to [4], the cation array in Ag_3PO_4 is similar to the 14,12-coordinated Cr_3Si (β-W) crystal structure that reflects the spatial arrangement of Ag and P atoms. If one neglects Ag–Ag contacts, a 4,12-coordinated **ith** underlying net (UH_3 structure type [16]) emerges that is a subnet of Cr_3Si. Lithium orthophosphate and orthoarsenate contain a Cu_3Sb-like cation array [4] that represents a distorted hexagonal close packing where the underlying net with only Cu-Sb (Li-P) contacts is trinodal 4,4,12-coordinated. The recently investigated crystal structure of K_3AsO_4 [75] is the first example of the complex trinodal 4,6,14-coordinated **wzz** underlying net.

3.3.3 Sulfates and Selenates

$\gamma = 1{:}1$. The **pcu-b** and **nia** underlying nets are quite common for sulfates and selenates (Table 11). Small 6-coordinated M^{2+} cations promote a **nia** cation array

Table 11 Underlying nets in sulfates and selenates

Underlying net	Sulfate/selenate	Correspondence	XO_4 coordination type
pcu-b (NaCl)	MSO_4 (M = Ca, Sr, Ba, Cd, Hg); $HgSeO_4$	Normal	K^{42}, K^{51}, K^{06}
nia (NiAs)	MSO_4 (M = Mg, Mn, Fe, Co, Ni, Cu, Cd, Zn); $MSeO_4$ (M = Mg, Mn, Co, Ni, Cu)	Normal	K^{6}
flu (CaF_2)	Li_2SO_4	Anti	K^{8}
FeB	MSO_4 (M = Ca, Sr, Ba, Pb, Eu); $BaSeO_4$	Normal	K^{43}, K^{61}
bcu-7-$P2_1/c$ (RhSi)	$CaSO_4$-HP, $MSeO_4$ (M = Sr, Pb)	Normal	K^{52}, K^{61}
sma	γ-$CaSO_4$		K^{42}
dia-b (ZnS, sphalerite)	MSO_4 (M = Be, Zn)	Normal	K^{4}
pts (PtS)	$PdXO_4$ (X = S, Se)	Normal	K^{4}
Ni_2In (BaF_2-HP)	M_2SO_4 (M = Li, Na, K, Rb, Cs, Tl); M_2SeO_4 (M = K, Cs, Tl)	Anti	K^{461}, K^{47}, K^{65}, K^{56}, K^{911}, $K^{(10)1}$
$TiSi_2$	M_2XO_4 (M = Na, Ag; X = S, Se)	Anti	K^{82}
alw (Rh_2O_3-HP)	$M_2(SO_4)_3$ (M = Fe, In, Y, Er); $M_2(SeO_4)_3$ (M = Fe, Sc, Yb)	Normal	K^{4}
cor (α-Al_2O_3)	$M_2(SO_4)_3$ (M = Al, Ga, Cr, Fe, In, Sc)	Normal	K^{4}
$PbCl_2$ (cotunnite)	α-$Zr(SO_4)_2$	Normal	T^{3}, K^{4}

[7] (Fig. 4), while 8-coordinated Ca and Hg provide a **pcu-b** underlying net (Fig. 3). At ambient conditions, sulfates and selenates with large alkaline-earth cations adopt a 7,7-coordinated FeB-like motif (Fig. 10) and transform to **pcu-b** only at high temperature. $CaSO_4$ has 7,7-coordinated underlying nets FeB and RhSi (monazite-like) under high pressure [76]. The high-temperature γ-$CaSO_4$ is an example of reorganization of the anhydrite cation array (**pcu-b**) to another 6,6-coordinated net with the **sma** topology (Fig. 17). Note that γ-$CaSO_4$ is obtained by a "soft chemistry" method (heating $CaSO_4{\cdot}0.5H_2O$, cf. the method of obtaining orthophosphates with the **sma** cation array; Table 10). 4-coordinated Be^{2+}, Zn^{2+}, and Pd^{2+} cations together with 4-coordinated S or Se cations form sphalerite- or PtS-like arrays. The topology is predetermined by the coordination figures of the M and X cations: tetrahedral coordination figures give rise to the sphalerite motif while the rectangle + tetrahedron combination ($PdXO_4$) results in the similar PtS (cooperite) array (Fig. 18).

$\gamma = 2{:}1$. Most sulfates and selenates of this type have the 5,6,11-coordinated Ni_2In-like cation array [16] (Fig. 6). In [7], caesium sulfate and selenate were related to the cotunnite ($PbCl_2$) structure type. This is an example of discrepancies between geometrical and topological descriptions obviously caused by the close topologies of the $PbCl_2$ and Ni_2In crystal structures. At the same time, the cation array in the high-temperature Na_2SO_4 phase was assigned to the Ni_2In type [6] that confirms the conclusion of the periodic-graph approach. At ambient conditions,

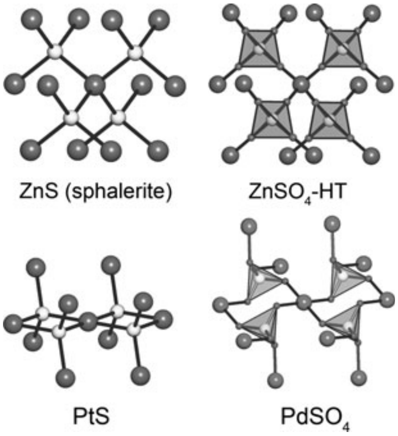

Fig. 18 Topological resemblances between (**a**) ZnS (sphalerite) net ($F\bar{4}3m$) and $ZnSO_4$; (**b**) PtS net ($P4_2/mmc$) and $PdSO_4$

Na_2SO_4 (thenardite), as well as the Ag_2SO_4 cation array, adopts the 5,10-coordinated $TiSi_2$-like motif [16]. This means that the reported relations between thenardite and the spinel structure type as well as between other Na_2SO_4 modifications and the olivine structure type [6] reflect geometrical similarities of the structure types, but do not take into account all their topological features. As was mentioned in Sect. 3.3.1, the olivine structure type is not topologically equal to the Ni_2In type, also the $TiSi_2$ underlying net does not coincide with the spinel-like net. This example demonstrates that visual analysis cannot detect some tiny topological differences, although the general (not strict) similarities of the motifs under consideration are unquestionable. The reader is referred to two chapters of this volume [55, 72] where the structures are analyzed visually, producing discrepancies with the results exposed here.

$\gamma = 2{:}3$. Like orthophosphates (Table 10), some sulfates and selenates of this γ ratio adopt two topological types of binary compounds: **alw** and **cor**. The corundum-like cation array typical for this γ ratio is realized for most sulfates of trivalent *d*-elements (Fig. 7); however, for large M cations **alw** is more preferable.

$\gamma = 1{:}2$. The only representative of this γ ratio, α-$Zr(SO_4)_2$, is related to cotunnite ($PbCl_2$) if one ignores two long (3.65Å) Pb–Cl contacts and considers the cotunnite net as 3,4,7-coordinated, not 4,5,9-coordinated.

3.3.4 Perchlorates, Perbromates, and Periodates

$\gamma = 1{:}1$. There are clear dependences of the underlying net topology on the kind of M^+ cation and XO_4^- anion (Table 12). For perchlorates, the increase in the M^+ cation size in the row Li–Na–K, Rb, Cs gives rise to the sequence **nia**–**pcu-b**–FeB at ambient conditions, while the cation arrays in the high-temperature modification of $MClO_4$ (M = K, Rb, Cs) decrease their topological density and transform to the **pcu-b** type. The FeB-like $NaClO_4$ was obtained by chance in the presence of cucurbit[5]uril ions in the mother solution [77]. Perbromates and periodates prefer to have denser

Table 12 Underlying nets in perchlorates, perbromates, and periodates

Underlying net	Perchlorates/perbromates/periodates	Correspondence	XO_4 coordination type
pcu-b (NaCl)	$MClO_4$ (M = Na, K, Rb, Cs, Tl, Ag)	Normal	K^{42}, K^{06}
nia (NiAs)	$LiClO_4$	Normal	K^{6}
lsz	$CsBrO_4$; MIO_4 (M = Na, K, Rb, Cs, Tl, Ag)	Normal	K^{8}, K^{62}, K^{44}
FeB	$MClO_4$ (M = Na, K, Rb, Cs); $MBrO_4$ (M = K, Tl)	Normal	K^{43}
nia-5,5-$P2_1/c$	$LiIO_4$		K^{5}
gfy (UCl_3)	$M(ClO_4)_3$ (M = La, Ce, Pr, Nd, Sm, Eu, Ho, Er, Tm, Yb)	Normal	T^{3}
ReO_3	$M(ClO_4)_3$ (M = Tm, Yb, Lu)	Normal	T^{11}

cation arrays (in particular, 8,8-coordinated scheelite-like **lsz**; Fig. 16c) than the corresponding perchlorates. The data of Table 12 agree with the results of Vegas and Jansen [7] as well as with other known relations between perhalogenates and other classes of oxoacid salts with tetrahedral anions (scheelite-like structures [78] as well as NiAs-like orthophosphates and sulfates [79], cf. Tables 9, 10, and 11).

$\gamma = 1{:}3$. This group is represented only by lanthanide perchlorates that exist in two crystalline forms: at ambient conditions the cation array is of the UCl_3 (**gfy**) type [80] (Fig. 9) for all lanthanides except Lu, and the topologically less dense ReO_3-like $Tm(ClO_4)_3$ and $Yb(ClO_4)_3$ were obtained at a high temperature [80, 81]. In both cases, the perchlorate anion is tridentate but connects to a different number of metal atoms (3 and 2 for T^3 and T^{11} coordination types, respectively) that results in the difference in topological density.

3.4 Uniformity of Cation Arrays in Inorganic Oxoacid Salts

The term “eutaxy” as applied to cation arrays means rather ordered, regular arrangement of the cations in the crystal space. In [2, 4], the eutactic placement was treated similarly to a close sphere packing with 12 cations in the vicinity of the given one. However, in the model of cation array the cations should be considered as point charges rather than the rigid bodies touching each other. In this case, the close-packing arrangement could not be a criterion of the “best” placement. In fact, in the most eutactic arrangement the cations should be allocated farthest from each other, i.e., the cation sublattice covers the crystal space most uniformly. The uniformity can be estimated with the formula [82]:

$$\langle G_3 \rangle = \frac{1}{3} \frac{\frac{1}{Z}\sum\limits_{i=1}^{Z} \int\limits_{\mathrm{VP}(i)} R^2 \mathrm{d}V_{\mathrm{VP}(i)}}{\left\{\frac{1}{Z}\sum\limits_{i=1}^{Z} V_{\mathrm{VP}(i)}\right\}^{\frac{5}{3}}},$$

where Z is the number of cations in the asymmetric unit of the array, $V_{\mathrm{VP}(i)}$ is the volume of the Voronoi polyhedron of the ith cation, R is the distance between the cation and a point inside its Voronoi polyhedron; $<G_3>$ is equal to the root-mean-square error of the corresponding space quantizer [83]. The $<G_3>$ value is computed irrespective of the structure topology; however, the topology of the ion array with a given $<G_3>$ value can be unambiguously determined from the corresponding packing graph. The least-distorted (i.e., the most uniform) array has the minimum $<G_3>$; in such an array the cation domains (space regions being most close to the corresponding cations) cover the crystal space most economically. The most uniform placement of points in three-dimensional space is the b.c.c. (**bcu-x**) lattice with $<G_3> = 0.0785433\ldots$, while close packings with $<G_3> = 0.07875\ldots$ [83] are less uniform. This means that the b.c.c. lattice with 14 (8 + 6) neighbors surrounding each cation in the array should also be important for eutactic arrangements. According to [15], the $<G_3>$ value can be used to determine the structure-forming role of the array: the most uniform array makes the main contribution to the Coulomb energy of the ionic structure.

This approach was applied to all kinds of ion arrays in inorganic oxoacid salts $M_y(LO_3)_z$ [15, 17]: cation (M), (L), (M + L), anion (O), and mixed cation–anion (M + O) arrays. It was shown that usually the most uniform array includes all cations (M + L), and the corresponding packing graph has the **bcu-x** (rarer **fcu**) topology. In general, the uniformity of the cation array increases along with the cation charge and size. For instance, in the series of alkaline carbonates M_2CO_3 the $<G_3>$ values for the (M) arrays decrease from 0.0876 (M = Li) to 0.0834 (M = Cs) [15]. It was shown [17] that in high-temperature and high-pressure phases the structure-forming cation arrays become more uniform because the ambient factors promote an increase in uniformity and symmetry of the structure-forming array. These results prove the model of cation array but focus the role of the b.c.c. packing along with the close packing motifs.

4 General Regularities in the Cation Arrays

The crystal structure data discussed above reveal the following general regularities in the cation arrays perceived as underlying nets of the oxoacid salts.

1. The underlying net usually has rather simple topology corresponding to a well-known topological type. Indeed, of the 569 crystal structures of oxoacid salts considered in this review, only 157 have novel topologies of their cation arrays. The remaining 412 cation arrays belong to 55 topological types of binary compounds or other binodal nets. For a given γ ratio there are a few (one or two) preferable (*default* [31]) underlying nets that frequently occur in nature; the rare nets can be treated as topological distortions of the default nets. The underlying nets can be of three types: (a) quite common (default) for different classes of inorganic compounds (Table 13); (b) typical only for a given class or

Table 13 Default underlying nets of frequency ≥8 in 569 crystal structures of inorganic oxoacid salts

Underlying net A_yX_z	Coordination number of A/X	No. of structures	Groups of oxoacid salts
$\gamma = 1{:}1$			
pcu-b (NaCl)	6/6	80	MLO_3 (L = B, C, N, S, Se, Cl, Br, I); MXO_4 (X = P, S, Se, Cl)
nia (NiAs)	6/6	56	MLO_3 (L = B, C, N, Se, I); MXO_4 (X = P, As, S, Cl)
msw (zircon)	6/6	25	MXO_4 (X = Si, Ge, P, As)
lsz (scheelite)	8/8	22	MXO_4 (X = Si, Ge, P, As, Br, I)
bcu-7-$P2_1/c$ (RhSi, monazite)	7/7	17	MXO_4 (X = Si, P, As, S, Se)
FeB	7/7	15	KNO_3; MXO_4 (X = S, Se, Cl, Br)
dia-b (ZnS, sphalerite)	4/4	9	MXO_4 (X = P, As, S)
bcu (CsCl)	8/8	8	MLO_3 (L = C, N)
$\gamma = 1{:}2$ (2:1)			
Ni_2In (BaF_2-HP)	11/5, 6	24	M_2CO_3; M_2XO_4 (X = Si, Ge, S, Se)
mgc ($MgCu_2$)	6/12	15	M_2XO_4 (X = Si, Ge)
rtl (TiO_2, rutile)	6/3	10	$M(LO_3)_2$ (L = Se, I)
pyr (FeS_2, pyrite)	6/3	9	$M(LO_3)_2$ (L = N, Se)
$\gamma = 2{:}3$ (3:2)			
alw (Rh_2O_3-HP)	6/4	10	$M_2(XO_4)_3$ (X = P, S, Se)
cor (α-Al_2O_3)	6/4	8	$M_3(BO_3)_2$; $M_2(SO_4)_3$; $Nb_2(PO_4)_3$

closely related compounds, like **mgc** ($MgCu_2$), this is often caused by an unusual γ ratio like 5:3 in $Mn_3^{II}Mn_2^{III}(SiO_4)_3$ [84] or 7:6 in $Fe_3^{II}Fe_4^{III}(AsO_4)_6$ [85]; (c) occurring occasionally due to special conditions of synthesis (high temperature, pressure, particular experimental methods like "soft chemistry"). All 165 cation arrays with novel topologies belong to types (b) and (c).

2. The overall topology of an underlying net is essentially predetermined by the geometrical forms of coordination figures of nodes. For example, if the net has square-planar coordination figures it unlikely corresponds to an oxoacid salt with tetrahedral anions, but can fit a compound with pyramidal anions. The form of the coordination figure depends on the relative sizes of cations and complex anions; the dependence is similar to that for simple ionic compounds [15]. The coordination capability of the oxoanion predetermines the coordination figure; the more flexible such capability the larger number of the overall topologies to which the oxoanion can fit (Figs. 5 and 15).
3. The size of cation influences the topological motif of the cation array; this is evident for the most abundant topological types **pcu-b** and **nia**: small or large M cations promote the formation of different underlying nets. Which topological type is realized depends on the nature of the L or X cation.
4. In high-pressure modifications, the topological density of the underlying net increases, while high-temperature polymorphs have a less dense underlying net than the title compound at ambient conditions.

5. In some cases, the cation array in an oxoacid salt corresponds to the underlying net of a metal-organic compound; no similar inorganic binary compound has been found so far. This could be a challenge to synthetic chemists to obtain such analog. This fact also shows that underlying nets in inorganic and metal-organic compounds have common topological properties.

The eutactic distribution of cations in the array is a consequence of their tendency to a uniform arrangement in the crystal space. This trend is influenced by the following features of the array:

1. The most preferable topological motifs (packing nets) for the cation arrays are b.c.c. and close packings; in most cases, the b.c.c. motif is the most uniform. Hence, the main structure-forming role in the oxoacid salts belongs to cations; the eutactic oxygen arrays are rather rare.
2. Increase in size and charge of the cations results in an increase in the array uniformity.
3. High temperature and pressure favor increase in the uniformity of the structure-forming (most uniform) cation array.
4. Increase in the uniformity changes the topological motif of the cation array: it tends to be b.c.c. The increase in the uniformity of the structure-forming array accompanies decrease in the uniformity of other ion sublattices [17].

These regularities seem to be valid not only for oxygen-stuffed cation arrays but also for ionic compounds containing other anions [86].

5 Concluding Remarks

The periodic-graph approach now is well developed for metal-organic coordination compounds [19] and can give fruitful results when analyzing typical inorganic substances. The main advantages of this approach over visual (even computer-aided) exploration of crystal structures are as follows: (1) its algorithms are formal, strict, and universal, and they are used for any crystal structure according to a common scheme; (2) the topology of an atomic net is unambiguously determined by a set of numerical indices; (3) the concept of the underlying net allows one to easily classify crystal structures of complex compounds by reducing them to simpler topologies and using computer databases of reference nets; (4) the concept of packing net formalizes the analysis of cation arrays: they are classified with the topological indices; and (5) the topological software provides fast processing hundreds and thousands of structures in a reasonable time.

The recent results of the topological analysis of cation arrays in the inorganic crystal structures described in this review underline the importance of the model of cation array and show that the number of preferable (“default”) topological motifs is rather small. We have good cause to believe that this fact, as well as the developed software, opens the door to a comprehensive taxonomy of inorganic ionic compounds. The experimental data on the high stability of particular topological motifs of cation arrays could be a reliable background for ab initio modeling of new inorganic substances and materials.

Acknowledgments This work was partially supported by a Cariplo Fellowship issued by Cariplo Foundation & Landau Network, Centro Volta (Como, Italy). The author thanks Prof. D.M. Proserpio for fruitful discussions of the periodic-graph problems and Dr. A. Vegas for thorough reading of the manuscript and useful comments.

References

1. Lebedev VI (1972) Foundations of new crystal chemistry. Int Geol Rev 14:543–547
2. O'Keeffe M (1977) On the arrangement of ions in crystals. Acta Crystallogr A 33:924–927
3. O'Keeffe M, Hyde BG (1981) The role of non-bonded forces in crystals. In: O'Keeffe M, Navrotsky A (eds) Structure and bonding in crystals. Wiley, New York
4. O'Keeffe M, Hyde BG (1985) An alternative approach to non-molecular crystal structures. With emphasis on the arrangements of cations. Struct Bond 61:77–144
5. Borisov SV (2000) Geometrical laws in inorganic chemistry. Crystallogr Rep 45:709–713
6. Vegas A, Grzechnik A, Syassen K (2001) Reversible phase transitions in Na_2S under pressure: a comparison with the cation array in Na_2SO_4. Acta Crystallogr B 57:151–156
7. Vegas A, Jansen M (2002) Structural relationships between cations and alloys; an equivalence between oxidation and pressure. Acta Crystallogr B 58:38–51
8. Krivovichev SV (2009) Structural crystallography of inorganic oxysalts. Oxford University Press Inc, New York
9. Santamaría-Pérez D, Vegas A (2003) The Zintl-Klemm concept applied to cations in oxides. I. The structures of ternary aluminates. Acta Crystallogr B 59:305–323
10. Santamaría-Pérez D, Vegas A, Liebau F (2005) The Zintl–Klemm concept applied to cations in oxides. II. The structures of silicates. Struct Bond 118:121–177
11. Vegas A, García-Baonza V (2007) Pseudoatoms and preferred skeletons in crystals. Acta Crystallogr B 63:339–345
12. Vegas A, Martin RL, Bevan DJM (2009) Compounds with a 'stuffed' anti-bixbyite-type structure, analysed in terms of the Zintl–Klemm and coordination-defect concepts. Acta Crystallogr B 65:11–21
13. Zintl E (1939) Intermetallische Verbindungen. Angew Chem 52:1–6
14. Hewaidy IF, Busmann E, Klemm W (1964) Die Struktur der AB-Verbindungen der schweren Alkalimetalle mit Zinn und Blei. Z Anorg Allg Chem 328:283–293
15. Blatov VA, Zakutkin YA (2002) Comparative topological analysis of simple anhydrous borates, carbonates and nitrates. Z Kristallogr 217:464–473
16. Ilyushin GD, Blatov VA, Zakutkin YA (2004) Orthotetrahedral crystal structures $M_y(TO_4)_z$ ($T = Si, Ge, P, As, S, Se, Cl, Br, I$): geometrical-topological analysis, quasi-binary representation, and comparison with the A_yX_z compounds by the method of coordination sequences. Z Kristallogr 219:468–478
17. Blatov VA, Peskov MV (2006) A comparative crystallochemical analysis of binary compounds and simple anhydrous salts containing pyramidal anions LO_3 ($L = S, Se, Te, Cl, Br, I$). Acta Crystallogr B 62:457–466
18. Blatov VA (2006) Multipurpose crystallochemical analysis with the program package TOPOS. IUCr CompComm Newsletter 7:4–38
19. Blatov VA, Carlucci L, Ciani G, Proserpio DM (2004) Interpenetrating metal-organic and inorganic 3D networks: a computer-aided systematic investigation. Part I. Analysis of the Cambridge structural database. CrystEngComm 6:377–395

20. Francl M (2009) Stretching topology. Nat Chem 1:334–335
21. Delgado-Friedrichs O, O'Keeffe M (2005) Crystal nets as graphs: terminology and definitions. J Solid State Chem 178:2480–2485
22. Blatov VA (2006) A method for hierarchical comparative analysis of crystal structures. Acta Crystallogr A 62:356–364
23. Blatov VA (2007) Topological relations between three-dimensional periodic nets. I. Uninodal nets. Acta Crystallogr A 63:329–343
24. Chung SJ, Hahn T, Klee WE (1984) Nomenclature and generation of three-periodic nets: the vector method. Acta Crystallogr A 40:42–50
25. Klee WE (2004) Crystallographic nets and their quotient graphs. Cryst Res Technol 39:959–968
26. Eon J-G (2005) Graph-theoretical characterization of periodicity in crystallographic nets and other infinite graphs. Acta Crystallogr A 61:501–511
27. Thimm G (2009) Crystal topologies - the achievable and inevitable symmetries. Acta Crystallogr A 65:213–226
28. Delgado-Friedrichs O, O'Keeffe M (2003) Identification of and symmetry computation for crystal nets. Acta Crystallogr A 59:351–360
29. Blatov VA, O'Keeffe M, Proserpio DM (2010) Vertex-, face-, point-, Schläfli-, and Delaney-symbols in nets, polyhedra and tilings: recommended terminology. CrystEngComm 12: 44–48
30. Baburin IA, Blatov VA (2007) Three-dimensional hydrogen-bonded frameworks in organic crystals: a topological study. Acta Crystallogr B 63:791–802
31. Ockwig NW, Delgado-Friedrichs O, O'Keeffe M, Yaghi OM (2005) Reticular chemistry: occurrence and taxonomy of nets and grammar for the design of frameworks. Acc Chem Res 38:176–182
32. Blatov VA (2001) Topological analysis of ionic packings in crystal structures of inorganic sulfides: the method of coordination sequences. Z Kristallogr 216:165–171
33. Wells AF (1954) The geometrical basis of crystal chemistry. Part 1. Acta Crystallogr 7:535–544
34. Delgado-Friedrichs O, O'Keeffe M, Yaghi OM (2007) Taxonomy of periodic nets and the design of materials. Phys Chem Chem Phys 9:1035–1043
35. O'Keeffe M, Peskov MA, Ramsden SJ, Yaghi OM (2008) The reticular chemistry structure resource (RCSR) database of, and symbols for, crystal nets. Acc Chem Res 41:1782–1789
36. Hyde ST, Delgado Friedrichs O, Ramsden SJ, Robins V (2006) Towards enumeration of crystalline frameworks: the 2D hyperbolic approach. Solid State Sci 8:740–752
37. Blatov VA, Proserpio DM (2009) Topological relations between three-periodic nets. II. Binodal nets. Acta Crystallogr A 65:202–212
38. Serezhkin VN (2007) Some features of stereochemistry of U(VI). In: Krivovichev SV, Burns PC, Tananaev IG (eds) Structural chemistry of inorganic actinide compounds, 1st edn. Elsevier, Amsterdam
39. Bevan DJM, Rossmanith E, Mylrea DK et al (2002) On the structure of aragonite – Lawrence Bragg revisited. Acta Crystallogr B 58:448–456
40. Antao SM, Hassan I (2007) $BaCO_3$: high-temperature crystal structures and the Pmcn → R3m phase transition at 811°C. Phys Chem Miner 34:573–580
41. Ono S, Kikegawa T, Ohishi Y, Tsuchiya J (2005) Post-aragonite phase transformation in $CaCO_3$ at 40 GPa. Am Mineral 90:667–671
42. Holl CM, Smyth JR, Laustsen HMS et al (2000) Compression of witherite to 8 GPa and the crystal structure of $BaCO_3$II. Phys Chem Miner 27:467–473
43. Wang J, Becker U (2009) Structure and carbonate orientation of vaterite ($CaCO_3$). Am Mineral 94:380–386
44. Dinnebier RE, Vensky S, Jansen M, Hanson JC (2005) Crystal structures and topological aspects of the high-temperature phases and decomposition products of the alkali-metal oxalates $M_2[C_2O_4]$ ($M = K, Rb, Cs$). Chem Eur J 11:1119–1129

45. Swainson IP, Dove MT, Harris MJ (1995) Neutron powder diffraction study of the ferroelastic phase transitionand lattice melting in sodium carbonate, Na_2CO_3. J Phys Condens Matter 7: 4395–4417
46. Leger JM, Haines J, Atouf A et al (1995) High-pressure x-ray- and neutron-diffraction studies of BaF_2: An example of a coordination number of 11 in AX_2 compounds. Phys Rev B 52: 13247–13256
47. Goubin F, Montardi Y, Deniard P et al (2004) Optical properties of $CeBO_3$ and CeB_3O_6 compounds: first-principles calculations and experimental results. J Solid State Chem 177: 89–100
48. Vegas A (1985) New description of the $Ca_3(BO_3)_2$ structure. Acta Crystallogr C 41: 1689–1690
49. Seifert-Lorenz K, Hafner J (2002) Crystalline intermetallic compounds in the K-Te system: the Zintl-Klemm principle revisited. Phys Rev B 66:094105-1-094105-15
50. Chen X, Xue H, Chang X et al (2006) Syntheses and crystal structures of the α- and β-forms of zincorthoborate, $Zn_3B_2O_6$. J Alloys Compd 425:96–100
51. Sastry PUM, Rajagopal H, Sequeira A (1994) Thallous nitrate(III); a single-crystal neutron study. Acta Crystallogr C 50:1854–1857
52. Weil M (2002) Preparation and crystal structures of two new modifications of mercury(II) selenite(IV), $HgSeO_3$, and the mixed-valent mercury(II) selenite(IV) selenide(-II), $(HgSeO_3)_3HgSe$. Solid State Sci 4:1153–1162
53. Koskenlinna M, Valkonen J (1995) Mercury(II) selenite. Acta Crystallogr C 51:1040–1042
54. Casas JS, Castellano EE, Ellena J et al (2008) Lead(II)-induced formation and coordination of 3, 4-dihydro-3-thioxo-1, 2, 4-triazin-5(2H)-one. Inorg Chem Commun 11:423–426
55. Vegas A (2011) Missing links in two structural journeys: From stuffed-wurtzite to $MoSi_2$. From stuffed-tridymite to Ba_2SnO_4. Struct Bond
56. Wontcheu J, Schleid T (2003) $Sc_2Se_3O_9$: Scandium(III) oxoselenate(IV) according to $Sc_2(SeO_3)_3$ with a hexagonal "lone-pair" channel structure. Z Anorg Allg Chem 629:1463–1465
57. Alexandrov EV, Blatov VA, Kochetkov AV, Proserpio DM (2010) Underlying nets in coordination frameworks: topology, taxonomy, prediction, and computer-aided analysis of the Cambridge Structural Database. CrystEngComm, submitted
58. Natarajan S (2004) Synthesis and structure of a three-dimensional organically templated zinc ethylenediphosphonate, $[NH_3(CH_2)_2NH_3][Zn_3\{O_3P(CH_2)_2\}_4]$. Z Anorg Allg Chem 630: 291–295
59. Steinhauser G, Luef C, Wildner M, Giester G (2006) Syntheses and crystal structures of $Pb(SeO_3)_2$ and two modifications of $Sn(SeO_3)_2$. J Alloys Compd 419:45–49
60. Sorokina NI, Ilyukhin VV, Pakhomov VI, Belov NV (1979) About the crystal structure of sodium iodate. Dokl Akad Nauk SSSR 249:613–616
61. Li J, Guo H-Y, Carey JR et al (1994) Synthesis and crystal stucture of a new alkaline-earth metal chalcogenide: barium ditelluride. Mater Res Bull 29:1041–1048
62. Zemva B, Lutar K, Jesih A et al (1991) Silver trifluoride: preparation, crystal structure, some properties, and comparison with AuF_3. J Am Chem Soc 113:4192–4198
63. Phanon D, Mosset A, Gautier-Luneau I (2007) New materials for infrared non linear optics. Syntheses, structural characterisations, second harmonic generation and optical transparency of $M(IO_3)_3$ metallic iodates. J Mater Chem 17:1123–1130
64. Schellenberg L, Jorda JL, Muller J (1985) The rhodium-silicon phase diagram. J Less Common Met 109:261–274
65. Tanaka K, Nawata K, Inui H, Yamaguchi M, Koiwa M (2001) Refinement of crystallographic parameters in refractory metaldisilicides. Mater Res Soc Symp Proc 646:N4.3.1–N4.3.5
66. Glaum R, Reehuis M, Stuesser N et al (1996) Neutron diffraction study of the nuclear and magnetic structure of the $CrVO_4$ type phosphates $TiPO_4$ and VPO_4. J Solid State Chem 126:15–21
67. Masse R, Durif A (1985) Etude structurale de la forme haute temperature du monophosphate debismuth $BiPO_4$. Compt Rend Heb Seances Acad Sci 300:849–851

68. Zhang FX, Lang M, Ewing RC et al (2008) Pressure-induced zircon-type to scheelite-type phase transitions on $YbPO_4$ and $LuPO_4$. J Solid State Chem 181:2633–2638
69. Cao G, Afeworki M, Kennedy GJ (2007) Crystal structure of an aluminophosphate EMM-8: a multi-technique approach. Acta Crystallogr B 63:56–62
70. Graetsch H (2000) Two Forms of aluminium phosphate tridymite from X-ray powder data. Acta Crystallogr C 56:401–403
71. Song Y, Zavalii PY, Suzuki M, Whittingham MS (2002) New iron(III) phosphate phases: crystal structure and electrochemical and magnetic properties. Inorg Chem 41:5778–5786
72. Vegas A (2011) LiFePO4: Dissection of a crystal structure. The parts and the whole. Struct Bond. doi:10.1007/430_2010_35
73. Shannon RD, Prewitt CT (1970) Synthesis and structure of a new high pressure form of Rh_2O_3. J Solid State Chem 2:134–136
74. Stock N, Frey SA, Stucky GD, Cheetham AK (2000) Synthesis and characterization of two manganese phosphonocarboxylates: $Mn_3(O_3PCH_2COO)_2$ and $Mn_3(O_3PCH_2CH_2COO)_2$. J Chem Soc Dalton Trans 4292–4296
75. Emmerling F, Idilbi M, Roehr C (2002) Neue Oxopnictate $A_3^IM^VO_4$: Darstellung und Kristallstruktur von A_3AsO_4 (A = K, Rb, Cs) und K_3BiO_4. Z Naturforsch B Chem Sci 57:599–604
76. Crichton WA, Parise JB, Antao SM, Grzechnik A (2005) Evidence for monazite-, barite-, and $AgMnO_4$ (distorted barite)-type structures of $CaSO_4$ at high pressure and temperature. Am Mineral 90:22–27
77. Zhang G-L, Li Y-T, Wu ZY, Song Y-L (2006) Sodium perchlorate in the space group *Pnma*. Acta Crystallogr E 62:i150–i151
78. Kalman A, Cruickshank DWJ (1970) Refinement of the structure of $NaIO_4$. Acta Crystallogr B 26:1782–1785
79. Wickleder MS (2003) Crystal structure of $LiClO_4$. Z Anorg Allg Chem 629:1466–1468
80. Pascal JL, Favier F, Cunin F et al (1998) Crystalline and molecular structures of anhydrous lanthanide perchlorates $Ln(ClO_4)_3$ with Ln = La, Ce, Pr, Sm, Eu, Ho, Er, Tm, and Lu. J Solid State Chem 139:259–265
81. Favier F, Pascal JL, Cunin F (1998) Thermal behavior and X-ray powder diffraction structures of two polymorphic phases of anhydrous $Yb(ClO_4)_3$. Inorg Chem 37:1776–1780
82. Blatov VA (2004) Voronoi-Dirichlet polyhedra in crystal chemistry: theory and applications. Cryst Rev 10:249–318
83. Conway JH, Sloane NJA (1988) Sphere packings, lattices and groups. Springer, New York
84. Arlt T, Armbruster T, Miletich R et al (1998) High pressure single-crystal synthesis, structure and compressibility of the garnet $Mn_3^{2+}Mn_2^{3+}(SiO_4)_3$. Phys Chem Miner 26:100–106
85. Weil M (2004) $Fe_3^{II}Fe_4^{III}(AsO_4)_6$, the first arsenate adopting the $Fe_7(PO_4)_6$ structure type. Acta Crystallogr E 60:i139–i141
86. Peskov MV, Blatov VA (2004) Comparative crystal-chemical analysis of binary compounds and *d*-metal halides containing tetrahedral anions. Russ J Inorg Chem 49:1042–1050

Struct Bond (2011) 138: 67–91
DOI: 10.1007/430_2010_35

FeLi[PO_4]: Dissection of a Crystal Structure

The Parts and the Whole

Angel Vegas

Abstract The structures of the dimorphic FeLi[PO_4] phosphate are analysed on the basis of their cation arrays. At ambient conditions, the compound, known as the mineral triphylite, is olivine type (***P***nma) (CaMg[SiO_4]) and transforms into the olivine-related $NaCaVO_4$-type (***C***mcm) structure, at high temperature and high pressure. This phase transition takes place with an exchange in the positions of the Li and Fe atoms, both filling octahedral voids. This feature, impossible to explain with the traditional model of cation-centred anion polyhedra, can be understood in the light of the extended Zintl–Klemm concept (EZKC) which contemplates as possible the electron transfer even between "cations". A detailed dissection of both structures leads to the conclusion that the observed phase transition triphylite → β-LiFe[PO_4] is controlled by the [FeP] cation subarrays which undergo a PbO-type → NiAs-type transition at high pressure. In addition to this relevant feature, it is shown that the [FeP] subarray, PbO type in triphylite, exits in the delithiated phase $FePO_4$. The EZKC allows that LiFe[PO_4] can be written with the pseudo-formula Li^+[Ψ-$FeSO_4$], so that the [FeP] subarray is converted into Ψ-[FeS], whose structure coincides with that of real FeS. The significant result is that the structure of FeS persists in the pseudoarrays Ψ-[FeS] of both Fe[PO_4] and LiFe[PO_4]. The "autopsy" also reveals that several substructures, formed by different pairs of atoms, co-exist with those of the PbO type and NiAs type, in triphylite and β-LiFe[PO_4], respectively. Fragments of metallic lithium, layers of metallic iron and the rocksalt LiCl are some of the structures that can be revealed through the dissection process. The conclusion is that the formation of any structure implies that several substructures need to be satisfied simultaneously. These multiple substructures act as if they were resonance structures which cooperate to the stabilization of the whole network.

Keywords Alloys · Cation arrays · Crystal chemistry · Phase transitions · Resonance structures · Zintl phases

---

A. Vegas
Instituto de Química Física "Rocasolano", CSIC, C/ Serrano 119, 28006 Madrid, Spain
e-mail: avegas@iqfr.csic.es

Contents

1 Introduction 68
2 Description of the Triphylite FeLi[PO_4] Structure 70
  2.1 Olivine FeLi[PO_4] and the Ni_2In Structure 71
  2.2 FeLi[PO_4] and the AlB_2 Structure 71
  2.3 The FeLiP Subarray and NiAs·FeLi[PO_4] and Li[ClO_4] 72
  2.4 FeLiP, and FeLi[PO_4]: The Extended Zintl–Klemm Concept 74
  2.5 The Li Subarray and the Structures of Elemental Li 76
3 The High Pressure Phase β-FeLi[PO_4] 78
  3.1 Relationships of β-FeLi[PO_4] with Fe[SO_4] and Li[ClO_4] 79
  3.2 The Exchange of Li and Fe in the Transition Triphylite → β-FeLi[PO_4] 80
4 FeLi[PO_4] and the High Temperature Phases of Na_2[SO_4] 80
  4.1 FeLi[PO_4], Ψ-Mg[SO_4] and Ψ-Fe[SO_4] in the Light of the EZKC 81
  4.2 The Olivine-Like Structures and the PbO-Type Blocks 84
  4.3 The Co-existing Structures FeS/Fe[SO_4], LiCl/Li[ClO_4] and FeLiP/FeLi[PO_4] 85
5 Conclusions 89
References 90

> Daß hier ein gemeinsames Prinzip und kein Zufall herrscht, ist wegen der sehr starken Analogie wahrscheinlich.
>
> It is probable that this is not a casual coincidence but the strong analogies must obey a General Principle.
>
> Wondratschek, Merker & Schubert, 1964

1 Introduction

The compound FeLi[PO_4] is one of the many quaternary olivine-like compounds. In common with many Li-containing oxides, it has been widely studied due to its potential use as anode batteries. The compound is dimorphic. At ambient conditions, the stable phase is the mineral triphylite whose structure was first determined by Yakubovich et al. [1]. It is olivine-like (***P***nma) and hence, isostructural to forsterite, Mg_2[SiO_4], and more properly to sinhalite AlMg[BO_4] (also CaMg[SiO_4]). At high temperature and pressure (around 80 GPa and 1,100 K), a metastable β-phase, with the $NaCaVO_4$-type structure (***C***mcm), was synthesized in a belt-type apparatus [2].

The two phases of FeLi[PO_4] are isostructural with two high temperature phases of Na_2[SO_4] which are obtained when the room temperature phase, V-Na_2[SO_4] (the mineral thenardite), is heated. By increasing temperature, the observed transition sequence is thenardite V-(***F***ddd) → III-***C***mcm → II-***P***nma → I-***P***6_3/mmc [3]. Both, III-Na_2[SO_4] (***C***mcm) (Na_2[CrO_4] type) and II-Na_2[SO_4] (***P***nma) (Mg_2[SiO_4] type) are the phases related to those of FeLi[PO_4].

The three high temperature phases of Na_2SO_4, i.e. ***C***mcm, ***P***nma and ***P***6_3/mmc, present strong topological similarities [3, 4], and their cation arrays are all of the Ni_2In type [5]. In case of the two phases of FeLi[PO_4], the [FeLiP]-arrays can also be considered of the Ni_2In type, but the two phases (***C***mcm and ***P***nma) differ in an important aspect, i.e. the positions of the Li and Fe atoms are exchanged [2]. Other aspects of the structures, like the octahedral coordination of both Li and Fe atoms and the tetrahedral coordination of the P atoms, remain unaltered in the HP phase and provide new examples of compounds, which undergo the olivine → spinel transition, where the coordination number of cations does not increase with pressure.

As it is well known, these coordination features, together with the interatomic distances, defining the cation-centred coordination polyhedra, are the unique structural data commonly used to study, describe and even "understand" crystal structures. It should be outlined that in many instances, the term "description" is inadequately used as an equivalent of "understanding". Following this tendency, the olivine-like structures are described as distorted *hcp* arrays of O atoms, with one half of the octahedral voids occupied by the big cations (e.g. Mg, Li, Fe) and one fourth of the tetrahedral voids occupied by the small cations (Si, P, B, etc.). In the case of ternary oxides, like $Mg_2[SiO_4]$ (forsterite, ***P***nma), all the Mg atoms occupy octahedral voids but are splitted into two distinct Wyckoff positions. The Si atoms in forsterite, also located at 4*c*, occupy tetrahedral holes.

When triphylite, LiFe[PO_4], is compared with forsterite ($Mg_2[SiO_4]$), one sees that the Li and Fe atoms, both occupying octahedral voids, are separated in the two Wyckoff positions 4*a* (0, 0, 0) and 4*c* (*x*, ¼, *z*), respectively. This separation, irrelevant in forsterite, becomes enigmatic in triphylite, as well as in other isostructural compounds such as CaMg[SiO_4] and sinhalite AlMg[BO_4]. If we assume the tendency of both Li and Fe atoms to occupy octahedral voids, one might expect a random distribution of both atomic species, indistinctly, in the two Wyckoff positions, just as if they were the Mg atoms in $Mg_2[SiO_4]$.

These features are indicative that the old crystal-chemical model, based mainly on closed packed arrays of anions, where cations are contemplated as "isolated charged spheres", is unable to give a satisfactory explanation of the principles governing crystal structures. It is also generally admitted that the derived rule, which attributes to the ionic size effects, a main role in determining the structure, has failed in explaining even most simple structures. The main conclusion is that the classical model can not account for the separation of both types of cations (Li and Fe) in triphylite.

Alternative approaches accounting for unexpected structural features have been reported by O'Keeffe and Hyde [5]. These authors realized that the oxygen subarrays showed a great irregularity (the O–O distances in $FeLiPO_4$ range from 2.40 to 3.74 Å), and also that, in a great amount of oxides, the cation arrays adopted structures of either elements or simple alloys. In view of these coincidences, the authors proposed to describe the structures as oxygen-stuffed alloys [5].

In the case of the olivine-like compounds ($Mg_2[SiO_4]$ and FeLi[PO_4]), the Mg_2Si (FeLiP) subarrays are in fact orthorhombic distortions of the hexagonal Ni_2In type. As it will be discussed in Sect. 4, the cation array in olivine is not properly of the Ni_2In type (***P***6_3/mmc), but it is an orthorhombic distortion (***P***nma) which is rather related to a stuffed NiAs-type structure. These features are in agreement with the topological analysis carried out by Blatov et al. [6, 7] which considers the cation array in olivine, not as Ni_2In type, but as a 4,5,9-*T*11 coordinated three-periodic net, following the ***TOPOS*** nomenclature [8]. The hexagonal structure appears uniquely in some compounds such as the hexagonal I-Na_2SO_4 phase and the HT-$Ca_2[SiO_4]$ (also $\boldsymbol{P}6_3/mmc$). The reader can find additional information in [9].

At this point, it is worth mentioning that the O'Keeffe and Hyde's approach had only a descriptive purpose and that, when applied, new questions arise, i.e. why is the Ni_2In-type structure that precisely adopted by the cation arrays of olivines? Of course, this is a new way of formulating the question asked above, that is, why cations occupy these special voids? Attempts for answering these questions have been advanced in the case of $Na_2[SO_4]$ [4, 10, 11].

The findings of O'Keeffe and Hyde [5] were, in fact, a generalization of an unexpected structural relationship, found earlier by Wondratschek, Merker and Schubert [12], between the cation array $[Ca_5P_3]$ of fluoroapatite ($Ca_5P_3O_{12}F$) and the Mn_5Si_3 alloy. At that time, this similarity was considered as an important matter, as deduced from the authors words (translated from German): "It is probable that this is not a casual coincidence but the strong analogies must obey a General Principle". Unfortunately, this important observation was ignored by inorganic chemists during more than 20 years.

Several articles have been published in the last few years aiming to deep in the understanding of this phenomenon [4, 11, 13–15]. In most cases, the structural similarities have been established from direct observation of the structures. For this reason, in recent papers, Blatov and co-workers [6–9] have provided a great number of examples substantiating the model of cation arrays by means of automatized computer crystallochemical analysis that allows for a systematic crystal-chemical analysis of complete sets of structures. This computer-aided comparison has given support to most of the already established relationships between alloys and cation arrays, leading so to many other so far unknown relationships. Even if they provide new insights of great interest in crystal chemistry, it should be emphasized that the relationships remain at a topological level.

Our idea, already expressed in earlier works [4, 14, 15], is that any topological relationship should be contemplated as the result of chemical interactions and should be explained in chemical terms. So, our aim in this work is to do a profound "dissection" of the two structures of $FeLi[PO_4]$ in the light of the extended Zintl–Klemm concept (EZKC). We intend to find new structural correlations which can help us to answer the two crucial questions quoted above, that is, why the Li and Fe atoms separate in triphylite and to account for the exchange of positions of the Li and Fe atoms in the high pressure β-phase. These kind of questions are "rarely asked" in crystallographic publications and, as far as we know, have ever been satisfactorily answered.

2 Description of the Triphylite $FeLi[PO_4]$ Structure

As said above, the cation array of triphylite $Fe[LiPO_4]$ (olivine-like) is an orthorhombic distortion of the hexagonal Ni_2In-type structure. The complete structure is represented in Fig. 1 where it is shown how the octahedral cations (Fe and Li) are

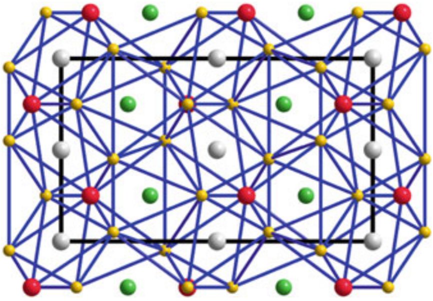

Fig. 1 The structure of the olivine-like FeLi[PO$_4$] projected on the ab plane. The colour codes are: *green* (Fe), *grey* (Li), *violet* (P) and *yellow* (O). This projection shows the *hcp* array of O atoms connected by blue lines

not distributed at random but separated in two different sets. The Li atoms are at 4*a* (0, 0, 0) and Fe atoms at 4*c* (*x*, ¼, *z*). This separation is an important aspect which is normally ignored in the crystal-chemical discussions. Because it is generally admitted that size effects play an essential role in the type of voids occupied by each cation, here the question is of special interest because both Li and Fe atoms are at octahedral voids, and there would be no reason for this precise observed splitting. The complete structure is shown in Fig. 1, which shows the great irregularity of the *hcp* array of O atoms. It has been suggested [5] that the irregularity implies that the classical description of structures based on closed packed array of anions should be considered as inadequate.

As mentioned above, our description will be based on the cation array which, in the case of olivine-like compounds, is of Ni$_2$In type. It should be remarked that even a simple structure, like the Ni$_2$In type, admits multiple descriptions which will be considered in the following sections.

2.1 Olivine FeLi[PO$_4$] and the Ni$_2$In Structure

The most frequent description of the Ni$_2$In structure consists of chains of trigonal prisms, formed by the (Li, Fe) atoms, which are centred by the P atoms. Thus, FeLi[PO$_4$] can be described as an O-stuffed [FeLiP] alloy whose structure is of the distorted Ni$_2$In type [5]. The cation array is represented in Fig. 2, after omitting the O atoms, which were drawn in Fig. 1.

2.2 FeLi[PO$_4$] and the AlB$_2$ Structure

A second description relates olivine to the AlB$_2$-type structure. More precisely, Ni$_2$In has been described as a superstructure of the AlB$_2$ type [16]. This relationship has also applied to hexagonal structures of related compounds, such as KZnP, which have been the object of theoretical calculations [17].

The AlB$_2$ structure consists of the $\mathbf{3^6}$ planar nets of Al atoms alternating with $\mathbf{6^3}$ graphite-like layers of B atoms. In the hexagonal Ni$_2$In structure (***P***6$_3$/mmc), the $\mathbf{3^6}$

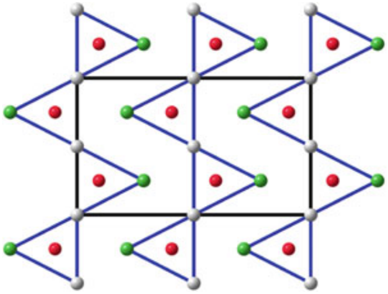

Fig. 2 The cation array of the triphylite FeLi[PO_4] structure, after omitting the O atoms. The FeLiP subarray forms a Ni_2In-like structure, with the Li and Fe atoms forming the trigonal prisms which are centred by the PO_4 groups. Colour codes: Fe (*green*), Li (*light grey*) and P (*red-violet*)

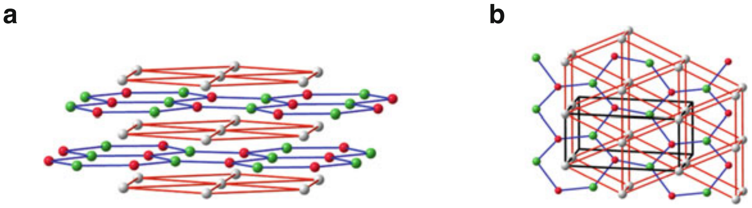

Fig. 3 (**a**) Alternative description of a Ni_2In type as a superstructure of the AlB_2-type. The Li atoms form the *hcp* $\mathbf{3^6}$ layers whereas the P and Fe atoms compose the graphite-like layers. (**b**) The same arrangement viewed along the *b* axis, almost perpendicular to the layers, to show the irregularity of the Fe–P graphite-like $\mathbf{6^3}$ nets. Colour codes as in Fig. 2

planar nets, formed by the Ni(1) atoms, alternate with the graphite-like layers formed by both Ni(2) and In atoms (Fig. 3a). It should be outlined that in both AlB_2 and Ni_2In, the graphite-like layers (B and NiIn, respectively) are completely regular, whereas in the olivine-like [FeLiP] subarray, the $\mathbf{6^3}$ planar nets show an orthorhombic distortion as seen in Fig. 3b. The distortion can be quantified by the values of the three Fe–P contacts (3.18, 3.23 and 2.89 Å).

If the atoms would be either C or Si atoms (Group 14 elements), this distortion would lead to a loss of the aromatic character, consistent with the formation of one double bond (2.89 Å) and two single ones with distances of 3.18 and 3.23 Å. It should be recalled that this bonding scheme is the only way of maintaining the four valences for each atom in a planar net. This argument, however, is difficult to extrapolate to the mixed FeP nets, even if we consider them as a III–V compound, like AlP for example, which normally adopt structures of the Group 14.

2.3 *The FeLiP Subarray and NiAs·FeLi[PO_4] and Li[ClO_4]*

A third description of the subarray derives from the NiAs-type structure. This relationship was already used to rationalize the Ni_2In structure in terms of the EZKC [4]. This concept establishes that, like in the Zintl phases [18, 19], the inorganic structures can be rationalized by assuming that electron transfer can also occur between any pair of cations, even if they are of the same kind [4].

By applying this concept to the Ni_2In structure, the Ni(1) atom transfers two electrons to the In atom, so that the $Ni(1)^{2+}$ becomes a pseudo-Fe atom (Ψ-Fe) and the In^{2-} becomes Ψ-Sb. Thus, Ni_2In converts into Ψ-Fe[NiΨ-Sb], where the [NiΨ-Sb] substructure is of the NiAs type. Note that the real NiSb compound is also of NiAs type! Consequently, Ni_2In can be described as a Ni-stuffed NiAs structure. The stuffing Ni(1) atoms occupy the centre of trigonal bipyramids, as seen in Fig. 4.

When this model is applied to FeLi[PO_4], we see that the *hcp* array is now formed by the P atoms, and the octahedra are filled by Li atoms. In this case, the Fe atoms are at the centre of the trigonal bipyramids, acting simultaneously as donor and stuffing agents. This is illustrated in Fig. 5, where the distortion of the *hcp* array of P atoms is made evident. The P octahedral network (Fig. 5a) is very irregular and flattened.

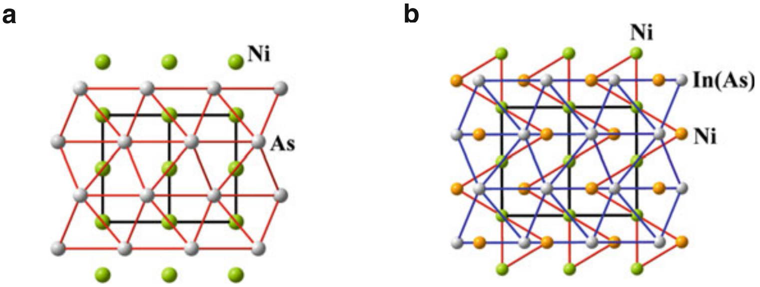

Fig. 4 (**a**) The NiAs structure viewed along [110]. *Red lines* connect the As atoms (*grey circles*) which form an hcp array with all octahedra filled with the Ni atoms (*green*). (**b**) The Ni_2In structure viewed along [110]. The Ni(1) atoms (*dark yellow spheres*) are stuffing the [NiΨ-Sb] subarray to form the NiAs (NiSb) structure. The *blue* contacts form the Sb octahedra. The *red lines* mark the trigonal prisms of Ni atoms which are occupied by the As atoms. Note that the NiAs structure is implicit in Ni_2In

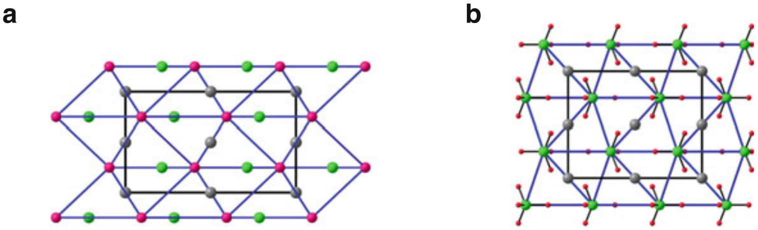

Fig. 5 (**a**) The FeLiP array in the ambient pressure phase of $FeLiPO_4$ (triphylite), showing the existence of a latent NiAs-type structure formed by both the P (*red-violet*) and Li (*light grey*) atoms. *Blue lines* connect the P atoms (*hcp* array) to depict the octahedral holes which are occupied by the Li atoms. The Fe atoms are at the centre of triangular faces. Colour codes as in previous figures. (**b**) The structure of $LiClO_4$, showing its similarity with the isoelectronic $(LiPO_4)^{2-}$. *Grey spheres* represent Li atoms. *Green* and *red spheres* represent the ClO_4 groups

This interpretation as a Fe-stuffed (LiP) array could be admitted if the charge transfer from Fe to P atoms is considered as reasonable. In this case, the compound should be formulated as pseudo-$Fe^{2+}[\Psi\text{-}LiClO_4]$. On the contrary, a charge transfer from Fe to the Li atoms seems to be poorly founded. This transfer would give rise to the pseudo-formula $Fe^{2+}[\Psi\text{-}BPO_4]$. Even if the two Fe electrons are distributed on both Li and P atoms, the pseudo-formula $Fe^{2+}[\Psi\text{-}BeSO_4]$ is obtained.

Our proposal is that the two last pseudo-formulae should be discarded because neither $Be[SO_4]$ nor $B[PO_4]$ are known to have cation arrays of the NiAs-type structure which, on the other hand, exists with heavier elements like in $Mg[SO_4]$ [20]. However, the pseudo-formula $[Li\Psi\text{-}ClO_4]$ is physically meaningful because the real compound $Li[ClO_4]$, recently synthesized [21, 22], is isostructural to $Cu[SO_4]$ ($MgSO_4$) type (***P***nma), with a $Li[\Psi\text{-}Cl]$ subarray of the NiAs type, as represented in Fig. 5b. It should be remarked that this interpretation seems more "plausible" because the real halide LiCl crystallizes in the strongly related rocksalt structure. However, the strong distortion of the *hcp* array of P atoms in triphylite (Fig. 5a) in comparison with the real $Li[ClO_4]$ structure (Fig. 5b) is a clear indication that other interpretations of the structure might be more appropriate, as it will be shown later.

2.4 FeLiP, and FeLi[PO$_4$]: The Extended Zintl–Klemm Concept

In the above section, we have seen the difficulties of finding a coherent interpretation of the [FeLiP] subarray on the basis of the Fe–P pair of atoms. The unique rational issue was the formation of the hugely distorted array of Fig. 5a, which could be related to the distortion of the graphite-like Fe–P layers drawn in Fig. 3.

However, if instead of drawing the Fe–P contacts running parallel to the *a* axis, we connect the same atoms with the blue lines drawn in Fig. 6a, then a new pattern

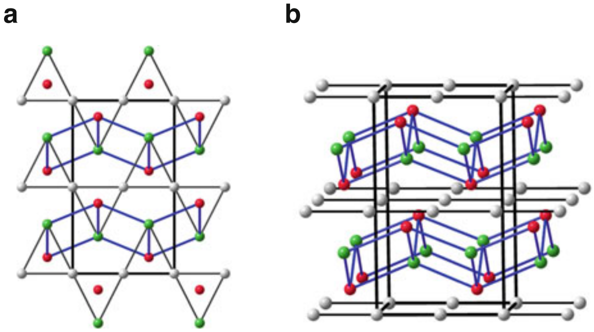

Fig. 6 (**a**) The FeLiP subarray of $FeLi[PO_4]$ projected on the ac plane. The drawing outlines the two views of the structure, i.e. the chains of trigonal prisms marked with *black lines* and also the new description in terms of blocks of the PbO-type drawn with *blue lines* connecting the Fe and P atoms (*green* and *red-violet spheres*, respectively). (**b**) A perspective view of the FeLiP subarray showing the four-connected skeleton of the Fe and P atoms

appears. If the Li atoms (grey spheres) are neglected, the remaining Fe and P atoms form a four-connected skeleton of the PbO type which alternate with the Li layers along the *a* axis. A perspective view of these blocks is represented in Fig. 6b. This PbO-type structure is also adopted by III–V compounds such as InBi [23].

The goodness of this interpretation becomes evident by applying the EZKC. The Li atom acts as donor, transferring its valence electron to the P atom which becomes Ψ-S, so that the [FeP] subarray can be formulated as [FeΨ-S]. The marvellous feature is that this is the structure of one of the phases of real FeS itself! The Li atoms have produced the conversion of the [FeP] subarray (FeΨ-S) into a true FeS structure.

Another feature which must be remarked upon is that the FeLiP subarray of triphylite (FeLi[PO$_4$]) adopts the same structure as the Zintl phase FeLiP [24], in which the [FeP] subarray is also of the PbO type. The three structures, i.e. FeLi[PO$_4$] [2], FeLiP [24] and the HT phase of FeS [25], are shown in Fig. 7 for comparison.

However, the most intriguing feature is how the FeS substructure is maintained when we add the Li atoms in the Zintl phase FeLiP, and even when four additional oxygens are inserted into the structure of the FeLi[PO$_4$] oxide (triphylite). *It is intriguing that such a structural motif remains when more and more atoms are added to the structure*. These compounds represent new examples of two general trends observed in many oxides. On the one hand, their cation arrays maintain the structures of their respective alloys [11]. On the other hand, the ***ZKC*** can be successfully applied to explain the cation arrays in oxides [4].

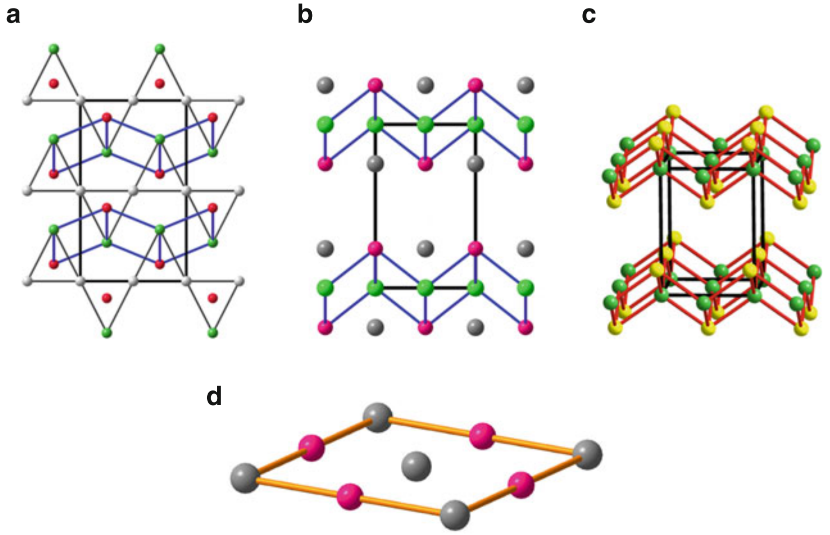

Fig. 7 (**a**) The cation array of FeLi[PO$_4$] (triphylite) showing its similarities with the structure of the Zintl phase FeLiP, drawn in (**b**) and with the FeS structure which is of the PbO type (**c**). In (**d**), we have separated one of the planar nets formed by the Li and P atoms in (**b**). They correspond to {100} planes of the rocksalt LiCl

When Fig. 7a ($FeLi[PO_4]$) is compared with Fig. 7b (FeLiP), it is advisable that the FeLiP subarray of triphylite differs slightly from the structure of the Zintl phase FeLiP. The differences reside in the location of the Li atoms. Thus, in the Zintl phase (Fig. 7b) the Li atoms are coplanar with the P atoms, forming so square planar nets, like those shown in Fig. 7d. However, in $FeLi[PO_4]$ (Fig. 7a), the same atoms are not anymore coplanar, probably due to the presence of the O atoms which produce a greater separation of the Li layers.

On the contrary, in FeLiP (Fig. 7b), the application of the Zintl–Klemm concept [18, 19] would explain that if the Fe atoms act as donors, would convert the P atoms into Ψ-Cl, forming so fragments of the rocksalt structure of real LiCl. These planes, similar to (100) planes of the LiCl unit cell, are shown in Fig. 7d.

The above discussion shows another interesting aspect of our dissection. It gives support to the recent approach of Vegas, Martin and Bevan [15] which suggests that, in any compound, any pair of atoms try to satisfy its structural requirements as much as possible. The fragments of the LiCl structure illuminates this important structural aspect because even the dimensions of the rocksalt structure of LiCl ($a = 5.13$ Å) are preserved in the Zintl phase FeLiP ($a' = 5.21$ Å) (Fig. 7d). In the same manner, the Fe–P distances, 4 × 2.34 Å, in the Zintl phase FeLiP are comparable to those of 4 × 2.25 Å in the high temperature phase of FeS (Fig. 7c). We will return later on this interesting aspect of crystal structures.

2.5 The Li Subarray and the Structures of Elemental Li

The Li subarray of triphylite $FeLi[PO_4]$ merits a special consideration. Fig. 8a repeats the representation of the cation subarray [FeLiP] of triphylite. It shows both the four-connected [FeP]-network and the intercalated Li layers. In Fig. 8b, the [FeP] network has been omitted to show how the Li subarray forms rectangular planar nets of dimensions 3.00 × 4.69 Å. These nets can be thought as fragments of the structures of elemental Li. Thus, in *fcc*-Li ($a = 4.32$ Å, $d_{\text{Li–Li}} = 3.05$ Å), the (1 1 0) planes contain rectangles of similar dimensions (3.05 × 4.32 Å), whereas in the *hcp*-Li structure ($a = 3.11$ and $c = 5.09$ Å), the (1 0 0) planes of the hexagonal cell contain similar rectangles of dimensions 3.11 × 5.09 Å.

These data clearly show that the Li subnet in triphylite $FeLiPO_4$ is formed by infinite planar nets comparable to the real crystallographic planes of both, *fcc*- and *hcp*-Li. In fact, the average dimensions of the rectangles in the elemental phases (3.08 × 4.70 Å) almost equal the values of 3.00 × 4.69 Å in triphylite. As it has been reported elsewhere [13], the fact that the metal structures are preserved so accurately in the compounds continues being a challenge for theoretical chemistry.

Besides the structural features, just discussed, triphylite shows a surprising chemical behaviour, i.e. $FeLi[PO_4]$ can be delithiated, giving rise to a new phase of $Fe[PO_4]$ which preserves the ***P***nma space group in both the crystal [26] and magnetic [27] structures. The important issue here is that the $Fe[PO_4]$ substructure of triphylite remains unaltered in the delithiated phase! (Fig. 8a, c).

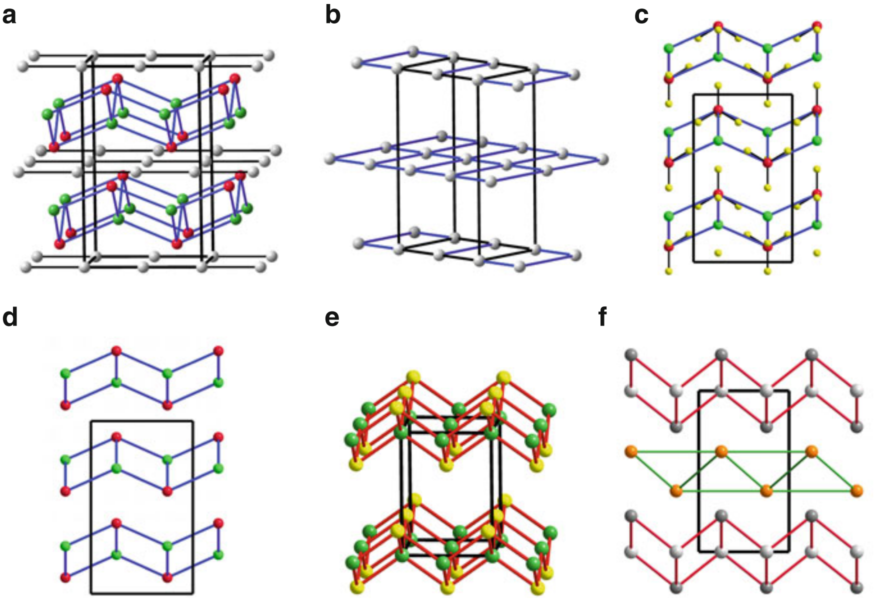

Fig. 8 (**a**) Perspective view of the triphylite FeLiP subnet, showing the Li layers intercalated between the four-connected FeP network. (**b**) The Li layers showing the rectangular nets comparable to those existing in *hcp*-Li and *fcc*-Li. (**c**) The delithiated Fe[PO_4] structure, projected on the ab plane. The O atoms are represented with *dark yellow spheres*. The Fe and P atoms are represented as in (**a**). (**d**) The same structure without the O atoms to show clearly its similarity with the FeS structure represented in (**e**) where the four connectivity is made evident. (**f**) The structure of the NaAlSi Zintl phase showing the PbO-like structure of the $[AlSi]^-$ polyanion

This recurrent framework could be, in principle, associated with the fact that in the Li-free compound, the FeP subnet corresponds to a (III)–(V) compound. Remember that the same skeleton is found in the Zintl phase NaAlSi [28], where the $[AlSi]^-$ Zintl polyanion, the (IV)–(IV) Ψ-Si array, is forming the same framework as represented in Fig. 8f. Equivalent isostructural oxides, constituted by either, (III)–(V) or (II)–(VI) cation arrays, are In[PO_4], Ti[PO_4], Cr[PO_4] and Mn[SO_4], among others.

The last compound, Mn[SO_4] [29], will serve us to illustrate how the EZKC can account for the observed structure in the delithiated Fe[PO_4] phase. Thus, the Li extraction takes place through a redox process where the Li^+ cations are reduced at expenses of the oxidation of Fe^{2+} to Fe^{3+}. This means that the oxidized [Fe^{III}P] subnet becomes isoelectronic with MnS, and hence the iron phosphide could be formulated as Ψ-MnS. Consequently, Fe[PO_4], isoelectronic to Mn[SO_4], could also be formulated as Ψ-Mn[SO_4], in view of the fact that the room temperature phase of Fe[PO_4] [27] adopts the same structure as real Mn[SO_4] [29].

The above interpretation can be correlated with the fact that the sulphide MnS undergoes the NaCl → ZnS (blende) transition at 473K [30, 31]). It has been suggested on the basis of theoretical calculations [32] that this transition could take place through an intermediate PbO-like phase. This intermediate phase, which has ever been reported for the binary compound FeP, could be a metastable arrangement stabilized in Fe[PO_4] as a consequence of the role played by the O atoms in forming high pressure phases of the alloys [11].

3 The High Pressure Phase β-FeLi[PO_4]

In this section, we will describe the structure of β-FeLi[PO_4], synthesized at high temperature and pressure [2]. Two important structural features distinguish this β-phase from the triphylite structure. The first one is a change in symmetry, from the space group ***P***nma of triphylite to the supergroup ***C***mcm in the HP phase β-FeLi[PO_4]. The second one is that the Li and Fe atoms exchange their position in the structure as it can be observed by comparing Fig. 9a with both Figs. 2 and 6a.

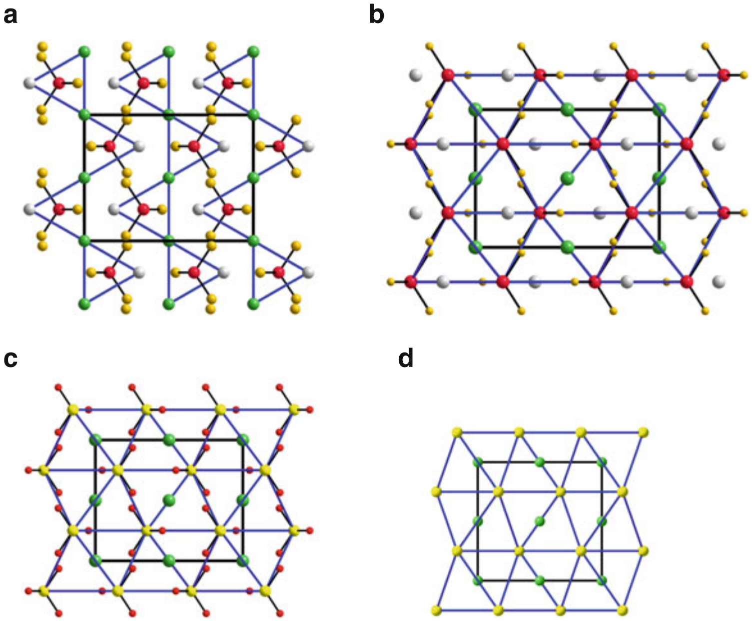

Fig. 9 (**a**) The structure of the high pressure phase of β-FeLi[PO_4] (***C***mcm) showing the exchange of the Li and Fe atoms with respect to the olivine-like phase (***P***nma) of triphylite (compare with Fig. 2). *Blue lines* highlight the trigonal prisms centred by the PO_4 groups. (**b**) The same structure in which the *hcp* array of P atoms (*red-violet spheres*) has been depicted. All the octahedral holes are occupied by the Fe atoms in contrast to the triphylite structure represented in Fig. 5a. (**c**) The structure of the ***C***mcm structure of $FeSO_4$ to show its similarity with that of Fe[PO_4] subarray represented in (**b**). (**d**) The structure of the orthorhombic phase of FeS (***C***mcm), a distortion of the NiAs type, to show its coincidence with both the Fe[PO_4] subarray (**b**) and the Fe[SO_4] structure drawn in (**c**)

Our discussion will be focused on the similarity of the cation arrays with the Ni$_2$In-type structure (Fig. 9a) and more precisely with the NiAs-type skeleton which is implicit in it. Special emphasis will be given to the characteristics defining each phase.

The differences between the cation arrays of both phases of FeLiPO$_4$ are simple. As discussed above, triphylite FeLi[PO$_4$] was described as a Fe-stuffed [LiΨ-Cl] array of the NiAs type in which the P atoms (Ψ-Cl) form a *hcp* array with all the octahedral voids filled by the Li atoms (Fig. 5a). Remember also that the pseudo-structure of Ψ-Li[ClO$_4$] in triphylite showed a great distortion with respect to that of real Li[ClO$_4$] [21, 22]. On the contrary, in β-FeLi[PO$_4$], the octahedra of the *hcp* array of P atoms are now filled by the Fe atoms, forming so a Li-stuffed [FeP] subarray (Fig. 9b).

3.1 Relationships of β-FeLi[PO$_4$] with Fe[SO$_4$] and Li[ClO$_4$]

If the EZKC [4] is applied to β-FeLiPO$_4$, the structure can be rationalized by assuming the one-electron transfer from the Li atom to the P atom which is converted into a Ψ-S. In this way, β-FeLiPO$_4$ should be formulated either as Li$^+$[FeP]$^-$ or as (Ψ-He)[FeΨ-S]. The result is that the cation array of the β-phase would contain, in fact, a Ψ-FeS substructure of the NiAs type [25]. In this arrangement, the Li atoms are located in trigonal bipyramids, as the Fe atoms did in triphylite. Consequently, β-FeLi[PO$_4$] can then be formulated as a Li-stuffed Ψ-Fe[SO$_4$] structure. This view of the structure is represented in Fig. 9b.

By examining the structure of Fe[SO$_4$] [33], also ***C***mcm, one sees that, once more, the structure of the pseudo-formula (Fig. 9b) coincides with that of real Fe[SO$_4$], which is represented in Fig. 9c. Moreover, if in both compounds the O atoms are neglected, the FeS subarrays of both compounds are identical to the high temperature phase of real FeS (also ***C***mcm) [34]. Again, the structure, as well as the space group, is maintained in FeS, Fe[SO$_4$] and Ψ-Fe[SO$_4$]! The three structures are shown in Fig. 9c, b and a, respectively.

The lack of similarity between the two phases, triphylite and β-FeLi[PO$_4$], becomes evident by comparing Fig. 9b with Fig. 5a (the colour code is the same in both figures). Although both drawings represent Li-stuffed NiAs-type structures, the important issue is that in β-FeLi[PO$_4$] (Fig. 9b) the [FePO$_4$] subarray has formed a NiAs-type arrangement which is much more regular than that formed by the [LiPO$_4$] subarray in triphylite (compare with Fig. 5a). Thus, although both structures are formed by an *hcp* array of PO$_4$ groups, the chemical nature of the stuffing atoms (Fe and Li, respectively) seem to play a decisive role in the formation of a "true" NiAs-type structure; that is, the structure is close to the hexagonal regularity in β-FeLi[PO$_4$] (Fig. 9b) but is highly distorted in triphylite (Fig. 5a). The reasons for these differences will be discussed below.

3.2 *The Exchange of Li and Fe in the Transition Triphylite → β-FeLi[PO$_4$]*

The questions that arise now are: Does the exchange of Fe and Li atoms have any physical meaning? Why the exchange takes place under pressure? To answer these questions, we must return to the interpretation of the structures in terms of the EZKC. In a first attempt, the exchange was thought to be a consequence of the inversion of the charge transfer between Li and Fe. However, we must remember that the approach which considered the triphylite FeLi[PO$_4$] structure (olivine-like) an Fe-stuffed Ψ-Be [SO$_4$] (or Ψ-B[PO$_4$]), with the Fe atoms acting as donors, was later left as inadequate.

The detailed analysis of both structures reveals that the important feature is that the structures of the respective [FeP] subarrays (Ψ-FeS) should be coincident with structures of real phases of the FeS sulphide, that is, the PbO type in triphylite and NiAs type in β-FeLiPO$_4$. Thus, by assuming the expected electron transfer from Li to Fe and/or P atoms, both skeletons can be explained in a rational way. Even more, differences in the structures of [FeP] subarrays would indicate that the PbO-type structure (Fig. 6a) existing in the ambient pressure phase (triphylite) is converted into the NiAs-type structure of β-FeLi[PO$_4$] under pressure. This transition, undergone by the [Ψ-FeS] subarray, must be correlated with the fact that real FeS, zinkblende at ambient conditions undergoes, under compression, the transitions ZnS → PbO → NaCl (NiAs).

The important result is not only the PbO → NiAs transition but also that when the Li atom transforms the FePO$_4$ subarray of β-FeLi[PO$_4$] into a Ψ-Fe[SO$_4$]; this transformation is not only formal, but Fe[PO$_4$] reproduces the structure of real Fe[SO$_4$] itself, whose [FeS] subarray is, in turn, identical to the NiAs-type phase of FeS. These ideas are clearly expressed in Fig. 9.

Now, we can give a satisfactory explanation of why the Fe and Li atoms exchange their positions. At ambient pressure (triphylite), both Fe and P atoms must form the PbO-type structure characteristic of FeS. At high pressure, the same atoms must form a high pressure phase of FeS, that is, the NiAs-type structure. In both cases, however, stable structures of Ψ-FeS are satisfied.

In support of our interpretation is the fact that when the Fe atoms are considered as donors, the LiP subarray (NiAs type) of triphylite forms the irregular, extremely flattened octahedra (Fig. 5a), which contrast with the regularity of Li[ClO$_4$] (Fig. 5b). On the contrary, if Li acts as donor, forming the Ψ-Fe[SO$_4$], represented in Fig. 9c, the structure drawn in Fig. 5a becomes useful and the two structures of FeLi[PO$_4$], interpreted as in Figs. 8a and 9b, for triphylite and the β-phase, respectively, become physically meaningful.

4 FeLi[PO$_4$] and the High Temperature Phases of Na$_2$[SO$_4$]

It has been mentioned above that the two phases of FeLi[PO$_4$] (***P***nma and ***C***mcm) are isostructural with two high temperature phases of Na$_2$[SO$_4$]. It must be recalled that the ambient pressure phase thenardite V-$Na_2[SO_4]$ undergoes, by increasing temperature, the following transitions sequence [3]:

$$\begin{aligned}\text{Thenardite}(\mathrm{V}-\mathrm{Na_2SO_4})(F\mathrm{ddd}) &\rightarrow \mathrm{III}-(C\mathrm{mcm}) \rightarrow \mathrm{II}-(P\mathrm{nma})\\ &\rightarrow \mathrm{I}-(P6_3/\mathrm{mmc})\end{aligned}$$

When these structures were described on the basis of their cation arrays [6, 7]), it was thought that the three phases could be contemplated as slight variants of the most symmetrical I-$Na_2[SO_4]$ (***P***6_3/mmc) whose cation subarray (Na_2S) is of the Ni_2In type (also ***P***6_3/mmc). This can be easily understood by looking at Fig. 10b, e, h. Recall that in the O'Keeffe and Hyde's approach [5], the cation array of olivine, $Mg_2[SiO_4]$, isostructural to II-Na_2SO_4 (***P***nma), was considered of the Ni_2In type.

In connection with this relationship, it was shown later [4] that the two structures, III- and II-$Na_2[SO_4]$ (***C***mcm and ***P***nma, respectively), should really regarded as intermediate steps in a longer "structural transition" which ends in the Ni_2In-type structure (***P***6_3/mmc) formed by Na_2S in the hexagonal I-$Na_2[SO_4]$ (***P***6_3/mmc). Thus, $FeLi[PO_4]$ and $Na_2[SO_4]$, with their two common phases (***C***mcm and ***P***nma), follow, in part, a similar structural behaviour.

Recall that these features are in agreement with the topological analysis carried out by Blatov et al. reported in this volume [9].

4.1 *$FeLi[PO_4]$, Ψ-$Mg[SO_4]$ and Ψ-$Fe[SO_4]$ in the Light of the EZKC*

We must recall that the [Na_2S] subarray in I-$Na_2[SO_4]$ (***P***6_3/mmc) was interpreted, following the EZKC, as Na^+[Ψ-MgS], where the [Ψ-MgS] subarray was formed by completely regular graphite-like layers like those represented in Fig. 10a [4]. The reader is also referred to Fig. 3 to recall its relationship with the AlB_2-type structure.

If we wish to deep in the application of the EZKC, Na_2SO_4 can be formulated as Na^+[Ψ-$MgSO_4$] if we admit that one Na atom transfers its valence electron to the other one, converting it into pseudo-magnesium (Ψ-Mg) and $[NaSO_4]^{1-}$ into Ψ-Mg [SO_4]. The consequence is that the structure of $Mg[SO_4]$ itself should necessarily appear in $Na_2[SO_4]$.

The impressive outcome is that $Mg[SO_4]$, dimorphic, with a ***C***mcm phase, stable at ambient conditions, and a high temperature phase of ***P***nma symmetry [20] are just the structures of both the III- and II-$Na_2[SO_4]$ phases (Fig. 10). The correlation is much more far reaching, i.e. in the pseudo-structure Ψ-$Mg[SO_4]$ as well as in real Mg [SO_4], the [MgS] subarray is a slightly distorted NiAs-type structure, reproducing at the same time, the NiAs structure of a metastable phase of MgS, obtained in thin films [35]. Recall that bulky MgS crystals are of the NaCl-type, a structure that is related to the NiAs-type. Thus, MgS, $Mg[SO_4]$ and Ψ-$Mg[SO_4]$ all have a NiAs-type arrangement as clearly shown in Fig. 10c, f, i, p. In Fig. 10p, the structure of $Fe[SO_4]$,

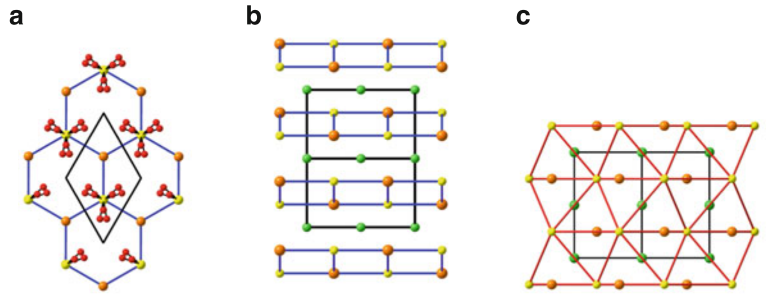

180°
Three aspects of I-Na_2SO_4($P6_3$/mmc)

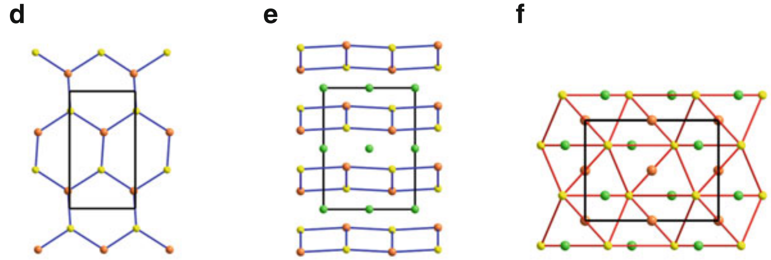

174°
The structure of II- Na_2SO_4(Pnma)

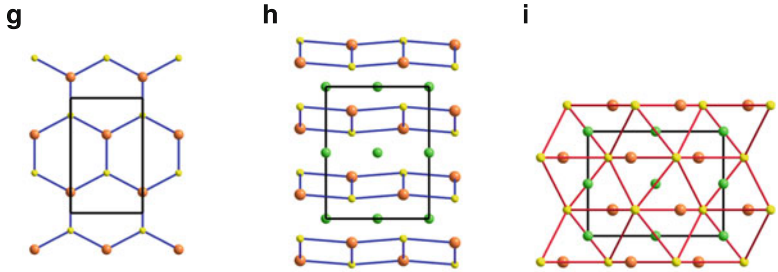

170°
The structure of III- Na_2SO_4(Cmcm)

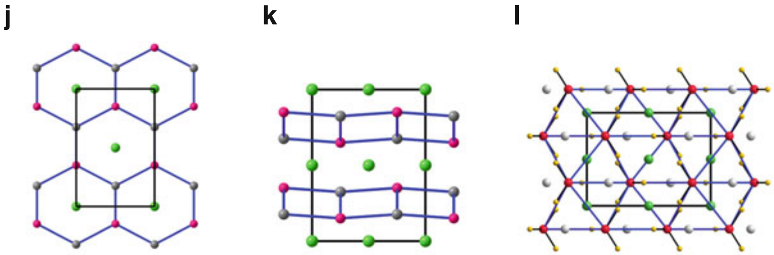

Three aspects of β-$LiFePO_4$ (Cmcm)

Fig. 10 (continued)

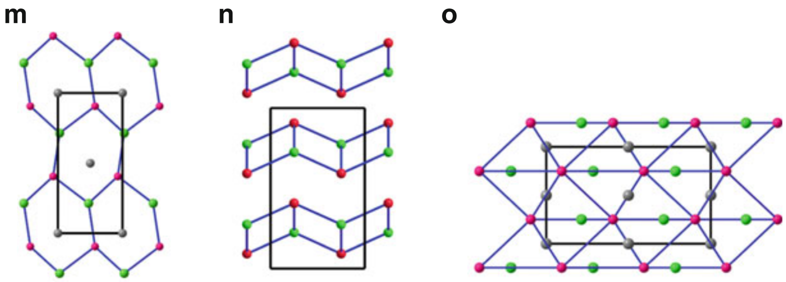

Three aspects of triphylite FeLi[PO_4] (*P*nma)

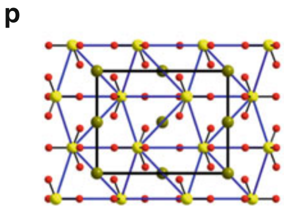

The structure of $FeSO_4$ (*C*mcm)

Fig. 10 Evolution of the structures of both Na_2[SO_4] and FeLi[PO_4], all of them considered as olivine-like compounds. The first row shows three aspects of the structure of I-Na_2[SO_4] (**P**6_3/mmc). In (**a**) the regular $\mathbf{6^3}$ layers are represented, formed by both S and Na atoms. The O atoms show clearly the rotational disorder. In (**b**) the structure is projected on the (110) plane to show the linear [NaS] blocks, with an S–Na–S angle of 180°. In (**c**) the Na-stuffed NiAs-type structure is drawn. The second row contains the similar drawings for II-Na_2[SO_4] (***P***nma). Note the small distortion of the graphite-like layers in (**d**), The lack of linearity in the [Na-S] blocks (angle of 174°) (**e**) and the rather regular NiAs-type structure in (**f**). The *third arrow* corresponds to III-Na_2[SO_4] (***C***mcm). Note the greater distortion of the hexagonal layers in (**g**) as well as the lower value of the S–Na–S angle (170°) in (**h**). The NiAs-type arrangement is also rather regular (**i**). The *fourth arrow* contains the same views of the high pressure β-FeLiPO_4. Note the irregularity of the [LiP] hexagons and the almost linear [FeP] blocks represented in (**j**) and (**k**), respectively. These distortions make that this HP phase(***C***mcm) should be better conceived as a Li-stuffed NiAs-type structure as drawn in (**l**). The *fifth arrow* collects the three views of the triphylite FeLi[PO_4] (***P***nma, olivine-like). The irregular [FeP] graphene-like layers are depicted in (**m**). In (**n**), the [FeP] blocks of the PbO type are clearly outlined. The great distortion of the Fe-stuffed NiAs-type structure represented in (**o**) clearly indicates that this phase should be contemplated as a Li-stuffed FeP array [Ψ-FeS] of the PbO type, as shown in Fig. 8. In (**p**), the NiAs-type structure of the two phases of Mg[SO_4] to be compared with the corresponding Na^+Ψ-Mg[SO_4] structures drawn in (**c**), (**f**) and (**i**)

isostructural to Mg[SO_4], has been represented as a reference for the Ψ-Mg[SO_4] shown in Fig. 10c, f, i.

As already discussed, the hexagonal I-Na_2[SO_4] (***P***6_3/mmc) is obtained at higher temperatures, leading to a Ψ-[MgS] subarray which forms the graphite-like layers depicted in Fig. 10a. These $\mathbf{6^3}$ nets might be regarded as a pseudo-[(II)–(VI)] compound which are forming a network characteristic of a (IV–IV) structure, like

C or Si. This feature should be related to the adamantane structures found in other (II)–(VI) compounds, such as ZnS, BeO and BeS (blende and wurtzite).

The regularity of the [Ψ-MgS] $\mathbf{6^3}$ layers might be related to the aromatic structure of graphite itself, in such a way that in each Na-S contact would be involved 1.5 electrons. This has been correlated with the rotational disorder of the SO_4 groups, whose O atoms try to capture a pair of electrons. Because the electrons are delocalized around the aromatic rings [4], this would provoke the simultaneous rotation of the sulphate groups. Looking at Fig. 10a, d, g, j, m, it is noteworthy that such a hexagonal phase has only been observed in $Na_2[SO_4]$, but neither in $Mg[SO_4]$ nor in $FeLi[PO_4]$.

4.2 The Olivine-Like Structures and the PbO-Type Blocks

We have analysed so far the graphite-like layers. However, the alternative Ψ-MgS skeletons, derived from a PbO-type array, merit a special comment. Thus, the skeletons in III-, II- and I-$Na_2[SO_4]$ represented in Fig. 10b, e, h form a continuous sequence of images, which will be discussed next.

In the III-phase (***C***mcm) (Fig. 10h), the Ψ-[MgS] subarray forms a distorted PbO-type structure with an S–Na–S angle of 170°, greater than in FeS (118°) (Fig. 8e). By increasing the temperature, the angle becomes closer to linearity, 174° in the II-phase (***P***nma) and becomes linear (180°) in I-$Na_2[SO_4]$ (***P***6_3/mmc), where simultaneously the graphite-like layers become regular hexagons (Fig. 10a, b).

If the sequence is completed with Fig. 10n and k, corresponding to $FeLi[PO_4]$, one can obtain a view of all intermediate steps in the complete transition from PbO to NiAs. Thus, the PbO-type structure is stabilized in the ambient pressure phase of triphylite $FeLi[PO_4]$ (Fig. 10n) and becomes closer to the NiAs type in the high temperature, high pressure, β-$FeLi[PO_4]$ [2]. It is also worth mentioning the simultaneous regularity of the PbO-type array in triphylite $FeLi[PO_4]$ (Fig. 10n) with the strong distortion of its NiAs-type structure represented in Fig. 10o, and how the regularity and distortion are inverted in β-$FeLi[PO_4]$, as shown in Fig. 10k, l.

A question that arises is why the PbO-type subarray has not been observed in $Na_2[SO_4]$. A possible reason for this is that $Na_2[SO_4]$ tries to reproduce the structure of pseudo-compounds derived from this composition. Thus, the only possibility should be Ψ-$Mg[SO_4]$, as observed in the mentioned ***C***mcm- and ***P***nma-phases (**III**- and **II**-$Na_2[SO_4]$), showing arrangements like that of Fig. 10p. This is equivalent to say that $Fe(LiPO_4)$ could also be formulated as $Fe^{2+}(LiPO_4)^{2-}$, equivalent to a Fe-stuffed Ψ-$Mg[SO_4]$ structure. Surprisingly, the structure shown in Fig. 10l is that of $Mg[SO_4]$ itself (Fig. 10p) [20].

In principle, a PbO-type array should not be discarded because, as far as we know, no systematic HT study has been carried out on $Mg[SO_4]$. If stable, such a phase should be obtained at very high temperatures.

Another interesting question arising from the above discussion is why triphylite $FeLi[PO_4]$ transforms into the β-phase (***C***mcm) without reaching the ***P***6_3/mmc, like $Na_2[SO_4]$ does. A possible explanation is that the transition occurs at high temperature and high pressure, and that such a second transition to a hexagonal phase could take place at even higher temperatures and/or pressures. Even if the Ni_2In-type structure has not been observed in FeLiP, other related compounds, such as KZnP, adopt this hexagonal structure [36] where regular $\mathbf{6^3}$ graphenes are formed by both the Zn and P atoms. This feature is consistent with the Zintl–Klemm concept, making that KZnP can be formulated, either as K^+[Ψ-GaP] or as K^+[Ψ-ZnS]. In any case, the pseudo-formulae correspond to (III)–(V) and (II)–(VI) compounds, respectively, which normally adopt structures of the Group 14. The fact that real ZnS forms the adamantane structure and the pseudo-compound [Ψ-ZnS] forms graphite-like layers gives support to our previous interpretations.

Although discussed above, a remarkable feature of the HP-HT-phase (β-FeLi [PO_4]) is that in the ***P***nma-phase (Fig. 10l), the P atoms form a much more regular array than in the ***C***mcm phase (Fig. 10o). In the latter, the P octahedra are almost identical to the S-octahedra present in real ***C***mcm-Fe[SO_4] [33]. In our opinion, this could indicate that at HP the Li atoms produce the stabilization of a real Fe[SO_4] structure, adopting even the same space group (***C***mcm).

Moreover, in both FeLi[PO_4] and Fe[SO_4], the respective FeP (Ψ-FeS) and and FeS subarrays (NiAs type) coincide with the structure of FeS itself! Recall that in the olivine-like phase, the FeP arrays (PbO type) were also similar to another phase of FeS with this type of structure. It is also interesting to remark that in the ***C***mcm phase the PbO-like blocks are formed by both Li and P atoms, and that they are more flattened than in the ***P***nma-phase where the same blocks are formed by the Fe–P pairs (compare Fig. 10k and n).

The impression is that the phase transition, undergone by FeLi[PO_4], involves a clear phase transition of the FeP subarray which seems to control the structure, adopting in both cases stable structures of FeS. The fact that in the olivine-like phase the P octahedra are filled by the Li atoms (and not by the Fe atoms) is a clear indication of the control exerted by the Fe–P pair of atoms, which form, on the other hand, the PbO-type array.

4.3 The Co-existing Structures FeS/Fe[SO_4], LiCl/Li[ClO_4] and FeLiP/FeLi[PO_4]

The PbO-type arrangements, present in the two phases of FeLi[PO_4], have been widely discussed along this chapter. However, there remain some aspects, concerning the metric of the structures, which were not discussed in deep, but which provide additional data to gain an insight into the challenge underlying in this approach as it was advanced earlier [4], i.e. why the substructures are preserved when more and more atoms are added to form a given compound?

The magnitudes, shown in Table 1, together with the drawings represented in Fig. 11 allow us to discover novel and unexpected structural features.

Table 1 The unit cell dimensions and interatomic distances of some of the substructures existing in the two phases of FeLi[PO_4]

Compound	Unit cell (Å)	d(Fe–Fe) (Å)	d(Ψ-LiCl) d(LiCl)	Figures
fcc-Fe	$a = 3.65$	2.58		
FeS (PbO type)	$a = 3.67$ $c = 5.04$	2.61		11a, b
FeLiP (Ψ-FeS)	$a = 3.69$ $c = 6.02$	2.61		11c
FeLiP (Ψ-LiCl)	$a = 5.22$ $c = 6.02$ mean $a = 5.49$	2.61	2.61, 2.89, 3.13	11d, e
LiCl	5.14		2.57	

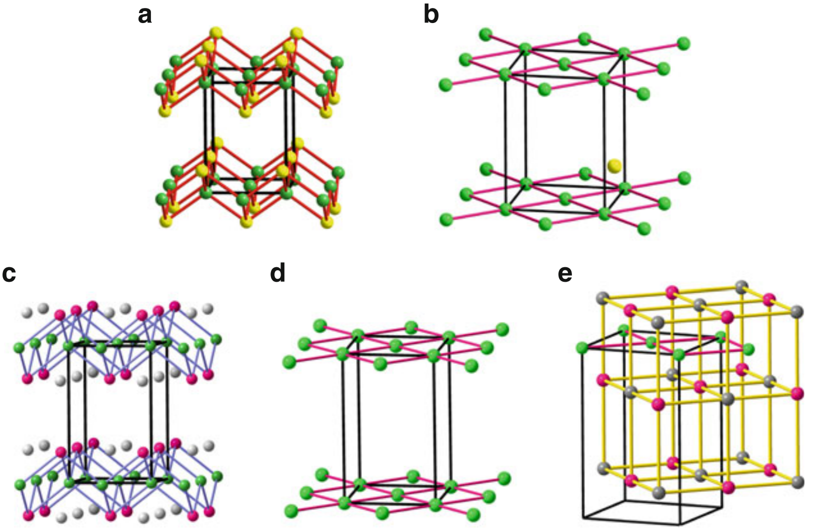

Fig. 11 (**a**) The PbO-type structure of FeS showing the tetra-connectivity of both Fe and S atoms. (**b**) The Fe subnet of FeS showing the $\mathbf{4^4}$ planar nets formed by the Fe atoms. They are equal to the (1 0 0) planes of *fcc*-Fe. (**c**) Perspective view of the structure of the Zintl phase FeLiP, showing that the Ψ-FeS subarray is identical to the FeS represented in (**a**). (**d**) The $\mathbf{4^4}$ planar nets formed by the Fe atoms in FeLiP. They coincide in topology and dimensions with those of (**b**). (**e**) The LiP subarray in FeLiP. It can be considered as a Ψ-LiCl structure (rocksalt) where alternate layers of cubes are occupied by the Fe atoms

In this section, we will focus on the structure of tetragonal FeS, represented in Fig. 11a. It can be considered as a (II)–(VI) compound, adopting consequently a four-connected such as PbO type in which both atomic species are four-connected, like in the Group 14 structures. Recall the $[AlSi]^{1-}$ subarray in the Zintl phase NaAlSi [28] (Fig. 8f).

If, in the FeS structure of Fig. 11a, the S atoms are omitted, one obtains the Fe subarray represented in Fig. 11b. It is formed by square $\mathbf{4^4}$ planar nets, coincident with (1 0 0) planes of *fcc*-Fe. At the bottom of Fig. 11b, one of S atoms has been maintained to show how they are capping the squares of the Fe subnet. As seen in Table 1, the dimensions of the $\mathbf{4^4}$ planar nets are almost equal in both *fcc*-Fe and FeS. Thus, the insertion of S atoms occurs without any alteration of the fragments of the *fcc*-Fe structure.

If we consider now the structure of the Zintl phase FeLiP [24], represented in Fig. 11c, we see that the Li atoms, acting as donors, convert the FeP subarray into Ψ-FeS, adopting so the structure of real FeS (Fig. 11a). Within this structure, there are two remarkable features.

The first one is the Fe subarray drawn in Fig. 11d. If both Li and P atoms are omitted in Fig. 11c, we obtain an array identical to the one existing in FeS (Fig. 11b). The most important outcome is that the $\mathbf{4^4}$ planar nets are identical in both compounds, as shown in Table 1. Thus, the Fe fragments are identical in *fcc*-Fe, FeS and FeLiP. Even the topology is maintained in triphylite FeLi[PO_4] (Fig. 8a).

The second aspect refers to the LiP subarray, which was considered above as a Ψ-LiCl arrangement. It was shown that the planar nets represented in Fig. 7d were in fact (1 0 0) faces of a LiCl structure. However, considering the whole unit cell of FeLiP, represented in Fig. 11e, it can be seen that the resemblance with the LiCl structure is even greater. Thus, both Li and P atoms are forming a slightly tetragonally distorted structure like that of LiCl. The dimensions of this unit cell, quoted in Table 1, clearly show their similarity with the real LiCl structure.

Within this NaCl-type structure, the Fe atoms are filling all the cubes of one layer, alternating with layers of empty cubes. This leads not only to the iron $\mathbf{4^4}$ planar nets, but also to the formation of the PbO-type blocks with the P atoms. If the same Fe atoms would occupy alternate cubes in all layers, then the FeP subarray would form a Li-stuffed Ψ-FeS array with the zinkblende type which was reported for FeS itself [37].

At this point, it seems convenient to discuss some differences existing between the NaAlSi type (Fig. 8f) and FeLiP (Fig. 11c) structures. In NaAlSi, the AlSi subarray is forming a Ψ-Si Zintl polyanion of the PbO type, whereas the Na atoms form bilayers located between the AlSi blocks. Said in other words, the Na atoms are not coplanar with the Al atoms as do the Li atoms in FeLiP. From a geometrical point of view, there would be no reason for the Na atoms centre the squares of Si atoms, as do the Li atoms in the LiP planes (Fig. 11c). Thus, by applying the EZKC, a hypothetical electron transfer from Al to Si would convert the Si atoms into Ψ-Cl. The distances between these Ψ-Cl are 5.84 Å, in such a way that if the Na atoms were coplanar with the Si atoms, both would produce pseudo-planar net of Ψ-NaCl, whose dimensions (5.84 Å) would be comparable to the unit cell of real NaCl (5.63 Å).

Because there is no steric hindrace for such an array, the explanation for the formation of the Na blocks, in NaAlSi, might well be electronic; that is, the Al atoms are not able to convert the NaAlSi Zintl phase into a pseudo Ψ-Ne[Ψ-NaCl] containing Ψ-NaCl planar nets. Thus, this pseudo-structure would not contribute to

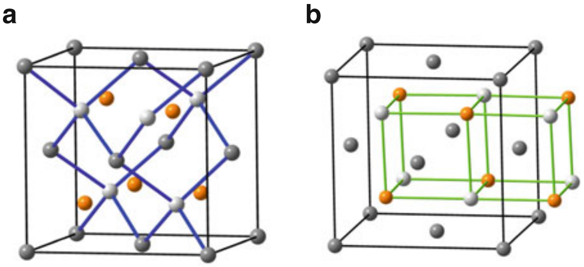

Fig. 12 The [NaAlSi] subarray of the high temperature phase of $NaAlSiO_4$ (carnegieite). (**a**) Drawing of the diamond-like skeleton formed by both Al (*light grey*) and Si (*dark grey*) atoms. *Brown spheres* represent Na atoms. (**b**) Drawing of the fluorite-like structure formed by the Na and Al atoms when filling the tetrahedral voids of the fcc-Si array. Both Na and Al atoms form the cubes which are filled alternately by the Si atoms

the formation of the NaAlSi structure. The result is that the Al atoms are forming, like Fe in FeLiP, $\mathbf{4^4}$ planar nets of dimensions 2.92 Å, similar to the (1 0 0) faces of *fcc*-Al, with Al-Al distances of 2.86 Å, whereas the Na blocks form fragments of *bcc*-Na, whose dimensions of $a = 4.13$, $d = 3.43$ Å, are in agreement with those of the elemental Na with $a = 4.21$, $d = 3.64$ Å [38].

The conclusion is that in the absence of any compatible NaSi phase, the Na atoms form blocks of their own structure. Thus, NaAlSi is thus the result of the simultaneous existence of Al metal, Na metal and the Ψ-Si structures. On the contrary, in FeLiP, Fe metal, LiCl and FeS co-exist in a "synergic" way.

The interpretation we have just made of the NaAlSi structure probably needs additional support, which can be provided by the related oxide $NaAlSiO_4$ and, specially, by its high temperature phase, the mineral carnegieite [39]. The structure is represented in Fig. 12a in which the O atoms have been omitted for clarity. The structure is cubic ($\boldsymbol{P}2_13$, $a = 7.30$ Å) and the AlSi subarray is forming an adamantane skeleton with the O atoms midway between the Al and Si atoms. Thus, the structure can be described as Na-stuffed cristobalite-like structure, with the [AlSi] subarray forming a Ψ-Si structure, as deduced from the ***ZKC***.

In Fig. 12b, we have represented the same structure but where its relationship with the fluorite structure has been emphasized. The Na and Al atoms are filling all the tetrahedral voids of the *fcc*-Si array, so that when the Na and Al atoms are connected, they form the cubes characteristic of the CaF_2 structures.

Two features are worthy of mention, i.e. the first one is that this array is that of the related Zintl phase LiAlSi. The second one is that high carnegieite is a metastable phase which can be maintained up to 963 K. The structure was determined at 1,023 K [39].

The conclusion we can extract is that, like in NaAlSi, also in $NaAl[SiO_4]$, the Al and Si atoms are forming the corresponding four-connected network. The alternative interpretation, consisting in that the Na-Si pair of atoms forms a NaCl-type structure, with Si at (0,0,0) and Na at (½, 0, 0) does not take place. Also in this case, the reason is that the Al atoms are not capable of transforming the Si atoms into Ψ-Cl. Instead, both

Na and Al atoms, behaving as an average Ψ-Mg, form the pseudo-structure Ψ-Mg_2Si with the antifluorite structure, just like Mg_2Si itself ($a = 6.35$ Å). The important consequence here is that such antifluorite-type structure has ever been obtained by heating the olivine-like $Mg_2[SiO_4]$ at elevated temperatures, although it has been obtained with $NaAl[SiO_4]$ which is its pseudo-compound Ψ-$Mg_2[SiO_4]$.

The case of the related compound $LiCs[SO_4]$ is also very illustrative, also supporting our interpretation. Thus, the [CsS] subarray forms a NaCl-type structure which can be interpreted as the result of the one-electron transfer from Li to S, converting it into Ψ-CsCl. On the other hand, if the transfer would occur from Cs to Li, then the subarray [LiS] would be converted into Ψ-BeS forming so a zinkblende structure in agreement with the structure of BeS itself. The structures of similar compounds such as LiMgP and LiAlP also agree with this approach.

5 Conclusions

Resulting from the detailed analysis given above, a profound analysis of the cation arrays of the inorganic structures provides many keys for the understanding of crystal structures. In many aspects, our results coincide with many of the topological similarities reported by Blatov and which are collected in this volume [9].

The main thesis, which has been published on several occasions [4, 14, 15], can be formulated in the following way: "The Extended Zintl–Klemm Concept, applied to any cation array, appears as the most useful tool for both, description and understanding of the structures". This statement leads to a second conclusion: "When a crystal structure is analysed in this way, one discovers that several structures co-exist simultaneously as if they would behave as resonance structures".

Focusing our discussion on $FeLi[PO_4]$, we see that in triphylite, the FeLiP subarray forms a distorted Ni_2In-like structure. The Ni_2In array has implicit a distorted graphite-like network formed by the FeP pair of atoms. The same FeP subarray converted into Ψ-FeS forms, at the same time, blocks of the PbO type (like in both, Cu_2Sb and NaAlSi), identical to one of the phases of FeS itself. Within this FeS substructure, infinite $\mathbf{4^4}$ planar nets of metallic Fe persist in the structure. Considering the [LiP] subarray, we discover a tetragonally distorted rocksalt structure, where fragments of real LiCl are formed. In this rocksalt structure, one half of the cubes are filled by Fe in alternate layers. If the Fe atoms were distributed in alternate cubes in the whole structure, they would form a zinkblende structure instead of the occurring PbO-type skeleton. In both cases, however, the rocksalt Ψ-LiCl exists!

In β-$FeLi[PO_4]$, the dissection leads to similar conclusions. The [FeLiP] subarray also forms a distorted Ni_2In-type structure. Within this subarray, if the Li atoms act as donors, the FeP pair of atoms, converted into Ψ-FeS, convert the compound into a Li-stuffed Ψ-$Fe[SO_4]$, forming an NiAs-type array, identical to that of real $Fe[SO_4]$ and also identical to another phase of FeS!

Another important conclusion is that this compound represents a new and significant example of what has previously been reported concerning the maintenance of the alloy structures in their respective oxides [11, 13, 14]. Thus, the structure of FeS (NiAs) remains when the O atoms are added to form Fe[SO_4] and persists, in FeLi[PO_4], when the Li atoms are present. Through this dissection, it is evident that the structures are not a mere set of spheres, mainly dominated by their size, but atoms arrange in a concerted manner so that each atom provokes (influences) the formation of the structures of the others, always leading to structures of recognizable simpler compounds.

The phase transition triphylite → β-FeLi[PO_4] can now be understood by the need of a PbO-type → NiAs transition in the [FeP] subarray. Once again, we can state that cations govern the structures and that they undergo their own phase transitions, even in the presence of "foreign atoms", as previously reported [4]. In view of this, we feel necessary to claim again for the statement of Wondratschek, Merker and Schubert [12] heading this article. The principle seems to be the EZKC.

Acknowledgements I am indebted to my colleagues David Santamaría-Pérez and Javier García for their patient reading of the manuscript and valuable suggestions.

References

1. Yakubovich OV, Simonov MA, Belov NV (1977) The crystal structure of a synthetic triphylite LiFe(PO_4). Dokl Akad Nauk SSSR 235:93–95
2. García-Moreno O, Álvarez-Vega M, García-Alvarado F, García-Jaca J, Gallardo-Amores JM, Sanjuán ML, Amador U (2001) Influence of the structure on the electrochemical performance of lithium transition metal phosphates as cathodic materials in rechargeable lithium batteries: a new high-pressure form of $LiMPO_4$ (M = Fe and Ni). J Mater Chem 13:1570–1576
3. Rasmussen SE, Jorgensen JE, Lundtoft B (1996) Structures and phase transitions of Na_2SO_4. J Appl Crystallogr 29:42–47
4. Vegas A, García-Baonza V (2007) Pseudoatoms and preferred skeletons in crystals. Acta Crystallogr B 63:339–345
5. O'Keeffe M, Hyde BG (1985) An alternative approach to non-olecular crystal structures.With emphasis on the arrangement of cations. Struct Bond 61:77–144
6. Ilyushin GD, Blatov VA, Zakutkin YuA (2004) Orthotetrahedral crystal structures $M_y(TO_4)_z$ (T = Si, Ge, P, As, S, Se, Cl, Br, I): geometrical-topological analysis, quasi-binary representation, and comparison with the A_yX_z compounds by the method of coordination sequences. Z Kristallogr 219:468–478
7. Blatov VA, Peskov MV (2006) A comparative crystallochemical analysis of binary compounds and simple anhydrous salts containing pyramidal anions LO3 (L = S, Se, Te, Cl, Br, I). Acta Crystallogr B 62:457–466
8. Blatov VA (2009) http://www.topos.ssu.samara.ru
9. Blatov VA (2011) Crystal structures of inorganic oxoacid salts perceived as cation arrays: a periodic-graph approach. Struct Bond. doi:10.1007/430_2010_34
10. Vegas A, Grzechnik A, Syassen K, Loa I, Hanfland M, Jansen M (2001) Reversible phase transitions in Na_2S under pressure: a comparison with the cation array in Na_2SO_4. Acta Crystallogr B 57:151–156
11. Vegas A, Jansen M (2002) Structural relationships between cation arrays and alloys; an equivalence between oxidation and pressure. Acta Crystallogr B 58:38–51

12. Wondratschek H, Merker L, Schubert K (1964) Beziehungen zwischen der Apatit- struktur und der Struktur der Verbindungen vom Mn_5Si_3-($D8_8$-)typ. Z Kristallogr 120:393–395, erratum correction: 478
13. Vegas A (2000) Cations in inorganic solids. Crystallogr Rev 7:189–283
14. Santamaría-Pérez D, Vegas A, Liebau F (2005) The Zintl-Klemm concept applied to cations in oxides. II. The structures of silicates. Struct Bond 118:121–177
15. Vegas A, Martin RL, Bevan DJM (2009) Compounds with a "stuffed" anti-bixbyite- type structure, analysed in terms of the Zintl-Klemm and coordination-defect concepts. Acta Crystallogr B 65:11–21
16. Zheng C, Hoffmann R (1989) Conjugation in the 3-connected net. The AlB_2 and $ThSi_2$ structures and their transition metals derivatives. Inorg Chem 28:1074–1080
17. Miller GJ (1996) Structure and bonding at the Zintl border. In: Kauzlarich SM (ed) Chemistry, structure and bonding of Zintl phases and ions. VCH, NewYork
18. Zintl E (1939) Intermetallische Verbindungen. Angew Chem 52:1–100
19. Klemm W (1958) Centenary lecture. Metalloids and their compounds with alkali metals. Proc Chem Soc London, Issue 12:329–341
20. Coing-Boyat J (1962) Structure de la forme haute temperature du sulfate anhydre de magnesium, β-$MgSO_4$. C R Acad Sci Paris 255:1962–1964
21. Wickleder MS (2003) Crystal structure of $LiClO_4$. Z Anorg Allg Chem 629:1466–1468
22. Henderson WA, Brooks NR (2003) Crystals from concentrated glyme mixtures. The single-crystal structure of $LiClO_4$. Inorg Chem 42:4522–4524
23. Makarov ES (1948) Crystal structure of InBi. Dokl Akad Nauk SSSR 59:899–899
24. Juza R, Langer K (1968) Ternäre Phosphide und Arsenide des Lithiums mit Eisen, Cobalt oder Chrom im Cu_2Sb-Typ. Z Anorg Allg Chem 361:58–73
25. King HE Jr, Prewitt CT (1982) High-pressure and high-temperature polymorphism of iron sulfide. Acta Crystallogr B 38:1877–1887
26. Andersson AS, Kalska B, Haggstrom L, Thomas JO (2000) Lithium extraction/insertion in $LiFePO_4$: an X-ray diffraction and Mossbauer spectroscopy study. Solid State Ionics 130:41–52
27. Rousse G, Rodríguez-Carvajal J, Patoux S, Masquelier C (2003) Magnetic structures of the triphylite LiFePO4 and of its delithiated form FePO4. Chem Mater 15:4082
28. Westerhaus W, Schuster HU (1979) Darstellung und Struktur von NaAlSi und NaAlGe. Z Naturforsch B 34:352–353
29. Coing-Boyat J (1959) Mailles cristallines et groupes d'espace des sulfates anhydres de Co(II) et de Mn(II). C R Acad Sci 248:2109–2111
30. Mehmed F, Haraldsen H (1938) Das magnetische Verhalten der allotropen Modifikationen des Mangan(II)-Sulfides. Z Anorg Allg Chem 235:193–200
31. Kennedy SW, Harris K, Summerville E (1980) Mechanism of thermal transformation of zinc blende to NaCl in MnS crystals. J Solid State Chem 31:355–359
32. Catti M (2002) First-principles study of the orthorhombic mechanism for the B3/B1 phase transition of ZnS. Phys Rev B 65:224115
33. Samaras D, Coing-Boyat J (1970) Refinement of the structure of α-$FeSO_4$. Bull Soc Fr Miner Cristallogr 93:190–190
34. Yamamoto A, Nakazawa H (1982) Modulated structure of the NC-type ($N = 5.5$) pyrrothite, $Fe_{1-x}S$. Acta Crystallogr A 38:79–86
35. Mittendorf H (1965) Röntgenographische und optische untersuchungen aufgedampfter Schichten aus Erdalkalichalkogenide. Z Phys 183:129
36. Savelsberg G, Schaefer H (1978) Ternary pnictides and chalkogenides of alkali-metals and Ib-IIb elements. Z Naturforsch B 33:370–373
37. Wintenberger M, Buevoz JL (1978) Magnetic structure of zinc blend type iron sulphide FeS. Solid State Commun 27:511–513
38. Smith HG, Berliner R, Jorgensen JD, Trivisonno J (1991) Pressure effects on the martensitic transformations in metallic sodium. Phys Rev B 43:4524–4526
39. Barth FW, Posnjak E (1932) Silicate structures of the cristobalite type. I. The structure of α-carnegieite, $NaAlSiO_4$. Z Kristallogr 81:135–141

Struct Bond (2011) 138: 93–132
DOI: 10.1007/430_2011_39

Rationalization of the Substructures Derived from the Three Fluorite-Related $[Li_6(M^VLi)N_4]$ Polymorphs: An Analysis in Terms of the "Bärnighausen Trees" and of the "Extended Zintl–Klemm Concept"

D.J.M. Bevan, R.L. Martin, and Ángel Vegas

Abstract The crystallographic, group and subgroup relationships are explored for mixed transition metal nitrides of the type: $Li_7M^VN_4$. The hypothetical parent M_8N_4 should have the anti-fluorite structure with the space group $Fm\bar{3}m$. However, the corresponding mixed-cation nitride $[Li_7V]N_4$ is actually tri-morphic comprising one tetragonal phase SG: $P4_2/nmc$ (α) and two cubic phases with space groups: $Pa\bar{3}$ (β) and $P\bar{4}3n$ (γ), respectively. These three polymorphs are clearly subgroups arising from lowering of symmetry of the parent space group, $Fm\bar{3}m$. Further decomposition of the pathways (or Bärnighausen Trees) reveals a rich variety of compounds derived from the subgroups and supergroups of the anti-fluorite parent structure. The most important outcome is that all the structures analysed in this work, which derive from the parent $Fm\bar{3}m$ space group of fluorite, can be identified as partial substructures in the three phases of Li_7VN_4. All these substructures can be rationalized as pseudo-compounds by assuming the appropriate electron transfer between the atoms forming the nitride, following the extended Zintl–Klemm concept (*EZKC*) that implies charge transfer between atoms, even if they are of the same kind.

D.J.M. Bevan (✉)
The Flinders University of South Australia, School of Chemical and Physical Sciences, Bedford Park, South Australia, Australia
e-mail: judge.bevan.@flinders.edu.au

R.L. Martin
Monash University, School of Chemistry, Clayton, Victoria, Australia
e-mail: Ray.Martin@sci.monash.edu.au

Á. Vegas
Instituto de Química-Física "Rocasolano", CSIC, C/ Serrano 119, 28006 Madrid, Spain

Keywords Bärnighausen trees · Bixbyite · Crystal chemistry · Fluorite · Group/subgroup relationships · High pressure · Inorganic structures · Lithium nitrides · Molecular nitrogen · Sodalite · Zintl–Klemm concept

Contents

1 Introduction 94
2 Group/Subgroup Relationships: The Bärnighausen Tree 95
3 The Gamma Phase of $Li_7V^VN_4$ 98
  3.1 Substructures in the Space Group $Pm\overline{3}n$ 98
  3.2 Substructures in the Space Group $P\overline{4}3n$ 105
  3.3 Substructures in the Space Group $I\overline{4}3m$ 112
  3.4 Substructures in the Space Group $Pn\overline{3}n$ (222) 114
  3.5 Substructures in Space Group $F\overline{4}3c$ 116
4 The β-Phase of $Li_7V^VN_4$ 118
  4.1 Substructures in the Space Group $Pa\overline{3}$ 120
  4.2 Substructures in the Space Group $Ia\overline{3}$ 123
  4.3 Substructures in Space Group $Fm\overline{3}$ 125
5 The Alpha Phase of $Li_7V^VN_4$ 125
  5.1 Li_6MoN_4, Li_6WN_4, Li_6ZnO_4 and Li_6CoO_4 125
  5.2 Tetragonal Zirconia 128
6 Conclusions 129
References 129

Abbreviations

CD	Coordination defect
EZKC	Extended Zintl–Klemm concept
fcc	Face-centred cubic
SG	Space group

1 Introduction

In a recent paper [1], the structures of Li_3AlN_2 and Li_3ScN_2 were explored in terms of the extended Zintl–Klemm concept (*EZKC*) [2, 3] and the coordination defect (*CD*) theories [4]. These compounds were described as Al(Sc)-stuffed anti-bixbyites, the "stuffing" atoms, Al(Sc), filling the cation vacancies, □, of the hypothetical, anti-fluorite structure, $Li_3\square N_2$, which are the 16*c* sites of the space group $\boldsymbol{Ia}\overline{3}$. These are also the Si sites of the high-pressure γ-Si phase. Clearly, the essentially anti-fluorite lattice of M_4N_2 has been decomposed by the reduction in symmetry from $\boldsymbol{Fm}\overline{3}\boldsymbol{m}$ to $\boldsymbol{Ia}\overline{3}$ into two sub-lattices or frameworks, namely those of anti-bixbyite, Li_3N_2, and of γ-Si, which can then be described as substructures of the parent. This outcome was first reported by Niewa et al. [5].

In that same paper [1], we extended this approach to the related but more complex compounds with the composition, $Li_7M^VN_4$, where M^V = P, Mn,V, Nb and Ta. Compounds of this composition are not altogether unexpected since a dimer of Li_3AlN_2 would have the composition $Li_6[Al^{III}]_2N_4$, which is isoelectronic with $Li_6[Li^{I}P^{V}]N_4$. Moreover, it is worth noting that if a tetramer of the anti-fluorite structure, Li_2O, were written as $Li_7[Li]O_4$, we could apply the *EZKC* to have each O atom donating one electron to the single Li atom, yielding $Li_7[Li^{-4}][O^{+1}]_4$; i.e. $Li_7[(\Psi\text{-N})^{V}](\Psi\text{-N})_4$, which is the N analogue of the known phosphorus, vanadium, manganese, niobium and tantalum compounds, $Li_6[Li^{I}M^{V}]N_4$. Our conclusion to that paper stated that "…a given compound might result from multiple resonance structures, which implies a partial delocalization of electrons. When these are distributed over all the atoms, the electron-count requirements for each structure are fulfilled." What we did not recognize at that time was that, in fact, the space group of each of the resonance structures discussed was a subgroup of the parent anti-fluorite-type space group, $\boldsymbol{F}m\bar{3}m$. In this chapter, we now extend this concept of substructures by exploring crystallographic group/subgroup relationships.

2 Group/Subgroup Relationships: The Bärnighausen Tree

The compound Li_7VN_4 is tri-morphic, and Niewa et al. [6] have described in some detail the high-temperature preparation of the *alpha* (tetragonal), *beta* (cubic) and *gamma* (cubic) polymorphs from the starting materials Li_3N and VN. Juza and co-workers [7, 8] had reported both the cubic β- and γ-phases as early as 1959; these were subsequently explored in more detail by a number of crystallographers (see below). The β-phase crystallizes in the space group $\boldsymbol{P}a\bar{3}$, with $Z = 8$, and its crystal structure has been explored recently in terms of the *EZKC* [1]. The compounds $Li_6[LiNb]N_4$ [9] and $Li_6[LiTa]N_4$ [10] are both isostructural with β-$Li_6[LiV]N_4$. The γ-$Li_7V^{V}N_4$ phase is also cubic ($\boldsymbol{P}\bar{4}3n$) with $Z = 8$, and the isostructural compounds $Li_7Mn^{V}N_4$ [7] and $Li_7P^{V}N_4$ [11] have been reported. The tetragonal α-phase ($\boldsymbol{P}4_2/nmc$, $Z = 2$) was first identified by Niewa et al. [6].

These same workers have studied the thermal behaviour and phase transitions between the three phases of Li_7VN_4, which seem to be related by reconstructive phase transitions because the observed transitions occurred only very slowly, although the differences in lattice energy must be quite small. They also point out that the three space groups involved are not related directly through a "Bärnighausen Tree" [6, 12] – a defining property for reconstructive phase transitions. However, all three compounds have space groups which are subgroups of the parent anti-fluorite-type space group $\boldsymbol{F}m\bar{3}m$.

Perhaps, the most fascinating aspect of these and many other observations is that so many structures derive from the parent fluorite-type or anti-fluorite-type structures. Niewa et al. [6] have already published three pathways ("Bärnighausen Trees") by which the three polymorphs of $Li_7V^{V}N_4$ are derived from the parent anti-fluorite-type structure of Li_2O. Now, thanks to the recent publication of International Tables for Crystallography, Vol. A1 [13], it has become relatively simple to explore in detail such pathways, and this we have done with a view to facilitating a search for substructures contained within each of these three polymorphs. This major publication lists all the relationships between the Wyckoff positions of a group and its immediate subgroups.

We focus attention initially on the γ-phase of Li_7VN_4. It is cubic, S.G. $\boldsymbol{P}\bar{4}3n$, with $a = 9.606$ Å and $Z = 8$ [6] and consider first the parent anti-fluorite structure of $Li_{64}O_{32}$. We then explore what happens to the various Li and O atoms if the symmetry were reduced from $\boldsymbol{Fm\bar{3}m}$ to $\boldsymbol{P}\bar{4}3n$ when we convert all 32 O atoms to N atoms and 8 of the 64 Li atoms to V atoms. We believe that, whatever subgroup of $\boldsymbol{Fm\bar{3}m}$ we might consider, the possible atom sites must have their counterparts in the parent $\boldsymbol{Fm\bar{3}m}$ space group itself. Expressed in another way, any particular framework of atoms in the subgroup is inherently present in the supergroup. We can then attempt to explain ***why*** it is that particular atoms of γ-$Li_7V^VN_4$ lodge in particular sites of the observed space group $\boldsymbol{P}\bar{4}3n$ to yield various substructures.

Table 1 is a summary of several possible pathways from the anti-fluorite-type unit cell of Li_2O in space group $\boldsymbol{Fm\bar{3}m}$ to γ-$Li_7V^VN_4$ with a doubled unit cell in space group $\boldsymbol{P}\bar{4}3n$. Table 2 provides just one example of a single Bärnighausen Tree (not the same as that of Niewa et al. [6]) which links the atom sites of γ-$Li_7V^VN_4$ to those of the parent anti-fluorite compound Li_2O. However, not all the pathways shown in Table 1 lead to the actual atom sites occupied by the atoms in γ-$Li_7V^VN_4$.

Table 1 Space group pathways from $Fm\bar{3}m$ to $P\bar{4}3n$. Transition from *red* to *black* indicates doubling of unit cell edge

Case 1	Case 2	Case 3	Case 4	Case 5	Case 6	Case 7
$\boldsymbol{Fm\bar{3}m}$	$\boldsymbol{Fm\bar{3}m}$	$\boldsymbol{Fm\bar{3}m}$	$\boldsymbol{Fm\bar{3}m}$	$\boldsymbol{Fm\bar{3}m}$	$\boldsymbol{Fm\bar{3}m}$	$\boldsymbol{Fm\bar{3}m}$
225	225	225	225	225	225	225
$\boldsymbol{Pn\bar{3}m}$	$\boldsymbol{Pn\bar{3}m}$	$\boldsymbol{Pn\bar{3}m}$	$\boldsymbol{F\bar{4}3m}$	$\boldsymbol{F\bar{4}3m}$	$\boldsymbol{Pm\bar{3}m}$	$\boldsymbol{Pm\bar{3}m}$
224	224	224	216	216	221	221
$\boldsymbol{Fd\bar{3}c}$	$\boldsymbol{P\bar{4}3m}$	$\boldsymbol{P\bar{4}3m}$	$\boldsymbol{P\bar{4}3m}$	$\boldsymbol{P\bar{4}3m}$	$\boldsymbol{P\bar{4}3m}$	$\boldsymbol{P\bar{4}3m}$
228	215	215	215	215	215	215
$\boldsymbol{F\bar{4}3c}$	$\boldsymbol{F\bar{4}3c}$	$\boldsymbol{I\bar{4}3m}$	$\boldsymbol{F\bar{4}3c}$	$\boldsymbol{I\bar{4}3m}$	$\boldsymbol{F\bar{4}3c}$	$\boldsymbol{I\bar{4}3m}$
219	219	217	219	217	219	217
$\boldsymbol{P\bar{4}3n}$	$\boldsymbol{P\bar{4}3n}$	$\boldsymbol{P\bar{4}3n}$	$\boldsymbol{P\bar{4}3n}$	$\boldsymbol{P\bar{4}3n}$	$\boldsymbol{P\bar{4}3n}$	$\boldsymbol{P\bar{4}3n}$
218	218	218	218	218	218	218

Case 8	Case 9	Case 10	Case 11	Case 12	Case 13
$\boldsymbol{Fm\bar{3}m}$	$\boldsymbol{Fm\bar{3}m}$	$\boldsymbol{Fm\bar{3}m}$	$\boldsymbol{Fm\bar{3}m}$	$\boldsymbol{Fm\bar{3}m}$	$\boldsymbol{Fm\bar{3}m}$
225	225	225	225	225	225
$\boldsymbol{Pm\bar{3}m}$	$\boldsymbol{Pm\bar{3}m}$	$\boldsymbol{Pm\bar{3}m}$	$\boldsymbol{Pm\bar{3}m}$	$\boldsymbol{Pm\bar{3}m}$	$\boldsymbol{Pm\bar{3}m}$
221	221	221	221	221	221
$\boldsymbol{Im\bar{3}m}$	$\boldsymbol{Im\bar{3}m}$	$\boldsymbol{Im\bar{3}m}$	$\boldsymbol{Fm\bar{3}c}$	$\boldsymbol{Fm\bar{3}c}$	$\boldsymbol{Fm\bar{3}c}$
229	229	229	226	226	226
$\boldsymbol{I\bar{4}3m}$	$\boldsymbol{Pn\bar{3}n}$	$\boldsymbol{Pm\bar{3}n}$	$\boldsymbol{Pn\bar{3}n}$	$\boldsymbol{Pm\bar{3}n}$	$\boldsymbol{F\bar{4}3c}$
217	222	223	222	223	219
$\boldsymbol{P\bar{4}3n}$	$\boldsymbol{P\bar{4}3n}$	$\boldsymbol{P\bar{4}3n}$	$\boldsymbol{P\bar{4}3n}$	$\boldsymbol{P\bar{4}3n}$	$\boldsymbol{P\bar{4}3n}$
218	218	218	218	218	218

Table 2 The full Bärnighausen Tree for Case 3

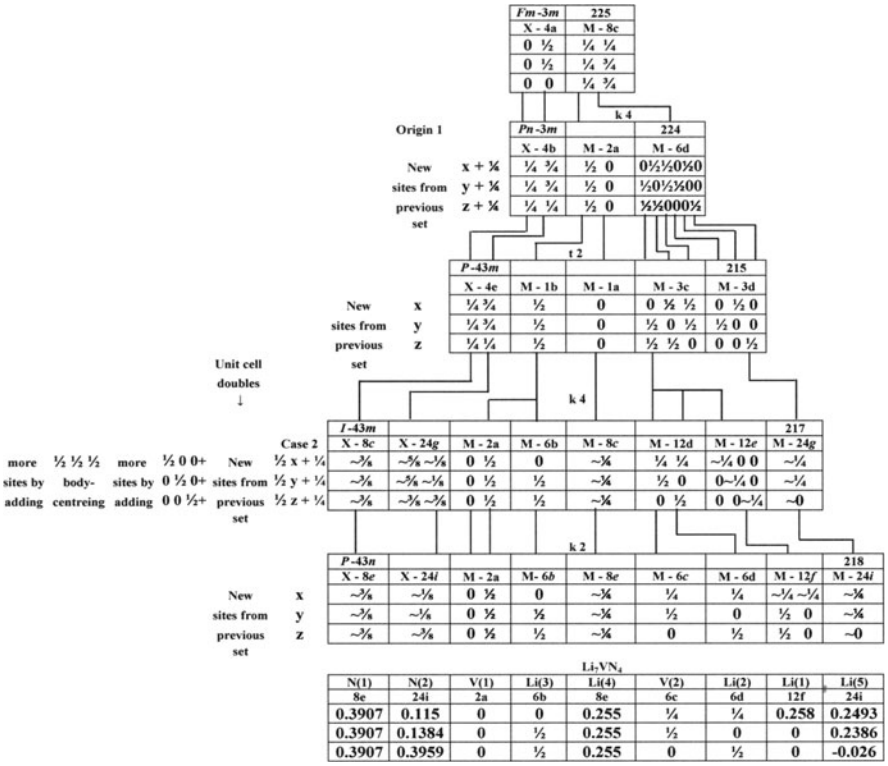

Fm-3*m*	225
X - 4a	M - 8c
0 ½	¼ ¼
0 ½	¼ ¾
0 0	¼ ¾

k 4

Origin 1

New sites from previous set

	Pn-3*m*		224
	X - 4b	M - 2a	M - 6d
x + ¼	¼ ¾	½ 0	0½½0½0
y + ¼	¼ ¾	½ 0	½0½½00
z + ¼	¼ ¼	½ 0	½½000½

t 2

New sites from previous set

	P-43*m*				215
	X - 4e	M - 1b	M - 1a	M - 3c	M - 3d
x	¼ ¾	½	0	0 ½ ½	0 ½ 0
y	¼ ¾	½	0	½ 0 ½	½ 0 0
z	¼ ¼	½	0	½ ½ 0	0 0 ½

Unit cell doubles ↓

k 4

more sites by adding ½ ½ ½ body-centreing

more sites by adding ½ 0 0+ 0 ½ 0+ 0 0 ½+

New sites from previous set

Case 2	*I*-43*m*							217
	X - 8*c*	X - 24*g*	M - 2a	M - 6b	M - 8*c*	M - 12d	M - 12*e*	M - 24*g*
½ x + ¼	~⅜	~⅝ ~⅛	0 ½	0	~¼	¼ ¼	~¼ 0 0	~¼
½ y + ¼	~⅜	~⅝ ~⅛	0 ½	½	~¼	½ 0	0~¼ 0	~¼
½ z + ¼	~⅜	~⅜ ~⅜	0 ½	½	~¼	0 ½	0 0~¼	~0

k 2

New sites from previous set

	P-43*n*								218
	X - 8*e*	X - 24*i*	M - 2a	M- 6*b*	M - 8*e*	M - 6*c*	M - 6d	M - 12*f*	M - 24*i*
x	~⅜	~⅛	0 ½	0	~¼	¼	¼	~¼ ~¼	~¼
y	~⅜	~⅛	0 ½	½	~¼	½	0	½ 0	~¼
z	~⅜	~⅜	0 ½	½	~¼	0	½	½ 0	~0

Li_7VN_4

N(1)	N(2)	V(1)	Li(3)	Li(4)	V(2)	Li(2)	Li(1)	Li(5)
8e	24i	2a	6b	8e	6c	6d	12f	24i
0.3907	0.115	0	0	0.255	¼	¼	0.258	0.2493
0.3907	0.1384	0	½	0.255	½	0	0	0.2386
0.3907	0.3959	0	½	0.255	0	½	0	-0.026

Notwithstanding, it is clear that each pathway has one of the four immediate supergroups of the space group ***P***$\bar{4}$3*n* (218), two *klassengleiche* and two *translationengleiche*, as its immediate precursor: these are ***I***$\bar{4}$3*m* (217), ***Pn***$\bar{3}$*n* (222), ***Pm***$\bar{3}$*n* (223), and ***F***$\bar{4}$3*c* (219), and each is a likely source for substructures within the γ-$Li_7V^VN_4$ structure.

In Table 2, the captions between the linked formatted tables define the nature of the transition – **k** for *klassengleiche* and **t** for *translationengleiche*, with the following number indicating the order, while those captions to the left of the tables indicate both changes in unit cell size and how the Wyckoff sites of each subgroup are derived from the immediate supergroup.

Table 2 illustrates just how we can use the group/subgroup relationships to explore the existence of substructures in Li_7VN_4, and this inevitably brings to the fore the question "what is a crystal structure?" Chemists have usually thought of structure in terms of the chemical compound involved, and so we talk of "the rock-salt structure", "the fluorite structure", etc. From the purely crystallographic point of view, however, a structure is simply a set of occupied sites pertaining to the underlying symmetry of a particular space group, *regardless of the chemical nature of the occupancy*. At issue in this context is the question whether or not any particular, derived substructure makes chemical sense. The pure crystallographer might take the view that this question is irrelevant.

3 The Gamma Phase of $Li_7V^VN_4$

The lattice sites occupied in the cubic compound γ-$Li_7V^VN_4$, space group $\boldsymbol{P}\bar{4}3n$, are listed below (see also Table 2):

Li(1) in 12*f* at (*x*, ½, ½): Li(2) in 6*d* at (¼, 0, ½): Li(3) in 6*b* at (0, 0, ½).
Li(4) in 8*e* at (*x, x, x*): Li(5) in24*i* at (*x, y, z*): V(2) in 6*c* at (¼, ½, 0).
V(1) in 2*a* at (0,0,0): N(1) in 8*e* at (*x, x, x*) and N(2) in 24*i* at (*x, y, z*).

The actual arithmetic data are given in Table 2.

Hence, the question then arises as to whether there are some compounds in $\boldsymbol{P}\bar{4}3n$ or in its immediate supergroups whose atoms occupy *some* of the above sites, and if so, whether there is a rational chemical argument as to why there should be this correspondence.

3.1 Substructures in the Space Group $Pm\bar{3}n$

3.1.1 The *A*15-Type Structure

We begin this discussion by recalling the comment by Schnick and Luecke [11] on the structure of the isomorphic compound, Li_7PN_4, as determined by them: "… distribution of P atoms in the cubic unit cell of Li_7PN_4 ($a = 936.48(3)$ pm) resembles a β-tungsten analogous arrangement (A15-type) as illustrated …" The archetypal *A*15 structure is that of the alloy Cr_3Si, and indeed the arrangements of P atoms in Li_7PN_4 and of V atoms in γ-$Li_7V^VN_4$ conform to the A15 type. This compound, Cr_3Si (and many like it), crystallizes in the S.G. $\boldsymbol{Pm}\bar{3}n$, which immediately precedes $\boldsymbol{P}\bar{4}3n$ in Cases 10 and 12 of Table 1. The Cr atoms are in site 6*c* at (¼, 0, ½) and the Si atoms are in site 2*a* at (0, 0, 0). However, these sites correspond to the sites 2*a* and 6*d* of $\boldsymbol{P}\bar{4}3n$, occupied by V(1) and Li(2), respectively, *not V(1) and V(2)* as implied by Schnick and Luecke [11]. Nevertheless, as we shall see, the V(1) and Li(2) arrangement is complementary to that of V(1) and V(2). The complete table of site equivalences, as given in [13], is shown in Table 3.

Thus, the pattern of the Cr_3Si structure is present in the structures of both γ-Li_7VN_4 and Li_7PN_4, although these latter patterns are considerably expanded with respect to the actual Cr_3Si structure: this derives from the fact that the cell edge of Cr_3Si is approximately half that of γ-Li_7VN4. Nevertheless, the patterns are the same, despite the bond lengths being very different, as is seen in identical views (near the [100] projection) in Fig. 1a, b, where the respective linkages define icosahedra in the same orientation. If we now depict the V(2) linkages in γ-Li_7VN_4

Table 3 Site equivalences between space groups $\boldsymbol{Pm\bar{3}n}$ and $\boldsymbol{P\bar{4}3n}$

$\boldsymbol{Pm\bar{3}n}$	$\boldsymbol{P\bar{4}3n}$
2*a*	2*a*
6*b*	6*b*
6*c*	6*d*
6*d*	6*c*
8*e*	8*e*
12*f*	12*f*
24*j*	24*j*

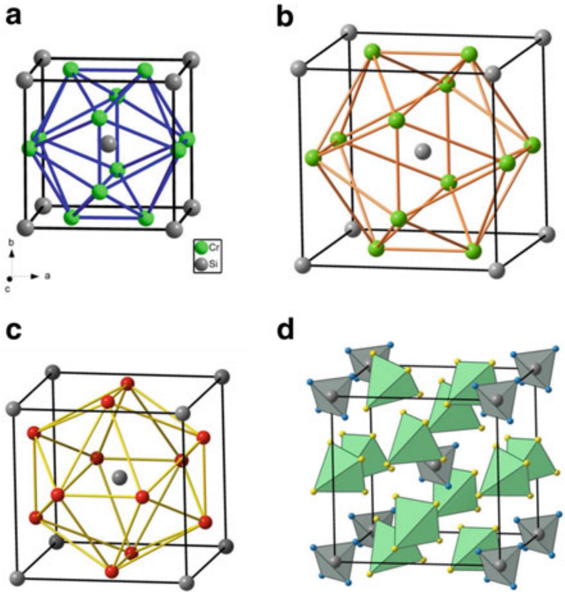

Fig. 1 (**a**) The *A*15 structure of the Frank–Kasper phase Cr_3Si ($a = 4.666$ Å). Cr atoms – *green*, Si atoms – *grey*, Cr–Cr bonds – *blue*, d(Cr–Cr) centring the faces are 2.28 Å, d(Cr–Cr) interfacial bonds are 2.79 Å. (**b**) Partial structure of Li_7VN_4 ($a = 9.6064$ Å) showing the pattern formed by Li(2) atoms – *green*, and V(1) atoms – *grey*. Li(2)–Li(2) bonds – *orange*. d(Li–Li) interfacial bonds are 5.88 Å. d(Li–Li) centring the faces are 4.80 Å. (**c**) The pattern formed by the V(1) and V(2) atoms in Li_7VN_4. V(1) atoms – *grey*, V(2) atoms – *red*. V(2)–V(2) bonds – *yellow*. d(V–V) interfacial bonds are 5.88 Å: d(V–V) centring the faces are 4.80 Å. (**d**) the Cr_3Si-type structure formed by the sub-array of the $Li(2)N(1)_4$ tetrahedra – *green* and the $V(1)N_4$ tetrahedra – *grey* in Li_7VN_4 ($a = 9.606$ Å). N(1) atoms – *blue*, N(2) atoms – *yellow*

in a precisely identical view, it is apparent that these also form an icosahedron, but one rotated by 90° with respect to the others. This is shown in Fig. 1c. Both icosahedra are centred by the V(1) atom, and we conclude that, in either orientation, both structures involving the pairs V(1)/Li(2) and V(1)/V(2) constitute substructures of the Cr_3Si (A15) type (as listed in Section 3).

It emerges from an inspection of Fig. 1a that the unit cell of Cr_3Si comprises a body-centred cube of composition Si_2 in which is inscribed an icosahedron of composition Cr_6. Likewise, Fig. 1b reveals that the structure of γ-Li_7VN_4 contains an identical substructure comprising a body-centred cube of composition $[V(1)]_2$ with an inscribed icosahedron of composition $Li(2)_6$. However, in this case there is also an alternative inscribed icosahedron of composition $V(2)_6$ which is arranged at 90° to the first. Taken together, these two icosahedra combine with the body-centred cube to form a body-centred cuboctahedron of composition $V(1)_2[V(2)_6]$ $[Li(2)_6]$. Not surprisingly, these structural patterns can be identified in all the substructures to be discussed below.

These discrepancies can be resolved very satisfactorily. In the case of γ-Li_7VN_4, the moieties comparable with the Si and Cr atom sites in Cr_3Si are the $V(1)N_4$ and the $Li(2)N_4$ tetrahedra, respectively, as shown in Fig. 1d: the discrete $V(1)N_4$ and $Li(2)N_4$ tetrahedra act in place of the single Si and Cr atoms, respectively, but have a much larger volume, which accounts for the difference in the cell sizes. We are equating Si atoms with $V(1)N(1)_4$ tetrahedra and Cr atoms with $Li(2)N(2)_4$ tetrahedra, these tetrahedra acting as pseudo-atoms. The composition of the substructure in the γ-Li_7VN_4 cell $[Li_{56}V_8N_{32}]$ is then simply $[Li(2)N_4]_6$ $[V(1)N_4]_2$, leaving the remaining 50 Li atoms and 6 V atoms as the "stuffing".

We are reminded of the well-known situation with the compound K_2PtCl_6 – there is a similar discrepancy between the cubic cell parameters for this compound and K_2O. If the $PtCl_6$ octahedron is considered as a single entity, we have the anti-fluorite-type structure with the larger $PtCl_6$ octahedron centred on the 4*a* site of space group $Fm\overline{3}m$ (225) and the K atoms in the 8*c* site.

As an aside, we know that the Cr_3Si alloy structure has been described previously as rod packing, i.e. rods of interweaving, strongly bonded Cr atoms in all three cubic directions, with Si atoms in the interstices between these rods [14, 15]. This is shown in Fig. 2a, drawn in the [111] projection, with different colours used to differentiate the three ⟨100⟩ cubic directions. Figure 2b shows the comparable drawing of rods of $Li(2)N_4$ tetrahedra in γ-Li_7VN_4.

We have explored further this rod relationship between the structures of Li_7VN_4 and Cr_3Si by considering only the cations of the former, bearing in mind that every

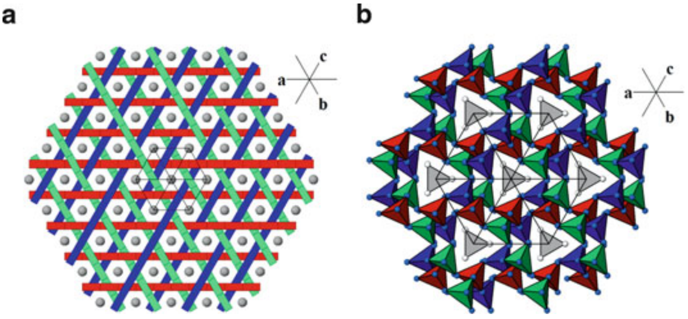

Fig. 2 (**a**) Rod packing in Cr_3Si. Cr–Cr rods interweave in all three cubic directions. Si atoms (*grey*) occupy the interstices. (**b**) Rod packing of $Li(2)N_4$ tetrahedra. Isolated $V(1)N_4$ tetrahedra – *grey*

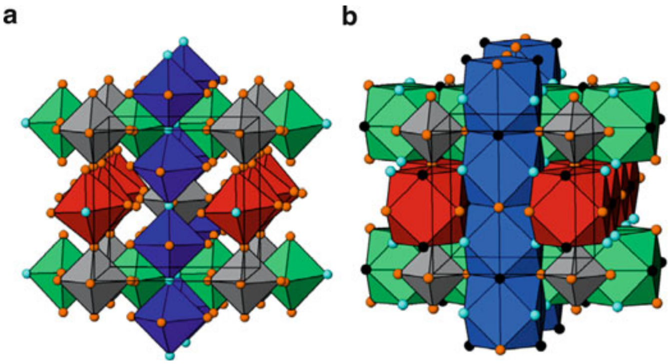

Fig. 3 (**a**) Corner-sharing rods of Li(2)N_4-centred octahedra: vertices are Li(4) atoms – *light blue*, Li(1) atoms – *brown*, isolated V(1)Li$(1)_6$ octahedra – *grey*. (**b**) Corner-sharing rods of Li(2)-centred cuboctahedra: vertices are V(2) atoms – *black*, Li(4)atoms – *light blue*, Li(1) atoms – *brown*. Corner-shared V(1)Li$(1)_6$ octahedra – *grey*

such cation lies at the centre of a Li(V)N_4 tetrahedron whose vertices are common always to eight such tetrahedra as a consequence of the anti-fluorite-type structure of Li_7VN_4. The Li(2)N_4 tetrahedra, shown in Fig. 2b, are themselves each at the centre of an octahedron of other LiN_4 tetrahedra: Fig. 3a shows only the central Li(4), Li(3) and Li(1) atoms of these peripheral tetrahedra, which are the vertices of the octahedra. Again, the rod structure is clearly shown, but now these octahedral rods share corners along the three cubic axes (delineated by red, blue and green), leaving the isolated V(1)Li$(1)_6$ octahedra, shown in grey, occupying the interstices between the rods. And we can take this approach still further to consider the polyhedron (Fig. 3b) centred by each of the rod octahedra: it is a cuboctahedron whose vertices are also LiN_4 tetrahedra (but not shown as such, only as the centreing Li atoms). These cuboctahedra now share corners, completely filling the unit cell, but leaving the V(1)Li$(1)_6$ octahedra in the interstices. The V(1)Li$(1)_6$ octahedra (grey) are no longer isolated but share corners with the cuboctahedra. Thus, the complete structure of Li_7VN_4 is now represented as cuboctahedral rods with isolated octahedra in the interstices, just as in the structure of Cr_3Si.

Although the chemical meaning of this structure will be described in Sect. 2.3.3, we can put forward a possible explanation as to why this structure type is chosen by the Li(2) and V(1) atoms of γ-Li_7VN_4 (and also by the V(2) and V(1) atoms). We treat here the respective Li(2)N_4 and V(2)N_4 tetrahedra as pseudo-atoms. If we take the parent structure as $Li_{56}[V_2Nb_6]N_{32}$ rather than $Li_{56}[V_2V_6]N_{32}$, then in Fig. 4d, the grey tetrahedra are still VN_4 but the red tetrahedra are now NbN_4. We rewrite the parent formula as $Li_{56}[(V_2N_8)(Nb_6N_{24})]$.

By applying the Zintl–Klemm concept, we first convert the N atoms to [Ψ-O], each N atom accepting one electron from a Li atom which then becomes [Ψ-He]: now we have the compound $Li_{24}(V_2[\Psi\text{-O}]_8)(Nb_6[\Psi\text{-O}]_{24}) + 32\ [\Psi\text{-He}]$. It should be added that the 6 of the 24 Li atoms are occupying a similar position as the 6 Nb atoms. Now we have the formula $Li_{18}[(V_2[\Psi\text{-O}]_8)(Nb_6[\Psi\text{-O}]_{24}[Li_6]) + 32\ [\Psi\text{-He}]$.

The 18 Li, which are now filling the $[(V_2[\Psi\text{-}O]_8)(Nb_6[\Psi\text{-}O]_{24}(Li_6)]$ skeleton, can donate 18 electrons which can be transferred to any of the other cations, i.e. 6 Li(2), 6 Nb or 2 V(2) atoms, allowing a redistribution of the electrons which can give rise to Ψ-Be, -B, -C, -Cr, -Mo, -Nb, -Ti, etc. All these pseudo-atoms are consistent with the fact that the compounds Ta_3Sn, Ta_3Pb, Ta_3Si, Cr_3Pt, Nb_3Pt, Mo_3Pt, Mo_3Ge, Mo_3Al, Nb_3Al and Ti_3Sb all have the *A*15 structure type (Cr_3Si) which is the structure built by the moieties $Nb_6V(2)_2$ and $Li(2)_6V(2)_2$. Note that the Li(2) atoms are the atoms capable of being converted into Ψ-B etc. In a wider sense, these pseudo-atoms are the lighter analogues of Al, Si, Ge, etc., with the same number of valence electrons.

Alternatively, we can take Na_7VN_4 as our parent structure and proceed in several different ways as follows: $Na_7VN_4 \rightarrow Na_{28}V_4N_{16} \rightarrow Na_{28}V_3N_{16}P$. The single P atom donates 1e to 1 V atom to give [Ψ–Cr] and [Ψ–Si], leaving 2 V atoms which then give rise to formula $\Psi\text{–}[CrV_2Si]$, a compound existing as the result of the mutual solubility of the Frank–Kasper phases Cr_3Si and V_3Si (*A*15-type).

An alternative explanation results from considering groups of atoms. Thus, each of the 6 $\Psi\text{-}[NbO_4]$ tetrahedra has a total electron count of $32 + 41 = 73$, and this is the total electron count of the element Ta. In similar fashion, the electron count for each VN_4 tetrahedron is $23 + 28 = 51$, which is the electron count for Sb. The result is the pseudo-compound Li-stuffed $\Psi\text{-}[Ta_3Sb]$ with the Cr_3Si-type structure, just like Ta_3Sb itself. Of course, this is not unexpected because $Ta_3Sb = [Ta_2{}^{1-}TaSb^{2+}] = \Psi\text{-}[W_2TaIn]$ whose electron count is an average of that of the Frank–Kasper phases Nb_3In, W_3Si, Ta_3Sn, Nb_3Ge or $(Nb,Mo)_3(Sn,Si)$.

Although this interpretation leaves 32 Li atoms (including the 6 Li(2) atoms) as filling atoms, we do not consider it as mere coincidence that the above electron counting yields the pseudo-formula $\Psi\text{-}Ta_3Sb$, in which elements of Group 15 are involved. We cite the fact that molecular N_2 at 4.9 GPa also adopts the Cr_3Si-type structure [16]. The *A*15 structure is shown in Fig. 4 for both $\gamma\text{-}O_2$ and $HP\text{-}N_2$, and Fig. 4d shows the equivalent arrangements of the LiN_4 and VN_4 tetrahedra.

Moreover, as it will be discussed later, this coincidence between the arrangement of pseudo-atoms (in the form of MN_4 tetrahedra) and that of Group 15 elements occurs in other structure types, and indeed, we see it as entirely reasonable to equate these pseudo-atoms in Li_7VN_4 and like compounds (such as Li_7PN_4) with N_2 molecules.

3.1.2 $CaPd_3O_4$

We have now looked further in space group $Pm\overline{3}n$ [17, 18] and found the compound $CaPd_3O_4$ [19], with Ca in 2*a* at 0,0,0; Pd in 6*c* at ¼, 0, ½ and O in 8*e* at (0.25, 0.25, 0.25). The corresponding sites in $\gamma\text{-}Li_7VN_4$ are V(1) at 0,0,0; Li(2) in 6*d* at ¼, 0, ½; and Li(4) in 8*e* at 0.255, 0.255, 0.255. Again, it is useful to compare the *atoms* in $CaPd_3O_4$ and the corresponding tetrahedra, $V(1)N_4$ and those centred by Li(2) and Li(4). The drawings are shown below in Fig. 5a, b,

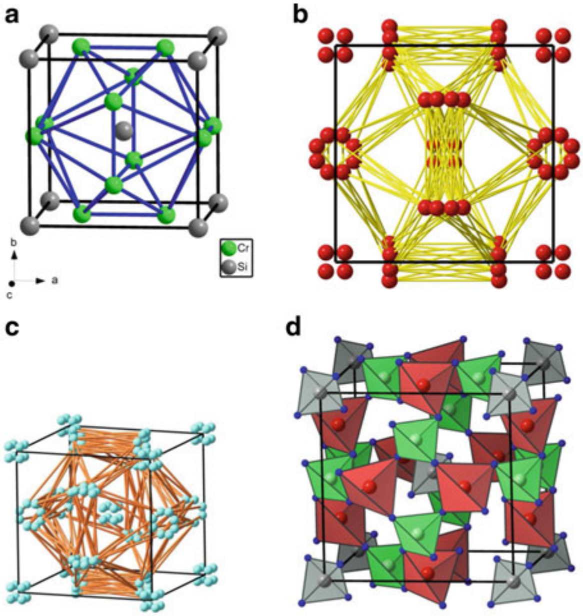

Fig. 4 (**a**) The *A*15 structure of the Frank–Kasper phase Cr_3Si. (**b**) The structure of γ-O_2 projected on (100). The O_2 molecules show rotational disorder, as shown by the multitude of intermolecular contacts, drawn in *yellow*. (**c**) A perspective view of the same array for the same structure of HP-N_2 (4.9 GPa). In (**d**) the Li_7VN_4 substructure, comprising the Li(2)N_4 (*green*), the V(1)N4 (*grey*) and the V(2)N_4 tetrahedra (*red*), is drawn. The two tetrahedral pairs, *green–grey* and *red–grey*, form two coexisting and interpenetrating Cr_3Si-type substructures, the latter pair corresponding to the Ψ-Ta_3Sb compound when V(2) is replaced by Nb (see text above)

from which it is evident that the structure can be described as a body-centred cube of composition Ca_2 with an inscribed Pd_6 icosahedron containing an encapsulated O_8 cube.

3.1.3 Pt_3O_4 and $FeGeV_2$

In similar fashion, we can relate the Pt_3O_4 structure to the above arrangement of LiN_4 tetrahedra, omitting the V(1)N_4 tetrahedra, since the Pt_3O_4 [20] structure is the same as that of $CaPd_3O_4$ [19] with the Ca atoms missing, i.e. a Pt_6 icosahedron housing an O_8 cube. An elegant way of justifying the formation of the Pt_6 icosahedron is as follows: If we rewrite the formula as Pt_6O_8 and assume that each O atom can formally accept two electrons, then we have $[Pt_6]^{+16}[O^{-2}]_8$, which implies the coexistence of 4 Pt(II) + 2 Pt(IV). This partitioning of the oxidation states, alone, cannot justify the structure but, if instead, we assume oxidation states of 4 Pt (IV) + 2 Pt(II), then, the Pt atoms donate $20e^-$ and the formula becomes $(2e^-)(2e^-)[Pt_6]^{+20}[O^{-2}]_8$. Of them, only 16 electrons can be accepted by the eight

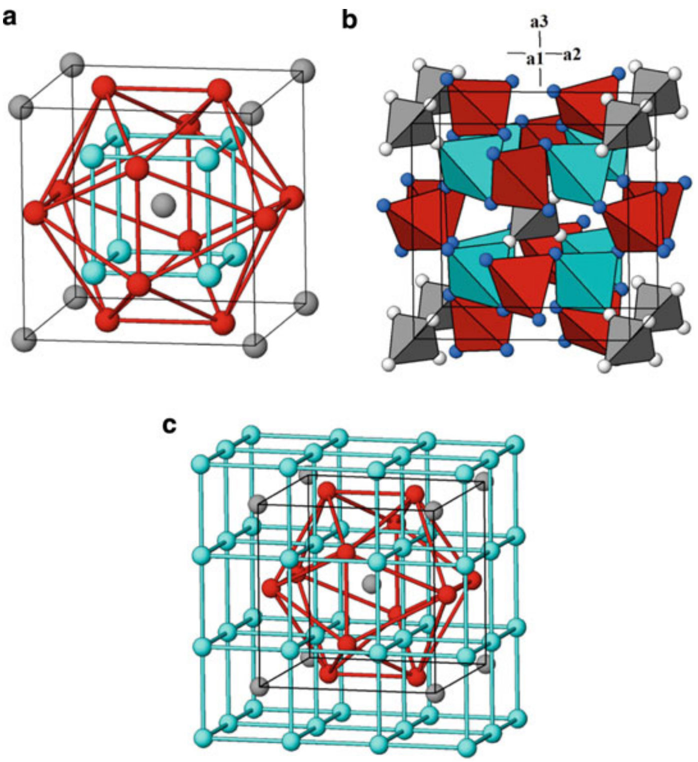

Fig. 5 (**a**) The structure of $CdPd_3O_4$ ($a = 5.747$ Å) to be compared with that of Li_7VN_4. Ca atoms – *grey*, Pd atoms – *red*, O atoms – *light blue*. (**b**) The structure of Li_7VN_4 ($a = 9.6064$ Å). V(1)N_4 tetrahedra – *grey*, Li(2)N_4 tetrahedra – *red*, Li(4)N_4 tetrahedra – *light blue*. (**c**) The insertion of the *A*15 $CaPd_3$ structure into an extended array of O atoms (*light blue cubes*) only partially occupied by Ca atoms – *grey*

O atoms, and the four remaining electrons could be then located as Lewis Pairs at the 2*a* sites (0, 0, 0; ½, ½, ½), giving rise to the pseudo-formula Ψ-(Os_2W_4)Ne_4 + $(2e^-)_2$. The two electron pairs (Lewis pairs) would occupy the 2*a* positions at (0, 0, 0; ½, ½, ½), like the Si atoms in the Cr_3Si. Because Pt(IV) and Pt(II) are equivalent to Ψ-[^{74}W] and Ψ-[^{76}Os], Pt_6O_4 should be equivalent to an O_8-stuffed Ψ-$Os_2W_4O_2$, a compound which has not been reported so far but which is close to the existing W_3O [21] which can be reformulated as $\Psi\text{-}W_2W_4O_2 = \Psi\text{-}W_2W_4(2e)_2$.

An alternative explanation would imply the existence of six Pt(IV) atoms donating a total of 24 electrons. Because only 16 can be accepted by the O atoms, the 8 remaining electrons would play the role of either 2 Ψ-^{4}Be (with a total of four electrons) or 2 Ψ-Si(Ge), with four valence electrons (Si, Ge). The difficulty of this model resides in the impossibility of locating four electrons at the same site. However, it is noteworthy how both pseudo-elements, Ψ-^{4}Be and Ψ-Si(Ge), lead to the pseudo-formulae which agree with those of real compounds having the *A*15 structure, i.e. Mo_3Be and W_3Ge, respectively.

In favour of the hypothesis of a mixed valence compound is the existence of the compound $Ca_{0.5}Pd_3O_4$, which is a defective $CaPd_3O_4$-type structure with one half of the Ca positions empty. In this way, we have the series $CaPd_3O_4$, $Ca_{0.5}Pd_3O_4$ and Pt_3O_4 where the fully occupied Ca positions in $CaPd_3O_4$ become empty in the platinum oxide.

Then there is the alloy structure $FeGeV_2$ ($a = 4.687$ Å) [22], shown below on the left, with the corresponding metal-centred tetrahedra of Li_7VN_4 ($a = 9.606$ Å) shown on the right (Fig. 6a, b). The derivation is straightforward, i.e. if the Fe atom donates one electron to each V atom, the compound becomes Ψ-Cr_3Ge (Cr_3Si-type).

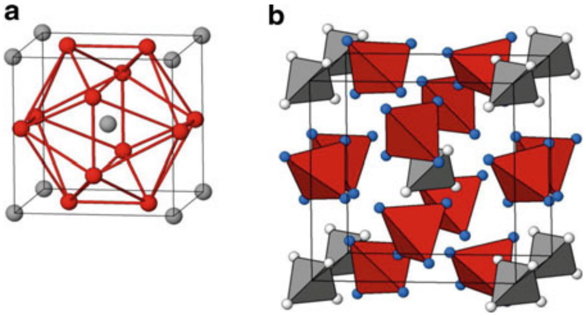

Fig. 6 (**a**) The structure of $FeGeV_2$ ($a = 4.687$ Å). Ge atoms – *grey*; Fe/V atoms – *red*. (**b**) Li_7VN_4 ($a = 9.606$ Å). $V(1)N_4$ tetrahedra – *grey*, $Li(2)N_4$ tetrahedra – *red*

3.2 Substructures in the Space Group $P\bar{4}3n$

3.2.1 Ag_3PO_4

A further search of the databases [17, 18] reveals the compound Ag_3PO_4 in space group $P\bar{4}3n$ [23]: it has Ag atoms occupying the site 6*d* (¼, 0, ½), which corresponds to the Li(2) site in Li_7VN_4. The O atoms occupy the 8*e* site, with coordinates (x, x, x) (with $x = 0.1486$). There are two other reported structures for Ag_3PO_4 [24, 25]. Both these determinations give the O sites as 8*e* (x, x, x) (with $x \sim 0.35$). We note that 0.35 is simply 0.5–0.15, and these determinations simply have the effect of inverting the VO_4 tetrahedra at the origins (Fig. 6a).

The topology of the Ag_3PO_4 structure and the substructure $V(1)_2Li(2)_6N_{32}$ of Li_7VN_4 is the same. Figure 7a, b illustrates this: the grey $V(1)N(2)_4$ tetrahedra of Li_7VN_4 correspond to the actual PO_4 tetrahedra in Ag_3PO_4, while the red $Li(2)N_4$ tetrahedra represent the Ag atoms, and are the reason for the much larger cell edge – 9.6064 Å for Li_7VN_4 compared with 6.06 Å for Ag_3PO_4. Once again, inspection of Fig. 7 reveals that the unit cell of Ag_3PO_4 is actually comprised of a body-centred cube of composition $(PO_4)_2$ in which is inscribed an icosahedron of composition Ag_6.

The structures of both Li_7PN_4 and Ag_3PO_4 show another similarity when we are comparing Ag atoms with the whole $Li(2)N(1)_4$ tetrahedra as pseudo-atoms.

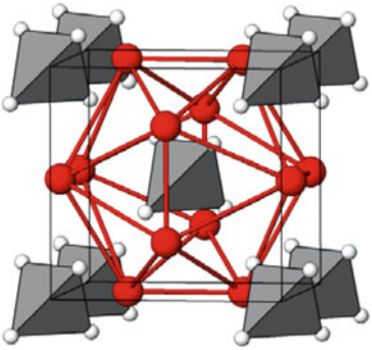

Fig. 7 Comparison of the structures of Ag_3PO_4 and $Li_7(P,V)N_4$. The structure of Ag_3PO_4, viewed along [100] ($a = 6.06$ Å). Ag atoms – *red*, PO_4 tetrahedra – *grey*. Compare with the Li_7VN_4 ($a = 9.606$ Å) represented in Fig. 6b

The composition of the equivalent pseudo-structure in the isomorphic Li_7PN_4 cell is then simply $[P(1)N_4]_2[P(2)N_4]_6$. We can easily transform the 2 $P(1)N_4$ tetrahedra to 2 $P[\Psi\text{-}O]_4$ by donation from Li atoms of one electron to each N atom in each $P(1)N_4$ tetrahedron, and so we have the required phosphate groups. The sub-array then becomes $[P(1)O_4]_2[P(2)O_4]_6$, leaving 18 Li atoms as "stuffing". Now the electron count for each $\Psi\text{-}[P(2)O_4]$ tetrahedron is 47, corresponding to the element Ag, so the sub-array can now be written as $\Psi\text{-}Ag_6(PO_4)_2$, with the observed structure.

It should be added that the existence of the complementary substructure $\Psi\text{-}Li_3PO_4$ could be seen as normal because another alkali phosphate, Na_3PO_4, is isostructural with the HT-phase of Ag_3PO_4 [23]. Both compounds have a cation array of the BiF_3 type which, surprisingly, is also adopted by several alkali-metal pnictides, such as the HP-phase of Na_3As [26]. Surprisingly, this structure is preserved in the HT-phase of Na_3AsO_4 [27]. Thus, in the same manner that Na_3As, Na_3AsO_4, Na_3PO_4 and HT-Ag_3PO_4 are related by their common BiF_3-type structure, the existence of a $(Li/Na)_3PO_4$ phase with the Ag_3PO_4 structure should not be discarded. In fact, it is implicit in Li_7PN_4 and $\gamma\text{-}Li_7VN_4$.

3.2.2 RuO_4 and OsO_2F_2

Figure 4d depicts both the tetrahedral pairs $V(1)N_4/Li(2)N_4$ and $V(1)N_4/V(2)N_4$. The arrangement of the first pair is also the topological equivalent of one form of the structure of RuO_4 [28], shown in Fig. 8a, while that of the second pair represents the OsO_2F_2 structure [29]. All the Li atoms are now missing from the depicted Li_7VN_4 substructure, a total of 56; so we have an alternative description of the full structure as "Li-stuffed RuO_4-type". In this compound, the body-centred cube comprises two $Ru(1)O_4$ tetrahedra with six $Ru(2)O_4$ completing the inscribed icosahedron.

Again, we can rationalize this RuO_4-type structure: we take as the parent $Li_{56}[(M^V)]_8N_{32}$ structure the compound $Li_{56}[Nb_2Nb_6]N_{32}$. The Li atoms donate one electron to each of the 32 N atoms, converting them to Ψ-O, and three electrons

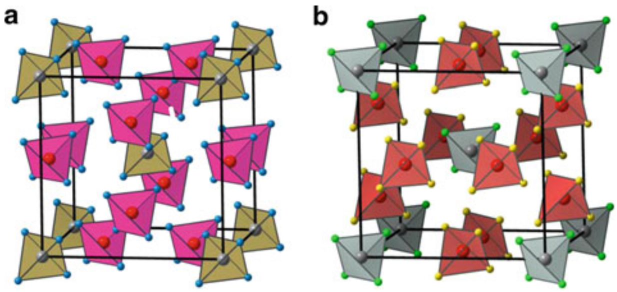

Fig. 8 (**a**) The structure of RuO_4 ($a = 8.509$ Å). Ru(1)O_4 tetrahedra – *brown*, Ru(2)O_4 tetrahedra – *pink*. O atoms – *blue*. (**b**) OsF_2O_2 ($a = 8.595$ Å). Os(2)F_4 tetrahedra – *grey*, Os(1)(F/O)$_4$ tetrahedra – *red*, F atoms – *green*, F/O atoms – *yellow*

to each of the eight Nb atoms to give [Ψ-He]$_{56}$ and [$(Nb^{-3})_2$ $(Nb^{-3})_6$][Ψ-O]$_{32}$. Nb^{-3} is Ψ-Ru, and so we have [Ψ-RuO_4] with both Ψ-Ru(1) and Ψ-Ru(2).

For the OsF_2O_2 structure, we take as parent the hypothetical $Li_{56}[Re_2Re_6]N_{32}$. Justification for this is that the compound $Li_{56}[Mn_2Mn_6]N_{32}$ does exist, and Re is in the same group. We require 48 electrons to convert the 32 N atoms to 16 [Ψ-O] and16 [Ψ-F] atoms and the remaining 8 from the 56 Li atoms to convert the Re to Ψ-Os. The nett result is [Ψ-He]$_{56}$ plus Ψ-[Os(F_2)(O_2)]. The resulting structure involves a body-centred cube comprising two Os(2)F_4 tetrahedra, the inscribed icosahedron being formed by six Os(1)(F/O)$_4$ tetrahedra.

3.2.3 Sodalite and Danalite

Another substructure of $Li_{56}[V(1)_2V(2)_6]N_{32}$ is that of the sodalite type typified by $Na_8[Al_6Si_6O_{24}](ClO_4)_2$ [30], derived from the hypothetical parent $Na_{56}[V(1)_2$ $V(2)_6]N_{32}$, where the V(2)N_4 tetrahedra correspond with SiO_4 tetrahedra, Na(2)N_4 tetrahedra with AlO_4 tetrahedra and V(1)N_4 tetrahedra with ClO_4 tetrahedra (Fig. 9a, b).

In rationalizing this substructure, we begin with the parent structure, $Na_{56}[P(1)_2P(2)_6]N_{32}$ (note the substitution of Li atoms by the Na atoms of the original sodalite). First, we convert the 32 N atoms to 32[Ψ-O] by the acceptance of 32 electrons from 32 Na atoms, leaving 24 Na atoms plus 32 [Ψ-Ne]. The formula becomes Na_{24}[Ψ-Ne]$_{32}$[$P(1)_2P(2)_6$][Ψ-O]$_{32}$. Within the [$P(1)_2P(2)_6$] group, we now have 2P(1) atoms accept 2e each from Na to form 2[Ψ-Cl], and we then associate with 2[Ψ-Cl] eight of the 32[Ψ-O] atoms to form 2[Ψ-ClO_4]: the pseudo-formula is now Na_{20}[Ψ-Ne]$_{36}$[[Ψ-ClO_4]$_2$ $P(2)_6$][Ψ-O]$_{24}$, which we rewrite as Na_{14}[Ψ-He]$_{36}$[$Na_6P(2)_6$][Ψ-O]$_{24}$[Ψ-ClO_4]$_2$. We need now to convert [$Na_6P(2)_6$] to [Al_6Si_6], and this requires that the 6 P(2) atoms donate 1e each and the six Na atoms accept 2e each, a net acceptance of 6e for the group, leading to a final pseudo-formula Na_8[Ψ-Ne]$_{42}$[Al_6Si_6] [Ψ-O]$_{24}$[Ψ-ClO_4]$_2$, a neon-stuffed sodium perchlorate sodalite.

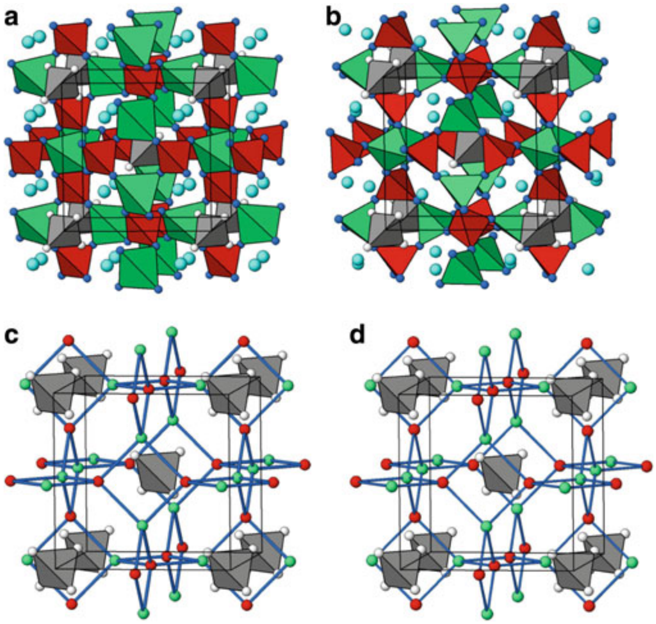

Fig. 9 (**a**) The sodalite-type sub-array in Li_7VN_4. $V(2)N_4$ tetrahedra – *red*, $V(1)N_4$ tetrahedra – *grey*. *Light blue atoms* are Li(4). (**b**) The sodium perchlorate sodalite structure. SiO_4 tetrahedra – *red*, AlO_4 tetrahedra – *green*. *Light blue atoms* are Na. ClO_4 tetrahedra – *grey*. (**c**) Sodalite-type framework in Li_7VN_4. $V(1)N_4$ tetrahedra – *grey*, V(2)–Li(2) bonds – *blue*, V(2) atoms – *red*, Li(2) atoms – *green*. (**d**) The sodalite framework in $Na_8[Al_6Si_6O_{24}](ClO_4)_2$. ClO_4 tetrahedra – *grey*, Al–Si bonds – *blue*, Si atoms – *red*, Al atoms – *green*

The various drawings are shown in Fig. 9a–d from which it emerges that the body-centred cubes comprise $V(1)N_4$ tetrahedra for $Li_{56}[V(1)_2V(2)_6N_{32}]$ and ClO_4 tetrahedra for sodalite. However, in each case, two icosahedra have been fused to create an inscribed cuboctahedron to complete the required frameworks.

Many other compounds with this elegant framework also satisfy the electron requirements: for example, the mineral danalite – $Fe_8[(BeSiO_4)_6]S_2$ [31], the borate $(B_{12}O_{24})(Zn_4O)_2$ [32] and $[Be_6As_6O_{24}](LiCl)_2$ [33] in which the sodalite-like III–V network can be achieved by the unique transfer of six electrons from 6 Li to 6 Be, which thus becomes 6 Ψ-B, the resulting formula being $[\Psi\text{-He}]_6[(\Psi\text{-B})_6As_6O_{24}](LiCl)_2$.

3.2.4 Colusite and Germanite

A further detailed search of the database in space group $\boldsymbol{P}\bar{4}3n$ has revealed the existence of the two minerals, colusite [34], $Cu_{26}[V_2As_4Sn_2]S_{32}$, and germanite [35], $Cu_{26}[Fe_4Ge_4]S_{32}$. Both are sphalerite-like structures, except that the VS_4 (CuS_4)

tetrahedra at the origins (Fig. 10a, colusite, Fig. 10b, germanite) share their edges rather than corners with the immediately surrounding tetrahedra. However, the predominant contacts involve corner-sharing, as in sphalerite.

We note that the split sites of these two structures are different: (As/Sn) for colusite is in site 6*c* (Cu(2) in germanite) and (Fe/As) for germanite is in 8*e* (Cu(2) in colusite). Figure 10c shows the corresponding drawing for a sphalerite-like component of Li_7VN_4 involving only the $V(1)N_4$, $V(2)N_4$, $Li(2)N_4$, $Li(3)N_4$ and $Li(5)N_4$ tetrahedra, whereas it is the $V(1)N_4$ tetrahedra at the origins which share edges. The close similarities are evident.

Here we are entering the whole complex realm of mineral chemistry where given mineral structures can contain a variety of different substitutions. According to Spry et al. [34] "… the elements Cu, V, As and S are essential components of colusite, whereas Sn, Sb, Fe and Ge are often present in significant quantities. Cu content can vary somewhat." The ideal, so-called high-tin colusite has the formula $Cu_{26}[V_2As_4Sn_2]S_{32}$, the As and Sn being disordered in the ratio of 2 to 1 on the 6*c* site of $\boldsymbol{P}\bar{4}3n$, and this is the composition whose structure was reported. "Low-tin"

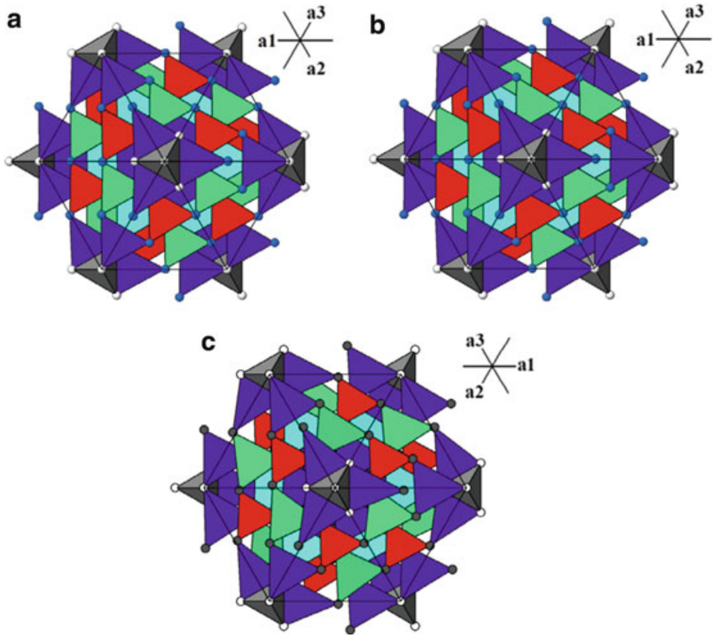

Fig. 10 (**a**) The structure of colusite (a = 10.621 Å) viewed along [111]. $(As/Sn)S_4$ tetrahedra – *green*, VS_4 tetrahedra – *grey*, $Cu(2)S_4$ tetrahedra – *light blue*, $Cu(3)S_4$ tetrahedra – *red*, $Cu(1)S_4$ tetrahedra – *purple*. (**b**) The equivalent structure of germanite (a = 10.5862 Å). $Cu(2)S_4$ tetrahedra – *green*, $Cu(1)S_4$ tetrahedra – *grey*, $Cu(3)S_4$ tetrahedra – *red*, $(Fe/As)S_4$ tetrahedra – *light blue*, $Cu(4)S_4$ tetrahedra – *purple*. (**c**) Li_7VN_4 [111] (a = 9.606 Å). $V(1)N_4$ tetrahedra – *grey*, $V(2)N_4$ tetrahedra – *red*, $Li(4)N_4$ tetrahedra – *light blue*, $Li(2)N_4$ tetrahedra – *green*, $Li(5)N_4$ tetrahedra – *purple*

colusite has the ideal formula $Cu_{24}[V_2As_6]S_{32}$, with two vacancies at the Cu sites. In both cases, all the copper present is in the +1 oxidation state.

The ideal formula for germanite is $Cu_{26}[Fe_4Ge_4]S_{32}$, the Fe and Ge being disordered on the 8e site of the space group in a 1:1 ratio, but again there is considerable variation in the reported formulae: Tettenhorst and Corbato [35] give the ideal formula as $[Cu^{1+}]_{16}[Cu^{2+}]_{10}[Fe^{3+}]_4Ge_4S_{32}$: Spiridinov [36] gives it as $[Cu^{1+}]_{20}[Cu^{2+}]_6[Fe^{3+}]_2Ge_6S_{32}$. Both reported structures are almost identical with the arrangement of the V(1), V(2), Li(1), Li(2), Li(4), N(1) and N(2) atoms in Li_7VN_4, as the diagrams above clearly show, so we would claim these two structures as genuine substructures of Li_7VN_4: only Li(3) and Li(5) of the full Li_7VN_4 structure are missing, so we can describe the Li_7VN_4 structure as both "Li-stuffed colusite" and "Li-stuffed germanite".

In attempting a chemical rationalization of these close relationships, we must first relate the colusite composition, $V_2Cu_{26}(As_4Sn_2)S_{32}$, to that of the parent $Li_{56}V_8N_{32}$. We would have to propose a hypothetical parental analogue $Li_{30}Cu(I)_{26}[V_2As_4Sb_2]P_{32}$, substituting 26 Cu(I) atoms for 26 of the 56 Li atoms, and then apply the *EZKC* approach as follows: the 30 Li atoms donate one electron each to convert 30 P atoms to 30 [Ψ-S] atoms, and the 2 Sb atoms donate 1 electron each to the remaining 2 P atoms, thereby becoming 2 [Ψ-Sn] and 2 [Ψ-S], respectively. The nett overall result is the pseudo-compound $\Psi\text{-}\{Cu_{26}[V_2As_4Sn_2]S_{32}\} + 30\ \Psi\text{-He}$.

In similar fashion, we might try to relate the germanite composition, $Cu_{26}[Fe_4Ge_4]S_{32}$, to the hypothetical parent $Li_{30}Cu_{26}[V_4As_4]P_{32}$, except that only 6 of these 26 Cu atoms are Cu(I), able to substitute directly for Li(I). If, however, we allow the full substitution, and consider the 20 Cu(II) atoms as 20 Cu(I) atoms plus 20 "free" electrons, these being free to donate to the rest of the structure as required, we can progress. We require 32 electrons to convert the 32 P atoms to 32 Ψ-S. The V atoms require three electrons each to convert to Ψ-Fe, and the As atoms donate one electron each to become Ψ-Ge. The nett electron requirement is achieved from the Li atoms and the free electrons. Things look better if we take the Spiridinov ideal formula, $[Cu(I)]_{20}[Cu(II)]_6[Fe(III)]_2Ge_6S_{32}$. In general terms, however, the variable compositions of complex minerals would seem to make any chemical rationalizations of the structures extremely complicated, and sometimes even impossible.

3.2.5 ZnS sphalerite

And while still focussing on these sphalerite-related structures, we now consider the sphalerite structure itself, taking ZnS as the archetype. The structure is shown in Figure 11a: the space group is $\boldsymbol{F\bar{4}3m}$ (216), a supergroup of $\boldsymbol{P\bar{4}3n}$. Figure 11b shows the corresponding tetrahedra of the Li_7VN_4 structure. From the Li_7VN_4 structure, half of the $V(1)N_4$ tetrahedra (one such) plus half of the $Li(3)N_4$ (three such) correspond with the Zn atoms, and half of the $Li(4)N_4$ tetrahedra (four such) correspond with the S atoms, so the sphalerite structure is clearly a substructure of Li_7VN_4. Once again we are equating single atoms of one phase with the larger tetrahedra of the other to explain the different cell edges, but in this case we have

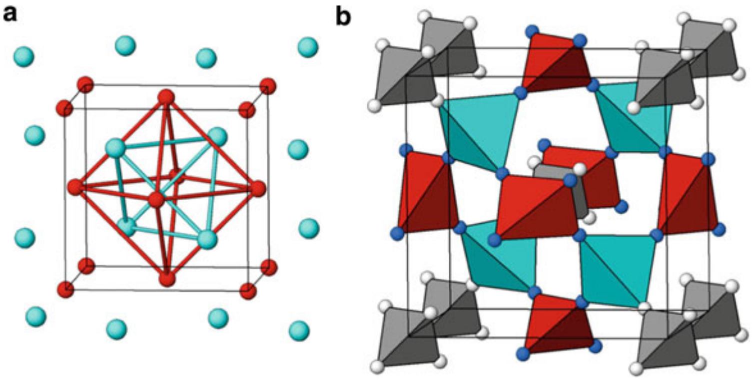

Fig. 11 (**a**) The zinc-blende structure ($a = 5.903$ Å). Zn atoms – *red*, S atoms – *light blue*, Zn–Zn bonds – *red*, S–S bonds – *light blue*. (**b**) Partial structure of γ-Li7VN4 showing the ZnS-like arrangement formed by the V(1)N4 tetrahedra – *grey*, the Li(3)N4 tetrahedra – *red* and the Li(4)N4 tetrahedra – *light blue*

the odd situation in which a LiN_4 tetrahedron equates to both a zinc atom on the one hand and a sulphur atom on the other. Now the electron count for the LiN_4 tetrahedron is 31, and the donation of one electron gives a count of 30, equivalent to Zn. Thus, the four Li(4)N_4 tetrahedra, when donating one electron each become equivalent to four Zn atoms. Acceptance of three electrons by the three Li(3)N_4 tetrahedra plus one electron by the V(1)N_4 tetrahedra gives a total count of 34 and 52 electrons respectively, which are those for the elements Se and Te. Recall that ZnSe and ZnTe crystallize in the same space group as ZnS.

Another possible chemical rationalization of the ZnS (sphalerite) substructure exists: we consider as parent compound, $Li_{56}[P(1)_2P(2)_6]N_{32}$, isostructural with γ-$Li_7VN_4$. The P(1)$N_4$ tetrahedra have a total of 43 electrons, but if we were to convert these to Ψ-[P(1)O_4] with the acceptance of 4 electrons from the Li atoms, we have a total of 47 electrons per tetrahedron, equivalent to Ψ-Ag. Again, converting the LiN_4 tetrahedra to Ψ-$[LiO]_4$ tetrahedra, with 35 electrons, this is equivalent to Ψ-Br. The resulting Ψ-[AgBr] is isoelectronic to the zincblende CdSe [37] so that an additional transfer of one electron from Ψ-$[LiO]_4$ to Ψ-[P(1)O_4], is required to get the Ψ-[CdSe]. We must also recall that a zincblende phase has been reported for AgI [38].

An alternative approach would be to ignore the cell-size differences and simply compare the various tetrahedra. There are two sets of atoms in Li_7VN_4 (Table 4) Table 4 corresponding to the two types of tetrahedra that were discussed in an earlier paper on the bixbyite structure [4].

We have drawn these two separate situations in the [111] projection (Fig. 12) to better illustrate the two sets of MN_4 tetrahedra, type - A and type - B, as discussed in that bixbyite paper. Each of the drawings shown above represents the zinc blende structure. Set A is simply Set B-stuffed blende-type; Set B is Set A-stuffed blende-type.

It is a matter of choice as to which of these two quite different representations is the more appropriate.

Table 4 The two sets of like-tetrahedra in the anti-fluorite-type Li_7VN_4

Set A	Set B
V(1) 2-fold	V(2) 6-fold
Li(3) 6-fold	Li(1) 12-fold
Li(5) 24-fold	Li(2) 6-fold
N(1) 24-fold	Li(4) 8-fold
N(2) 8-fold	N(1) 24-fold
	N(2) 8-fold

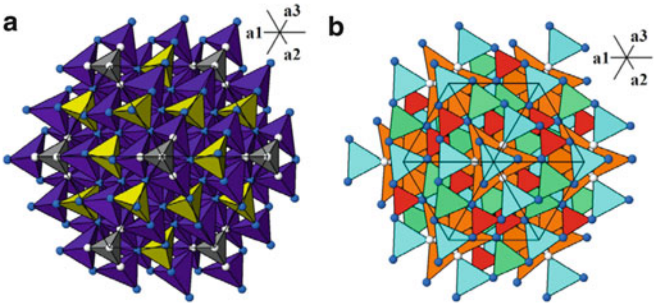

Fig. 12 (**a**) Set A of the zinc-blende-type array in Li_7VN_4 formed by the $V(1)N_4$ tetrahedra – *grey*, the $Li(3)N_4$ tetrahedra – *yellow* and the $Li(5)N_4$ tetrahedra – *purple*. (**b**) The set B of the zinc-blende-type array in Li_7VN_4 formed by the $V(2)N_4$ tetrahedra – *red*, the $Li(2)N_4$ tetrahedra – *green*, the $Li(4)N_4$ tetrahedra – *light blue*, the $Li(1)N_4$ tetrahedra – *brown*

3.3 Substructures in the Space Group $\boldsymbol{I}\bar{4}3m$

We now explore the space group $\boldsymbol{I}\bar{4}3m$, one of the four immediate precursor supergroups to $\boldsymbol{P}\bar{4}3n$. Inspection of Table 2 can reveal the various equivalences between the lattice sites, and these are summarized as follows:

The $\boldsymbol{P}\bar{4}3n$ sites are 2*a*, 6*b*, 6*c*, 6*d*, 8*e*, 12*f* and 24*i*, and of these the 2*a*, 6*b* and 8*e* sites are identical with the corresponding sites in $\boldsymbol{I}\bar{4}3m$. The 6*c* and 6*d* sites of $\boldsymbol{P}\bar{4}3n$ are equivalent to the 12*d* sites in $\boldsymbol{I}\bar{4}3m$ while the 12*f* sites of $\boldsymbol{P}\bar{4}3n$ are equivalent to the 12*e* sites of $\boldsymbol{I}\bar{4}3m$. The general set, 24*i*, of $\boldsymbol{P}\bar{4}3n$ has the *y* and *z* parameters nearly the same in the case of Li_7VN_4, so that there is a close relationship between these sites and the 24*g* (*z, x, x*) sites of $\boldsymbol{I}\bar{4}3m$. This sets the stage for comparisons of the Li_7VN_4 structure in $\boldsymbol{P}\bar{4}3n$ with its precursor structures in $\boldsymbol{I}\bar{4}3m$.

3.3.1 $Al_6Ca_4O_{13}$

First, is a comparison between the structure of $Al_6Ca_4O_{13}$ [39] in $\boldsymbol{I}\bar{4}3m$ and some elements of Li_7VN_4 in $\boldsymbol{P}\bar{4}3n$ (Fig. 13). The equivalent atom sites for the drawings below are indicated.

Here we have a thoroughly mixed-up situation in which the $V(1)N(2)_4$ tetrahedra of Li_7VN_4 correspond to the OCa_4 tetrahedra of $Al_6Ca_4O_{13}$, and the 12-fold

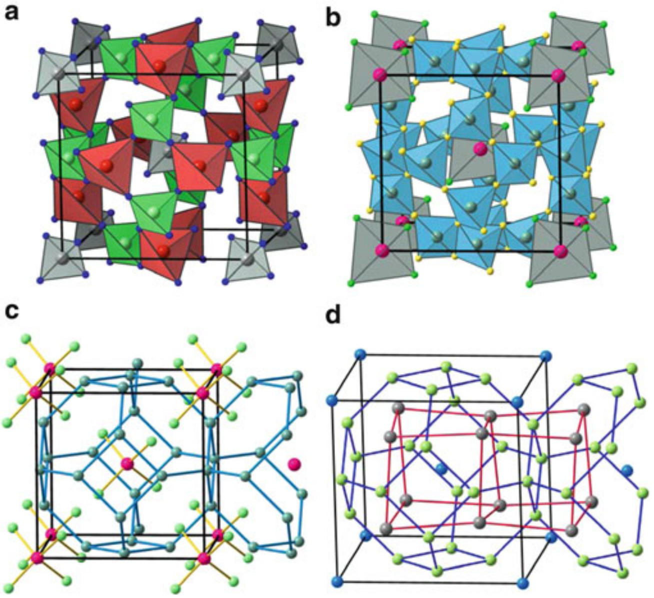

Fig. 13 Comparison of a sub-array in Li_7VN_4 ($\boldsymbol{P}\bar{4}3n$, $a = 9.606$ Å) with the structure of $Ca_4Al_6O_{13}$ ($\boldsymbol{I}\bar{4}3m$. $a = 8.86$ Å). The former is shown in (**a**), with the $V(1)N_4$ tetrahedra – *grey*, $V(2)N_4$ tetrahedra – *red* and $Li(2)N_4$ tetrahedra – *green*. The latter structure is shown in (**b**) with $O(2)Ca_4$ tetrahedra – *grey*, $AlO(1)_4$ tetrahedra – *blue*, Ca atoms – *green*, O(1) atoms – *yellow*. (**c**) The sodalite-type framework in $Ca_8[Al_{12}O_{24}]O_2$ is outlined by the Al–Al bonds – *blue*: Al atoms – *dark grey*. The OCa_4 tetrahedra are at the origins: O atoms – *red*, Ca atoms – *green*. (**d**) The same framework formed by the Al atoms in $Ca_8[Al_{12}O_{24}](WO_4)_2$: W atoms – *blue*, Al atoms – *green*, Ca atoms – *dark grey*

tetrahedral set, $AlO(1)_4$, of $Al_6Ca_4O_{13}$ corresponds with the two 6-fold tetrahedral sets, $V(2)N(1)_4$ and $Li(2)N(1)_4$ of Li_7VN_4. We note immediately that the patterns of Figs. 13a, b (as depicted further in Fig. 13c) are the same as those in Figs. 9a, b: in other words, these patterns conform to the sodalite-type framework, and we rewrite the formula as $Ca_8[Al_{12}O_{24}]O_2$ to reflect this fact. The ultimate reason for the formation of the sodalite-like network is that the six Ca atoms provide 12 electrons to the Al atoms, converting them into Ψ-Si, as occurs in other similar compounds. In this context, the formula should be written as $(Ca^{+2})_6[Al_{12}O_{24}]^{-12}(CaO)_2$, equivalent to $[\Psi\text{-}Ar]_6[\Psi\text{-}Si_{12}O_{24}](CaO)_2$.

From a purely crystallographic viewpoint, there is no doubt that the $Ca_8[Al_{12}O_{24}]O_2$ structure is a substructure of Li_7VN_4, a fact that can only be rationalized chemically on the basis that, in both compounds, a four-connected, sodalite-like network is obtained. In the case of Li_7VN_4, the skeleton is III-V [Ψ-BP], whereas in $Ca_8[Al_{12}O_{24}]O_2$ the network is IV-IV, formed by Ψ-Si atoms, both structures being related through the common sodalite-like framework. Indeed, there is a general trend for many structures to form four-connected nets, characteristic of the Group 14 elements, these networks being rationalized by using the *EZKC* [40].

Further exploration in this space group yielded the structures of several alloys (Cu_5Zn_8, Fe_3Zn_{10} and $La_6Ni_6P_{17}$) and that of U_2F_9 with atom sites quite closely related to their counterparts in Li_7VN_4. But the site correspondences are not sufficiently close, in our view, to claim these as genuine substructures.

3.4 Substructures in the Space Group $Pn\bar{3}n$ (222)

There are very few entries in the data base for the space group $Pn\bar{3}n$, and of these only two are of relevance here. These are the isostructural compounds $Nd_5Mo_3O_{16}$ and $CdY_4Mo_3O_{16}$. Both are superstructures of fluorite, CaF_2, and have the standard MX_2 composition. This is in contrast to the compound, γ-Li_7VN_4, which we have described as an anti-fluorite superstructure M_2X. The comparisons are interesting, and shed new light on the whole issue of substructures. The reported structures have the second origin, which puts this at the 8*c* site, so we have transformed the coordinates to refer to Origin 1, which then allows a direct comparison with those of γ-Li_7VN_4. The equivalent sites are given in [13] (Table 5).

Table 5 Site-equivalences between space groups $Pn\bar{3}n$ and $P\bar{4}3n$

$Pn\bar{3}n$				$P\bar{4}3n$
8*c*	→	+ ¼, ¼, ¼	→	8*e*
12*d*	→	+ ¼, ¼, ¼	→	6*c* + 6*d*
12*e*	→	+ ¼, ¼, ¼	→	12*f*
16*f*	→	+ ¼, ¼, ¼	→	8*e* + 8*e*
48*i*	→	+ ¼, ¼, ¼	→	24*i* + 24*i*

This implies that the equivalent sites in $P\bar{4}3n$ are those of $Pn\bar{3}n$ to which are added ¼, ¼, ¼. We have already identified $CdY_4Mo_3O_{16}$ as being a fluorite-type superstructure, and if we now construct the Bärnighausen tree (Table 6) relating M_8O_{16} (fluorite) to the $CdY_4Mo_3O_{16}$ structure in $Pn\bar{3}n$, and thence to the Li_7VN_4 structure in $P\bar{4}3n$ an interesting feature emerges: the cation and anion equivalences of the Li_7VN_4 substructure are those for a fluorite-related rather than an anti-fluorite-related structure.

3.4.1 $CdY_4Mo_3O_{16}$

In $CdY_4Mo_3O_{16}$ (a = 10.688 Å) in $Pn\bar{3}n$ with Z = 4 [41], the four Cd atoms and four Y atoms are in 8*c* at (¼, ¼, ¼), with half occupancy for each: the equivalent site in γ-Li_7VN_4 is Li(4), close to (¼, ¼, ¼), and the other equivalents are: Mo in 12*d* ≡ V(2) + Li(2) in 6*c* and 6*d* and the remaining Y in 12*e* ≡ Li(1) in *12f*. O(2), in 16*f*, and O(1), in 48*i*, giving a total of 64 O atoms in the $CdY_4Mo_3O_{16}$ structure, only half of which have their equivalents in the N atoms of Li_7VN_4: these unoccupied sites are shown in Table 6 by fainter links. Missing from the Li_7VN_4 structure are the V(1), Li(3) and Li(5) atoms, exactly those of the type-A set discussed above in relating the Li_7VN_4 substructure to the sphalerite structure. Thus, both

Table 6 The Bärnighausen Tree relating fluorite to $CdY_4Mo_3O_{16}$

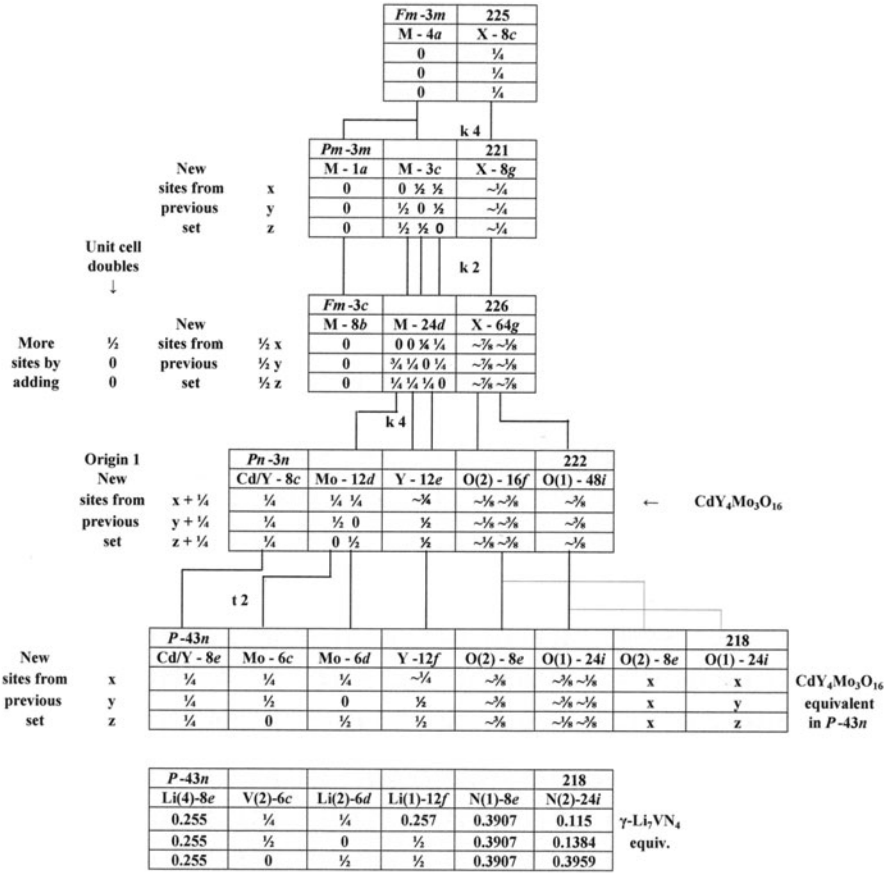

Fm-3*m*	225
M - 4*a*	X - 8*c*
0	¼
0	¼
0	¼

Pm-3*m*		221
M - 1*a*	M - 3*c*	X - 8*g*
0	0 ½ ½	~¼
0	½ 0 ½	~¼
0	½ ½ 0	~¼

Fm-3*c*		226
M - 8*b*	M - 24*d*	X - 64*g*
0	0 0 ¾ ¼	~⅞ ~⅛
0	¾ ¼ 0 ¼	~⅞ ~⅛
0	¼ ¼ ¼ 0	~⅞ ~⅞

Pn-3*n*				222
Cd/Y - 8*c*	Mo - 12*d*	Y - 12*e*	O(2) - 16*f*	O(1) - 48*i*
¼	¼ ¼	~¾	~⅛ ~⅜	~⅜
¼	½ 0	½	~⅛ ~⅜	~⅜
¼	0 ½	½	~⅛ ~⅜	~⅛

P-43*n*							218
Cd/Y - 8*e*	Mo - 6*c*	Mo - 6*d*	Y -12*f*	O(2) - 8*e*	O(1) - 24*i*	O(2) - 8*e*	O(1) - 24*i*
¼	¼	¼	~¼	~⅜	~⅜ ~⅛	x	x
¼	½	0	½	~⅜	~⅜ ~⅛	x	y
¼	0	½	½	~⅜	~⅛ ~⅜	x	z

P-43*n*					218
Li(4)-8*e*	V(2)-6*c*	Li(2)-6*d*	Li(1)-12*f*	N(1)-8*e*	N(2)-24*i*
0.255	¼	¼	0.257	0.3907	0.115
0.255	½	0	½	0.3907	0.1384
0.255	0	½	½	0.3907	0.3959

the anion-deficient $CdY_4Mo_3O_{16}$-type structure and its Li_7VN_4 substructure counterpart are of the zinc-blende type, again, a four-connected network!.

Summing up, we have the V(2), Li(2), Li(4) and Li(1) cations of Li_7VN_4 equating to the cations of $CdY_4Mo_3O_{16}$, that is to say the set B cations identified in our earlier discussion of the zinc-blende-type substructures, and half the anions of this latter compound ($CdY_4Mo_3O_{16}$) equating to the N(1) and N(2) atoms of Li_7VN_4. The 32 missing cations from Li_7VN_4 are V(1), Li(3) and Li(5), the same atoms of the type-A set discussed previously in the context of the zinc-blende-type substructures. Thus, we can formally describe our Li_7VN_4 structure as an anion-deficient $CdY_4Mo_3O_{16}$ – type structure stuffed with these 32 missing cations: the substructure formula is $Li_{26}V_6N_{32}$ (see Fig. 14).

It is also remarkable that, in $CdY_4Mo_3O_{16}$, the 12 Mo atoms form a sodalite-like cage, as shown in Fig. 15, just like the Li and V atoms do in γ-Li_7VN_4 (cf. Fig. 9). The interest is even greater if we take into account that this cage is the result of two

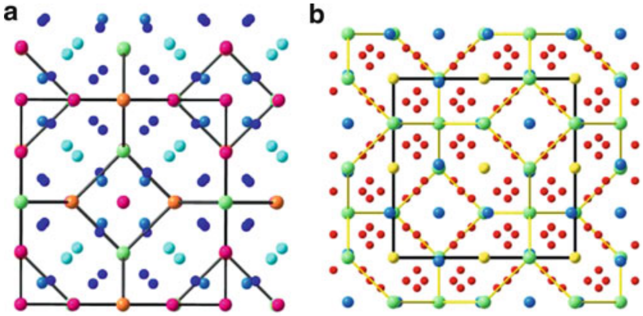

Fig. 14 (**a**) The γ-Li_7VN_4 structure projected on (100). Li(4) atoms – *light blue*, V(2) + Li(2) – *green* and *brown*, respectively, are connected to form the sodalite-like cage, Li(1) – *red*, N(1) – *dark blue*, N (2) – *blue*. Note that the Li(4) atom sites deviate from the ideal positions (¼, ¼, ¼) corresponding to the yellow atoms in (**b**). (**b**) The related structure of $CdY_4Mo_3O_{12}$. Cd/Y sites – *yellow*, Mo sites – *green*: these are connected to form the sodalite cage: Y atoms – *blue*, O atoms – *red*

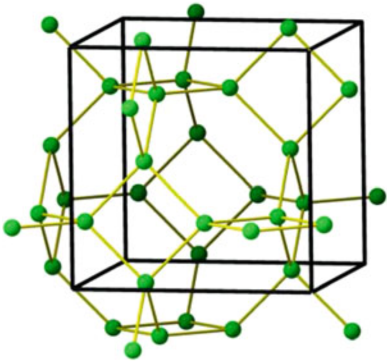

Fig. 15 The sodalite-type cage formed by the Mo atoms in both $CdY_4Mo_3O_{16}$ and $Nd_5Mo_3O_{12}$

complementary icosahedra like those existing in the *A*15 structure of the Cr_3Si type. This is consistent with the existence of the *A*15 structure in several Mo alloys such as Mo_3Zr and Mo_3Ga. It is as if the pair Cd/Y occupying the Si sites in Cr_3Si (the Zr sites in Mo_3Zr) serves as the catalyst allowing the interconversion of Mo_3(Y/Cd) into Ψ-Mo_3Zr ↔ Ψ-Mo_3In by the mutual transfer of only one electron between Cd and Y.

3.5 Substructures in Space Group $F\bar{4}3c$

Many compounds listed in the database have essentially the cubic boracite structure. Boracite itself, as reported in [42], has the formula $Mg_3B_7O_{13}Cl$ and is cubic above 538 K. The cell edge is 12.0986 Å with $Z = 8$ and the space group is $\boldsymbol{F}\bar{4}3c$. Table 7 shows how the atom sites of $\boldsymbol{F}\bar{4}3c$ relate to those of $\boldsymbol{P}\bar{4}3n$.

What this means is that the coordinates of atoms in γ-Li_7VN_4, with space group $\boldsymbol{P}\bar{4}3n$, are to be calculated from those of boracite by adding (¼, ¼, ¼) to the boracite lattice sites. So we need to compare two drawings, one of the boracite structure itself and that of γ-Li_7VN_4 in $\boldsymbol{P}\bar{4}3n$ with the coordinate shifts indicated.

Table 7 Site equivalences between space groups $\boldsymbol{F}\bar{4}3c$ and $\boldsymbol{P}\bar{4}3n$

$\boldsymbol{F}\bar{4}3c$	$\boldsymbol{P}\bar{4}3n$
8*a*	2*a* + 6*b*
8*b*	8*e*
24*c*	24*i*
24*d*	(6*c* + 6*d* + 12*f*)
32*e*	(8*e* + 24*i*)
48*f*	(2 × 24*i*)

3.5.1 Nickel Boracite

The drawing for Ni-boracite [43] is shown in Fig. 16a, but without the O(2) atoms in the general site 96*h*. Figure 16b shows all of the γ-Li_7VN_4 structure. The topological equivalence of the two is obvious.

So what about the missing O(2) atoms of the boracite drawing? Their function provides a very elegant twist to the story! The B(1) atoms are tetrahedrally

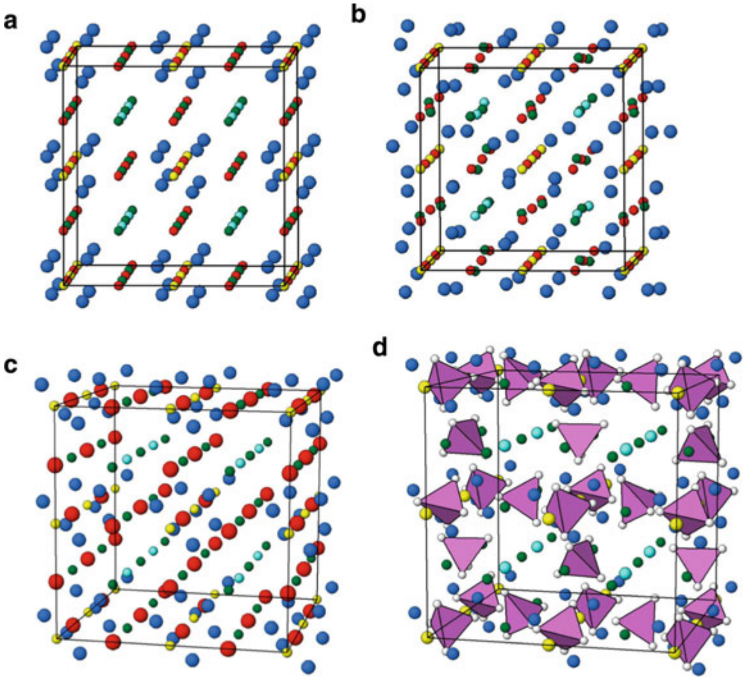

Fig. 16 (**a**) The atomic array of nickel boracite $Ni_3B_7O_{13}I$ (a = 12.016 Å) viewed near the [100] projection, but less the less the O(2) atoms, which are omitted for clarity: O(1) atoms – *yellow*, I atoms – *light blue*, Ni atoms – *dark green*, B(1) atoms – *red*, B(2) atoms – *blue*. (**b**) The equivalent projection of Li_7VN_4 (a = 9.606 Å): N(1) + N(2) atoms – *blue*; V(1) Li(3) atoms – *yellow*, Li(4) atoms – *light blue*, Li(5) Li(1) atoms – *dark green*, Li(1) + Li(2) atoms – *red*. (**c**) Perspective view near [100] of the $Ni_3B_7O_{13}I$ structure. Ni atoms – *dark green*; I atoms – *light blue*; O(1) atoms – *yellow*; B(2) atoms – *red*, and enlarged for emphasis, O(2) atoms – *blue*. (**d**) The $Ni_3B_7O_{13}I$ structure: the same projection as (**c**) but with the B(1)O(2)$_4$ tetrahedra – *pink* (not all shown)

coordinated by these O(2) atoms, and all the latter are thus accounted for: if we draw these tetrahedra, it is clear that they can be considered as entities in their own right and responsible for the lattice expansion from ~9.6 Å in Li_7VN_4 to ~12 Å in boracite. Figure 16c shows this very well. And so we have a 1:1 correspondence between the two structures, as seen above, where the 24 $B(1)O(2)_4$ tetrahedra of the unit cell in boracite correspond to the 24 MN_4 tetrahedra of Li_7VN_4 comprising $6V(2)N_4$, $6Li(2)N_4$ and $12Li(1)N_4$ tetrahedra. We note also that the 32 B(2) atoms of boracite are equivalent to the 32 N atoms of Li_7VN_4, i.e. 24 N(1) and 8 N(2).

4 The β-Phase of $Li_7V^VN_4$

This structure is also *cubic* [5, 6], but its space group, $\boldsymbol{Pa}\overline{3}$ (Z = 8), is different from that of the γ-phase. The lattice sites are given in Table 8.

Moreover, this space group requires the formula to be written as $Li_6[LiV]N_4$ since one Li atom and the V atom are ordered on two separate eightfold sites. In an earlier publication on “stuffed” anti-bixbyite structures, we applied the *EZKC* [1] by supposing that four of the six Li atoms donate four electrons to the four N atoms, converting them to four (Ψ-O) (pseudo-oxygen), and that the two remaining Li atoms of this group transfer two electrons to the [LiV] group to create the $[LiV]^{-2}$ group, with a total of eight electrons. These can then be formally distributed as $(Li^{-3}) \equiv$ (Ψ-C) and $(V^{+1}) \equiv$ (Ψ-Ti), where the symbol Li^{-3} implies the acceptance by Li of three electrons to give (Ψ-C), and the symbol V^{+1} implies the donation by V of one electron to give (Ψ-Ti). The [LiV] group is now isoelectronic with (Ψ-CTi). The overall loss of six electrons by the six Li atoms outside the square brackets is equivalent to the formation of six isoelectronic (Ψ-He) atoms; so the nett effect of all these electron transfers is the pseudo-compound, Ψ-(He_6CTiO_4), a hypothetical “C/Ti-stuffed sesquioxide, He_3O_2”, or what is essentially a V/Li-stuffed sesquinitride, Li_3N_2.

It is worth noting that alternative distributions of the eight electrons within the square brackets are possible, leading to the following: $[Li^{-2}V^0] \equiv$ [(Ψ-B)V]; $[Li^{-1}V^{-1}] \equiv$ [(Ψ-Be)(Ψ-Cr)]; and $[Li^0V^{-2}] \equiv$ [Li(Ψ-Mn)]. The corresponding pseudo-compounds would be Ψ-($He_6[BV]O_4$), Ψ-($He_6[BeCr]O_4$) and Ψ-($He_6[LiMn]O_4$), respectively.

Table 9 shows the five possible subgroup pathways by which a doubled unit cell with the space group $\boldsymbol{P}a\overline{3}$ can be derived from the parent fluorite unit cell with space group $\boldsymbol{F}m\overline{3}m$. Table 10 shows the Bärnighausen Tree for Case 3, which is not quite identical with that first published by Niewa et al. [6].

Table 8 The lattice sites for β-Li_7VN_4

Atom	Site	*x*	*y*	*z*
V	8*c*	0.3703	0.3703	0.3703
Li(1)	8*c*	0.1250	0.1250	0.1250
Li(2)	24*d*	0.1320	0.3830	0.1360
Li(3)	24*d*	0.3570	0.3790	0.1141
N(1)	8*c*	0.2610	0.2610	0.2610
N(2)	24*d*	0.4858	0.2575	0.4786

Table 9 Space group pathways from $Fm\bar{3}m$ to $Pa\bar{3}$. Transition from *red* to *black* indicates doubling of the unit cell

Case 1	Case 2	Case 3	Case 4	Case 5
$Fm\bar{3}m$	$Fm\bar{3}m$	$Fm\bar{3}m$	$Fm\bar{3}m$	$Fm\bar{3}m$
225	225	225	225	225
$Fm\bar{3}$	$Pm\bar{3}m$	$Pm\bar{3}m$	$Pm\bar{3}m$	$Pm\bar{3}m$
202	221	221	221	221
$Pm\bar{3}$	$Fm\bar{3}c$	$Pm\bar{3}$	$Pm\bar{3}$	$Fm\bar{3}m$
200	226	200	200	225
$Ia\bar{3}$	$Fm\bar{3}$	$Ia\bar{3}$	$Fm\bar{3}$	$Fm\bar{3}$
206	202	206	202	202
$Pa\bar{3}$	$Pa\bar{3}$	$Pa\bar{3}$	$Pa\bar{3}$	$Pa\bar{3}$
205	205	205	205	205

Table 10 The full Bärnighausen Tree for Case 3 above

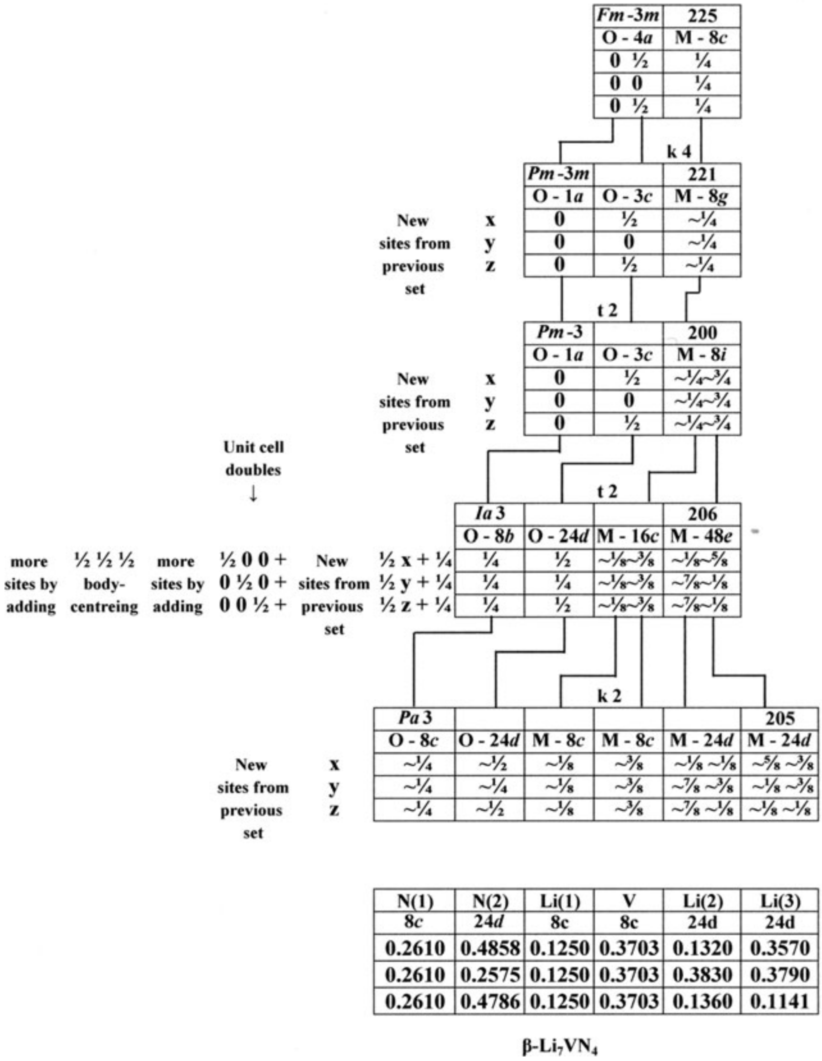

Fm-3*m*	225
O - 4*a*	M - 8*c*
0 ½	¼
0 0	¼
0 ½	¼

Pm-3*m*		221
O - 1*a*	O - 3*c*	M - 8*g*
0	½	~¼
0	0	~¼
0	½	~¼

Pm-3		200
O - 1*a*	O - 3*c*	M - 8*i*
0	½	~¼~¾
0	0	~¼~¾
0	½	~¼~¾

Ia 3			206
O - 8*b*	O - 24*d*	M - 16*c*	M - 48*e*
¼	½	~⅛~⅜	~⅛~⅝
¼	¼	~⅛~⅜	~⅞~⅛
¼	½	~⅛~⅜	~⅞~⅛

Pa 3					205
O - 8*c*	O - 24*d*	M - 8*c*	M - 8*c*	M - 24*d*	M - 24*d*
~¼	~½	~⅛	~⅜	~⅛ ~⅛	~⅝ ~⅜
~¼	~¼	~⅛	~⅜	~⅞ ~⅜	~⅛ ~⅜
~¼	~½	~⅛	~⅜	~⅞ ~⅛	~⅛ ~⅛

N(1)	N(2)	Li(1)	V	Li(2)	Li(3)
8*c*	24*d*	8c	8c	24d	24d
0.2610	0.4858	0.1250	0.3703	0.1320	0.3570
0.2610	0.2575	0.1250	0.3703	0.3830	0.3790
0.2610	0.4786	0.1250	0.3703	0.1360	0.1141

β-Li_7VN_4

From all this, it is clear that there are only two immediate supergroups of $\boldsymbol{P}a\bar{3}$, viz. $\boldsymbol{I}a\bar{3}$ and $\boldsymbol{F}m\bar{3}$.

4.1 Substructures in the Space Group *Pa*$\bar{3}$

4.1.1 Molecular N_2 at 20 K

We look first for substructures in the $\boldsymbol{P}a\bar{3}$ space group itself. A study of the databases [16, 17] reveals immediately the crystal structure of molecular α-N_2 at 20 K [44]; the N atoms occupy the site 8*c* of $\boldsymbol{P}a\bar{3}$, with coordinates 0.0530, 0.0530, 0.0530. The comparable component of β-Li_7VN_4 is the Li(1)N_4 tetrahedron, thus accounting for the greater cell edge of β-Li_7VN_4 compared with that of N_2 (a = 5.661 Å). In the N_2 structure, the N–N distance is 1.04 Å, whereas the Li(1)-Li(1) distance in β-Li_7VN_4 is 4.47 Å.

Figure 17a–g illustrates the molecular N_2 story. We note in particular that in Fig. 17b the pairs of VN_4 tetrahedra, linked by brown lines, act like the N_2 molecules in Fig. 17a.

There are two important features arising here, one being that we can consider the V atoms, belonging to Group 15, to be behaving as N_2 molecules, despite being at the centres of VN_4 tetrahedra. Looked at differently, we have the electron count for the VN_4 tetrahedra as 51, corresponding to Ψ-$^{(51)}$Sb, also in Group 15. And even more surprising is the following: the eight LiN_4 tetrahedra have a total electron count of 31 electrons each, and we can then allow each to accept two electrons from the remaining Li atoms to form Ψ-BN_4 tetrahedra, with an electron count of 33 each, just the count for As, also belonging to Group 15. Thus, both the LiN_4 and the VN_4 tetrahedra are behaving structurally as Ψ-As and Ψ-Sb, respectively. In addition, the complete set of V(1)N_4 and Li(1)N_4 tetrahedra (formed by combining Fig. 17b, c) give rise to the skeleton shown in Fig. 17d. As reported earlier [5], this array resembles the structure of high-pressure γ-Si, drawn in Fig. 17e. This insight led to the novel interpretation of the "stuffed" bixbyite structures reported by Vegas et al. [1] in terms of the *EZKC*. As reported in that paper, the γ-Si(Ge) structure is, in fact, formed by two interpenetrating nets of the high-pressure, high-temperature phase of nitrogen [45] (again, Group 15), in which there are no longer N_2 molecules: instead, the N atoms form a 3D skeleton as shown in Fig. 17e.

A careful comparison of Fig. 17d–f can help to understand the process. Following the 8-N rule, in γ-Si(Ge) (Fig. 17e) each Ge atom forms four similar bonds (2.40–2.48 Å). If we assume that each Si atom accepts one electron, the resulting N (Si^{-1} = Ψ(P)), where Ψ means pseudo, must be three-connected, forming thus the 3D structure of nitrogen (Fig. 17e) which results from the splitting of the two equal nets that were forming the γ-Si(Ge) structure.

This can be clearly seen in Fig. 17f which represents the [VLi(1)] sub-array in β-Li_7VN_4 [1]. The network, Ψ-[BV], as in the III–V compounds, should also be four-connected. However, the four (Ψ-B)-V distances are unequal (3 × 3.40; 1 × 3.91 Å),

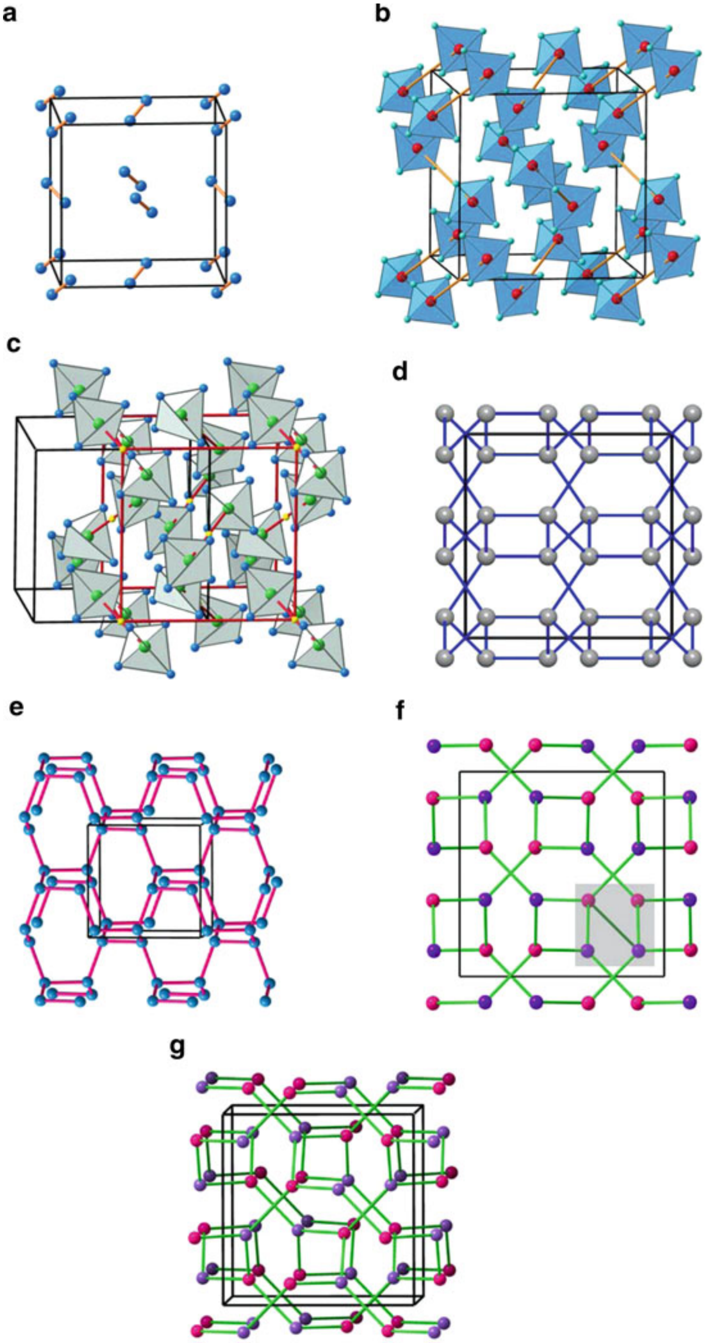
a
b
c
d
e
f
g

indicating that the four-connected network maintains in part the threefold connectivity of the N. This longer contact (3.91 Å) is drawn in the shaded square of Fig. 17f.

Because this is the unique long contact drawn, the reader can appreciate the interweaving of the two N-like networks. What is really surprising is that β-Li_7VN_4 provides evidence of how two interconnected α-N_2 nets, when compressed, lead to the formation of the 3D nitrogen [45]. Expressed in other words, the characteristics of both the molecular and the 3D structures of nitrogen can be recognized in the nitride!

4.1.2 Cu_3WO_4

Further searching revealed the compound Cu_3WO_4 [46] in space group $Pa\bar{3}$. The data are as follows:

W in 8*c* at 0.1170, 0.1170, 0.1170: **Cu** in 24*d* at 0.4044, 0.2457, 0.1376:

O(1) in 24*d* at 0.2193, 0.3016, 0.0891: **O(2)** in 24*d* at 0.4446, 0.4636, 0.1953.

Comparing these figures with the corresponding data for β-Li_7VN_4, it is clear that the W-atom sites correspond with the Li(1) site, and the copper sites are in fair agreement with those for Li(2) – a Cu site at 0.904, 0.254, 0.862 compares with a Li (2) site at 0.885, 0.368, 0.870: there is some significant difference in the *y*-parameter, but this is not major. The two drawings are shown in Fig. 18a, b, where we compare the WO_6 octahedra of Cu_3WO_4 with the Li(1)N_4 tetrahedra of β-Li_7VN_4. The Li(1)–Li(1) distance in β-Li_7VN_4 is 4.47Å, and the W–W distance in Cu_3WO_4 is 3.97Å. Looking at Fig. 18, it is evident that the structure can also be described as a $[WO_6]_2$ body-centred cube with an inscribed Cu_6 icosahedron.

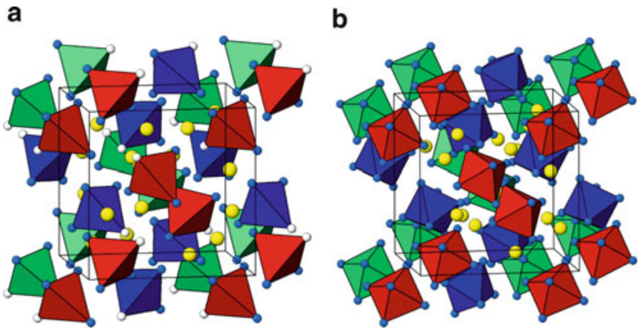

Fig. 18 (**a**) The structure of β-Li_7VN_4 (a = 9.586 Å), represented by Li(1)N_4 tetrahedra at three mean levels: $x = 1$ – *red*; $x = 0.5$ – *blue*; $x = 0$ – *green*. Li(2) atoms – *yellow*. (**b**) The structure of Cu_3WO_4 (a = 9.797 Å) represented by WO_6 octahedra at three mean levels: $x = 1$ – *red*; $x = 0.5$ – *blue*; $x = 0$ – *green*. Cu atoms – *yellow*

Fig. 17 (**a**) The fcc-array of N_2 molecules in α-N_2 at 20 K (a = 5.661 Å). N–N bonds (1.04 Å). (**b**) β-Li_7VN_4 (a = 9.599 Å). Pairs of VN_4 tetrahedra – *blue*, which, when linked, form the same fcc array as the N_2 molecules: V atoms – *red*. (**c**) The same array formed by the Li(1)N_4 tetrahedra – *grey*, but displaced by a/2: Li(1) atoms – *green*. *Small yellow spheres* are drawn at the centre of the Li–Li contacts to help identify the *fcc* cell. (**d**) The four-connected network of the HP phase γ-Si. (**e**) The HT, HP phase of 3D nitrogen. (**f**) The [Li(1)V] network of β-Li_7VN_4 showing its similarity with γ-Si(Ge). It also shows the two interconnected nets as drawn in (**e**): the *dark green diagonal link* drawn in the *grey square* is the V-Li contact. (**g**) Perspective view of the same array as that in (**f**) to show the two N-subnets

4.2 Substructures in the Space Group $Ia\bar{3}$

The site equivalences are given in Table 11 below.

Table 11 Site equivalences between space groups $Pa\bar{3}$ and $Ia\bar{3}$

$Pa\bar{3}$ ($a\ b\ c$: x, y, z)	**$Ia\bar{3}$** ($a\ b\ c$: x, y, z)	**$Pa\bar{3}$** ($-b\ a\ c$: ¼ − y, x − ¼, z + ¼)	**$Ia\bar{3}$** ($a\ b\ c$: x, y, z)
4*a* + 4*b*	8*a*	8*c*	8*a*
8*c*	8*b*	4*a* + 4*b*	8*b*
2 × 8*c*	16*c*	2 × 8*c*	16*c*
24*d*	24*d*	24*d*	24*d*
2 × 24*d*	48*e*	2 × 24*d*	48*e*

4.2.1 Anti-Bixbyite-Type Structure

In the light of what we have already discussed in the earlier paper mentioned above [1], namely, that β-Li_7VN_4 is a "stuffed" anti-bixbyite structure, it is immediately obvious that the anti-bixbyite structure in space group $Ia\bar{3}$, typified by such compounds as Mg_3N_2, Ca_3N_2, Zn_3N_2, Mg_3P_2, Be_3N_2 [47], is also a substructure of β-Li_7VN_4. The equivalent sites are collected in Table 12.

Table 12 Equivalent sites for Mg_3N_2 and β-Li_7VN_4

		Mg_3N_2			β-Li_7VN_4				
Atom	Site	*x*	*y*	*z*	Atom	Site	*x*	*y*	*z*
Mg	48*e*	0.389	0.152	0.382	Li(2)	24*d*	0.380	0.104	0.313
		0.111	0.348	0.118	Li(3)	24*d*	0.130	0.385	0.132
N(2)	8*b*	0.250	0.250	0.250	N(1)	8*c*	0.261	0.261	0.261
N(1)	24*d*	0.500	0.250	0.522	N(2)	24*d*	0.485	0.260	0.479

Drawings (Fig. 19a, b) of the nitrogen-centred N(1)Mg_6 octahedra for Mg_3N_2, together with the N(2)Li(2)$_6$ and N(2)Li(3)$_6$ octahedra of β-Li7VN$_4$, show the virtually identical structures.

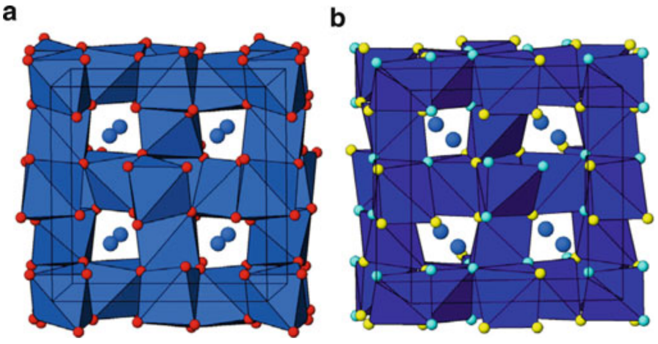

Fig. 19 (**a**) The structure of the anti-bixbyite-type Mg_3N_2 (a = 9.972 Å): N(1)Mg_6 octahedra – *blue*, N(2) atoms – *blue*, Mg atoms – *red*. (**b**) β-Li_7VN_4 (a = 9.6064 Å): N(2)Li(2)$_6$ and N(2)Li(3)$_6$ octahedra – *blue*, N(1) atoms – *blue*, Li(2) atoms – *yellow*, Li(3) atoms – *light blue*

The Mg_3N_2 substructure in β-Li_7VN_4, written as $Li_6[LiV]N_4$, involves only the Li_6N_4 components; the two eightfold sites occupied by [LiV] are absent, and the sites of these in the β-Li_7VN_4 structure correspond with those of the cation vacancies in the 16*c* sites of the ***Ia***$\overline{3}$ space group, as we have already discussed in an earlier paper [1]. If we were to assume the transfer of the six valence electrons of the [LiV] group, one to each of the remaining six Li atoms, these would then become Ψ-Be, leaving [Ψ-HeKr] as the stuffing in the pseudo-compound Ψ-Be_3N_2, with the anti-bixbyite structure, just like in α-Be_3N_2 itself [47].

Moreover, as also discussed in that earlier paper, this 16*c* site is the site of the Si atoms in the high-pressure β-Si phase; so this β-Si structure is yet another substructure of β-Li_7VN_4, and we have already discussed in some detail why this should be so.

4.2.2 The Rare-Earth C-Type Structure

The database for this space group also lists a large number of oxides with the bixbyite-type structure, typified by the C-type rare-earth oxides, e.g. Y_2O_3. The setting chosen by Paton and Maslen [48], with Y in site 8*b* at 0.25, 0.25, 0.25, as opposed to the original Geller setting of Mn in site 8*a* (0, 0, 0) in his determination of the bixbyite structure [49], allows a *direct* comparison between the occupied sites in C-type Y_2O_3 (SG ***Ia***$\overline{3}$) and those of β-Li_7VN_4 in space group ***Pa***$\overline{3}$ (see Table 12). This comparison is shown in Table 13 and Fig. 20a, b to demonstrate in a simple way the *structure/anti-structure* relationship.

Table 13 Corresponding atom sites in Y_2O_3 and β-Li_7VN_4

Y_2O_3 in ***Ia***$\overline{3}$			β-Li_7VN_4 in ***Pa***$\overline{3}$		
Y(1)	8*e*	0.25, 0.25, 0.25	N(1)	8*c*	0.2609, 0.2609, 0.2609
Y(2)	24*d*	0.50, 0.25, 0.533	N(2)	24*d*	0.4850, 0.2600, 0.4790
O	48*e*	0.111, 0.346, 0.122	Li(2)	24*d*	0.1300, 0.3850, 0.1320
		0.389, 0.154, 0.378	Li(3)	24*d*	0.3800, 0.1040, 0.3630

These data simply demonstrate the *structure/anti-structure* relationship. Inspection of Fig. 20a, b seems to indicate that the Y sites, red in Fig. 20a, match the Li(2) and Li(3)

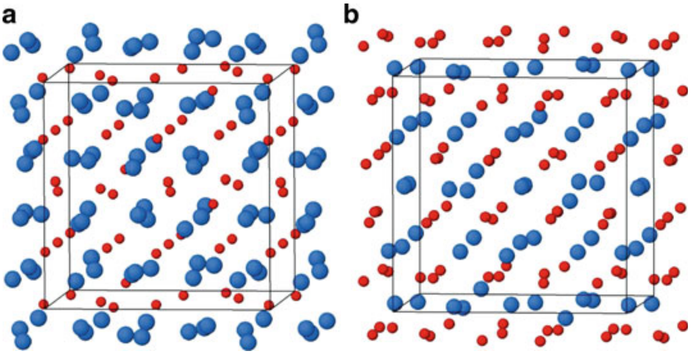

Fig. 20 (**a**) The Y_2O_3 structure viewed near [100]. Y atoms – *red*, O atoms – *blue*. (**b**) The anti-bixbyite structure formed by the Li(2), Li(3) and N atoms of β-Li_7VN_4 (a = 9.606 Å). N atoms – *red*, Li(2) and Li(3) atoms – *blue*

sites (blue in Fig. 20b). This makes sense because if we take the tetrahedron $^{31}[LiN_4] = \Psi\text{-}^{31}Ga$, we obtain a pseudo-atom of the Group 13 (recall the bixbyite-type structure of In_2O_3). Similarly, if we replace Li by Na, we get $^{39}[NaN_4] = \Psi\text{-}^{39}Y$.

4.3 Substructures in Space Group $Fm\overline{3}$

Table 14 shows the Bärnighausen Tree for Case 4 above. As can be seen, there are two branches, *only one of which leads to the lattice sites of β-Li_7VN_4 in space group* $\boldsymbol{P}a\overline{3}$.

However, a search of the database in space group $Fm\overline{3}$ reveals that for all the structures reported, the sites 4*a* and 4*b* are occupied, implying the complete absence of substructures of β-Li_7VN_4 in this space group.

5 The Alpha Phase of $Li_7V^VN_4$

This polymorph, first identified by Niewa et al. [6], is tetragonal ($a = 6.757$, $c = 4.882$ Å, $V = 222.92$ Å^3, S.G. $\boldsymbol{P}4_2/nmc$), and these same authors derived the “Bärnighausen Tree” relating its space group to that of the anti-fluorite-type parent, Li_2O. We show this relationship again in Table 15, although presented somewhat differently.

5.1 Li_6MoN_4, Li_6WN_4, Li_6ZnO_4 and Li_6CoO_4

Other very similar compounds to α-Li_7VN_4 have been reported in the same space group. These are Li_6MoN_4 [50] with $a = 6.673$, $c = 4.925$ Å, $V = 219.3$ Å^3 and Li_6WN_4 [51] of very similar dimensions: clearly, these compounds are Li-deficient, anti-fluorite-type superstructures. We note, however, that Li_7NbN_4 and Li_6MoN_4 are isoelectronic, as are Li_7TaN_4 and Li_6WN_4. Moreover, early work by Juza et al. [52] suggested the probable existence of the compound Li_6CrN_4, which would be isoelectronic with Li_7VN_4.

Li_7VN_4 is then simply a Li-stuffed Li_6CrN_4 structure. In terms of the *EZKC*, one Li atom donates one electron to V to give Ψ-Cr, resulting in the compound $Li_6(\Psi\text{-}Cr)N_4$. In the same way, if we take our parent compound as Li_7NbN_4 and have one Li atom donate an electron to the Nb atom, the result is a skeleton of the type Ψ-[Li_6MoN_4]. Table 16 lists the atom sites of α-Li_7VN_4 and Li_6MoN_4, and Fig. 21a, b shows their structures near the [001] projection.

There are also oxide analogues of these nitrides, Li_6ZnO_4 and Li_6CoO_4, first studied by Hoppe et al. [53, 54].

Table 14 The Bärnighausen Tree for Case 4 above

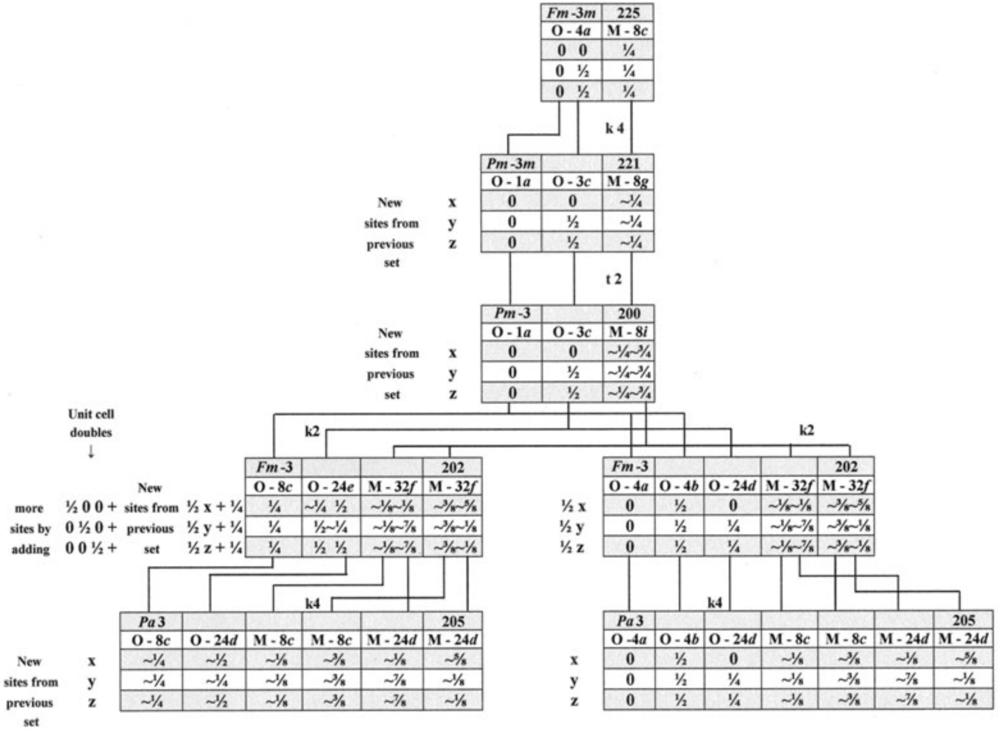

Fm-3*m*	225
O - 4*a*	M - 8*c*
0 0	¼
0 ½	¼
0 ½	¼

New sites from previous set

	Pm-3*m*		221
	O - 1*a*	O - 3*c*	M - 8*g*
x	0	0	~¼
y	0	½	~¼
z	0	½	~¼

New sites from previous set

	Pm-3		200
	O - 1*a*	O - 3*c*	M - 8*i*
x	0	0	~¼~¾
y	0	½	~¼~¾
z	0	½	~¼~¾

more sites by adding: ½ 0 0 + / 0 ½ 0 + / 0 0 ½ +

New sites from previous set

	Fm-3			202
	O - 8*c*	O - 24*e*	M - 32*f*	M - 32*f*
½ x + ¼	¼	~¼ ½	~⅛~⅛	~⅜~⅝
½ y + ¼	¼	½~¼	~⅛~⅞	~⅜~⅛
½ z + ¼	¼	½ ½	~⅛~⅞	~⅜~⅛

	Fm-3				202
	O - 4*a*	O - 4*b*	O - 24*d*	M - 32*f*	M - 32*f*
½ x	0	½	0	~⅛~⅛	~⅜~⅝
½ y	0	½	¼	~⅛~⅞	~⅜~⅛
½ z	0	½	¼	~⅛~⅞	~⅜~⅛

New sites from previous set

	*Pa*3					205
	O - 8*c*	O - 24*d*	M - 8*c*	M - 8*c*	M - 24*d*	M - 24*d*
x	~¼	~½	~⅛	~⅜	~⅛	~⅝
y	~¼	~¼	~⅛	~⅜	~⅞	~⅛
z	~¼	~½	~⅛	~⅜	~⅞	~⅛

	*Pa*3						205
	O -4*a*	O - 4*b*	O - 24*d*	M - 8*c*	M - 8*c*	M - 24*d*	M - 24*d*
x	0	½	0	~⅛	~⅜	~⅛	~⅝
y	0	½	¼	~⅛	~⅜	~⅞	~⅛
z	0	½	¼	~⅛	~⅜	~⅞	~⅛

N(1)	N(2)	Li(3)	V	Li(2)	Li(1)
8*c*	24*d*	8c	8c	24d	24d
0.2609	0.4848	0.1321	0.3722	0.119	0.632
0.2609	0..2597	0.1321	0.3722	0.901	0.1397
0.2609	0.4787	0.1321	0.3722	0.8652	0.1151

β-Li_7VN_4

Table 15 The Bärnighausen Tree relating space groups $\boldsymbol{Fm\overline{3}m}$ and $\boldsymbol{P4_2/nmc}$

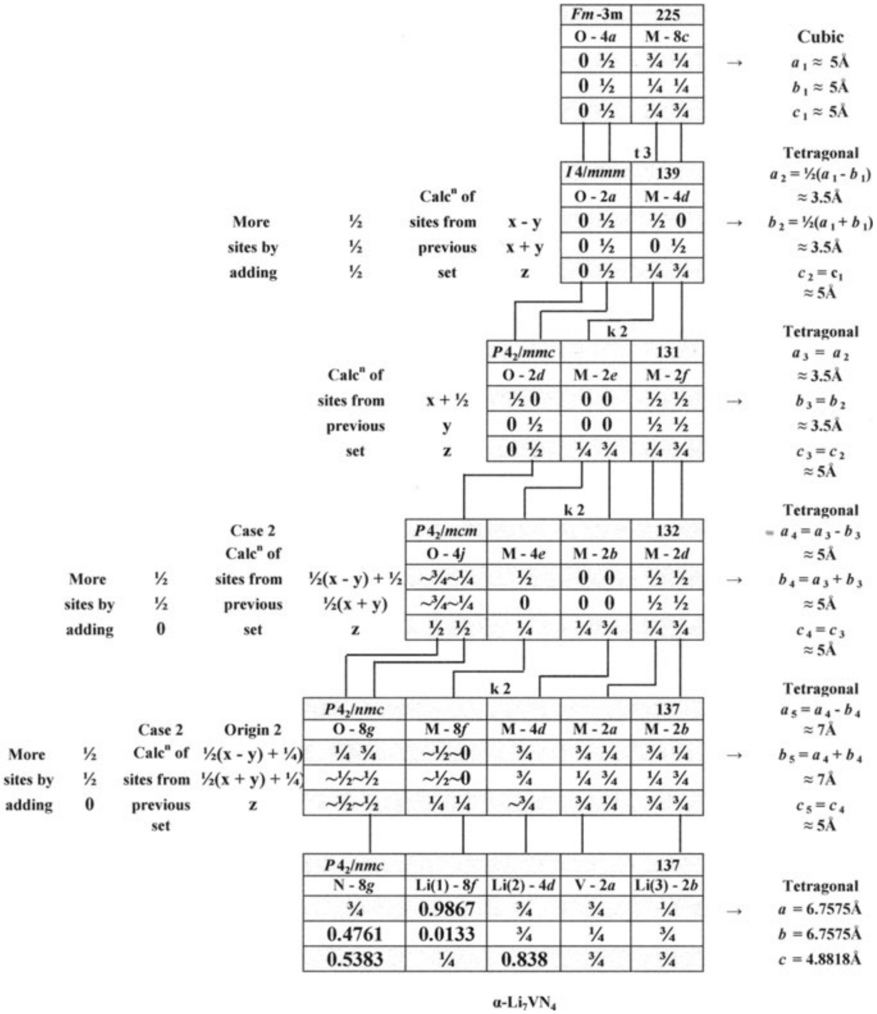

Table 16 Comparison of sites occupancies in the related structures α-Li_7VN_4 and Li_6MoN_4 as represented in Fig. 21

α-Li_7VN_4 $P4_2/nmc$	Wyckoff site	*x*	*y*	*z*	Li_6MoN_4 $P4_2/nmc$	Wyckoff site	*x*	*y*	*z*
V-red	2*a*	¾	¼	¾	Mo	2*a*	¾	¼	¾
Li(1) – grey	8*f*	0.9867	0.0133	¼	Li(1)	8*f*	−0.0368	0.0368	¼
Li(2) – green	4*d*	¾	¾	0.838	Li(2)	4*d*	¾	¾	0.8358
Li(3) – violet	2*b*	¼	¾	¼	Li(3)	Missing	Missing		
N-blue	8*g*	¾	0.4761	0.5383	N	8*g*	¾	0.4761	0.5383

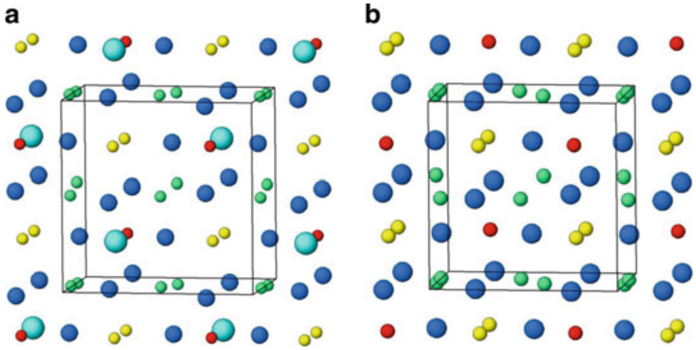

Fig. 21 (**a**) The α-Li_7VN_4 structure viewed near [001]. V atoms – red, Li(1) atoms – green, Li(2) atoms – yellow, Li(3) atoms – light blue, large to indicate that these are missing in the analogue structure of Li_6MoN_4, N atoms – blue. (**b**) The Li_6MoN_4 structure. Mo atoms – red, Li(1) atoms – green, Li(2) atoms – yellow, N atoms – blue. Li(3) atoms are missing

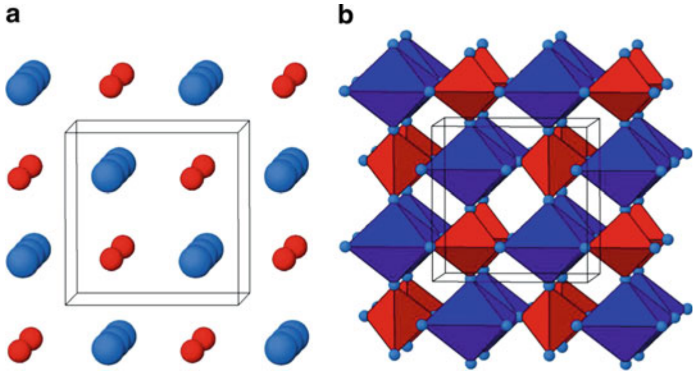

Fig. 22 (**a**) Tetragonal zirconia: Zr atoms – *red*, O atoms – *blue*. (**b**) α-Li_7VN_4: Li(2)N_4 tetrahedra – *blue*, VN_4 tetrahedra – *red*

5.2 Tetragonal Zirconia

Further search for substructures in this same space group yielded the well-known tetragonal zirconia structure [55]. In this structure, the Zr atoms are in site 2*b* and the O atoms in site 4*d*, corresponding to the sites of Li(2) and V, respectively, in α-Li_7VN_4. However, there is almost a factor of four between the volumes of α-Li_7VN_4 and tetragonal zirconia; so once again we have a correspondence between the two Zr atoms and the four O atoms of the zirconia structure [55], on one hand, and the two VN_4 tetrahedra and the four Li(2)N_4 of α-Li_7VN_4, on the other hand. This is shown in Fig. 22a, b.

If we consider the Nb analogue of α-Li_7VN_4, *viz.*Li_7NbN_4, 3 Li atoms can donate an electron to 3 N atoms, converting these to 3 Ψ-O atoms, while the Nb atom can donate an electron to the remaining N atom, giving a total of 4 Ψ-O atoms and a single Ψ-Zr atom: in other words, the pseudo-compound Li-stuffed Ψ-[ZrO_2].

6 Conclusions

We set out to exploit the new data contained in [13] to search for possible substructures within the three reported modifications of the compound Li_7VN_4, and this we have done. We have also attempted a chemical rationalization for these substructures. It now seems obvious that all these interrelationships are implicit in the parent fluorite-type (or anti-fluorite-type) structures.

If we return to the question posed early in this discussion as to “What is a crystal structure”, we now take the view, as quoted earlier, “from the purely crystallographic perspective, a structure is simply a set of occupied sites pertaining to the underlying symmetry of a particular space group, **regardless of the chemical nature of the occupancy**”.

However, the structural relationships, we have described in this work, clearly indicate that these are not merely a geometrical result, but they have chemical sense as revealed by the Zintl–Klemm concept. In this regard, the maintenance of the pseudo-structures of nitrogen, described in Sects. 3.1.1 and 4.1.1, is paradigmatic.

On the other hand, what prompted this investigation was the recent publication of International Tables of Crystallography, Vol. A1 [13], without which it would not have been possible for us to proceed. The very detailed information relating to groups and subgroups contained therein is probably not common knowledge, and accordingly, we express our admiration and thanks to its editors and contributors.

Acknowledgement D.J.M.B and R.L.M put on record their immense gratitude to their respective daughters, Hilary and Lisa, for their help in this work.

References

1. Vegas A, Martin RL, Bevan DJM (2009) Compounds with a “stuffed” anti-bixbyite-type structure, analysed in terms of the Zintl-Klemm and coordination-defect concepts. Acta Crystallogr B 65:11–21
2. Santamaría-Pérez D, Vegas A (2003) The Zintl-Klemm concept applied to cations in oxides. I. The structures of ternary aluminates. Acta Crystallogr B 59:305–323
3. Santamaría-Pérez D, Vegas A, Liebau F (2005) The Zintl-Klemm concept applied to cations in oxides. II. The structures of silicates. Struct Bond 118:121–127
4. Bevan DJM, Martin RL (2008) The role of the coordination defect: a new structural description of four fluorite-related sesquioxide minerals, bixbyite (Mn_2O_3), braunite (Mn_7SiO_{12}), braunite II ($CaMn_{14}SiO_{24}$), parwelite ($Mn_{10}Sb_2As_2Si_2O_{24}$), and their structural relationships. J Solid State Chem 181:2250–2259
5. Niewa R, Zherebtsov D, Leoni S (2003) $Li_3(ScN_2)$: the first nitridoscandate(III) – tetrahedral Sc coordination and unusual MX_2 framework. Chem Eur J 9:4255–4259
6. Niewa R, Zherebtsov D, Hu Z (2003) Polymorphism of heptalithium nitridovanadate(V) $Li_7[VN_4]$. Inorg Chem 42:2538–2544
7. Juza R, Anschuetz E, Puff H (1959) Die Struktur von Li_7VN_4 und Li_7MnN_4. Angew Chem 71:161
8. Juza R, Gieren W, Haug J (1959) Herstellung und Eigenschaften ternaerer Nitride von Vanadium, Niob und Tantal der Zusammensetzung Li_7MeN_4. Z Anorg Allg Chem 300:61–71

9. Vennos D, DiSalvo F (1992) Structure of lithium niobium nitride. Acta Crystallogr C 48:610–612
10. Wachsmann Ch, Jacobs HJ (1992) Darstellung und Struktur des Lithiumnitridotantalats(V) Li_7TaN_4. J Alloys Compd 190:113–116
11. Schnick W, Luecke J (1990) Synthesis and crystal structure of lithium phosphorus nitride Li_7PN_4: the first compound containing isolated PN_4-tetrahedra. J Solid State Chem 87:101–106
12. Bärnighausen H (1980) Group–subgroup relations between space groups. MATCH Commun Math Chem 9:139–175
13. Wondratschek H, Müller U (eds) (2008) International tables for crystallography A1. Kluwer, Dordrecht
14. Hyde BG, Andersson S (1989) Inorganic crystal structures. Wiley, New York
15. O'Keeffe M, Hyde BG (1996) Crystal structures. Mineralogical Society of America, Washington
16. Cromer DT, Mills RL, Schiferl D, Schwalbe LA (1981) The structure of N_2 at 49 kbar and 299 K. Acta Crystallogr B 37:8–11
17. ICSD Inorganic Crystal Structure Database (2010) Fachinformationszemtrum, Karlsruhe (Germany). www version by P. Hewat, ILL Grenoble (France)
18. Villars P, Cenzual K (2010) Pearson's crystal data: crystal structure database for inorganic compounds. ASM International® Materials Park, OH, USA
19. Muller O, Roy R (1971) Synthesis and crystal chemistry of some new complex palladium oxides. Adv Chem Ser 98:28–38
20. Muller O, Roy R (1965) Formation and stability of the platinum and rhodium oxides at high oxygen pressures and the structures of Pt_3O_4, β-PtO_2 and RhO_2. J Less Common Met 16:129–146
21. Haegg G, Schoenberg N (1954) "β-Tungsten" as a tungsten oxide. Acta Crystallogr 7:351–352
22. Kanamatsu K (1986) Stability of the crystal structure of $(Fe,V)_3M$ and (Fe,Ni)M (M = Si, Ge, Sn) and its analysis based on rigid band model. Trans Jpn Inst Met 27:225–232
23. Masse R, Tordjman I, Durif A (1976) Affinement de la structure cristalline du monophosphate d'argent Ag_3PO_4. Existence d'une forme haute temperature. Z Kristallogr 144:76–81
24. Helmholz L (1936) The crystal structure of silver phosphate. J Chem Phys 4:316–322
25. Newsam JM, Cheetham AK, Tofield BC (1980) Structural studies of the high-temperature modifications of sodium and silver orthophosphates, II-Na_3PO_4 and II-Ag_3PO_4, and of the low-temperature form I-Ag_3PO_4. Solid State Ionics 1:377–393
26. Beister HJ, Syassen K, Klein J (1990) Phase transition in Na_3As under pressure. Z Naturforsch B 45:1388–1392
27. Palazzi M, Rémy F (1971) Polymorphism of anhydrous trisodium arsenate and phosphate Na_3AsO_4 and Na_3PO_4-radiocrystallographic study. Bull Soc Chim Fr:2795–2795
28. Pley M, Wickleder MS (2005) Two crystalline modifications of RuO_4. J Solid State Chem 178:3206–3209
29. Burbank J (1974) X-ray study of an osmium oxyfluoride of unknown composition. J Appl Crystallogr 7:41–44
30. Brenchley ME, Weller MT (1994) Synthesis and structures of $M_8(AlSiO_4)_6.(XO_4)_2$, M = Na, Li, K; X = Cl, Mn sodalites. Zeolites 14:682–686
31. Antao SM, Hassan I, Parise JB (2003) The structure of danalite at high temperature obtained from synchrotron radiation and Rietveld refinements. Can Mineral 41:1413–1422
32. Smith-Verdier P, García-Blanco S (1980) Redetermination of the crystal structure of anhydrous zinc metaborate $(Zn_4O)(BO_2)_6$. Z Kristallogr 151:175–177
33. Harrison WTA, Gier TE, Stucky GD (1994) Two lithium chloroberyllo (phosphate/arsenate) sodalites $Li_4Cl(BePO_4)_3$ and $Li_4Cl(BeAsO_4)_3$. Acta Crystallogr C 50:471–473
34. Spry PG, Merlino S, Wang S, Zhang XM, Buseck PR (1994) New occurrences and refined crystal chemistry of colusite, with comparisons to arsenosulvanite. Am Mineral 79:750–762

35. Tettenhorst RT, Corbato CE (1984) Crystal structure of germanite, $Cu_{26}Ge_4Fe_4S_{32}$, determined by powder X-ray diffraction. Am Mineral 69:943–947
36. Spiridonov EM (1987) On the composition of germanite. Dokl Akad Nauk SSSR 295: 477–481
37. Kulakov MP, Balyakina IV (1991) Solid state wurtzite–sphalerite transformation and phase boundaries in ZnSe–CdSe. J Cryst Growth 113:653–658
38. Adams LH, Davis BL (1962) Rapidly running transitions at high pressure. Proc Natl Acad Sci USA 48:983–990
39. Ponomarev VI, Kheiker DM, Belov NV (1970) Crystal structure of tetracalcium trialuminate – the aluminate analogue of sodalite. Kristallografiya 15:918–921
40. Vegas A, García-Baonza V (2007) Pseudoatoms and preferred skeletons in crystals. Acta Crystallogr B 63:339–345
41. Bourdet JB, Fournier JP, Kohlmuller R, Omaly J (1982) A structural study of cadmium yttrium molybdate $CdY_4Mo_3O_{16}$. Acta Crystallogr B 38:2371–2374
42. Sueno S, Clark JR, Papika JJ, Konnert J (1973) Crystal-structure refinement of cubic boracite. Am Mineral 58:691–697
43. Thornley FR, Kennedy NS, Nelmes RJ (1976) Structural studies of boracites: IV. Thermal motion in cubic $Ni_3B_7O_{13}I$ at 77 K. J Phys C 9:681–692
44. Donohue J (1961) A refinement of the positional parameter in α-nitrogen. Acta Crystallogr 14:1000–1001
45. Eremets MI, Gavriliuk AG, Trojan IA, Dzivenko DA, Boehler R (2004) Single-bonded cubic form of nitrogen. Nat Mater 3:558–563
46. Gebert E, Kihlborg L (1969) The crystal structure of a new copper wolfram oxide, Cu_3WO_6. Acta Chem Scand 23:221–231
47. Reckeweg O, Lind C, Simon A, DiSalvo FJ (2003) Rietveld refinement of the crystal structure of α-Be_3N_2 and the experimental determination of optical band gaps for Mg_3N_2, Ca_3N_2 and $CaMg_2N_2$. Z Naturforsch B 58:159–162
48. Paton MG, Maslen EN (1965) A refinement of the crystal structure of Yttria. Acta Crystallogr 19:307–310
49. Geller S (1971) Structure of α-Mn_2O_3, $(Mn_{0.983}Fe_{0.017})_2O_3$ and $(Mn_{0.983}Fe_{0.017})_2O_3$ and relation to magnetic ordering. Acta Crystallogr B 27:821–828
50. Gudat A, Haag S, Kniep R, Rabenau A (1990) Ternaere Nitride des Lithiums mit den Elementen Cr, Mo und W. Z Naturforsch B 45:111–120
51. Yuan WX, Hu JW, Song YT, Wang WJ, Xu YP (2005) Synthesis and structure of the ternary nitride Li_6WN_4. Powder Diffr 20:18–21
52. Juza R, Haug J (1961) Herstellung und Eigenschaften der ternaeren nitride von chrom, molybdaen und wolfram der zusammensetzung Li_9MeN_5. Z Anorg Allg Chem 309:276–282
53. Luge R, Hoppe R (1986) Ein neues cobaltat mit inselstruktur: $Li_6(CoO_4)$. Z Anorg Allg Chem 534:61–68
54. Untenecker H, Hoppe R (1987) Ein neues oxozincat: Li_6ZnO_4. Z Anorg Allg Chem 551:147–150
55. Sham EL, Aranda MAG, Farfán-Torres EM, Gottifredi JC, Martínez-Lara M, Bruque S (1998) Zirconium titanate from Sol–Gel synthesis: thermal decomposition and quantitative phase analysis. J Solid State Chem 139:225–23

Struct Bond (2011) 138: 133–198
DOI: 10.1007/430_2010_38

Concurrent Pathways in the Phase Transitions of Alloys and Oxides: Towards an Unified Vision of Inorganic Solids

Ángel Vegas

Abstract The study of phase transitions is usually restricted to two to three transformations. Examples of such transitions include the $CaF_2 \rightarrow PbCl_2 \rightarrow Ni_2In$ in alloys, the NaCl → CrB → CsCl or the well documented transformation olivine → spinel of the oxides $\boldsymbol{A_2X}O_4$. These transitions, traditionally regarded as partial processes, have prevented the construction of wider structure maps. One of the scarce examples of these maps was reported by Léger and Haines (Eur J Solid State Inorg Chem 34:785–796, 1997) concerning the phase transitions of $\boldsymbol{AX_2}$ compounds (dihalides and dioxides), where increasing the coordination number of the $\boldsymbol{A}$ atom is linked to the pressure increase. The structural information, collected in these maps, is always of interest because it limits the number of possible transition paths which may relate a structure-type into another. However, a careful analysis of the partial phase transitions undergone by different compounds, at high temperature and high pressure, reveals that the partial transitions are not isolated processes but they overlap, forming a long, rational pathway that connects all the structures in a coherent manner. Alloys and their related oxides show a similar trend along their concurrent pathways which complement each other. In this work, the analysis is restricted to the $\boldsymbol{AX_2}$ alloys and their corresponding oxides $\boldsymbol{AX_2}O_4$, and the results demonstrate that there exists a unifying principle that can be inferred through the simultaneous analysis of all the phase transitions involved in the concurrent *structural journeys* carried out by both types of compounds. The $\boldsymbol{AX_2}$ alloys begin the *walk* in the fluorite-type structure, ending in the $MoSi_2$-type structure. In the case of the oxides $\boldsymbol{AX_2}O_4$, their cation arrays follow a concurrent pathway that, starting at the filled fluorite-type structure, ends in the final Sr_2PbO_4-type structure. These structural "*journeys*" also allows for the discovery of several "*missing links*" (*structure types*) which fit into the general sequence and help one understand the whole transitions pathway as a rational process, which takes place simultaneously in the alloys as well as in the cation arrays of the oxides. Very recent works show that alkali metals (Na and K) also join

---

Á. Vegas
Instituto de Química-Física "Rocasolano", CSIC, C/ Serrano 119, 28006 Madrid, Spain
e-mail: avegas@iqfr.csic.es

the *walk*. The extended Zintl–Klemm concept (*EZKC*) and the concept that relates of oxidation–pressure–temperature effects provide a basis for understanding the observed transitions.

Keywords Alloys · Cation arrays · Extended Zintl–Klemm concept · High pressure · Metals · Oxides · Phase transitions

Contents

1 Introduction 135
2 From Fluorite to Spinel: The Structures of Na_2S and Their Oxides, Na_2SO_3 and Na_2SO_4 137
  2.1 The Cation Array of Thenardite (V-Na_2SO_4) and $TiSi_2$: The First “Missing Link” 140
  2.2 Two Parallel Transitions: Olivine → Thenardite → Spinel and $Ni_2In \rightarrow TiSi_2 \rightarrow MgCu_2$ 141
  2.3 A Possible Mechanism for the $Ni_2In \rightarrow TiSi_2 \rightarrow MgCu_2$ Transitions 143
  2.4 The Opposite Way: From Olivine to Fluorite 145
3 The Important Information Contained in Na_2SO_3: Its Comparison with Na_2S 146
  3.1 Na_2SO_3 and the Ni_2Al Alloy 147
  3.2 A Mechanism for the $CaF_2 \rightarrow Ni_2Al$ Transition 150
  3.3 Can the Internal Pressure Be Estimated? 152
  3.4 Na_2SO_2: A Hypothetical Compound with the Anti-Fluorite Structure? 154
4 The Complete *Journey* from Fluorite to the Laves Phases 154
5 Oxidation, Temperature and Pressure 156
6 The Third Missing Link: The Fe_2P Structure 159
  6.1 Description of $BaCl_2$ and Its Relation to the CoSn-Type Structure 161
  6.2 The $BaCl_2$ and $LaCl_3$ Structures 162
  6.3 The Ba Subarray in Hexagonal $BaCl_2$ 164
  6.4 $BaCl_2$: The Cotunnite-Type Phase and Its Relation to the Fe_2P-Type Structure 167
  6.5 Oxides Derived from the Fe_2P Structure: $LiNaSO_4$ and $LiCaPO_4$ 168
7 The High-Temperature Fe_2P → Wurtzite Transition 169
8 The Post-Spinel Structures Under Pressure 170
  8.1 The Structure of Ca_2SnO_4 and Related Compounds 172
  8.2 Extension to Mn_2GeO_4: The Olivine-, Spinel- and Sr_2PbO_4-Type Structures 176
  8.3 Ca_2SnO_4 and the FeB Structure 179
9 The Structure of Ba_2SnO_4 183
  9.1 The Ca_2SnO_4- and Ba_2SnO_4-Type Structures and the Decomposition Processes 185
  9.2 The Phases of CaGe, Ca_2Ge and the $CaGeO_3$ and Ca_2GeO_4 Oxides 186
10 The Question of the Charge Transfer Between Cations: Arguments Accounting for the Structures of the Group 14 Elements 188
11 Conclusions 189
References 193

Abbreviations

bcc sc	Body-centred cubic, simple cubic
bct	Body-centred tetragonal
CN	Coordination number
ELF	Electron localization function

EZKC	Extended Zintl–Klemm concept
hcp fcc	Hexagonal close-packed, face-centred cubic
HP	High pressure
HT	High temperature
LP	Lewis pair
LT	Low temperature
RT	Room temperature
TCTP	Tri-capped trigonal prism

> *… La flamme ne subsiste point sans l'air; donc, pour connaître l'un, il faut connaître l'autre … Donc, toutes choses étant causées et causantes, aidés et aidantes, médiates et inmédiates, et toutes s'entretenant par un lien naturel et insensible qui lie les plus éloignées et les plus différantes, je tiens impossible de connaître les parties sans connaître le tout, non plus que de connaître le tout sans connaître particulièrement les parties.*
>
> *… A flame can not exist without the air; therefore, to understand one, one must comprehend the other.… Thus, since all things affect and are affected, help and are helped, mediate and are mediated, and all is held together by an invisible web which links even the most distant and different things, I hold that it is equally impossible to comprehend the parts without understanding the whole, as it is to comprehend the whole without understanding the parts individually.*
>
> ***Pensées.*** *Blaise Pascal (1623–1662)*

1 Introduction

The similar structural consequences of oxidation and pressure were noted, as early as 1994 [1]. It was deduced from the experimental observation of the pressure-induced CrB → CsCl transition in the BaSn alloy [2]. The unexpected result was that the HP phase of BaSn (CsCl type) was identical to the cation array of the $BaSnO_3$ perovskite. The similarity applies not only to the structure (both cells belong to the space group $Pm\overline{3}m$) but also in the dimensions, with unit cell parameters of both approximately 4.10 Å. The outcome was that the insertion of three O atoms, in the BaSn alloy, produced the same effect as the application of an external pressure. This idea was developed in an extensive review concerning the role of cations in the structures of oxides [3]. It was later confirmed with more than 100 examples of similar structural identities [4].

Although some isolated examples, such as the pairs Ca_2Si/Ca_2SiO_4 and Y_5Si_3/$Y_5Si_3O_{12}F$, had been considered by O'Keeffe and Hyde [5], the importance of the structures analysed by Vegas et al. [3, 4] resides in the observation that the cation subarray, in the oxide, maintains under ambient conditions the structure of the parent alloy in some cases, whereas, in others, the cations adopt the structures of HP phases of the same alloy.

This alternative behaviour was interpreted, in a qualitative way, assuming that the pressure exerted by the O atoms could be proportional to the O-content.

However, this amazing outcome suggested the need of new HP experiments to understand the physical meaning of this challenging phenomenon.

New high-pressure experiments were carried out by in situ synchrotron X-ray diffraction techniques for Li_2S [6], Na_2S [7] and K_2S [8]. Our aim was to corroborate whether the HP phases of these sulphides were isostructural to the cation subarrays of their corresponding oxides (sulphites and sulphates). Na_2S undergoes several phase transitions at HP [7], and Na_2SO_4 has several HT polymorphs [9]. This pair of compounds serves us as an illustrative guide, although other oxides, such as Na_2SO_3, will also be considered.

Under ambient conditions, Na_2S is anti-fluorite, undergoing the double transition anti-fluorite (CaF_2) → anti-cotunnite (anti-$PbCl_2$) → Ni_2In type at high pressures [7]. This sequence follows the trend of other fluorite-like compounds [10]. The importance of this result is that the final HP phase (Ni_2In type) corresponds to the cation-array structure of the HT phases of Na_2SO_4, which in turn has the olivine-type structure.

It should be emphasized here that in agreement with the topological analysis carried out by Blatov and co-workers [11–13], the cation array of olivine (***P***nma) is erroneously assigned to the Ni_2In type (***P***6_3/mmc). In fact, of the three HT phases of Na_2SO_4 [9], only one is strictly olivine-like (***P***nma) and only one is strictly Ni_2In type (***P***6_3/mmc). These similarities have been discussed in several articles [4, 7, 14] and will also be discussed below. They are significant because they connect with the well-known olivine → spinel transition, occurring at very high pressures, for compounds like Mg_2SiO_4 and Fe_2SiO_4, among others. It should be emphasized that the equivalent transition Ni_2In → Cu_2Mg has never been reported for the alloys.

The olivine → spinel transition has also been reported for Na_2MoO_4, a compound which, like Na_2CrO_4, is isostructural to the olivine-like, HT phase of Na_2SO_4 (***P***nma). The importance of these relationships is greater if it is noted that Na_2MoO_4 does not undergo the direct olivine → spinel transition but undergoes a double transition involving an intermediate phase which is isostructural to the room-temperature phase of Na_2SO_4 (***F***ddd), known as the mineral thenardite. Thus, Na_2MoO_4 undergoes the transitions **spinel** → **thenardite** → **olivine** at temperatures of 873 K and 913 K, respectively [15].

Because the intermediate phase (thenardite type) is coincident with the room temperature phase of sodium sulphate (V-Na_2SO_4), Na_2MoO_4 may be viewed as a bridge connecting the binary structures CaF_2 and $MgCu_2$, as well as oxides like HT-Li_2SO_4 (anti-fluorite) with the Na_2MoO_4 (spinel-type) structure. It should be added that the Na_2S subarray of thenardite (V-Na_2SO_4) was first identified as $TiSi_2$ type [11–13], a phase which has not yet been found for the sulphide Na_2S [14].

This means that, in the same manner that the thenardite-type structure is the intermediate step in the olivine → spinel transition, a similar transformation might occur in the Ni_2In → Cu_2Mg transition through the intermediate $TiSi_2$, i.e. Ni_2In → $TiSi_2$ → Cu_2Mg. It has also been reported [16] that, at more elevated pressures, spinels transform into other structure types, like Ca_2SnO_4 and Ba_2SnO_4, which finally decompose into a mixture of phases.

All these results show that, up to now, all these phase transitions, either in alloys or in oxides, have been regarded as partial, isolated processes (involving only one to two steps) and also that the behaviour of the alloys M_2X has not been correlated with that of the corresponding M_2XO_4 oxides. However, when all the structures are viewed from a wider perspective, one can discover unexpected bridges, especially when the transitions of alloys and oxides are examined in a concerted way.

The aim of this study is to travel through all the structures, starting in the fluorite and finishing in the decomposition process. The structures will be analysed in the light of the oxidation–pressure equivalence, considering at the same time that the HT is opposite to the application of pressure and that opposite transitions can also occur. In some cases, the cation arrays will be explained in terms of the *EZKC* [14] to put all the structures under a common basis.

Such a complete study, including the whole transitions, has not been reported previously. It is really a hard task. However, the discovery of the $TiSi_2$ structure in thenardite [11, 14] as well as the structure-type formed by the Na_2S subarray in Na_2SO_3 induced us to think that these arrays could be the *missing links* in the complete *structural route* of Na_2S under pressure and alerted us to the possibility that other *structures* could appear. This allows the assembling of the pieces to form the complete chain going from the CaF_2 type to the $MgCu_2$ type, or even to the cation array of the final ternary phase Ba_2SnO_4.

Many of the compounds described in this work were the object of individual studies. Others were analysed in the frame of phase transition studies, such as the HT study on Na_2SO_4 [9] and the double transition *spinel → thenardite → olivine* in Na_2MoO_4 [15]. We must add the HT, HP studies on Mn_2GeO_4 which inform us about the opposite transitions spinel → olivine at HT and also of the spinel → Sr_2PbO_4-type transition at HP [17–19]. And finally, we will examine the compound Ca_2GeO_4 [20, 21], which at HT transforms into a filled wurtzite, whereas under pressure converts into the Ba_2SnO_4 type, a transition that also conforms to the principles discussed here.

When all these partial transitions are put together, and the "missing links" are inserted in the path, the apparent lack of connection between some phase transitions disappears, obtaining a global view of the process which, beginning either in the wurtzite or fluorite structures, ends with a "programmed" decomposition of the final Sr_2PbO_4- and Ba_2SnO_4-type phases [16].

2 From Fluorite to Spinel: The Structures of Na_2S and Their Oxides, Na_2SO_3 and Na_2SO_4

At ambient conditions, Na_2S is anti-fluorite [22], undergoing the reversible transitions anti-fluorite → anti-cotunnite ($PbCl_2$) type → Ni_2In type at about 7 and 16 GPa, respectively [7]. The three experimentally observed structures of Na_2S are illustrated in Fig. 1.

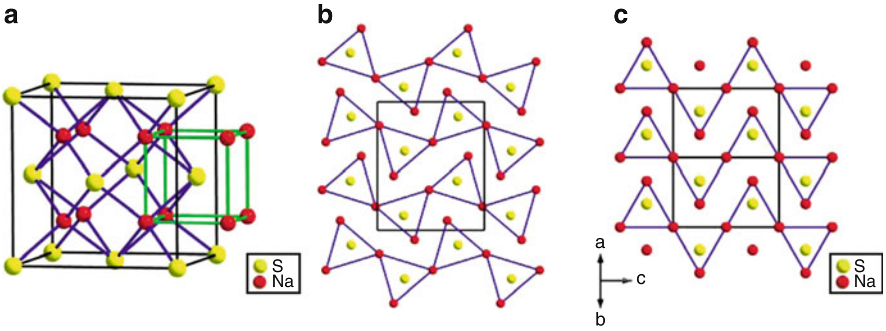

Fig. 1 The three structures of Na_2S. S (*yellow*), Na (*red*). (**a**) The anti-fluorite structure stable at ambient conditions. (**b**) The anti-cotunnite (anti-$PbCl_2$) structure, stable at 7 GPa. (**c**) The Ni_2In-type structure obtained at 16 GPa. In (**b**) and (**c**), *blue lines* connect the Na atoms forming the TCTP centred by the S atoms

As it has been discussed above, it has been suggested [4, 14] that the transitions *Fluorite* → *Cotunnite* → *Ni_2In* might continue onward to reach the structure of the cubic Laves phases (*Ni_2In* → *$MgCu_2$*). The reason for this assumption is that, even if never observed in alloys, this transition is implicit in the well-known *olivine (Ni_2In-related)* → *spinel ($MgCu_2$)* transition. The only theoretical study on this possible Na_2S phase predicts [23] the unstability of the $MgCu_2$-type structure, even at pressures of 1 Mbar.

The relationships between the phases of Na_2S and Na_2SO_4 have been widely discussed [4, 7, 14]. However, we intend to delve more deeply into these relationships by discussing them in the framework of the whole set of structures involved in the complete pathway CaF_2 type → $MgCu_2$ type. All these structures are collected in Scheme 1 (see below) which contains the structures of the binary alloys as well as those of corresponding oxides. Our discussion will begin with the structure of thenardite (V-Na_2SO_4) which is the stable phase under ambient conditions.

Within the concept that relates oxidation and pressure, probably, the most unexpected feature is that the Na_2S subarray of thenardite ($TiSi_2$ type) does not correspond to any of the three HP phases of Na_2S [7]. However, it has been reported [9] that, by increasing temperature, thenardite (V-Na_2SO_4) undergoes the following transitions:

$$\begin{array}{lllll}\text{Thenardite } \mathbf{V}\text{-}(F\text{ddd}) & \rightarrow \mathbf{III}\text{-}(C\text{mcm}) & \rightarrow \mathbf{II}\text{-}(P\text{nma}) & \rightarrow \mathbf{I}\text{-}(P6_3/\text{mmc}) \\ \qquad\qquad\quad \text{TiSi}_2 & \quad \text{CrVO}_4\text{-type} & \quad \text{olivine-type} & \quad \text{Ni}_2\text{In-type}\end{array}$$

The three HT phases of Na_2SO_4 are related to the olivine structure and, in the same manner, their Na_2S subarrays are related to the Ni_2In alloy [5], although it should be remarked that only the **II**-phase is olivine-like and also that only the hexagonal **I**-phase is strictly of the Ni_2In type. This feature is especially important because the I-phase is the only phase whose Na_2S substructure is fully coincident

Structure-type	Alloys	Filled Blendes Filled fluorites	Filled Wurtzites
Fluorite (CaF_2)	Li_2S, Na_2S Na_2Se,Ag_2S	CsLi(CrO_4),CsLi(MoO_4) $LiNaSO_4$ HT-Li_2SO_4 (Fluorite)	Ca_2GeO_4, CaSiO4$_2$ $KLiSO_4$, $KLiBeF_4$
↓			
?	Ni_2Al	Na_2SO_3,K2SO$_3$, HT-$Cs_2(SO_4)$	Na_2SeO_3
Fe_2P	$BaCl_2$		$LiCaPO_4$, $LiNaSO_4$
↓			
Cotunnite $PbCl_2$	Li_2S, Na_2S, Rb_2S, Ag_2S, $BaCl_2$	$CsLiCrO_4$, $KLiSO_4$ Cs_2SO_4, K_2SO_4	Na_2SO_4, Ag_2SO_3 Ca_2SiO_4
↓			
Ni_2In	Na_2S, K_2S Rb_2S	HP-Li_2SO_4, HT-Na_2SO_4 HT-K_2SO_4, $KLiSO_4$ HP-CsLiCrO4	*olivines* HT-Na_2MoO_4 HT-Ca_2GeO_4, Mn_2GeO_4 HT-Ca_2SiO_4,
↓			
$TiSi_2$	Rb_2S ?	Na_2SO_4	HT-Na_2MoO_4 Na_2SeO_4
↓			
Laves phases $MgCu_2$	FeMoGe VCoSi $Ge_{0.45}MnNi_{1.55}$ Ψ-Mn_2Ge		*spinels* Na_2MoO_4 HP-Mn$_2$GeO4
↓			
Sr_2PbO_4 SrPb +Sr (CuAu +Sr)	CaPb is CuAu-type		Ca_2SnO_4 HP-Mn_2GeO_4
↓			
$MoSi_2$			Ba_2SnO_4 HP-Ca_2GeO_4
↓			↓ at HP
			Decomposition (see Table 4)

Scheme 1 This scheme contains all the phase transitions undergone by the AB_2 alloys and the related oxides AB_2O_4 at high temperatures or pressure. Partial transitions overlap producing

with the hexagonal HP phase of Na_2S (Ni_2In type). Both structures (sulphide and sulphate) belong to the space group ***P***6_3/mmc [7].

The thermal behaviour of V-Na_2SO_4 has been interpreted [14] in the light of the *oxidation–pressure relationship* [1, 24]. According to this idea, the pressure exerted by oxygens could depend on the O contents. Thus, in thenardite, with four O atoms inserted into Na_2S, cations adopt the $TiSi_2$-type structure. It is worthy of mention that the $TiSi_2$ structure contains fragments and features of cubic Laves phases [4, 7]. It seems that four O atoms produce an internal pressure which is not high enough to attain the $MgCu_2$-type structure, characteristic of spinels.

Consequently, the thenardite structure could be regarded as an intermediate step in the olivine → spinel transition [14]. Thus, when thenardite is heated, the pressure is partly released and the cations adopt the structures of lower pressure phases, e.g. those found in the olivine-like structure (Ni_2In type) of III-, II- and I-Na_2SO_4.

The lack of coincidence of the cation array of thenardite with any known structure of Na_2S was interpreted by Vegas et al. [14] as an indicative of the formation of an intermediate structure between cotunnite and Ni_2In type. However, such an assumption requires the previous identification of the structure type that forms the cations in thenardite, to rationalize its structure in the framework of our concept relating *oxidation and pressure* [1, 24].

2.1 *The Cation Array of Thenardite (V-Na_2SO_4) and $TiSi_2$: The First "Missing Link"*

A wide search in the crystallographic databases allowed us to find that the structure of the Na_2S subarray of thenardite V-Na_2SO_4 (***F***ddd) was of the $TiSi_2$ type [14]. At that time, we were not aware that this structural similarity had been previously reported by Blatov et al. [11–13].

An interesting question is whether the $TiSi_2$-type structure, formed by cations in the oxides Na_2SO_4, Na_2MoO_4 and Na_2CrO_4, could also be stable for the alkali sulphides. This phase was not observed in the high-pressure experiments carried out by us on Na_2S [7]. However, further theoretical calculations [23] predicted the existence of a stable ***F***ddd phase for the analogue Rb_2S. Although this phase was not identified, the coincidence with the space group of thenardite led us to identify

Scheme 1 (continued) altogether the "structural journey" described along this chapter. The journey begins in the fluorite structure ending in the $MoSi_2$-type structure which decomposes at more elevated pressures. Column 1 contains the structure types involved in the transitions. In column 2 are collected all the binary compounds AB_2 that undergo the partial transitions. Columns 3 and 4 contain the corresponding oxides AB_2O_4 whose cation arrays undergo transitions similar to those of column 2. Column 2, on the one hand, and columns 3 and 4, on the other hand, build the two concurrent pathways of the phase transitions followed by alloys and oxides and which we have denoted as "Structural Journeys"

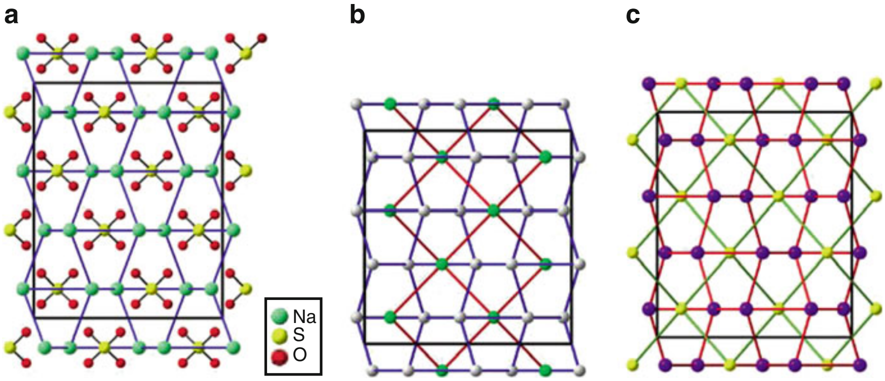

Fig. 2 (**a**) The structure of V-Na_2SO_4 (thenardite) showing its similarity with that of $TiSi_2$ (**b**). In thenardite, the Na and S atoms are represented by *green* and *yellow spheres*, respectively. The O atoms (*red spheres*) are bonded to S atoms to identify the SO_4 groups. In $TiSi_2$, the Si and Ti atoms are represented by *grey* and *green spheres*, respectively. The Ti atoms, connected by *red lines*, form a *diamond*-like network drawn in Fig. 4. (**c**) The $TiSi_2$-type structure predicted for Rb_2S. *Purple* and *yellow spheres* are Rb and S atoms, respectively. The adamantane structure of S atoms is drawn with *green lines*

the aristotype $TiSi_2$ [11–14], whose structure is drawn in Fig. 2 together with those of V-Na_2SO_4 and Rb_2S (all of them ***F***ddd).

The structural coincidence of thenardite (V-Na_2SO_4) and Rb_2S provides a new example of how HP phases of lighter elements appear as stable phases, under ambient conditions, for heavier elements of the same group. Thus, if the $TiSi_2$-type structure is predicted for Rb_2S at relatively low pressures, the same structure should be obtained at higher pressures for Na_2S. Consequently, the Na_2S subarray of thenardite might well be regarded as a Na_2S alloy (of the $TiSi_2$ type) which is stabilized by the pressure exerted by the O atoms.

2.2 Two Parallel Transitions: Olivine → Thenardite → Spinel and Ni_2In → $TiSi_2$ → $MgCu_2$

The discussion in the above subsection indicates that the $TiSi_2$-type structure might well be an intermediate step in the Ni_2In → $MgCu_2$ transition in the same manner that thenardite could be an intermediate phase in the olivine → spinel transition.

Interestingly, the double transition **spinel** → **thenardite** → **olivine** has been observed in Na_2MoO_4, as shown in Scheme 1. This compound, spinel type at ambient conditions, transforms to thenardite at 873 K which then converts into the olivine structure at 913 K [15]. The equivalent $MgCu_2$→ $TiSi_2$ → Ni_2In transitions have not been reported so far. However, theoretical calculations are in progress to see whether this double transition could take place in any binary AB_2 compound.

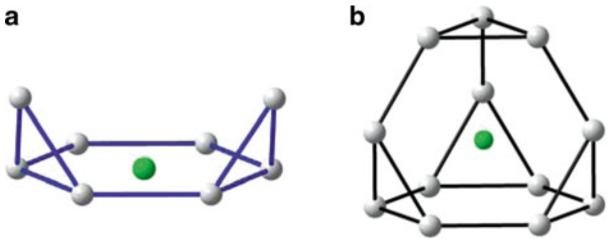

Fig. 3 (**a**) The Si_8 group extracted from the Si array in $TiSi_2$. The Ti atoms (*green*) are centering the hexagons of the graphite-like layers. (**b**) The $MgCu_{12}$ truncated tetrahedron existing in both Laves phases ($MgCu_2$) and spinels (Mg_2SiO_4). The Mg atoms (*green*) centre the Cu_{12} polyhedra

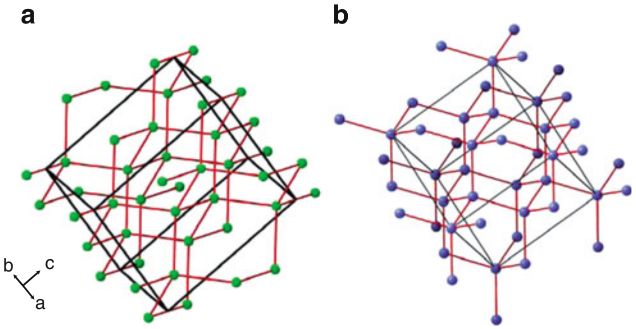

Fig. 4 (**a**) The *diamond*-like array of Ti atoms in $TiSi_2$. (**b**) The same array formed by the Si atoms in the spinel Mg_2SiO_4

Before anything else, the $TiSi_2$-type structure will be described briefly (Fig. 2b). It consists of graphite-like layers of Si atoms (Na atoms in thenardite) whose Si_6 hexagons are centred by the Ti atoms (S atoms in thenardite). The Si and the Ti atoms in $TiSi_2$ (Na and S atoms in thenardite) complete altogether hexagonal close-packed layers (*hcp*). The Ti subnet (green spheres) is four-connected, forming a distorted diamond-like network, represented separately in Fig. 4a. Surprisingly, this network is the same as that formed by the *X* atoms (Si atoms) in spinels, for instance in Mg_2SiO_4. Remember that the Si atoms occupy the centre of the Mg_{12} truncated tetrahedron, as shown in Fig. 3b. Stated in other words, in a hypothetical phase transition $TiSi_2 \rightarrow MgCu_2$, the adamantane structure of the Ti subnet in $TiSi_2$ would remain unaltered in the $MgCu_2$ structure, as it is shown in Fig. 4.

The *hcp*-layers formerly described are perpendicular to the *c* axis and are stacked in a *…ABCDABCD…* sequence. When Si atoms of two adjacent layers are connected, one can identify fragments (Fig. 3a) of the complete truncated tetrahedra $MgCu_{12}$ (Fig. 3b). Those fragments contain 8 of the 12 Si atoms which form the truncated tetrahedron existing in both the cubic Laves phases ($MgCu_2$ type) and spinels [5].

2.3 A Possible Mechanism for the Ni_2In → $TiSi_2$ → $MgCu_2$ Transitions

Finding a topological mechanism for the Ni_2In → $TiSi_2$ → $MgCu_2$ transitions is a difficult task. However, we have discovered new structural relationships between both the Ni_2In and the $TiSi_2$ structures, which deserve a special discussion that is presented next.

It has been reported [14, 24] that the hexagonal Ni_2In-type structure can be regarded as a superstructure of the AlB_2 type (MgB_2). In this structure, both graphite-like ($\mathbf{6^3}$ planar nets) and *hcp* ($\mathbf{3^6}$) layers alternate along the *c* axis, as shown in Fig. 5a. Hereafter, these layers will be denoted as **G** (graphite-like) and **H** (hexagonal).

In AlB_2, the **G** layers are formed by only B atoms, whereas in Ni_2In they are formed by both Ni(2) and In atoms, producing in this way a doubling of the *c* axis of the AlB_2 unit cell (Fig. 5a). The H layers are then formed by the Ni(1) atoms. It is worthy of mention that the **G** and **H** layers are complementary in such a way that the atoms of the **H** layer are capping the centre of the graphene hexagons. Thus, compression of either the AlB_2 or the Ni_2In structures, along the *c* axis, would result in the formation of a denser, hexagonal close packed (*hcp*) layer (**G** + **H**) stacked in the …*AAAA*… sequence. These layers are identical to those of $TiSi_2$, although in this last case they are stacked in the …*ABCDABCD*… sequence. Such a filled hexagon (**G** + **H**) is drawn in Fig. 3a and one complete layer is drawn in Fig. 5c.

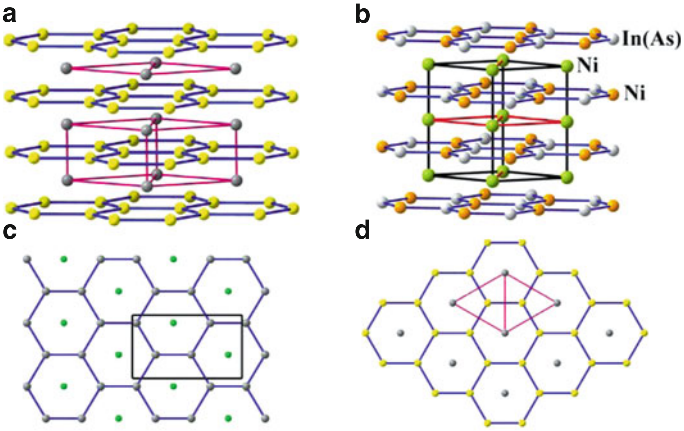

Fig. 5 (**a**) The structure of AlB_2 showing the **G** (boron, *yellow* atoms) and **H** (aluminium, *grey* atoms) layers. (**b**) The Ni_2In-type structure to illustrate the intergrowth of **G** (NiIn) and **H** (Ni) layers. Recall that this structure is the same than that of Fig. 6b. (**c**) An isolated (**G** + **H**) layer which forms the $TiSi_2$ (*C*54) structure. Both the Si (*grey spheres*) and Ti atoms (*green spheres*) are coplanar and are projected onto the *ab* plane. Compare with Fig. 2b. (**d**) The structure of AlB_2 projected on the *ab* plane to show the similarity with the (**G** + **H**) layers

Thus, external pressure and/or low temperatures would favour the formation of the mixed (**G** + **H**). This agrees with the experimental conditions at which the thenardite-like structure of Na_2MoO_4 is formed. Recall that Na_2MoO_4 spinel type at RT undergoes the **spinel** → **thenardite** → **olivine** transitions by increasing temperatures. Consequently, if the olivine-like phase is cooled, which is equivalent to the application of pressure, the thenardite-like structure is formed [15], that is, both the G and H layers would collapse into the (**G** + **H**) layers (Fig. 5c). This also agrees with the behaviour of thenardite itself, i.e. the high O contents stabilize the $TiSi_2$-type array of Na_2S [4, 14], but at high temperature the thenardite → olivine transition takes place. As discussed above, at higher temperatures the hexagonal Ni_2In-type structure is formed by the Na_2S subarray in I-Na_2SO_4 [9].

The mineral sinhalite, $AlMgBO_4$, can also be discussed in this context. Its structure was reported from a natural sample [25], but it was also synthesized [26] under hydrothermal conditions, at pressures ranging from 20 to 80 kbar and temperatures of 1,473 K. Sinhalite belongs to the olivine family (***P***nma), with Al and Mg atoms at the 4*a* and 4*c* sites, respectively. It must be recalled that the olivine structure is an orthorhombic distortion of both the hexagonal Ni_2In-type array (***P***6_3/mmc) and the MgB_2-type structure. By comparing sinhalite with the Ni_2In-type structure (Fig. 5b), one sees that the distorted graphite-like layers of sinhalite, formed by B and Mg atoms, alternate with $\mathbf{3^6}$ planar nets of Al atoms. An admitted rule is that, within a group of the *Periodic Table*, the structures of the heavier elements correspond to the high-pressure phases of the lighter ones. Thus, if in sinhalite, $AlMgBO_4$, the B atom was replaced by another Al atom, one would obtain the formula of spinel, $MgAl_2O_4$. Thus, a greater Al content (Al is heavier than B) would produce a phase stable at a higher pressure, such as spinel $MgAl_2O_4$ itself. The conclusion is that the olivine → spinel transition can also be induced by inserting heavier elements.

We must recall here that the silicon nitride Si_3N_4 (isoelectronic to $MgAl_2O_4$) transforms into a cubic spinel at above 150 GPa and temperatures exceeding 2,000 K [27]. The possible stability of an olivine-like structure for this nitride has also been explored from theoretical calculations [28]. If this olivine-like phase could exist, then the model of the graphene layers (**G**) of silicon would become chemically meaningful, as these layers would be graphene layers of elemental silicon.

Another aspect that merits attention and could be intimately related to the olivine → spinel transition is the existence of the so-called inverse spinels. An enormous amount of literature has been written to try to interpret the mixing of the so-called ***A*** and ***B*** atoms, occupying partially the two sites, 8*b* and 16*c*, reserved for cations. Although the existence of inverse spinels has been mostly justified in terms of both size and crystal field effects, we believe that the stabilization of different A_2B alloys, with variable occupancy of the sites, could play an important role. This possibility, which has not been considered so far, merits to be explored in the future. In this respect, the formation of a thenardite-like structure as an intermediate phase could account for many of these features.

2.4 The Opposite Way: From Olivine to Fluorite

Until here, we have dealt with the olivine → spinel transition path. Now we will discuss the phases located on the upper row of Scheme 1, i.e. the phases existing in the olivine → fluorite path.

We have seen that Na_2SO_4 has three HT polymorphs [9]. Although the three phases, i.e. **III**-(***C***mcm, olivine-related) (463 K), **II**-(***P***nma, olivine-like) (493 K) and **I**-Na_2SO_4 (***P***6_3/mmc) (521 K), are all related to olivine [4, 7, 14], we will restrict our comments to the hexagonal phase I-Na_2SO_4 whose Na_2S subarray is isostructural to the hexagonal HP phase of Na_2S itself (Ni_2In type) [7] (compare Fig. 1c and Fig. 5b).

As stated above, the pressure-induced thenardite → spinel transition involves the simultaneous $TiSi_2$ → $MgCu_2$-type transition in the cation arrays. This transformation clearly illuminates that the structure of thenardite is midway between olivine and spinel [14]. For this reason, when thenardite is heated, the internal pressure exerted by oxygens is released, giving rise to the olivine-related structures of the III, II and I phases, with the simultaneous $TiSi_2$ → Ni_2In transition of the Na_2S subarray. The exact coincidence of both the structure of I-Na_2SO_4 and that of HP-Na_2S (both ***P***6_3/mmc) is shown in Fig. 6.

In this context, one would expect that, at higher temperatures (equivalent to lower pressures), I-Na_2SO_4 could further transform into a β-K_2SO_4 type (with the anti-cotunnite structure) (Fig. 1b), following the inverse pathway of Na_2S under pressure (Fig. 1). There is at present no experimental evidence of this transition in Na_2SO_4, but the transformation occurs in the ternary sulphate $KLiSO_4$ above 948 K [29] (see Scheme 1). A comparison of the K_2SO_3 and K_2SO_4 structures is expected to provide new insights about these transitions. We discuss it below in Sect. 5.

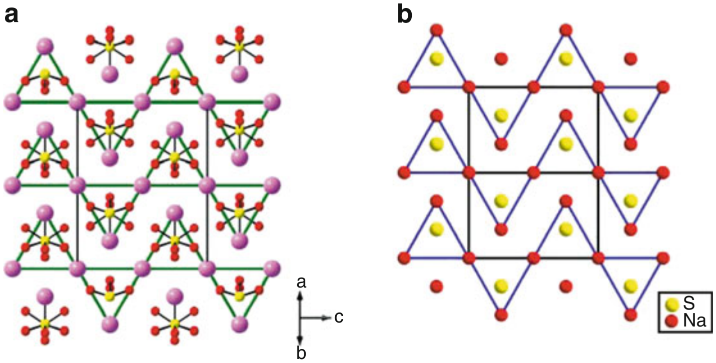

Fig. 6 The structures of I-Na_2SO_4 (**a**) and that of the HP-Na_2S (**b**) projected on the (110) plane of the hexagonal (***P***6_3/mmc) cells, showing the identical arrangement of both Na_2S arrays. The figure emphasizes the Na_6 trigonal prisms which are filled by S atoms (*yellow spheres*) in Na_2S (**b**) and by (SO_4) groups in Na_2SO_4 (**a**), where the rotational disorder is made evident

Following the above reasoning, it is plausible that at higher temperatures some compounds could reach the Ca_2F-type structure (Fig. 1). The reader can find examples of such transitions in Scheme 1, as well as in reference [14]. Although this transformation is not to be expected in Na_2SO_4, the anti-cotunnite → anti-fluorite transition has been observed in the alloys Ag_2S [30] and $BaCl_2$ [31].

It should be remarked that compounds such as $LiCs(CrO_4)$, $LiCs(MoO_4)$ and $LiCs(WO_4)$ collected in Scheme 1 do not transform, when heated, into an anti-CaF_2 structure. Instead, cations form a stuffed zincblende structure, in which the Li atoms together with the Cr (Mo, W atoms) form a blende-type skeleton. The bigger Cs atoms, on the contrary, form a rocksalt array with the same Cr atoms [30]. In contrast, a different behaviour is shown by the structures of Li_2SO_4 in the pressure–temperature space. The compound is phenacite-like at ambient conditions, but at 848 K it transforms into the anti-fluorite structure [32]. Hence, at HT, the Li_2S subarray recovers the anti-fluorite structure of Li_2S itself [7]. In this context, we refer the reader to the article of Vegas, Martin and Bevan [33] to see how the blende-type structure is implicit in fluorite if we assume the existence of resonance structures in inorganic compounds.

In connection with this, it is worth remarking that at 723 K and 7.2 GPa, Li_2SO_4 adopts the orthorhombic structure of III-Na_2SO_4 (***C***mcm) [34]. This feature is, in our opinion, of great interest because it provides evidence about the olivine → anti-fluorite transition. Although unobserved in Na_2SO_4, it takes place in the corresponding lithium compound, passing through the intermediate phenacite-like structure. Could phenacite then be considered as a first missing link?

In this respect, it should be stressed that a direct *thenardite* (***F***ddd) → *cotunnite* (***P***nma) transition occurs in Na_2SeO_4 (Scheme 1). However, the intermediate Ni_2In type, existing in Na_2SO_4, has not been detected in the analogue Na_2SeO_4. As mentioned above, another interesting example is provided by the room temperature phase of $CsLi(CrO_4)$ (cotunnite-like, ***P***nma), which undergoes the transition cotunnite → olivine (***P***nma) at 427 K, and a further olivine → cubic ($\boldsymbol{F}4\bar{3}m$) at 573 K (see Scheme 1) [30]. The cubic phase is, in fact, a Cs-filled zincblende structure.

3 The Important Information Contained in Na_2SO_3: Its Comparison with Na_2S

In the former section, we have been concerned with the phases of Na_2SO_4. However, in Scheme 1 one can see a big question mark (**?**) situated midway between the CaF_2 and the cotunnite structures. To understand the insertion of this mark, we must recall that the internal pressure should be proportional to the oxygen contents [3, 4]. When the O-content decreases, as in Na_2SO_3, a lower internal pressure should be expected and, consequently, the Na_2S subnet should form a structure characteristic of lower pressure phases of Na_2S. Thus, any of the two HP phases (Ni_2In, cotunnite type), or even the anti-fluorite, should be appropriate structures in Na_2SO_3. However, the analysis of its structure reveals that the Na_2S

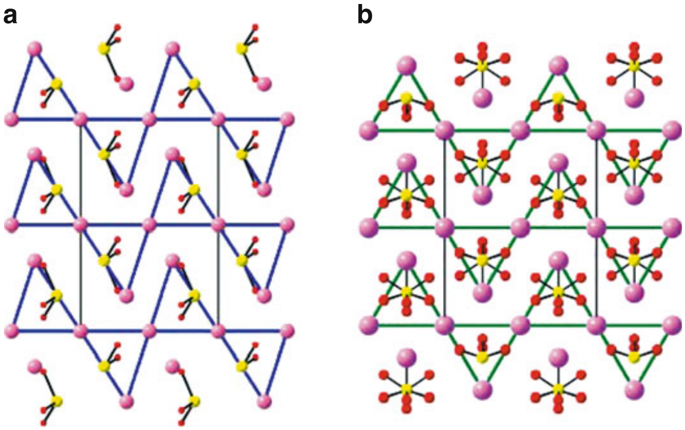

Fig. 7 (**a**) The trigonal structure ($\boldsymbol{P}\bar{3}$) of Na_2SO_3, projected on (110) showing the distorted trigonal prisms of Na atoms (*violet spheres*) and the SO_3 groups, displaced from the centre of the trigonal prisms. (**b**) The hexagonal structure ($\boldsymbol{P}6_3$/mmc) of I-Na_2SO_4 (Ni_2In type) to see the analogies and differences with Na_2SO_3

subarray is neither cotunnite type nor Ni_2In type (Fig. 1), and the identification of this intermediate is needed.

Alternatively, the analysis of double alkali sulphates shows that $LiNaSO_4$ crystallizes, at ambient conditions, in the CaLiPO4-type structure which, in turn, has a cation subarray of the $BaCl_2$ (Fe_2P) type. Thus, the fact that $LiNaSO_4$ transforms at 818 K into a cubic (supposedly) stuffed blende-type structure together with the $Ni_2In \rightarrow PbCl_2$ transition undergone by $LiKSO_4$ at HT [30, 35] leads to assume that the Fe_2P-type (anti-$BaCl_2$) structure might well be another intermediate phase in this part of the journey. This alternative structure will be discussed in detail later.

Now we will focus on the analysis of the Na_2S subarray of Na_2SO_3 to see whether it fits into the general scheme of transitions depicted in Scheme 1. The structure of Na_2SO_3 [36, 37] is trigonal, $\boldsymbol{P}\bar{3}$ ($Z = 2$) and is represented in Fig. 7a. The Na atoms occupy the sites Na(1) at 1*a* (0, 0, 0), Na(2) at 1*b* (0, 0, 1/2) and Na(3) at 2*d* (1/3, 2/3, 0.6667), and the S atoms are situated at 3*d* (1/3, 2/3, 0.173). A first inspection of the structure reveals that its cation array does not correspond to any of the expected phases (Fe_2P, filled-wurtzite or CaF_2).

3.1 Na_2SO_3 and the Ni_2Al Alloy

The Na_2SO_3 structure admits several descriptions. We will start with that which relates Na_2SO_3 to the high-temperature phase I-Na_2SO_4 ($\boldsymbol{P}6_3$/mmc). Both structures are represented in Fig. 7. To highlight their similarity in Fig. 7a we have drawn only those Na–Na contacts that form distorted Na_6 tricapped trigonal prisms (TCTPs), which are equivalent to those of I-Na_2SO_4 (Fig. 7b). The distortion of the TCTP, in the sulphite, occurs because the Na(3) atom (at $z = 0.6667$) and the S atom (at $z = 0.1730$) are displaced from the ideal positions, at $z = ¾$ and $z = ¼$, respectively, of the Ni_2In-type structure.

Thinking of this array as a distortion of the Ni_2In type, one could affirm that the insertion of three O atoms almost reaches the Ni_2In-type structure, but that the pressure is not high enough as to stabilize the regular $\boldsymbol{P}6_3/mmc$ structure. Small displacements (≈0.5 Å) of both Na (3) and S atoms, in opposite directions along the *c* axis (horizontal axis in Fig. 8a), would produce the Ni_2In-type array. The impression is that *the Na and S atoms are in the right way, moving towards the expected positions*.

A second approach to the structure is obtained when only the Na–Na contacts of 3.77 Å are drawn. In this case, the contacts, represented in Fig. 8b, define a slightly

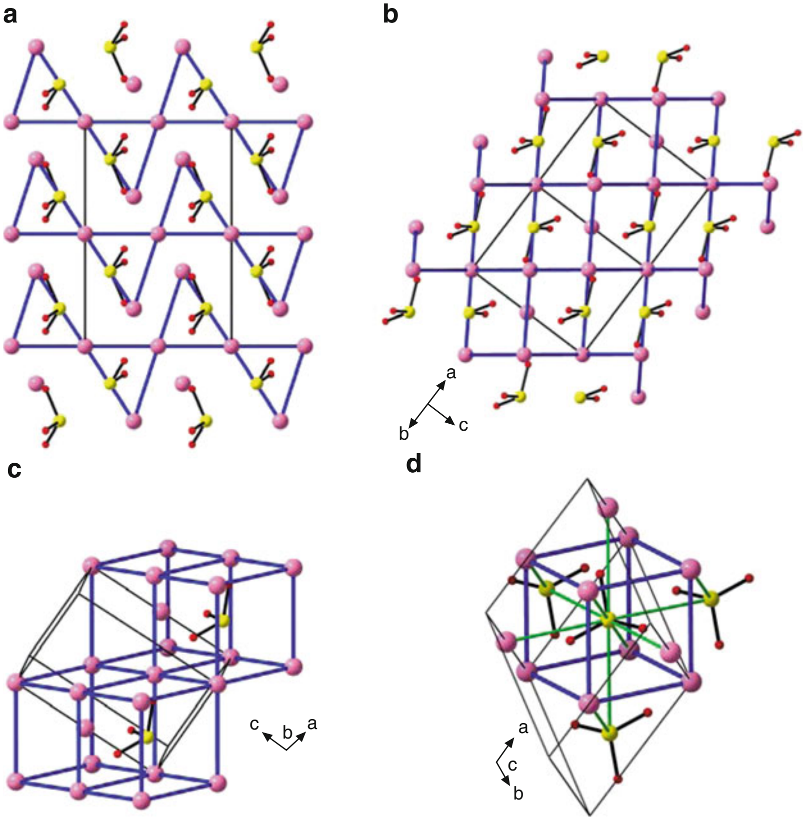

Fig. 8 (**a**) The trigonal structure ($\boldsymbol{P}\bar{3}$) of Na_2SO_3, projected on (110) emphasizing the description based in the distorted trigonal prisms. (**b**) The same projection rotated clockwise around the projection axis. The Na–Na contacts outline the distorted Na_8 cubes which are centred either by Na atoms or by SO_3 groups. This arrangement is seen in perspective in (**c**). (**d**) An alternative view of the structure showing an isolated Na_8 cube, filled by a SO_3 group, to show the complete coordination of the S atoms (8 + 6)

rhombohedrally distorted simple cubic network ($\alpha = 87.07°$), formed by only the Na(1) and Na(3) atoms. These two representations of the structure are drawn in Fig. 8a, b for comparison. However, the rhombohedra can be better observed in Fig. 8c, d, where it can be seen that two-thirds of these Na rhombohedra are occupied by the SO_3 groups, whereas one-third is filled by the Na(2) atoms.

If the O atoms are omitted, the Na and S atoms compose fragments of an anti-fluorite-type structure with the S atom centering the distorted cube (compare Fig. 8c and Fig. 1). As discussed above, the remaining cubes (1/3), centred by the Na(2) atoms, are in fact fragments of a *bcc*-Na structure (Fig. 8c). In summary, the cation array in Na_2SO_3 is, in fact, an anti-fluorite structure whose empty cubes have been filled by Na atoms, and where anti-fluorite- and *bcc*-Na-fragments coexist.

It should be outlined that this almost *bcc* type of environment for both S and Na(2) atoms was recognized by Blatov [13].

This type of arrangement is related to the BiF_3-type structure, formed by compounds such as Cs_3Bi [38] and Fe_3Si [39]. Both types of structures coincide in the existence of the respective Na_8 (Fe_8, Cs_8) cubes, forming a simple cubic (*sc*) array. However, the different stoichiometry makes BiF_3 and Na_2S differ in that, in Na_2SO_3, only one-third of the cubes are centred by S atoms. On the contrary, in Fe_3Si (Cs_3Bi), alternate cubes are occupied by either Fe(Cs) or Si(Bi) atoms. The result is that each Fe_8Si cube is surrounded by six unlike cubes, whereas in Na_2SO_3 each $Na_8(SO_3)$ cube is surrounded by three like and three unlike cubes (Fig. 8c).

Because in both anti-fluorite and Na_2SO_3 the Na:S ratio is 2:1, it is clear that the Na_2SO_3 array is also related to fluorite, as if the empty Na_8 cubes of fluorite were now filled by Na and S atoms. Thus, the filling of the empty cubes leads necessarily to a denser structure, in agreement with the concept relating the equivalence between oxidation and pressure [1, 4]. Thus, the insertion of three O atoms in the anti-fluorite array of Na_2S would provoke a more compact structure, although the pressure is not enough to reach the already mentioned $PbCl_2$-, Fe_2P- and Ni_2In-type arrays. The most important outcome, however, is that the structure of Na_2SO_3 provides a very valuable information, namely the fluorite → cotunnite transition takes place through an intermediate and, up to now, *unknown step*.

At this point, the crucial question is whether the cation array in Na_2SO_3 corresponds to the structure of a new alloy or, on the contrary, it can be regarded as a mere distortion of the Ni_2In-type structure. *This question is, by no means banal because the possible new alloy must necessarily fit into the general scheme of compounds and phase transitions of the alloys quoted in Scheme 1.* Although the structural similarity between Na_2SO_3 and Ni_2In had already been pointed out [4, 40], it is only now, through our research results, that the corresponding alloy has been identified, *unveiling* the unknown quoted in Scheme 1, so that

$$\mathbf{? = Ni_2Al}$$

In summary, the Na_2S subarray, in Na_2SO_3, is isostructural to the Ni_2Al alloy ($\boldsymbol{P}\bar{3}m1$, $Z = 2$) [41], as shown in Fig. 9a, b. Therefore, the Ni_2Al-type structure becomes the *second missing link* of Scheme 1. Nevertheless, Na_2SO_3 is not the

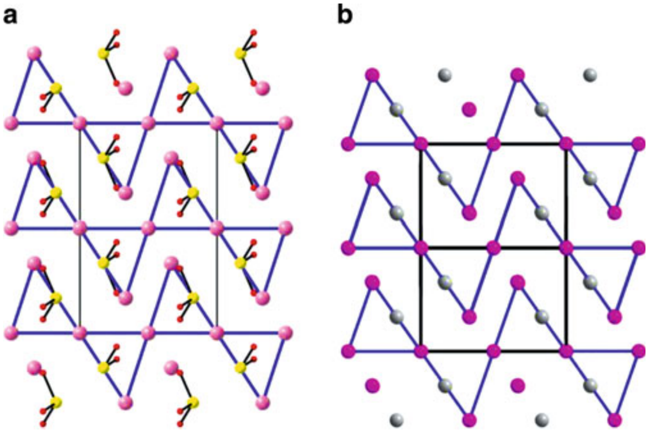

Fig. 9 (**a**) The structures of Na_2SO_3, projected on (110). The Na_2S subarray is identical to that of the Ni_2Al alloy represented in (**b**). (**b**) The structure of the Ni_2Al alloy, projected on (110). *Purple* and *grey spheres* represent Ni and Al atoms, respectively

unique compound adopting this structural type. K_2SO_3 and the high-temperature phase of Cs_2SO_4 (stable above 993 K), adopt also the same cation array. These compounds will be discussed later. For the moment, the reader can visualize their structures in Fig. 12.

3.2 A Mechanism for the $CaF_2 \rightarrow Ni_2Al$ Transition

In the above section, we have briefly discussed the direct structural relationship between both the CaF_2 and Ni_2Al structures. The connection was established at a qualitative level, by considering the Ni_2Al array as a filled anti-fluorite structure. However, both structures could be more strongly related if we were able to deduce a plausible transition mechanism leading to the Na_2S subarray (Ni_2Al type) through a simple displacement of atomic layers in the anti-fluorite Na_2S.

The comparison between both arrays is facilitated if we put both structures, CaF_2 ($\boldsymbol{F}m\bar{3}m$) and Na_2SO_3 ($\boldsymbol{P}\bar{3}$), on a common hexagonal frame. It is well known that a *fcc*-network contains implicit a primitive rhombohedral cell ($\boldsymbol{R}\bar{3}m$). In the anti-fluorite Na_2S, the $\boldsymbol{R}$ cell has dimensions of $a = 4.61$ Å, $\alpha = 60°$, with S atoms at (1*a*): (0, 0, 0) and Na atoms at (2*c*): (1/4, 1/4, 1/4; 3/4, 3/4, 3/4). The corresponding threefold hexagonal cell ($\boldsymbol{R}\bar{3}m$) has dimensions of $a = 4.61$, $c = 11.29$ Å, with S atoms at (3*a*): (0, 0, 0) and Na atoms at (6*c*): (0, 0, *z*), with $z = 1/4$. The anti-fluorite structure referred to this $\boldsymbol{R}$ cell is represented in Fig. 10.

Following the group–subgroup relationships, the symmetry of the anti-fluorite Na_2S can be lowered in the sequence $\boldsymbol{R}\bar{3}m \rightarrow \boldsymbol{P}\bar{3}m1 \rightarrow \boldsymbol{P}\bar{3} \rightarrow \boldsymbol{P}3$. Because Na_2SO_3 is $\boldsymbol{P}\bar{3}$, the transformation Na_2S (anti-fluorite) → Na_2S (Ni_2Al) will be carried out in

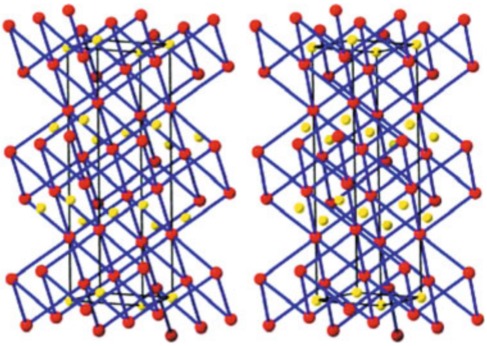

Fig. 10 Stereopair of the structure of Na_2S (CaF_2 type) referred to a hexagonal ***R*** cell. The figure shows the layers of both filled and empty Na_8 cubes (characteristic of the anti-fluorite structure), which in this view are alternating along the *c* axis

Table 1 Atomic coordinates of the cubic anti-fluorite structure of Na_2S referred to the trigonal unit cell ($\boldsymbol{P}\bar{3}$) of dimensions $a = 4.61$, $c = 11.27$ Å represented in Fig. 10. These positions are splitted in the non-centrosymmetric S.G. ***P***3

Atom	Wyckoff position	*x*/*a*	*y*/*b*	*c*/*z*
S	1*a*	0	0	0
S	2*d*	1/3	2/3	2/3
Na	2*c*	0	0	1/4
Na	2*d*	1/3	2/3	0.4167
Na	2*d*	1/3	2/3	0.9167

the common subgroup of lowest symmetry, that is, ***P***3. The atomic coordinates of Na_2S (anti-fluorite), in the $\boldsymbol{P}\bar{3}$ hexagonal cell, are collected in Table 1.

An inspection of Fig. 10 allows us to propose a plausible mechanism for the $CaF_2 \rightarrow Ni_2Al$ transition. As can be readily observed in Fig. 10, the Na cubes are oriented in such a way that their body diagonals run parallel to the *c* axis of the hexagonal cell but where, both, Na and S atoms are placed in separated layers perpendicular to *c*. The transition can be, then, thought of as a cascade displacement of these atomic layers. The first step is the migration of the Na(1) atoms located at (0, 0, 1/4) (the lower corner of an empty cube) towards the centre of the cube situated at (0, 0, 1/2). This displacement corresponds to *c*/4 (2.83 Å) and produces the filling of the empty cubes of the fluorite by other Na atoms.

The empty corners are now occupied by the adjacent layer of Na atoms, migrating from (2/3, 1/3, 1/12) to (0, 0, 1/4), thus completing the filled cubes. Next, the S atoms at (0, 0, 0) are displaced to (1/3, 2/3, 1/6) and, finally, the next layer of Na atoms at (1/3, 2/3, −1/12) migrates to (2/3, 1/3, 1/12). Thus, the displacement of the first layer provokes that of the adjacent layers, producing a "*domino-like*" effect. All the translations are defined by the vector $\boldsymbol{t} = (\mathbf{1/3}\,\boldsymbol{a} - \mathbf{1/3}\,\boldsymbol{b} + \mathbf{1/6}\,\boldsymbol{c})$ corresponding to displacements of 3.24 Å. The resulting structure is drawn in Fig. 11.

It should be remarked that the regular Na_8 cubes, in fluorite, are rhombohedrally distorted in Na_2SO_3 with an average edge of 3.81 Å and average S–Na distances of 8 × 3.29 Å. In Na_2S, the equivalent distances are 3.27 and 8 × 2.83 Å.

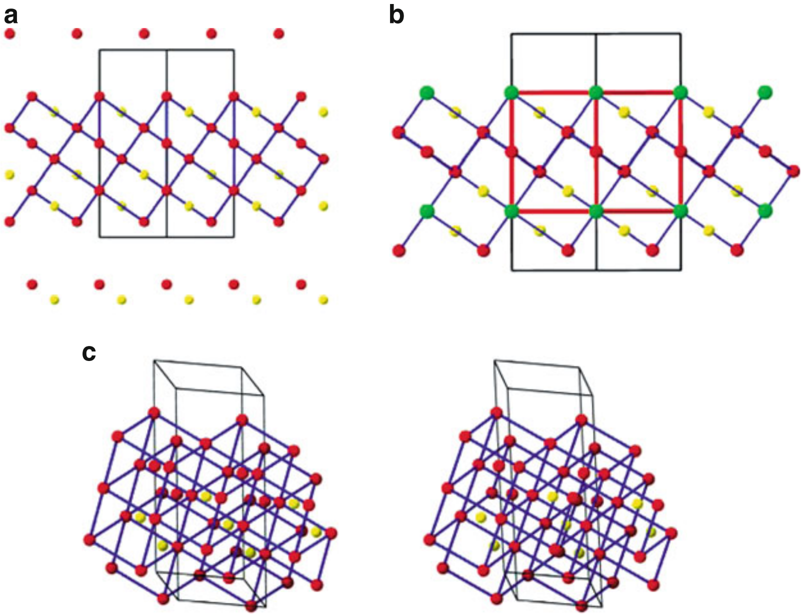

Fig. 11 (**a**) The final structure of the Ni_2Al type, after the displacement of the atomic sheets in the fluorite-like Na_2S. (**b**) The same view where the Na atoms located at the origin have been coloured (*green*) to outline (*red lines*) the denser new unit cell comparable to that of Na_2SO_3. (**c**) Stereopair showing the filling of the cubes

The structural block of Na_2S, depicted in Fig. 11a, is inserted into a hexagonal ***R*** unit cell which has served as a frame for the structural transformation (compare with the cation array of Na_2SO_3 shown in Fig. 8b). In this figure, the contiguous blocks are separated by voids as a consequence of the graphical process of creating a denser fragment (Ni_2Al) from a bigger unit cell. The reader can easily deduce that these voids are non-existing in a real transformation.

The block represented in Fig. 11a contains 1.5 unit cells along c. Of course, in the real physical process these blocks close up to form a continuous arrangement. The unit cell dimensions of Na_2S in the hypothetical Ni_2Al-type structure would be $a = 4.61$, $c = 5.63$ Å, comparable to the values of $a = 5.46$, $c = 6.18$ Å in Na_2SO_3. This real unit cell of Na_2S with the Ni_2Al-type structure is outlined with red lines in Fig. 11b. The final atomic coordinates are collected in Tables 2 and 3. Figure 11c is a 3D view of the Ni_2Al-type structure to be compared with Fig. 8c.

3.3 Can the Internal Pressure Be Estimated?

As stated above, in Na_2SO_3 (Ni_2Al type), two-thirds of the $Na(1)_8$ cubes are filled by S atoms, forming so fragments of an anti-fluorite structure, whereas one-third of

Table 2 Atomic coordinates of Na and S atoms, in the Ni_2Al-type structure, obtained after the displacements applied to the layers of the anti-fluorite structure, leading to the structure of Fig. 11a. The transformation is made in the non-centrosymmetric ***P***3 space group. The original coordinates and cell dimensions are those quoted in Table 1. As seen in Fig 11a, the *c* axis of the final unit cell is reduced to ½ of the original unit cell with values of $a = 4.61$, $c = 5.63$ Å

Atom	Wyckoff position	*x*/*a*	*y*/*b*	*c*/*z*
S	1*b*	1/3	2/3	1/6
S	1*b*	1/3	2/3	2/3
S	1*c*	2/3	1/3	1/3
Na	1*a*	0	0	1/4
Na	1*a*	0	0	1/2
Na	1*a*	0	0	3/4
Na	1*b*	1/3	2/3	0.4167
Na	1*c*	2/3	1/3	0.5833
Na	1*c*	2/3	1/3	0.0833

Table 3 Atomic coordinates of Na_2SO_3 (***P***3) as derived from the experimental determination of the crystal structure. Compare with the values listed in Table 2. In both structures, the Na_2S subarrays are Ni_2Al type. The unit cell dimensions are $a = 5.509$, $c = 6.473$ Å. The insertion of O atoms produces an expansion of the unit cell axes (compare with those of Table 2)

Atom	Wyckoff position	*x*/*a*	*y*/*b*	*c*/*z*
Na	1*a*	0	0	0
Na	1*a*	0	0	0.5368
Na	1*b*	1/3	2/3	0.8351
Na	1*c*	2/3	1/3	0.1798
S	1*b*	1/3	2/3	0.3395
S	1*c*	2/3	1/3	0.6877
O	3*d*	0.2200	0.4302	0.2344
O	3*d*	0.8640	0.6667	0.7689

them are centred by the Na(2) atoms, forming fragments of *bcc*-Na (Fig. 8). In the Na_8S cubes, the S–Na distances are 1 × 3.05, 1 × 3.13, 3 × 3.30 and 3 × 3.33 Å (mean value 3.28 Å), hence longer than the equivalent bonds in the anti-fluorite Na_2S structure (8 × 2.83 Å). However, in the *bcc*-Na blocks, the distorted cubes have edges of 3.76 Å and Na–Na distances of 2 × 3.09 and 6 × 3.32 Å (mean value 3.25 Å), dimensions that are smaller than the unit cell of elemental *bcc*-Na at ambient conditions ($a = 4.29$, $d = 8 \times 3.72$ Å) [42]. The result is that in Na_2SO_3, the anti-fluorite fragments are expanded at the expense of the Na blocks, which are compressed.

From the equation of state of Na [42], it can be deduced that in Na_2SO_3 the dimensions of the Na-centred rhombohedra ($a = 3.76$ Å) are in the range of stability of *bcc* phase under pressure, in such a way that the unit cell parameter of 3.76 Å would correspond to a pressure of about 5.3 GPa. It should be remembered that at this pressure, the anti-fluorite → anti-cotunnite transition has not yet occurred in Na_2S. The diffraction peaks of the anti-cotunnite phase begin to appear at 6.4 GPa [7], in agreement with the fact that the Ni_2In-type structure is not reached in Na_2SO_3.

The important question that rises here is whether the Metal–Metal distances, observed in the oxides can be taken as an *internal barometer* that gives insight about the internal pressure at which cations are subjected.

Looking again at Figs. 9 and 11, it can be ensured that in Na_2SO_3, the Na_2S subarray is formed by blocks of anti-fluorite, although coexisting with an incipient Ni_2In-type structure. Even in an exhaustive dissection of the structure, one is able to recognize fragments of a cotunnite-type structure.

We must emphasize, however, that the internal pressure exerted by three O atoms is not enough to stabilize the high-pressure phases of Na_2S, and, hence, the Ni_2Al-type structure appears as an intermediate stage in the transitions path of Na_2S.

3.4 *Na_2SO_2: A Hypothetical Compound with the Anti-Fluorite Structure?*

In Scheme 1, it can be seen that the number of oxides with an anti-fluorite-related structure is scarce. Examples are the HT phases of both Li_2SO_4 and $CsLi(CrO_4)$. This can be interpreted as if the insertion of O atoms into anti-fluorite structure of the alloys produced an internal pressure, difficult to overcome at high temperature. As is readily seen, all the oxides collected therein contain either three or four oxygens per formula, and the subsequent question that arises is whether a compound with a lower O-content, such as Na_2SO_2, could exist and whether it could maintain the anti-CaF_2-type structure for the Na_2S subarray.

4 The Complete *Journey* from Fluorite to the Laves Phases

We have seen that the $TiSi_2$-type structure (Na_2S subarray in thenardite V-Na_2SO_4) might well be an intermediate step in the $Ni_2In \rightarrow MgCu_2$ transition [14]. Their structural relationships were discussed in Sect. 2.2 and were based on the fact that $TiSi_2$ possesses structural fragments of both the initial and the final phases. We must also recall that this double transition has only been reported for the oxide Na_2MoO_4 [15] (see Scheme 1).

In the same manner, it has been discussed that the Ni_2Al-type structure, found in Na_2SO_3, should be considered as an intermediate step in the $CaF_2 \rightarrow Ni_2In$ transition, so that our model forces the Na_2S subarray of Na_2SO_3 (Ni_2Al type) to fit into the set of structures and phase transitions quoted in Scheme 1, as it will be explained below.

We have already justified and described that phenacite could also be an intermediate phase in the fluorite → Ni_2In transition as deduced from the data reported for Li_2SO_4. Finally, as it will be discussed later, the Fe_2P-type structure might be the fourth missing link in the series collected in Scheme 1.

Thus, the four structures we have just discussed, i.e. phenacite, Ni_2Al, Fe_2P and $TiSi_2$, are meaningful and could serve as the thread that connects other experimental results, which have been considered so far as isolated events. It seems then convenient to deal with all these structural and chemical features as a global phenomenon, in the light of three variables that are intimately related, although their relative contributions, as well as their influence in the structural transformations, are still far from being quantified and completely understood. These three variables are *oxidation, temperature and pressure*.

The first intuition is that at low pressures, Na_2SO_3 could reach the hexagonal structure of the HT phase of I-Na_2SO_4 (***P***6_3/mmc) [9]. This possible transformation would imply a Ni_2Al-type → Ni_2In-type transition for the Na_2S subarray that is consistent with the general trend, already mentioned, which makes structures of compounds of lighter element adopt, when compressed, the structures of similar compounds with heavier elements of the same group. Thus, applied to our particular case, this trend would make that the Ni_2Al-type structure transforms under pressure into the Ni_2In-type structure (indium is heavier than aluminium, within the Group 13). Moreover, considering that an increase in temperature releases pressure, one could expect that, at HT, the Ni_2Al alloy could even transform into a CaF_2-type structure. Such transitions have never been observed in alloys but, as seen in Scheme 1, the cotunnite-like $CsLi(CrO_4)$ does indeed convert into a stuffed blende-type structure at HT. However, such an intermediate phase has not been reported for Na_2SO_3.

The experimental data on both Na_2S and Na_2SO_4 support that a similar transition could take place in these systems, as it will be described below. In the high-pressure experiments on Na_2S [7], only the $CaF_2 \rightarrow PbCl_2 \rightarrow Ni_2In$ transitions were observed. The intermediate Ni_2Al-type structure was neither detected, although, considering the structural behaviour of the oxides (sulphates), its existence should not be discarded. Thus, the stabilization of the lower pressure Ni_2Al-type structure in Na_2SO_3 (see Fig. 9) and the existence of the higher-pressure Ni_2In-type structure in I-Na_2SO_4 [9] (Fig. 7b), with a higher O-content, is consistent with the relationship *oxidation–pressure*.

This argument, which could be regarded as speculative, is nevertheless confirmed, in our opinion, by the structural changes observed in Cs_2SO_4 (see Scheme 1). In this sulphate, the Cs_2S subarray is cotunnite type at room temperature, but at 993 K it transforms into the Na_2SO_3 type (Ni_2Al type) (Fig. 12a, b), as expected if we consider that pressure is released by increasing temperature. In other words, the Ni_2Al-type structure becomes cotunnite type by lowering temperature. In connection with this, it should be remarked that the topology assigned to Cs_2SO_4 differs from that given by Blatov [13].

Now, we are in conditions of writing the complete *Structural Journey* going from CaF_2 to $MgCu_2$. The experimental data of Scheme 1 lead to the following sequence:

$$\mathbf{CaF_2 \rightarrow \underset{phenacite}{Ni_2Al} \rightarrow \delta\text{-}Ni_2Si \Leftrightarrow \theta-Ni_2Si(Ni_2In) \rightarrow TiSi_2 \rightarrow Fe_2P \rightarrow MgCu_2}$$

Note that both the **δ-Ni_2Si** (cotunnite-type) and **θ-Ni_2Si** (Ni_2In-type) phases have been connected through a "two-headed" arrow to indicate that their relative stability can vary from one compound to another. In some cases, like Ni_2Si itself,

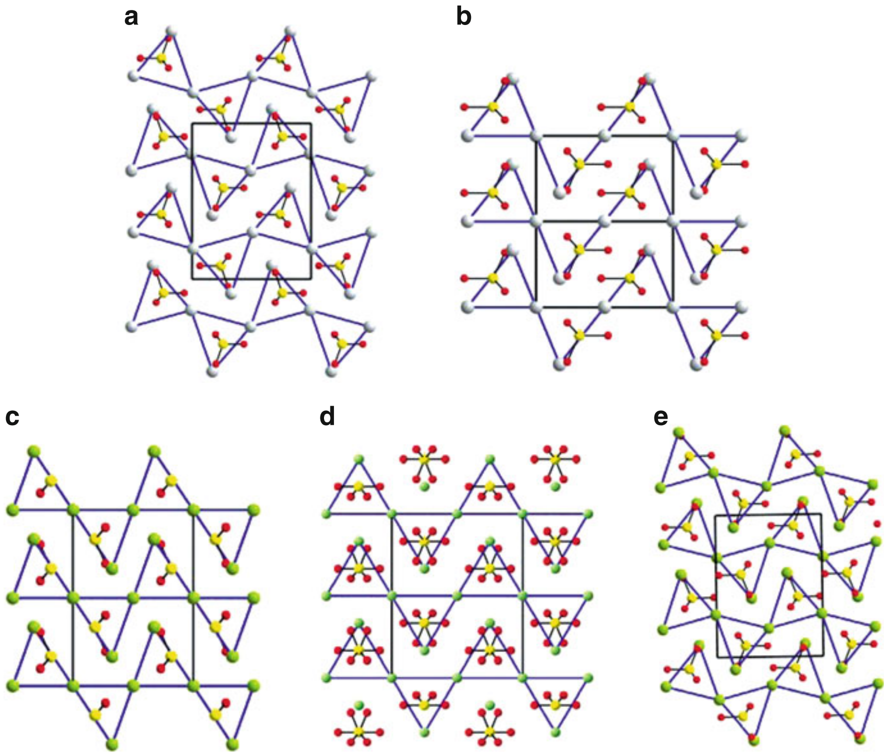

Fig. 12 The structures of the two phases of Cs_2SO_4. (**a**) The cotunnite-like structure stable at ambient conditions. (**b**) The HT phase in which the Cs_2S subarray forms the Ni_2Al-type structure, as in Na_2SO_3 and K_2SO_3. (**c**) The trigonal structure of K_2SO_3, isostructural with Na_2SO_3. It is projected on (110) to show the K_2S subarray of the Ni_2Al type. (**d**) The HT structure of K_2SO_4, isostructural to the HT phase I-Na_2SO_4 (compare with Fig. 7). (**e**) The structure of the low temperature phase (Pnma) of β-K_2SO_4

the δ phase is stable at ambient conditions whereas the θ-phase is obtained at HT (lower pressures). On the contrary, in Na_2S, the $PbCl_2 \rightarrow Ni_2In$ transition occurs by increasing pressure. The same occurs in oxides, such as β-K_2SO_4, cotunnite-like at RT, which transforms into Ni_2In type above 859 K. On the contrary, $KLiSO_4$ undergoes the inverse transition $Ni_2In \rightarrow PbCl_2$ at 941 K.

5 Oxidation, Temperature and Pressure

At this point, it is convenient to delve in depth in the phase transitions of Cs_2SO_4. Although advanced in the above Sect. 4, its structural changes deserve an additional discussion, specially as regards its comparison with its analogues K_2SO_3 and K_2SO_4. Here, beyond what was advanced in the previous section, our aim is to discuss the structural changes of this family of compounds, by considering

$$\begin{array}{ccccccc} CaF_2 & \rightarrow & Ni_2Al & \rightarrow & Ni_2In & \rightarrow & \delta\text{-}Ni_2Si \\ \text{O-free} & & O_3 & & O_4 & & O_4 \\ & & & & \textbf{HT} & & \textbf{LT} \end{array}$$

Increasing temperature **Increasing pressure**
⇐ ⇒

Scheme 2 The different structures types of the cation arrays of Na_2S as a function of the O-content, temperature and pressure and phase transitions occurring between them. The CaF_2 structure occurs in the O-free Na_2S. Three O atoms in Na_2SO_3 produce the Ni_2Al type structure. In Na_2SO_4, four O atoms provoke the Ni_2In and cotunnite structures

simultaneously the three decisive factors influencing the formation of a given cation array, i.e. *the O-content, temperature and pressure*.

In the above sections, we described some of these structures in a rather simple manner. Now, we intend to observe them as the result of more complex influences, even though our analysis will remain at a qualitative level. The structures under discussion are represented in Fig. 12.

At ambient conditions, Cs_2SO_4 (like K_2SO_4 and Rb_2SO_4) is cotunnite type (Fig. 12a) [43] and provides a new example of how the structure of the alloy (Cs_2S) (anti-$PbCl_2$) [44] is preserved in the oxide Cs_2SO_4. The important issue is that, at HT, Cs_2SO_4 transforms into the Na_2SO_3-type structure (Fig. 12a, b). Thus, at high temperature, pressure is released and the Cs_2S array undergoes the inverse $PbCl_2 \rightarrow Ni_2Al$ transition. A further transition to the anti-fluorite structure has not been observed so far.

K_2SO_3 and K_2SO_4 also provide examples on how the three factors act, in a concerted way, to produce structures characteristic of our "*structural journey*". For instance, K_2S is fluorite type at ambient conditions [45]. When three O atoms are inserted, K_2SO_3 is formed [46]. The compound is isostructural to Na_2SO_3 and, hence, the K_2S subarray is Ni_2Al type (Fig. 12c). The addition of a fourth O atom, to form K_2SO_4 [47], would be equivalent to a pressure increase and, consequently, the K_2S subarray converts into the anti-cotunnite structure (anti-$PbCl_2$) of β-K_2SO_4 (Fig. 11e). Above 885 K, the β-phase transforms into the hexagonal phase α-K_2SO_4 [48], isostructural to I-Na_2SO_4, with a Ni_2In-type subarray where the SO_4 groups show rotational disorder, as seen in Figs. 7b and 12d, respectively [9].

The sequence of structures represented in Fig. 12c–e clearly illustrates how the cation arrays in the oxides follow the same transitions sequence as the alloy itself. As reported elsewhere [4, 14], the key issue is that cations undergo their own phase transitions in spite of the presence of oxygens. In Scheme 2 are summarized the different structures adopted by the Na_2S subarrays, as a function of the three factors.

The structural relationships just discussed should not be contemplated as a mere paper exercise. Rather, they are physically sound for the following reasons:

1. The first one is that the denser array of the Ni_2Al type links the Na_2SO_3 structure with the *origin of the structural walk* (the anti-fluorite structure).
2. The second reason is more complex but also easily understandable. It is related to the well-known empirical rule applied to phase transitions of elements under

pressure, which establishes that, within a group of the Periodic Table, the ambient pressure structures of heavier elements are stabilized by the lighter ones at high pressures. As it has been discussed above, the Ni_2Al alloy could transform into an Ni_2In type under pressure, in the same manner that, at high temperature, it might undergo the Ni_2Al → CaF_2 transition. Although these experiments have never been carried out, the behaviour of the Li_2S, Na_2S and K_2S alloys [6–8], as well as the same subarrays in the corresponding oxides, strongly support these hypotheses.

3. The third reason is connected to the equivalence between oxidation and pressure and its relationship with the oxygen contents. In this respect, the structures of Na_2SO_3 will be compared with those of Na_2SO_4. We have seen that the transition path in Na_2S under pressure is *anti-fluorite → anti-cotunnite → Ni_2In type* [7].

When four O atoms are inserted into the Na_2S matrix, they exert a pressure which exceeds that needed to form the Ni_2In-type subarray, but insufficient to reach the $MgCu_2$-type structure. We have seen that the cation subarray ($TiSi_2$ type), in thenardite (V-Na_2SO_4), is an intermediate step in the olivine → spinel transition (Fig. 3), and that, when temperature increases, the pressure is partly released and the Ni_2In-type subarray is recovered. This means that the Na_2S subarray follows, by heating, an opposite pathway to that followed under pressure (Fig. 1).

In the case of Na_2SO_3, with a lower O-content, the Na_2S subarray is Ni_2Al type [41] (Fig. 9). We have mentioned previously how small displacements (≈0.5 Å) of both the Na (3) and the S atoms would lead to the Ni_2In-type structure, an idea that is in agreement with recent studies on iron silicides [49]. One of them, Fe_2Si, extremely difficult to obtain as a pure phase was synthesized [50] by rapid quenching from very high temperatures. Its structure is represented in Fig. 13b, to show that the atomic coordinates of the corresponding Fe and Si atoms are intermediate between those of Ni_2In and Ni_2Al types.

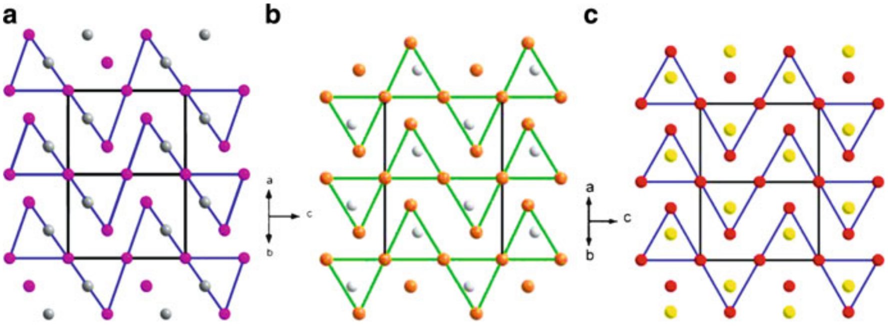

Fig. 13 The structures of the three compounds intimately related: (**a**) Ni_2Al, (**b**) Fe_2Si and (**c**) Ni_2In (also HP-Na_2S). The figures suggest that a possible Ni_2Al → Ni_2In phase transition might occur by a continuous displacement of both Ni(Fe) atom and the Al(Si), following the sequence (**a**) → (**b**) → (**c**), up to reach the most symmetrical Ni_2In (HP-Na_2S) structure

When the three former structures are compared (Fig. 13), the suspicion is that the transition $Ni_2Al \rightarrow Ni_2In$ could occur through a continuous displacement of both the Ni(1) and the Al [Fe, Si] atoms. In this way, the structure of Fe_2Si [50] might be regarded as an instantaneous "picture", captured during the quenching process, that is, as the Ni_2Al-type structure is progressing towards the Ni_2In type. This hypothesis is supported by theoretical calculations carried out on Fe_2Si, which predict the Ni_2In type (***P***6_3/mmc) as the most stable phase (Rodríguez-Hernández et al. 2005, unpublished results). In other words, at HT, the Ni_2In-type structure *begins the walk* towards the CaF_2-type array, passing through the Ni_2Al-type structure (question mark in Scheme 1). Note that a small displacement of ≈0.15 Å of both Fe(2) and Si atoms, in Fe_2Si, leads to the Ni_2In-type structure. Recall in this regard how CsLi (CrO_4) reaches a cubic phase structure, related to fluorite, passing through the intermediate cotunnite-type structure (see Scheme 1).

The structures of Fe_2Si and Ni_2In (Fig. 13b, c) also conform to the equivalence between oxidation and pressure. Thus, in fayalite (Fe_2SiO_4), the insertion of oxygen stabilizes an undistorted Fe_2Si subarray of the Ni_2In type.

6 The Third Missing Link: The Fe_2P Structure

In Sect. 4, it was discussed the possibility that the Fe_2P-type (anti-$BaCl_2$) structure could be an intermediate arrangement in the $Ni_2In \rightarrow PbCl_2$ transition [30, 35]. In support of this assumption are the phases observed in the double alkali sulphates $LiKSO_4$ and $LiNaSO_4$, collected in Scheme 1.

The structure of Fe_2P (***P***$\bar{6}$2m) was reported as early as 1930 [51]. Since then, more than 100 isostructural compounds have been collected in the structural databases (ICSD, PCD). It has been pointed out [52] that no Fe_2P polymorph is known with the Co_2Si (cotunnite-like) structure type. However, solid solutions of the phosphides M_2P (M = Cr, Mn, Fe, Co, Ni), such as Mn_2P, Fe_2P and Ni_2P, are hexagonal (***P***$\bar{6}$2m), as is barringerite, $(Fe,Ni)_2P$, whereas Co_2P remains in the cotunnite-like Co_2Si type. It is noteworthy that the orthorhombic phase of $(Fe, Ni)_2P$, known as the mineral allabogdanite and having the Co_2Si-type structure, has been found in the Onello meteorite [52]. On the contrary, FeMnP undergoes the $Fe_2P \rightarrow Co_2Si$ phase transition above 1,473 K [53].

Among the Fe_2P-type compounds, one of them, $BaCl_2$, is of special interest in the context of this chapter. It is likewise included in Scheme 1. At ambient conditions, $BaCl_2$ is cotunnite type (Co_2Si) (***P***nma) [54], but on dehydration of $BaCl_2{\cdot}2H_2O$ [31], two additional polymorphs were obtained, i.e. Fe_2P type (***P***$\bar{6}$2m) and Co_2Si type (***P***nma) (cotunnite-like). At even higher temperatures (1,200 K), a β-phase with the anti-fluorite structure (***F***m$\bar{3}$m) was observed [31]. Thus, that dehydration process has revealed the important double transition $Fe_2P \rightarrow Co_2Si \rightarrow CaF_2$.

More recent high-pressure studies [55, 56] have permitted the observation of a double transition cotunnite → post-cotunnite → Fe_2P type at pressures of about 18 and 30 GPa, respectively. Thus, the hexagonal phase (***P***$\bar{6}$2m) of $BaCl_2$ can be

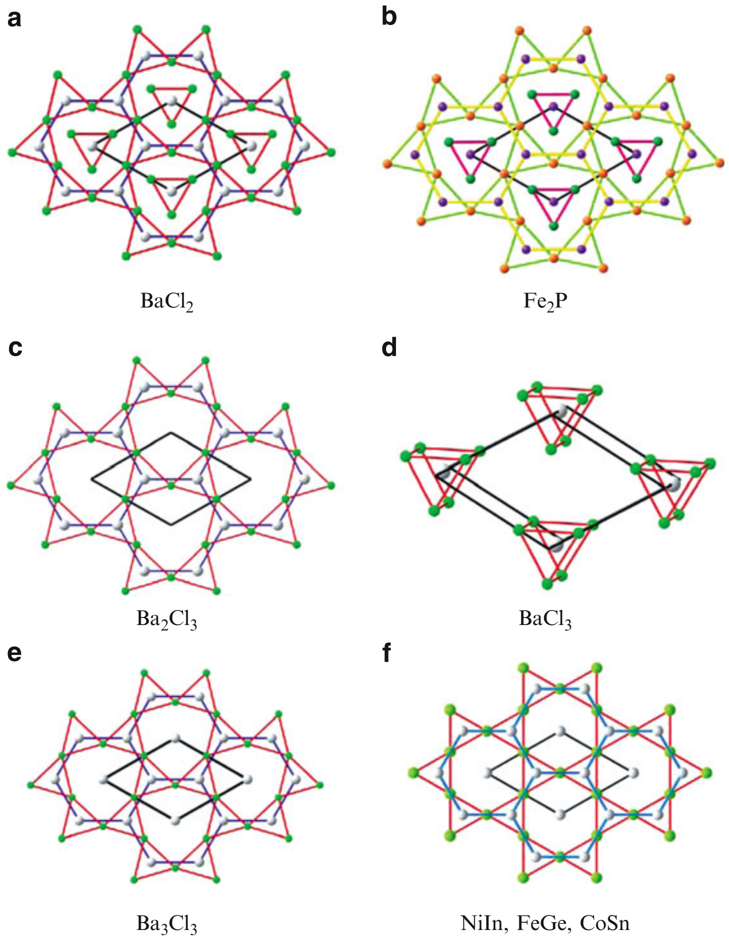

Fig. 14 (**a**) The hexagonal ($P\bar{6}2m$) structure of BaCl$_2$ projected on the *ab* plane. *Grey* and *green spheres* represent Ba and Cl atoms, respectively. (**b**) The aristotype Fe$_2$P structure showing the graphite-like layers formed by the P atoms (*purple spheres*) and the two types of tricapped trigonal prisms (TCTPs) formed by the Fe atoms (*green* and *light brown spheres*). (**c**) The structure of BaCl$_2$ in which the columns of TCTP centred at the cell origin have been omitted. The result is a frame of stoichiometry Ba$_2$Cl$_3$. (**d**) The subarray formed by Ba(1) and Cl(2) forming the columns omitted in (**c**). They form the columns of TCTP of composition BaCl$_3$ which are related to the LaCl$_3$ structure. (**e**) The same structure projected in (**c**) but adding the Ba(1) atoms, located at the origin, producing so a stoichiometry Ba$_3$Cl$_3$ which is a distortion of the NiIn, CoSn and FeGe structures represented in (**f**)

obtained in two independent ways [31, 56]. The unit cell dimensions are $a = 8.10$, $c = 4.65$ Å, $Z = 3$, with atoms occupying four crystallographically independent sites, i.e. Cl(1) at 3*g*, Cl(2) at 3*f*, Ba(1) at 2*d* (1/3, 2/3, 1/2) and Ba(2) at 1*a* (0, 0, 0). In Fig. 14a, b are represented the structures of BaCl$_2$ and Fe$_2$P, respectively, and the Co$_2$Si-type structure of BaCl$_2$ is shown in Fig. 18c.

6.1 Description of $BaCl_2$ and Its Relation to the CoSn-Type Structure

The description of the hexagonal structure of $BaCl_2$ (Fe_2P type) is not easy. Hyde and Andersson [57] described it on the basis of the so-called TCTPs, like those existing in both the cotunnite- and the Ni_2In-type structures. These prisms are formed by six Cl (Fe) atoms and are centred by Ba and P atoms, respectively. Three additional Cl atoms cap the lateral faces of the prisms, giving rise to a $CN = 9$ for the central Ba (P) atoms (Fig. 14b).

The structure can also be described by considering only the Ba(1) and Cl(2) atoms. In this case, the novelty is that we obtain a partial skeleton of composition Ba_2Cl_3, formed by interconnected $BaCl_6$ trigonal prisms. This subarray is represented in Fig. 14c and shows that the prisms are sharing the edges perpendicular to the projection plane, forming distorted hexagonal tunnels that run parallel to the *c* axis. These tunnels are centred by the Ba(2) atoms.

Contrarily, when only the remaining Ba(2) and Cl(1) atoms are taken into account, columns of trigonal prisms of composition $BaCl_3$ are formed (Fig. 14d). They are located at the origin of the cell, filling the hexagonal tunnels of Fig. 14c. Thus, $BaCl_2$ can be regarded as the sum of two substructures, Ba_2Cl_3 and $BaCl_3$, which are complementary, forming jointly the structure of Fig. 14a. The stoichiometry can then be written as $Ba_2Cl_3 + BaCl_3$, equivalent to $BaCl_2$.

If the Ba(2) atoms, at (0, 0, 0), centering the hexagonal tunnels, are included into the Ba_2Cl_3 subarray of Fig. 14c, the partial formula becomes Ba_3Cl_3. This new skeleton, drawn in Fig. 14e, is in fact a distortion of the hexagonal RT phase of NiIn (CoSn type), represented in Fig. 14f. By comparing both figures, one sees that the distortion consists of a slight deviation of the Cl atoms from the line connecting the Ba atoms. Recall that Ba and Cl atoms are not coplanar.

When the Cl atoms are connected by red lines (Fig. 14e), one obtains planar nets, which are a distortion of the regular **3.6.3.6** nets (Kagomé nets) forming the NiIn (CoSn)-type structure (Fig. 14f). It should be reminded that such Kagomé nets are also forming part of the cubic Laves phases (Cu subarray in $MgCu_2$) and, hence, are also present in the cation array of spinels. In $BaCl_2$, Fe_2P and CoSn, the Kagomé nets are eclipsed (…*AAA*… sequence), whereas in $MgCu_2$ they are stacked in a … *ABCABC*… sequence, perpendicular to [1 1 1].

The interest of this analysis of the $BaCl_2$ structure resides in that it allows for a simple and rational explanation of the two skeletons in which we have partitioned the $BaCl_2$ structure. Once more, the explanation conforms to the ***EZKC*** [14, 33]. Thus, starting with the substructure Ba_3Cl_3, composed of Ba(1), Ba(2) and Cl(1) (Fig. 14e) and assuming that each Ba atom transfers one electron to the three remaining Cl(2) atoms (the green atoms drawn in Fig. 14d), we would obtain the pseudo-formula $(\Psi\text{-Ar})_3(\Psi\text{-CsCl})_3$, which is a pseudo-compound of stoichiometry 1:1 (Ψ-CsCl) that adopts the structure of the CoSn (NiIn) type filled with three Ψ-Ar atoms (Fig. 14f).

This interpretation could be regarded as artificial because this structure has not been found for any alkali halide. For this reason, an alternative explanation would consist in the one-electron transfer from the Cl(1) to the Cl(2) atoms. Recall that this electron transfer between atoms of the same kind was already applied to other compounds [14, 33, 58, 59]. In this case, Cl(2) and Cl(1) atoms would then convert into Ψ-Ar and Ψ-S, respectively, and the substructure would then adopt the formula $(\Psi\text{-Ar})_3(\Psi\text{-BaS})_3$, also a filled 1:1 compound of pseudo-formula BaS.

In common with alkali halides, no alkaline-earth chalcogenide crystallizes in this structure type. However, if the ***EZKC*** is applied to the aristotype Fe_2P, both pseudo-formula and structure become meaningful and can be explained satisfactorily, as described below.

Thus, if in the aristotype Fe_2P we apply the ***EZKC*** [14] and assume that the P atom donates one electron to one of the Fe atoms, Fe_2P is converted into Co[Ψ-FeSi], which can also be written as Fe[Ψ-CoSi]. In both pseudo-compounds, the respective Ψ-[FeSi] and the Ψ-[CoSi] moieties are isoelectronic to other compounds of the NiIn type such as FeGe, FeSn and CoSn. Note that this structure is obtained if we omit the Fe(2) atoms (Ψ-Co) in Fe_2P (Fig. 14b), leading to the NiIn-type structure represented in Fig. 14f. It should be also remarked that the omitted atoms, Fe (Ψ-Co), are those forming the columns of trigonal prisms (green spheres in Fig. 14b). *The conclusion is straightforward, i.e. the NiIn (CoSn)-type structure of compounds like FeGe, and CoSn is implicit in* Fe_2P.

6.2 The $BaCl_2$ and $LaCl_3$ Structures

The above description and explanation of the $Ba(1)_2Cl(2)_3$ substructure in terms of the CoSn-type structure will facilitate the understanding of the complementary $Ba(2)Cl(1)_3$ moiety that forms the columns of trigonal prisms (Fig. 14d). The 1:3 stoichiometry corresponds to compounds such as $TiCl_3$ [60] and Cs_3O [61]. However, in these compounds, where the respective Ti and O atoms are also hexacoordinate, the columns are formed by face-sharing octahedra instead of the trigonal prisms formed by the $BaCl_3$ subarray. Hyde and Andersson [57] already noticed that this $BaCl_3$ and the corresponding PFe_3 subarray showed strong similarities with the structure of $LaCl_3$ [62]. Both structures, $LaCl_3$ and Fe_2P, can be compared in Fig. 15. The similarities and differences between them will be commented next.

Looking at Fig. 15, we see that both structures are formed by trigonal prisms of Cl(Fe) atoms. In $LaCl_3$ (Fig. 15a), the prisms columns are isolated if we consider only the six Cl atoms forming the prisms. However, they are interconnected if we take into account that three additional Cl atoms, belonging to three adjacent columns, are capping the lateral faces of the former ones, and completing the so-called TCTPs, following the term used by Hyde and Andersson [57].

Contrarily, in $BaCl_2$ (Fe_2P), the equivalent prisms are condensed by sharing common edges and form hexagonal channels (Fig. 15b). For a better understanding

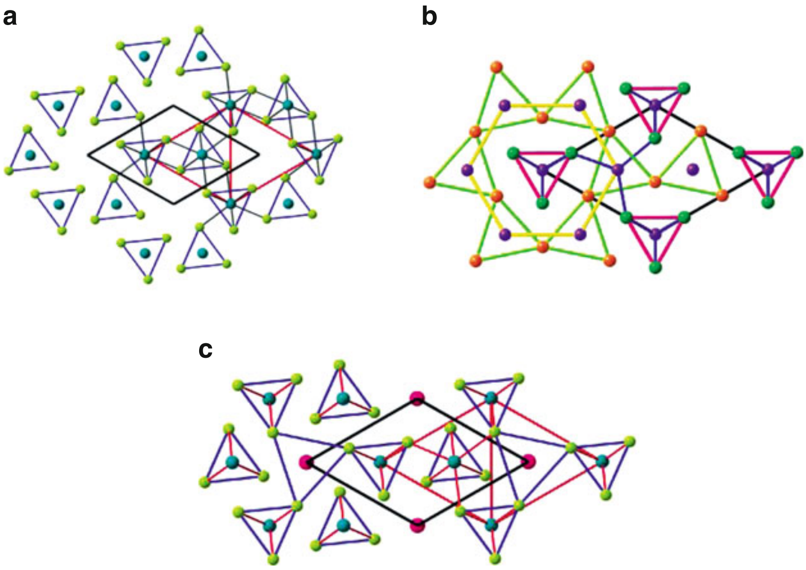

Fig. 15 (**a**) The hexagonal structure (***P***6_3/m) of $LaCl_3$ projected on the *ab* plane. La-*blue*, Cl-*green*. The unit cell, marked with *black lines*, contains two columns of TCTP. Each La atom is surrounded by six Cl atoms of the trigonal prisms, plus three Cl atoms coplanar with the La atoms, completing so the $CN = 9$. An alternative unit cell (*red lines*) has been drawn by displacing the origin along [1 1 0] in which the columns of TCTP coincide with those of Fe_2P that are centred at the cell origin in (**b**). (**c**) The $LaCl_3$ structure projected as in (**a**) but where fictitious La atoms (*red spheres*) have been inserted at the origin to show the ideal formation of a structure similar to that of Fe_2P. In this notional structure, the hexagonal tunnels are formed by alternating small and great trigonal prisms centred by La and red-La atoms, respectively

of both structures, the $LaCl_3$ structure (Fig. 15a) has been modified in the following way: on the one hand, an alternative unit cell has been drawn with red lines so that the columns of trigonal prisms are centred at the cell origin, and match those existing in the Fe_2P structure of Figs. 14b and 15b. On the other hand, we have added one fictitious atom (red sphere) located at the origin of the real unit cell as depicted in Fig. 15c. It is also noteworthy that a structure similar to that of Fe_2P (Fig. 15b) can be built with the aid of that “red” atom. The hexagonal tunnels formed in Fe_2P can also be achieved in Fig. 15c by joining the smaller La-centred prisms with the bigger ones that are centred by the fictitious “red” atoms.

Taking as reference the “red” unit cell of $LaCl_3$ (Fig. 15a, c), we see that the left half of the cell contains one TCTP that is formed by six Cl atoms (green spheres) and is centred by the La atom (blue sphere). The nine La–Cl bonds have been drawn with red lines to emphasize that each trigonal prism is surrounded by other three, displaced c/2 with respect to the central one.

If we look now at Fig. 15b (Fe_2P), we see that the corresponding trigonal prism, also located at the left half of the unit cell, is formed by six Fe atoms (brown spheres) and is centred by the P atom (violet sphere). Also here, the P atom is coordinated by nine Fe atoms, three of which belong to the surrounding prisms. These three additional contacts are highlighted with blue lines in Fig. 15b.

Next, the structural differences will be remarked. Thus, in Fe_2P (Fig. 15b), each TCTP is surrounded by another six. Three of them, formed by the Fe atoms represented as brown spheres in Fig. 15b, are at the same height, and the other three, formed by the Fe atoms represented by medium green spheres, are displaced c/2 (Fig. 15b). On the contrary, in $LaCl_3$ (Fig. 15a), each TCTP is surrounded by only three columns, also displaced c/2, as it can be seen in Fig. 15a.

The most significant outcome of this structural dissection of $BaCl_2$ is that the Ba(2)Cl$(1)_3$ subarray reproduces fragments of the $LaCl_3$ structure [62]. This feature is, by no means, a coincidence, for it can also be rationalized in terms of the ***EZKC*** [14, 33, 63, 64], as it was the Ba_2Cl_3 subarray (Fig. 14c). Thus, if the Ba_2Cl_3 moiety transferred one electron to the Ba(1) atom, the former would become (Ψ-Cs)$BaCl_3$, whereas the latter, formed by Ba(1)Cl$(2)_3$, would convert into $(BaCl_3)^{-1}$. This pseudo-anion can be written as Ψ-$LaCl_3$ and is just the subarray represented in Fig. 14d. Because Ba and La are contiguous elements, the application of the ***EZKC*** results, in this special case, in a marvellous coincidence between the structures of Ψ-$LaCl_3$ and $LaCl_3$ itself! This justifies the use of $LaCl_3$ as a referent isostructural compound.

Another relevant consequence of this analysis is that *the hexagonal* $BaCl_2$ *structure is the result of two structural species that are interwoven*, i.e. $BaCl_3$ ($LaCl_3$ type) and Ba_2Cl_3, the fitting of the two entities being achieved through the common atom, Ba(1) at (0, 0, 0), which serves as a "*joker*" for both the CoSn (NiIn-type) and $LaCl_3$-type substructures.

The dimensions of both unit cells illuminate this feature. $LaCl_3$ ($\boldsymbol{P}6_3/m$) has $a = 7.48, c = 4.37$ Å and $BaCl_2$ ($\boldsymbol{P}\bar{6}2m$) has $a = 7.60, c = 4.35$ Å. They are almost identical, but their contents differ from La_2Cl_6 to Ba_3Cl_6. Thus, La_2Cl_6 needs one additional La atom to match the stoichiometry of $BaCl_2$ ($BaCl_3 + BaCl = Ba_2Cl_4 = BaCl_2$). This lacking atom is just the one drawn as a red sphere in Fig. 15a.

The important conclusion is that both substructures are interwoven. It seems that a sort of mutual (feedback) exchange of information occurs between them. We must emphasize that the insertion of the $BaCl_3$ prisms into the hexagonal tunnels (Fig. 15b) is not a question of space-filling. The $BaCl_3$ substructure needs the arrangement of the BaCl (CoSn type) subnet to extend its structure (Fig. 15). They necessitate each other, and it is by means of their coupling that both entities can fulfil their own structural requirements as much as possible.

6.3 The Ba Subarray in Hexagonal $BaCl_2$

If the Cl atoms are neglected, the resulting Ba subnet corresponds to that of the ω-Ti phase [65], which is a variant of the AlB_2-type structure discussed in Sect. 2.3 (Fig. 5). This Ba subarray is represented in Fig. 16a and can be compared with the

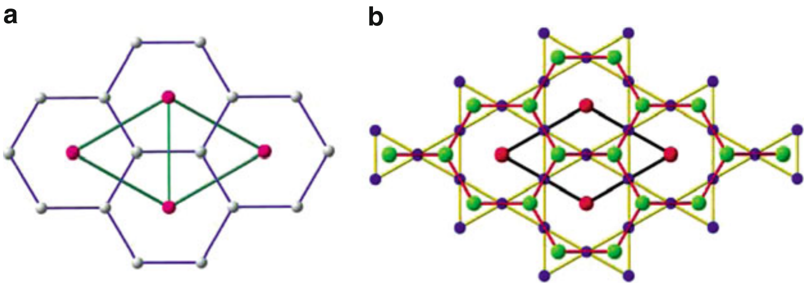

Fig. 16 (**a**) The Ba subarray in hexagonal $BaCl_2$ ($\boldsymbol{P}\bar{6}2m$) projected onto the *ab* plane. The *red spheres* represent the Ba(1) atoms at (0, 0, 0), forming hcp layers ($\mathbf{3^6}$ planar nets). The *grey spheres* represent the Ba(2) atoms at (1/3, 2/3, 1/2) forming graphite-like layers ($\mathbf{6^3}$ planar nets). The structure is identical to that of ω-Ti and similar to the AlB_2 structure drawn in Fig. 5d. (**b**) The structure of TaN ($\boldsymbol{P}6/mmm$) projected on the *ab* plane. *Red* and *green spheres* represent Ta atoms. *Blue circles* are N atoms

AlB_2 structure, drawn in Fig. 5a, d. Looking at Fig. 16a, which is comparable to Fig. 14e, one sees that the Ba (1) atoms (grey) form graphite-like $\mathbf{6^3}$ planar nets at $z = 0$. These $\mathbf{6^3}$ nets alternate with $\mathbf{3^6}$ layers formed by the Ba(2) atoms ($z = 1/2$), represented by red spheres in Fig. 16a. Note that all Ba atoms were represented by grey spheres in Fig. 14e. Compare also with the projection of the AlB_2 structure, represented in Fig. 5d.

An inspection of the nitride TaN [66] and of the suboxide δ-$TiO_{0.5}$ [67] reveals that both the Ta and Ti atoms are forming an ω-Ti structure type. In the case of δ-$TiO_{0.5}$, Andersson [67] had already noticed its structural relation to the ω-phases of some binary alloys of titanium, but his observation becomes meaningful when the ω-Ti phase was discovered some years later by Jamieson [65]. This phase of Ti belongs to the AlB_2-type structure and is formed by alternate $\mathbf{3^6}$ (*hcp*) and $\mathbf{6^3}$ (graphite-like) layers of Ti atoms, so that $TiO_{0.5}$ represents a new example of how the metallic nets are preserved in their oxides [3, 4, 67].

The comparison of the structures of TaN and δ-$TiO_{0.5}$ merits a further discussion. As shown in Fig. 16b, the structure of TaN is similar to the Ba_3Cl_3 subarray (Fig. 14e). More precisely, their cation arrays are coincident as it is shown in Fig. 16a.

The explanation of such similarities could be seen as a challenge, in view of the different chemical character of the atoms involved in these compounds (Ba, Ti, Ta, In, etc.), specially when the most relevant feature is the general appearance of the $\mathbf{6^3}$ (graphite-like) planar nets. This structural motif, characteristic of carbon (Group 14 elements), is also formed by pseudo-atoms (Ψ-C) (in the Klemm's approach) such as the B atoms in AlB_2 or MgB_2 (Fig. 5). In this context, we must recall that the formation of skeletons of the Group 14 was suggested to be a general trend in forming inorganic crystal structures [14]. Thus, the existence of such graphite-like layers in both ω-Ti and δ-$TiO_{0.5}$ is in agreement with the fact that, in anatase (TiO_2), the Ti atoms form a diamond-type network [68], a behaviour that is also consistent with the fact that in LiYGe [69], with a Fe_2P-type structure, it is precisely the Ge atoms which form the ω-Ti structure.

In the remaining compounds, namely $BaCl_2$, NiIn, NaBaP and NTa, the $\mathbf{6^3}$ layers can also be justified in terms of the ***EZKC*** [14]. In NaBaP [70], the transfer of one electron from Na to Ba converts the compound into (Ψ-Ne)(Ψ-LaP). An additional transfer of one electron from P to La would give rise to the transformation of P into Ψ-Si, hence justifying that the P atoms form the ω-Ti skeleton. As it will be seen below, the situation would be equivalent to that of $BaCl_2$. If we assume that the electron is transferred from Na to P, we would obtain the pseudo-array Ψ-BaS structure (isoelectronic to LaP!).

It should be remembered that these unexpected electron transfers have given satisfactory explanations of many structural skeletons [14, 33, 63, 64]. In $BaCl_2$ (Fig. 14a), although the one-electron transfer from each Cl atom to the Ba atom cannot be ensured, the compound is isoelectronic with the non-existing HfS_2. The importance of this relationship is the existence of the monosulphide HfS, with the WC-type structure. This structure, which shows some similarities with the TaN structure, differs, however, in that it does not contain the graphite-like layers. Instead, the W and C atoms form alternate $\mathbf{3^6}$ nets of W and C atoms.

This fact is important because the nitride TaN exists in both polymorphs, i.e. the TaN type (NiIn type) [66] (Fig. 16b) and the WC type [71]. Both phases, TaN and WC, undergo the TaN → WC phase transition at HT and HP. In any case, the existence of a II-VI compound, like Ψ-BaS, with a IV-IV structure is, by no means, a rare occurrence.

In the compound TaN and in NiIn, the transfer of one electron from Ta and Ni to the N and In atoms, respectively, would lead to the pseudo-formulae Ψ-HfO and Ψ-CoSn. In both cases, Ψ-Hf and Ψ-Sn atoms reproduce the ω-Ti structure, as in δ-$TiO_{0.5}$ [67]. Finally, in LiYGe (Fe_2P type) [68], the Ψ-ZrGe substructure is also ω-Ti type (Fig. 17).

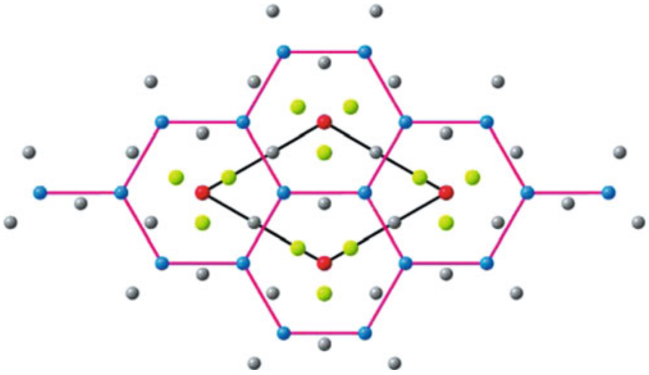

Fig. 17 The hexagonal structure of LiYGe (Fe_2P type) [69]. *Grey spheres* represent Y atoms. *Green spheres* are Li atoms, and *blue* and *red spheres* represent the Ge atoms which form the ω-type structure characteristic of the Group 14 elements

6.4 $BaCl_2$: The Cotunnite-Type Phase and Its Relation to the Fe_2P-Type Structure

We have seen that at ambient conditions $BaCl_2$ is cotunnite type (Co_2Si type) (***P***nma) [54] (recall that cotunnite is the mineral $PbCl_2$). Although this structure has been drawn repeatedly in this chapter, it is represented again, in Fig. 18, for the sake of comparison with the Fe_2P-type structure. We intend to highlight the similarities between both phases, contributing in this way to a better understanding of the transition $Fe_2P \rightarrow Co_2Si$ occurring between them [31, 55].

The $BaCl_2$ structure has been described, in previous sections, as related to both CoSn- and $LaCl_3$-type structures. In addition, we have remarked the peculiar ω-Ti-type structure of the Ba subarray. However, a careful inspection of Fig. 18a shows that, in the Fe_2P-type structure, there are implicit blocks of the cotunnite structure. Thus, the Fe_2P structure can also be thought of as the condensation of the zigzag chains of $BaCl_6$ trigonal prisms, i.e. the so-called TCTP [57], which form the cotunnite structure drawn in Fig. 18c. The resulting structure has a reflection twinning through the common plane $(\bar{1}1\ 0)$ (Fig. 18a).

An effective way of remarking this coincidence is to eliminate some of the atoms forming Fig. 18a, in such a way that two such zigzag chains become isolated, as shown in Fig. 18b. The chains are identical to those existing in the real cotunnite-like $BaCl_2$ represented in Fig. 18c, and the reader can see that if the two isolated chains of Fig. 18b approach each other, the cotunnite structure (Fig. 18c) can be reconstructed. This mechanism is only proposed as a didactic tool, just to show the similarities between both phases, but the real transition should occur through a reconstructive mechanism involving all atoms. A similar geometrical mechanism was proposed by Hyde and Andersson [57].

The two structure types must be very close in energy, as deduced from the structure of the compound NbCoB [72], which is an intergrowth of slabs of both Co_2Si- and Fe_2P-type structures. From the experimental data reported for $BaCl_2$ [55],

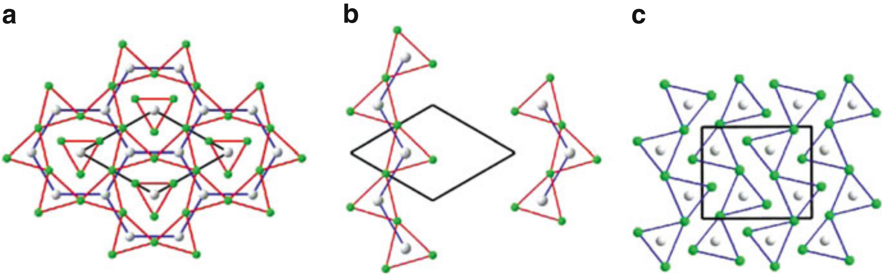

Fig. 18 (**a**) The hexagonal ($\boldsymbol{P}\bar{6}2m$) phase of $BaCl_2$, showing the TCTP centred by the Ba atoms. (**b**) Zigzag chains of trigonal $BaCl_6$ prisms existing in hexagonal $BaCl_2$. The chains have been isolated by eliminating both one Ba and one Cl atom from the array shown in (**a**). If the two chains approached each other, the cotunnite (Co_2Si-type) structure represented in (**c**) would be reconstructed

the high-pressure Co_2Si → Fe_2P-type transition involves a contraction from 63.1 $Å^3$ to 58.8 $Å^3$ per formula unit.

Our final comment will be devoted to remark the similarities between the Ba_3Cl_3 subarray of $BaCl_2$ (Fig. 14e), on the one hand, and the NiIn (CoSn-type) structure (Fig. 14f), on the other hand. The drawings evince that the BaCl subarray is related to the NiIn structure in the same manner that cotunnite is related to Ni_2In. Recall the additional cotunnite → Ni_2In transitions of Na_2S at HP [7] (Fig. 1) and the $\delta \rightarrow \theta$ transition, reported for Ni_2Si at HT [73].

6.5 Oxides Derived from the Fe_2P Structure: $LiNaSO_4$ and $LiCaPO_4$

In the previous sections, we have dealt with the structures of binary alloys of the Fe_2P type, but this skeleton also exists in the cation arrays of some oxides, such as $LiNaSO_4$ [74] and $LiCaPO_4$ [75]. These oxides crystallize in the S.G. $\boldsymbol{P}3_1c$, a subgroup of $\boldsymbol{P}\bar{6}m2$ (Fe_2P) by doubling the *c* axis. The similarities between the LiNaS subarray (LiCaP) and the structure of Fe_2P are reflected in Fig. 19a, b. $LiNaSO_4$, above 750 K, transforms into a cubic phase, probably a filled blende-type structure of which only the unit cell parameters are known [76]. A similar transition has not been reported, however, for $LiCaPO_4$.

If the Fe_2P-type structure is close in energy to that of the $PbCl_2$ type, the former might well be an alternative intermediate in the $PbCl_2$ → CaF_2 transition, fitting therefore into the general trend of the journey discussed in this chapter. Thus, in the same manner that Ag_2S undergoes a Co_2Si → CaF_2 transition [77] (see Scheme 1), a similar Fe_2P → CaF_2 transition could also take place.

In this context, it should be expected that, by increasing temperature, the oxides under discussion, i.e. $LiNaSO_4$ and $LiCaPO_4$, could stabilize the lower pressure phases, i.e. fluorite (or stuffed blende). It cannot be discarded that the HT phase of $LiNaSO_4$ could also adopt the cubic structure ($\boldsymbol{P}\bar{4}3m$) of $CsLiMoO_4$ [78], also a cubic phase in which the Na atoms are located at (1/2, 1/2, 1/2) forming with the

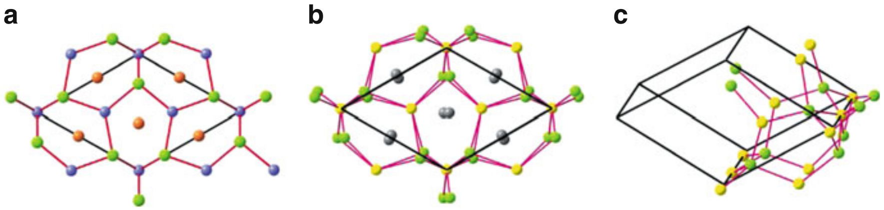

Fig. 19 (**a**) The structure of Fe_2P projected on the *ab* plane. *Green* and *brown spheres* represent Fe atoms. *Purple spheres* are P atoms. Both, Fe(1) and P atoms are connected by *red lines*. (**b**) The similar structure formed by the cations array LiNaS in $LiNaSO_4$. The Na atoms become Ψ-Ne and are represented by *grey spheres*. Li (*green*) and S (*yellow*) atoms form the Ψ-BeS subnet which is connected with *red lines*. (**c**) Perspective view of part of the Ψ-BeS subnet showing the three-, four-, and six-coordination of S(1), Ψ-Be(Li) and S(2), respectively

S atoms a rocksalt structure, whereas the LiS pair would form a zincblende-type arrangement. Here, we must recall the $PbCl_2 \rightarrow CaF_2$ transition undergone by $BaCl_2$ at 1,200 K [31].

The fact that the LiCaP subarray is a superstructure of Fe_2P is not surprising. It is strongly related to the property that alloys such as NaBaP [70] and NaSrP [79] adopt the same superstructure. These coincidences are additional examples of structural identity between alloys and oxides [4].

In sum, this section clearly shows that the Fe_2P structure is another "*missing link*" in the structural walk marked in Scheme 1. The phase transitions undergone by $BaCl_2$ suggest that it could probably be located between cotunnite and Ni_2In; in any case, close to the thenardite-type structure.

We must also discuss the skeleton formed by the Fe and P atoms (Li and S in $LiNaSO_4$) in the light of the general principle proposed by Vegas and García-Baonza [14] according to which, in any structure, a pair of atoms try to form a skeleton of the Group 14 elements. For instance, in the cation subarray of $LiNaSO_4$, represented in Fig. 19b, the transfer of one electron from Na to Li leads to the pseudo-formula (Ψ-Ne)[Ψ-BeS]. The formula inserted between brackets corresponds to a II-VI compound (yellow and green spheres in Fig. 19c).

All the Ψ-Be atoms are tetrahedrally coordinated by four S atoms. In contrast, the S atoms present two types of coordination, that is, the S(1) atoms are hexacoordinate, whereas the S(2) atoms are three-connected. Because the ratio S(1):S(2) is 1:2, and the mean *CN* is 4 for both S and Ψ-Be. Also, in this case, the four-connection applies to the whole cation array, as seen in Fig. 19c.

The Fe_2P-type structure evidences a cut-off in the general fourfold connection of unlike atoms which is completely lost *along the way* in both thenardite and spinel (note that we are always referring to either alloys or cation arrays in oxides). In Fe_2P, the situation is a compromise, with *CN* of 3, 4 and 6. This is a clear indication that the Fe_2P-type structure could join thenardite as an intermediate step in the olivine → spinel transition. We cannot adventure, at present, in which order the changes take place. The fact that the number of isostructural compounds is scarce indicates that the range of stability of these structures must be very narrow, transforming rapidly into the spinel structure. Should they be considered then as short life or *small stability range* structures?

7 The High-Temperature $Fe_2P \rightarrow$ Wurtzite Transition

In Sect. 2, we noted the reversibility of the $Ni_2In \Leftrightarrow CaF_2$ transitions in Li_2S [6] and Na_2S [7]. It was also outlined the phenacite → anti-CaF_2 transition of Li_2SO_4 at high temperatures [32].

These features are also supportive of the tendency of cations to form four-connected skeletons, characteristic of the Group 14 elements [14]. Thus, in the HT phases of both $NaLiSO_4$ [76] and $CsLi(MoO_4)$ [80], the blende-type networks of the atom pairs [LiS] and [LiMo], respectively, can be justified by the electron

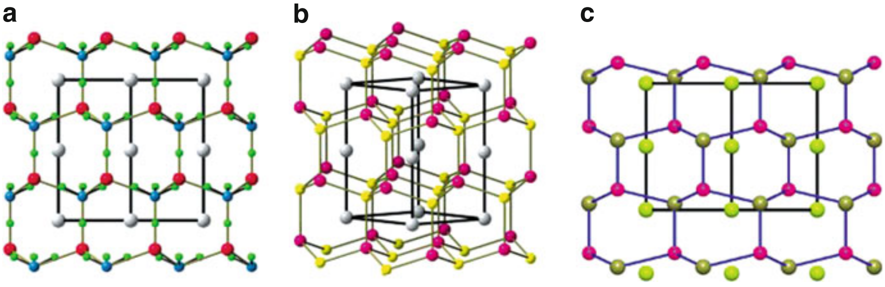

Fig. 20 (**a**) The structure of $KLiBeF_4$ projected on (110). Both the Li and Be atoms (*red* and *blue*, respectively) are forming a wurtzite-like array stuffed with the K atoms (*grey*). The F atoms (*small green spheres*) are located close to the hypothetical Li–Be bonds. (**b**) A perspective view of the $KLiSO_4$ exhibiting the same wurtzite-like array of the $[LiS]^-$ subarray (*red* and *yellow* spheres). The K atoms are also filling the four-connected network. The O atoms have been omitted for clarity. (**c**) The cation array of the hexagonal HT phase of Ca_2GeO_4. The Ca (1) atoms located at (0, 0, 0) and (0, 0, 1/2) form $\mathbf{3^6}$ (*hcp*) layers. Both the Ca (2) and Ge atoms produce a four-connected, distorted wurtzite-like network. The O atoms have been omitted

transfer from Na (Cs) to the most electronegative Li atoms. The same occurs with the HT phase of $CsLi(CrO_4)$ [81] which is converted into (Ψ-Xe)[Ψ-$BeCrO_4$], with a blende-type Ψ-BeCr subarray.

It is important to remark that $KLiBeF_4$ [58], with a cation array of the Fe_2P type, transforms into filled wurtzite-like structures at HT, as it can be seen in Fig. 20a, b, respectively. The related $LiKSO_4$ also adopts this wurtzite-type arrangement [59]. In terms of the ***EZKC***, this transition would imply that the most electropositive K atoms would transfer one electron to the Li atoms converting them, respectively, into K^+[Ψ-$BeBeF_4$] and K^+[Ψ-$BeSO_4$], whose Be and BeS skeletons are, in turn, wurtzite type.

In the case of the anti-fluorite-type compounds Na_2S and Li_2SO_4, the electron transfer between atoms of the same kind could be seen as weakly founded, because each Na(Li) atom is forming, with the S atom, two indistinguishable structures, which have been interpreted as resonance structures [33]. However, the formation, at HT, of a stuffed wurtzite-type structure by Ca_2GeO_4 (Fig. 20c) gives support to our approach. In this special case, the two Ca atoms are located in unequivalent positions. Because in ZnS the blende → wurtzite transition occurs at HT, it is also possible that our *walk*, depicted in Scheme 1, might well commence with this new polymorph. The phase transitions undergone by Ca_2GeO_4 will be analysed in greater extent below.

8 The Post-Spinel Structures Under Pressure

The structural sequence initiated with the anti-fluorite structure does not stop at the spinel structure. At higher pressures, the $\boldsymbol{AB}_2$ binary alloys and the spinel-type oxides ($\boldsymbol{AB}_2O_4$) undergo additional phase transitions.

Liu and Bassett [16] have summarized the behaviour of some $\boldsymbol{AB}_2O_4$ oxides under pressure, which can be illustrated with the olivine-like Mn_2GeO_4. Under pressure the latter undergoes a first transition to the spinelloid β-phase (***I***mma), followed by a second transition to a Sr_2PbO_4-type structure [19]. At more elevated pressures, the compound decomposes into two components (perovskite + rocksalt) [16].

On the contrary, the compound Ca_2GeO_4, also olivine type at ambient conditions [20], shows a different response. At HT, Ca_2GeO_4 transforms into a Ca-stuffed tridymite-like structure, whereas, under pressure, the compound undergoes the olivine → Sr_2TiO_4 (Ba_2SnO_4) transition, which also decomposes at more elevated pressures [16]. These decomposition processes will be discussed in depth below.

More recent studies have shown that spinels of formula $\boldsymbol{M}_2MgO_4$, such as Al_2MgO_4, may adopt under pressure any of the interrelated Fe_2CaO_4-, Mn_2CaO_4- or Ti_2CaO4-type structures [82]. The different $\boldsymbol{M_2X}O_4$ oxides do not follow a uniform pattern. Thus, Al_2ZnO_4 remains, up to 43 GPa, in the cubic spinel structure [83], whereas Fe_2ZnO_4 transforms into either a Fe_2CaO_4- or a Ti_2CaO_4-type structure beyond 24 GPa [84].

In Mn-containing spinels $Mn_2\boldsymbol{X}O_4$, cubic-to-tetragonal transitions have been observed at pressures as low as 12 GPa [85], and in a more recent paper [86] a double phase transition has been reported for the cubic spinel Ga_2ZnO_4. A first cubic → tetragonal (Mn_2ZnO_4 type) transition is followed by a second transition to the orthorhombic marokite structure (Mn_2CaO_4), related to that of Sr_2PbO_4 type (also Ca_2SnO_4).

In Table 4 are collected several germanates, stannates and titanates and their behaviour under pressure, as reported by Liu and Basset [16]. This information will help the reader to follow all the structures we will describe next, as well as the phase transitions and final decompositions experienced by these compounds under compression.

The intermediate tetragonal spinel structure will be neglected because its cation array is a slight distortion of the cubic polymorph. In the same way, some structure types, such as Mn_2CaO_4 (mineral marokite), Ti_2CaO_4 and Fe_2CaO_4, strongly

Table 4 Crystal structures, at 1 bar (**X**), and decomposition products at high pressure (**H**) of the compounds A_2GeO_4, A_2SnO_4 and A_2TiO_4

Compound	Spinel	Ilmenite + Rocksalt	Sr_2PbO_4 Ca_2SnO_4	Ba_2SnO_4	Corundum + Rocksalt	Rocksalt + Rutile	Perovskite + Rocksalt	Rocksalt + Fluorite[a]
Mg_2GeO_4	X					H		H
Mn_2GeO_4	X	H(?)	H					H
Ca_2GeO_4				H				
Co_2SnO_4	X					H		H
Zn_2SnO_4	X	H(?)						H
Ca_2SnO_4			X				H	H
Mg_2TiO_4	X	H						H[b]
Fe_2TiO_4	X	H			H[b]			H[b]
Cd_2TiO_4			X(?)				H	H

[a] Recall the transformation SnO_2 (rutile) → SnO_2 (fluorite). The transition TiO_2 (rutile) → fluorite-related also occurs some below 25 GPa

[b] These phase separations have been confirmed in the ilmenite-type titanates

related to the Sr_2PbO_4 type, will not be considered. Our discussion will commence with the isostructural Ca_2SnO_4 compound.

8.1 The Structure of Ca_2SnO_4 and Related Compounds

Ca_2SnO_4 belongs to the Sr_2PbO_4 type (***P***nma) [87, 88]. As seen in Table 4, this structure remains stable, under compression, up to its decomposition into the perovskite $CaSnO_3$ and the rocksalt CaO phases, i.e. no phase transition has been observed so far.

Another interesting compound is Mn_2GeO_4 [18]. It is spinel at ambient conditions but transforms into the Sr_2PbO_4 type under pressure, decomposing at higher pressures. Two decompositions have been reported [16], i.e. $MnGeO_3$ (ilmenite) + CaO (rocksalt) and the alternative GeO_2 (fluorite) + 2 MnO (rocksalt) (Table 4).

On the other hand, Sr_2SnO_4 has four polymorphs (***C***mca, ***P***4_2/ncm, ***P***ccn, and ***I***mmm). All these phases, closely related between them, are slight distortions of the Ba_2SnO_4-type structure (***I***4/mmm) [89] which at more elevated pressures decompose into perovskite + rocksalt (Table 5). The data discussed above can be summarized by saying that the $\boldsymbol{M}_2\boldsymbol{X}O_4$ oxides can follow the pressure-induced transitions Al_2MgO_4 (spinel) → Sr_2PbO_4 → Ba_2SnO_4. At higher pressures, they decompose in different ways, as summarized in Table 4. The new structural types Sr_2PbO_4 and Ba_2SnO_4 have been added to Scheme 1.

Next, we will focus on the description of the Ca_2SnO_4 structure which is orthorhombic (***P***bam), with $a = 5.64$, $b = 9.69$, $c = 3.26$ Å, $Z = 2$ and is projected along the shortest c axis in Fig. 21. The Ca_2Sn subarray is drawn in Fig. 21a.

At first glance, the structure can be described as a set of almost regular tetragonal prisms of Ca atoms (green), filled by Sn atoms (grey). The prisms share faces forming columns along the c axis. One of these columns is at the centre of the unit cell of Fig. 21a and has been isolated in Fig. 21d. The dimensions of these Ca prisms (3.18 × 3.26 × 5.27 Å) acquire a special importance to understand the structure. It is worth mentioning that we have not found any binary alloy isostructural to the Ca_2Sn subarray. This important exception will be discussed later.

Figure 21a clearly shows that the columns of prisms are tilted around the c axis. This tilting gives rise to additional Ca–Ca contacts that form fragments with the

Table 5 The unit cell dimensions (in Å) of the $BaSnO_3$ and BaO fragments co-existing in Ba_2SnO_4. They are compared with the corresponding values in the pure phases, i.e. the $BaSnO_3$ perovskite, the HP phase of the BaSn alloy (CsCl type) and the BaO (NaCl type). These fragments are depicted in Fig. 20

	Ba_2SnO_4	$BaSnO_3$	BaSn	BaO
$BaSnO_3$	4.14 × 4.14 × 3.8 mean 4.05	$a = 4.11$	$a = 4.05$ Å	a = 5.72 $d_{Ba–Ba} = 4.08$
BaSn	$a = 4.12$	$a = 4.11$	$a = 4.10$ Å	–
BaO	$a = 5.75$	$a = 5.81$	–	$a = 5.53$ $d_{Ba–Ba} = 3.91$

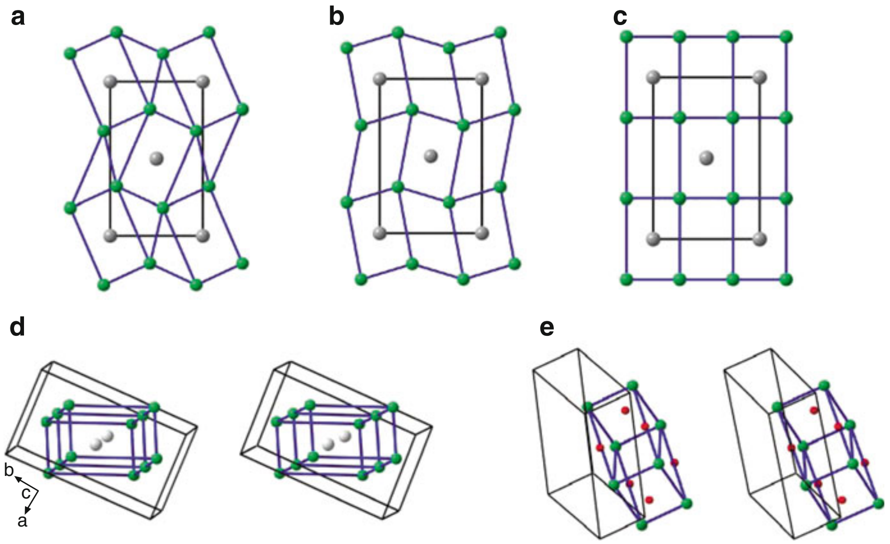

Fig. 21 (**a**) The Ca_2Sn subarray of the structure of Ca_2SnO_4, viewed along the *c* axis. The almost tetragonal prisms of Ca atoms (*green spheres*) are centred by the Sn atoms (*grey spheres*). (**b**) Artificial tilting of the prisms to see how the real structure could be derived from an ideal structure represented in (**c**) where tilting has been completed. (**d**) Stereopair showing the blocks of $SnCa_8$. (**e**) Stereopair showing the Ca blocks which connect the different blocks of prisms. Note that the O atoms have also been drawn to show the simultaneous existence of CaO fragments

topology of the *fcc*-Ca structure. Such a fragment is isolated in Fig. 21e, where we have drawn the Ca–Ca contacts. The O atoms have been included to show that these blocks are really fragments of a CaO (rocksalt) structure. Within these fragments, the most significant Ca–Ca distances are 3.17, 3.26, 3.58 Å and 5.27 Å. The mean value of the three shortest distances is 3.34 Å, which in the frame of a *fcc* structure would correspond to a unit cell of $a = 4.72$ Å. This value almost equals the unit cell of the rocksalt CaO ($a = 4.81$ Å, $d_{\text{Ca–Ca}} = 3.40$ Å) (compare with 3.34 Å in Ca_2SnO_4). Because the *fcc* structure of elemental Ca is maintained in CaO, the fragments connecting the prisms also conform to the *fcc* topology.

Taking as reference Fig. 21d, if the diagonals of the bases of prisms are drawn, we obtain two almost perpendicular (1 0 0) faces of a CaO-like structure. This new fragment is represented in Fig. 22 and corresponds to one half of a unit cell of CaO, where two Ca atoms have been substituted by two Sn atoms. As seen in Fig. 22, the Sn atoms are located close to the centre of the two (1 0 0) faces of an ideal cubic structure. The mean Ca–O–Ca distance is 4.91 Å, a value that compares well with the unit cell of CaO (4.81 Å). However, the Ca and the Sn atoms, rather than a *fcc*-Ca unit cell, form one half of the unit cell of a CuAu-type alloy.

Coming again to Fig. 21a–c, it is clear that the tilting of the prisms is not capricious but responds to the need of preserving the structure of CaO and, hence, of *fcc*-Ca. Thus, the ideal structure formed with untilted Sn-filled prisms

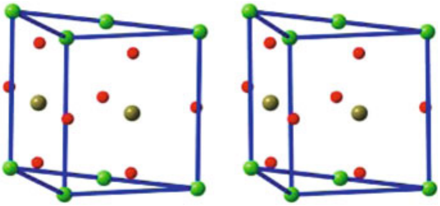

Fig. 22 Stereopair of a fragment of the Ca_2SnO_4 structure. It coincides with a unit cell of CaO, which has been truncated by the (110) plane. Both the (001) and $(00\bar{1})$ faces are centred by Ca atoms, whereas both the (100) and (010) are centred by Sn atoms. The latter have dimensions of 4.55 × 5.27 Å (mean, 4.91 Å). Note that some O atoms are displaced from the Ca–Ca edges towards the Sn atoms, to satisfy the Sn–O distance

(Fig. 21c) should be, in principle, unstable and should convert, through a concerted rotation, into the real structure of Fig. 21a, forming in this way the additional Ca–Ca contacts.

The coexistence of the $SnCa_8$ prisms and the Ca blocks suggests that the Ca_2Sn subarray might be formulated as the sum of CaSn + Ca. If the O atoms are taken into account, Ca_2SnO_4 could then be contemplated as an intergrowth of $CaSnO_3$ + CaO. This "conceptual decomposition" is based on both the topology and the distances in the Ca blocks represented in both Figs. 21d, e and 22.

The partial formula $CaSnO_3$, and hence the cation subarray CaSn, has the stoichiometry of a perovskite, such as the real one $CaSnO_3$ [90], a compound that has also been obtained as ilmenite type [91]. Surprisingly, the $SnCa_8$ prisms in Ca_2SnO_4 (Fig. 21d) are neither perovskite- nor ilmenite-like.

In view of this discrepancy, it is important to consider again the dimensions of the prisms (3.18 × 3.26 × 5.27 Å), which can here be averaged to tetragonal prisms with $a = 3.22$ and $c = 5.27$ Å. The important outcome is that these dimensions are comparable to the unit cell of elemental Indium (***I***4/mmm, $a = 3.25$, $c = 4.95$ Å). An analysis of the cubic In_2O_3 structure [92] has shown that the structure of elemental In remains almost unchanged in the bixbyite-type oxide In_2O_3, where there exit distorted tetragonal prisms of In with dimensions of 3.35 × 3.35 × 5.06 Å (compare with the CaSn prisms).

This coincidence is by no means casual. It becomes physically meaningful if we assign to the CaSn pair (II–IV) of atoms the same role as the isoelectronic In (III) or Sc atoms (*C*-Sc_2O_3 is also bixbyite type). In fact, if we apply the ***EZKC*** [14], the transfer of one electron from Sn to Ca would convert them into Ψ-In and Ψ-Sc, respectively. Then, the $CaSnO_3$ moiety could be formulated as [Ψ-ScΨ-In]O_3 and regarded as a fragment of the bixbyite-type oxides Sc_2O_3 and In_2O_3. Recall that in these sexquioxides, the structure of the parent metal is preserved [92].

On the other hand, we mentioned above that the columns of $SnCa_8$ prisms are also fragments of an AuCu-type structure (***P***4/mmm) (Fig. 22). This structure is found in similar compounds such as InMg (3.24 × 4.48 Å), $Ga_{0.4}Mn_{1.6}$, FeSe, AlTi, CsI, BiNa (3.46 × 4.80 Å), *and surprisingly in CaPb (3.62 × 4.49 Å) and in InSc itself (3.20 × 4.32 Å)!*

The correlation between $CaSnO_3$ and the bixbyite type finds support in the two facts that $CaSnO_3$ is also obtained as an ilmenite-type polymorph [91], and that, at the same time, In_2O_3 undergoes the bixbyite → corundum transition at 65 kbar and 800–1,300 K [93] (note the structural similarities between ilmenite and corundum structures). Thus, it is not surprising that $CaSnO_3$, when forming part of the Ca_2SnO_4 compound, adopts one of the stable structures of the isoelectronic In_2O_3, i.e. in this case, fragments of the bixbyite-type structure.

If Ca_2SnO_4 had adopted the ideal structure of Fig. 21c, with alternate columns of both empty and Sn-filled prisms of Ca atoms, the empty prisms would produce the new Ca–Ca contacts with the adjacent prisms. This would be achieved by tilting the filled prisms, producing a denser packing of the Ca atoms as illustrated by the sequence of structures represented in Figs. 21a, b, c and 22.

When the O atoms are considered we obtain Fig. 23a, which shows how the Sn atoms are coordinated octahedrally by six O atoms. The SnO_6 octahedra share edges, forming chains parallel to the *c* axis (perpendicular to the projection plane). These octahedral chains are really fragments of the rutile-like structure of SnO_2, represented in Fig. 23b, and are arranged as if the columns of Ca_2SnO_4 would be ready to reconstruct the rutile structure in case the Ca_2O_2 fragments disappear.

In Fig. 23a, we see that O atoms are located at the middle point of the longest edges of the $SnCa_8$ prisms. These O atoms have a double role. On the one hand, they form Ca–O–Ca edges like in the rocksalt CaO structure (Fig. 22). On the other hand, they contribute to form the fragments of the rutile-like SnO_2 structure. Taking this feature into account, it is easy to imagine that if the Ca–O–Ca edges could be eliminated, the structure would collapse producing the rutile-like network depicted in Fig. 23b. The impression therefore is that the Ca_2SnO_4 structure would be "*well prepared*" to reconstruct the SnO_2 (rutile-type) structure.

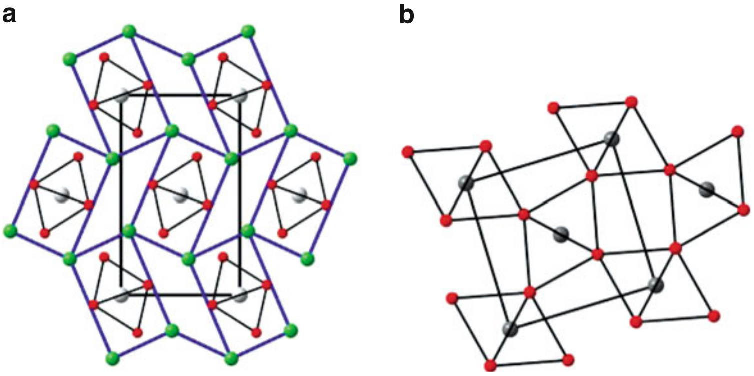

Fig. 23 (**a**) The structure of Ca_2SnO_4, viewed along the *c* axis, in which the O atoms (*red spheres*) have been drawn. The SnO_6 octahedra share edges forming chains perpendicular to the projection plane. (**b**) The structure of the rutile-type SnO_2 showing the similarity of the SnO_6 octahedra in both compounds. The tetragonal unit cell of SnO_2 has dimensions of $a = 4.74$, $c = 3.19$ Å and is projected on the *ab* plane

This interpretation could justify why some of the compounds listed in Table 5 produce ilmenites and rutiles as sub-products of decomposition. We will see later that the appearance of perovskites can also be explained.

8.2 Extension to Mn_2GeO_4: The Olivine-, Spinel- and Sr_2PbO_4-Type Structures

Mn_2GeO_4 crystallizes in three polymorphs. At ambient conditions it is olivine-like (***P***nma) [17], undergoing two high-pressure high-temperatures transitions [19]. The first one is a tetragonal spinelloid β-phase (***I***mma), transforming at higher pressures into the Sr_2PbO_4-type structure (***P***bam).

Although Mn_2GeO_4 is isostructural with Ca_2SnO_4, a detailed discussion of its structure will doubtless clarify many of the peculiarities discussed about Ca_2SnO_4. The relationships that can be established between the cation subarray of Ca_2SnO_4 and the corresponding Ca:Sn alloys will be of special importance.

In the Ca–Sn system, two phases have been reported. The first one is Ca_2Sn (***P***nma, anti-$PbCl_2$ type) [94]. The second one is CaSn, CrB type, undergoing the pressure-induced CrB → CsCl-type transition [2]. In addition to these alloys, it should be recalled that the fragments of the SnO_2 (Fig. 22) can be justified if we formulate the compound as $(CaO)_2SnO_2$.

We have seen that the existence of blocks of a bixbyite-type structure was interpreted as if a II-IV compound (CaSn) was chemically equivalent to a III-III subarray, such as elemental indium. Thus, $(CaO)CaSnO_3$ should be equivalent to $CaO(\Psi\text{-}In_2O_3)$, in which $\Psi\text{-}In_2O_3$ are fragments of real $C\text{-}In_2O_3$ (also $C\text{-}Sc_2O_3$). Thus, the equivalence between the CaSn subarray and the In structure is evident.

Ca_2SnO_4 can also be compared with the Ca_2Sn alloy. The latter is anti-$PbCl_2$, whereas the oxide stabilizes a Ca_2Sn subarray which could not be related to any known alloy. This was the reason why, in the above section, the Ca_2Sn substructure was fragmented to find relationships with other structures.

This feature contrasts with that shown by the related compounds Ca_2Ge and Ca_2GeO_4 [94]. It is especially problematic when we try to explain the formation of Ca_2SnO_4 (Sr_2PbO_4 type) in terms of the *equivalence oxidation–pressure*. Because the Ca_2Sn subarray is anti-$PbCl_2$ type, it should be expected that, when oxidized, the Ca_2Sn subarray should necessarily undergo the complete transition series Ni_2Si → Ni_2In → $TiSi_2$ → $MgCu_2$ → Ca_2Sn. Of these, only the initial and the final states have been identified, the former for Ca_2Sn and the latter in Ca_2SnO_4. This implies that Ca_2Sn is forced to undergo the direct transition Ni_2Si to $Ca_2Sn[O_4]$.

This extreme transition does not occur in Ca_2GeO_4 (see Scheme 1). At ambient conditions the compound is olivine-like [20]. As discussed above, at high temperature, it transforms into a Ca-stuffed wurtzite-like network of composition $CaGeO_4$, and under compression it becomes Ba_2SnO_4 type [16, 21]. Thus, Ca_2Ge is observable as $Ca^{2+}[\Psi\text{-}Ge_2O_4]$, as Ni_2In type and finally as Mo_2Si type, which is the structure type of the Ba_2Sn subarray in Ba_2SnO_4.

These difficulties are partially solved by examining the compound Mn_2GeO_4. This olivine-like phase [17] is transformed into a modified spinel (***I***mma) at 6.4 GPa and 1,513 K, and a second phase (***P***bam), of the Sr_2PbO_4 type, is obtained at the same pressure, but at a lower temperature (1,113 K) [19]. That means that the denser phase ***P***bam transforms into the modified spinel (***I***mma) by increasing temperature, following the behaviour of the data collected in Scheme 1.

In what follows, the cation arrays of the three phases of Mn_2GeO_4 will be discussed in connection with the Mn_2Ge alloy. Only one phase has been reported for Mn_2Ge. It is Ni_2In type (***P***6_3/mmc) and is stable above 1,063 K [95]. The important issue here is that this structure corresponds to the cation array of the olivine-like phase of Mn_2GeO_4 [17].

Because the oxide is also stable as a modified spinel structure (***I***mma), and also in view of that the Ni_2In-type structure is only stable above 1,063 K, the question arises whether Mn_2Ge could undergo a $Ni_2In \rightarrow MgCu_2$-type transition, giving therefore support to the existence of the modified spinel Mn_2GeO_4. As far as we know, such a cubic Laves phase has never been reported. However, related Laves phases of compositions $MnNi_{1.3}Ge_{0.7}$ and $MnNi_{1.55}Ge_{0.45}$ have been synthesized [96]. The former is hexagonal, $MgZn_2$ type (***P***6_3/mmc) and the latter is $MgCu_2$ type ($\boldsymbol{F}d\bar{3}m$).

Although these compounds do not have the stoichiometry of the cation array of Mn_2GeO_4, the pseudo-formula Ψ-Mn_2Ge can be easily obtained by applying the ***EZKC*** in the following way.

$MnNi_{1.55}Ge_{0.45}$ can be reformulated as $MnNi(1)Ni(2)_{0.55}Ge_{0.45}$. Following the pseudo-atom ***EZKC***, if we consider that Ni(1) donates three electrons to $Ni(2)_{0.55}$, $Ni(1)^{3+}$ would become pseudo-Mn [Ψ-Mn(1)], whereas $[Ni(2)_{0.55}]^{3-}$ is converted into the hypothetical $Ni(2)^{5.5-}$ cation. This formal charge is much greater than that needed to convert Ni(2) into Ψ-Ge (four electrons). Thus, with the reported stoichiometry, the pseudo-formula Mn_2Ge cannot be attained. However, if we admit small variations in the composition of the alloy, the pseudo-formula Ψ-Mn_2Ge is possible. This assumption is made on the basis of the lack of accuracy in the composition of many of these alloys and considering also that, in many instances, the powder diffraction data short of the accuracy needed to obtain reliable values of the site occupancy factors [96].

Thus, the slightly modified formula of $Mn_{1.1}Ni_{1.50}Ge_{0.4}$ could also be re-written as $Mn_{1.1}Ni(1)_{0.9}Ni(2)_{0.6}Ge_{0.4}$. Proceeding in the same manner, the electron transfer from Ni(1) to Ni(2) would give rise to a Ψ-Mn_2Ge formula, corresponding to the cation array of the high-pressure spinelloid Mn_2GeO_4 [19].

We must also mention that the structures of the isoelectronic compounds FeGeMo and VCoSi are hexagonal Laves phases ($MgZn_2$ type), and that the related compound $ZrV_{0.5}Mn_{0.5}Ni$ adopts the cubic $MgCu_2$-type structure. An adequate electron transfer, involving V, Mn and Ni atoms, entails that $ZrV_{0.5}Mn_{0.5}Ni$ can be formulated as Ψ-ZrCoMn, coincident with the "real alloy" ZrCoMn, a cubic Laves phase [97].

We have discussed so far the structural relationships of the pair Mn_2Ge/Mn_2GeO_4, making special emphasis on the well-known relationships olivine-spinel (spinelloid) and the corresponding Ni_2In ⇔ $MgCu_2$-type transition. At the same time, it has been shown that the phase transitions undergone by both oxides and alloys follow the expected behaviour shown by many other similar compounds listed in Scheme 1.

We think, however, that the formation of the HP phase Sr_2PbO_4-type structure of Mn_2GeO_4 [18, 19] deserves an additional analysis, especially, when the partial substructures of Mn_2GeO_4 are compared with those of the own Ca_2SnO_4.

The discussion of the structure of Ca_2SnO_4, based on the drawings of Figs. 21–23, can be extended to the isostructural Mn_2GeO_4 [18, 19]. These simple structures will be useful for several reasons. First, they will show the parallelism between both the Ca_2Sn and Mn_2Ge arrays, in spite of the strong chemical differences of both Ca and Mn. Second, they will help to understand the structure of the Ca_2Sn (Mn_2Ge) skeleton itself. Finally, the consideration of these alloys will show that the structures of the oxides (Ca_2SnO_4 and Mn_2GeO_4) fit into the framework developed in Scheme 1.

Let us begin our discussion by establishing the analogy of Mn_2GeO_4 structure with the fragments of the byxbyite-type structure discovered in Ca_2SnO_4. Thus, if the compound is formulated as $MnGeO_3$ + (MnO), we see that both moieties, $MnGeO_3$ and $CaSnO_3$, form ilmenite-like structures under compression [91, 98]. We must stress that the related compounds $Mn_{0.7}Co_{0.3}GeO_3$ [97] and In_2O_3 [93] are also ilmenite type at high temperatures and pressures. In addition to this, we must recall that, at ambient conditions, *C*-In_2O_3 has its Mn-containing analogue [99], i.e. Mn_2O_3, the mineral bixbyite itself!

In the previous Sect. 8.1, we accounted for the similarity of the CaSn array in the sub-structure $CaSnO_3$ with the isoelectronic elemental indium, and hence with the *C*-In_2O_3 structure [92]. Now, we can add that in thin films, elemental Mn also adopts the In-type structure (***I***4/mmm) [100]. Moreover, the existence of the isostructural alloy $Ge_{0.23}Mn_{0.77}$ [101] is a clear indication that MnGe could also well adopt this structure type, as it occurs in the Mn_2GeO_4 oxide. These features would be an appealing justification of the isostructurality of both Ca_2SnO_4 and Mn_2GeO_4 compounds.

The reader can find additional support in Fig. 23, where it is remarked that the Ca (Mn) tetragonal prisms were centred by GeO_6 (SnO_6) octahedra. These octahedra, as in Ca_2SnO_4, are likewise fragments of the high-pressure rutile-like phase of GeO_2 [102] (Fig. 22b). The structure also contains fragments of the *fcc*-array of Mn (Ca), which are in fact halves of unit cells of the rocksalt manganosite (MnO) [103] (Figs. 21 and 22).

The unit cell dimensions of all the structures involved also give support to these relationships. Thus, in Mn_2O_3 (bixbyite), the Mn atoms form a distorted *fcc*-array whose tetragonal unit cell has average dimensions $a = 3.35$, $c = 4.72$ Å. The corresponding prisms, in the high-pressure phase of Mn_2GeO_4, have dimensions of $a = 2.95$, $c = 5.04$ Å, whereas in the rocksalt phase of MnO the corresponding dimensions are $a = 3.14$, $c = 4.45$ Å. The GeO_2 rutile-type fragments in HP-Mn_2GeO_4 are separated by a distance of 2.87 Å, along the *c* axis. This value agrees with the *c* axis of 2.88 Å in pyrolusite (the rutile-type MnO_2) and also with the same parameter in HP-GeO_2 (2.87 Å) [102]. When all these magnitudes are compared, one sees that the structure of HP-Mn_2GeO_4 [18, 19] is a compromise to satisfy all these structural and geometrical requirements.

As an example, we can outline that the shortest Mn–Mn distances, i.e. 3.35 Å in bixbyite (Mn_2O_3) [98], 2.88 Å in pyrolusite (MnO_2) [104], 2.87 Å in the rutile-like, HP-GeO_2 [102] and 3.14 Å in manganosite (MnO) [103] average to a value of 3.06 Å, which is quite close to that of 2.95 Å observed in Mn_2GeO_4. This is the value of the projection axis in Fig. 20 [18, 19].

8.3 Ca_2SnO_4 and the FeB Structure

We have mentioned in this section that we could not find any A_2B alloy isostructural to the cation subarray of Ca_2SnO_4. However, the subarrays Ca_2Sn and Mn_2Ge, drawn in Figs. 21a and 23a, admit an alternative interpretation. When Fig. 21a is rotated around the projection axis, Fig. 24a is obtained. On the right side in Fig. 24b, we have drawn the FeB structure (***P***nma), viewed along **b**. In spite of their different stoichiometry (A_2B vs. AB), both structures exhibit a surprising similarity in projection. The FeB-type structure is adopted by the cation arrays of many oxides, such as BaS in barite ($BaSO_4$), $BaMnO_4$, $BaFeO_4$, $BaSeO_4$, $SnSO_4$ and $PbSeO_4$ [5],

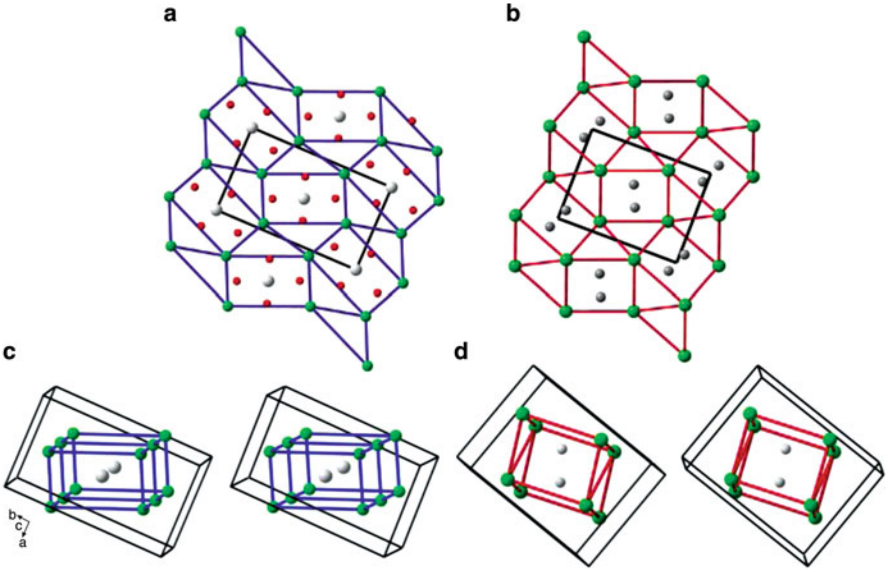

Fig. 24 (**a**) The structure of Ca_2SnO_4 (as in Fig. 16a), but rotated around the projection axis to facilitate its comparison with the TiSi structure (FeB type, ***P***nma), represented in (**b**). In (**c**) and (**d**), we have drawn the isolated Sn-filled prisms which centre the respective unit cells. [57]

and was dissected by Vegas et al. [105]. Although FeB is considered as the aristotype, we will take, for convenience, the isostructural TiSi alloy as the reference compound [106].

The resemblance of both structures (Ca_2SnO_4 and FeB) disappears when the structures are drawn in perspective, as it can be observed in Fig. 24c, d. As stated above, in Ca_2SnO_4, the central prisms Ca_8Sn (3.26 × 3.17 × 5.27 Å) are close to the unit cell of Indium (***I***4/mmm) (a = 3.25, c = 4.95 Å) (Fig. 24c), whereas in TiSi (FeB) the prisms are trigonal and are filled with the Si(B) atoms (Fig. 24d).

To illustrate these differences, the two sorts of prisms are drawn in Fig. 25. They are projected along the fourfold and threefold axes in Ca_2Sn (Fig. 24a) and TiSi (Fig. 24c), respectively. This drawing reflects clearly the difference in stoichiometry which entails that, in Ca_2Sn (2:1), the Sn atoms are surrounded by 8 Ca atoms, in contrast to the Ti_6 trigonal prisms, filled by the Si atoms in the TiSi (FeB) structure (1:1).

In spite of the discrepancies between both patterns (Fig. 25a, c), the TiSi structure (Fig. 25c) could ideally be derived from that of Ca_2Sn (Fig. 25a), by eliminating one half of the Ca atoms. This would lead to the drawing of Fig. 25b, which corresponds to the stoichiometry 1:1 (CaSn), as in TiSi. In this state, the Ca and Sn atoms should rearrange to form the trigonal prisms of the TiSi structure (Fig. 25c). To achieve this, the Ca atoms of the upper and lower lines of Fig. 25b should move in opposite directions along the c axis (the shortest axis) leading to the pattern of TiSi (Fig. 25c). The opposite conversion (TiSi → Ca_2Sn) could also be imagined if two Ti atoms are added to the TiSi trigonal prisms (Fig. 25c). In this case, atoms must move to convert two rhombs into two squares, as illustrated in Fig. 24a.

We believe that this is the appropriate point to reaffirm the formulation of the Ca_2Sn subarray as Ca + CaSn, in the same manner that, as was advanced in the previous Sect. 7, Ca_2SnO_4 can be contemplated as the intergrowth of blocks of $CaSnO_3$ (In_2O_3 type) and CaO (rocksalt).

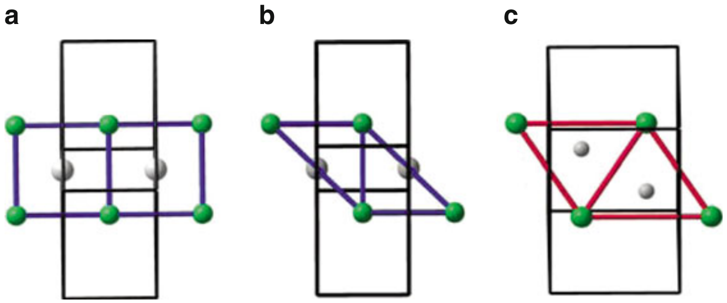

Fig. 25 (**a**) The tetragonal prisms of Ca_2Sn, viewed along the fourfold axis. If the Ca atoms located at the *upper right* and the *lower left* corners were eliminated, as shown in (**b**), the remaining atoms would rearrange to form the pattern of the trigonal prisms of TiSi, which are represented in (**c**)

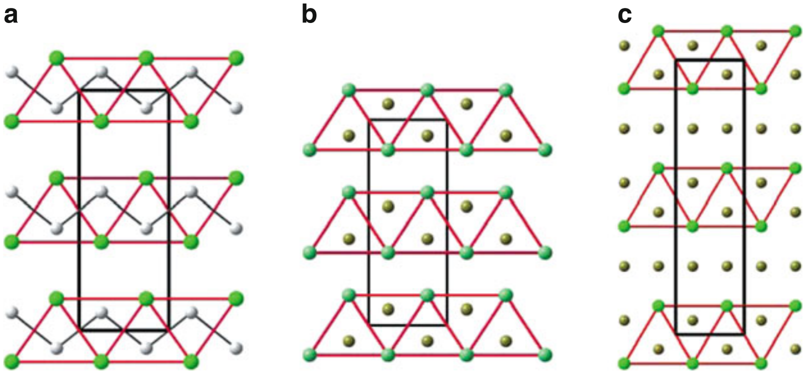

Fig. 26 (**a**) The structure of CaSn (CrB type), projected on the *bc* plane. The trigonal prisms of Ca atoms (*green spheres*) are filled by the Sn atoms (*grey spheres*). (**b**) The same structure formed by TiSi. The trigonal prisms (Ti atoms) are filled by the Si atoms. (**c**) The *C*49 structure of $TiSi_2$ (***C***mcm), projected on the *bc* plane. The blocks of trigonal prisms are identical to those of the *B*33 structure in (**b**). The additional Si atoms have been intercalated between these blocks, forming slightly distorted $\mathbf{4^4}$ planar nets

This relationship makes sense when we apply the ***EZKC*** [14, 33], because the Ca_2Sn structure can be derived from that of TiSi. Thus, at ambient conditions, the ***M***Sn (***M*** = Ca, Sr, Ba) binary alloys are *B*33 (CrB-type, ***C***mcm). This structure, represented in Fig. 26a, is formed by walls of trigonal prisms of Ca(Ti) filled by Sn and Si atoms, respectively. It is remarkable that the CrB structure appears in the Pearson's Crystal Database (2008) as a FeB-stacking variant. Further evidence supporting such similarities as well as our hypothesis is the FeB–CrB polymorphism existing in some related alloys such as ZrSi and ZrGe [107]. In the case of ZrSi, the CrB → FeB transition occurs above 1,853 K [108].

At this point, we could then describe the Ca_2Sn structure as the insertion of a Ca atom into a CaSn structure of the TiSi type. In other words, the "new" Ca atom causes the previous CaSn array to adopt the TiSi-type structure. This reasoning is a mere application of the ***EZKC*** and can be explained as follows.

If Ca_2Sn is formulated as Ca(CaSn), and we admit that the first Ca atom transfers two electrons to the (CaSn) pair, the compound becomes Ca^{2+}[Ψ-TiSn)], where the Ψ-TiSn moiety adopts the TiSi-type structure. It is worthy of mention that the analogue ZrGe [107] is also TiSi type! We must recall how the ***EZKC*** gave a satisfactory explanation of the Ni_2In structure, inducing the pseudo-formula Ni^{2+}[NiΨ-Sb], and hence the formation of a Ψ-NiSb (NiAs-type) structure [14].

In order to provide examples that could enhance our arguments, we have searched for related structures in which comparable processes could occur. We have found a meaningful example in the pair TiSi/$TiSi_2$, whose structures are depicted in Fig. 26b, c, respectively.

The relevant key issue here is that $TiSi_2$ (*C*49) (***C***mcm) can be formulated as Si (TiSi), and hence it can be thought of as formed by simply inserting one additional Si atom between the CrB-type blocks of the TiSi (*B*33) structure. These new Si atoms form $\mathbf{4^4}$ planar nets (Fig. 26c), and if we were able to extract the monolayers of Si atoms, the TiSi structure (Fig. 25b) would be reconstructed!, a similar “exercise” to that practiced in Ca_2Sn (Fig. 25). The difference with Ca_2Sn resides in that in the FeB-type structure, the insertion of an additional atom entails that the trigonal prisms are converted into square prisms, a pattern that results more difficult to identify as a derivation of the FeB structure. However, in $TiSi_2$, the permanence of the TiSi-blocks (CrB type) makes their relationship more visible (Fig. 26).

The ***EZKC*** can also account for the $TiSi_2$ structure. If the Ti atom donates one electron to one Si atom, the pseudo-formula $Si^{1-}(\Psi\text{-ScSi})$ is formed. This pseudo-structure corresponds, in fact, to the real ScSi compound [109], which is just *B*33 (CrB type). Again, an impressive coincidence! The unit cell constants of ScSi: $a = 3.99$, $b = 9.88$, $c = 3.66$ Å are comparable to those of $TiSi_2$: $a = 3.61$, $b = 13.79$, $c = 3.65$ Å.

The relevance of this example is twofold: on the one hand, the strong relationship existing between CrB- and FeB-type structures; on the other hand, the already mentioned polymorphism (CrB and FeB type) of both ZrSi and ZrGe [107] that helps to understand the Ca_2SnO_4 structure. In view of this, the ***M***Sn (***M*** = Ca, Sr, Ba) compounds might also stabilize the FeB-type structure under the appropriate conditions of temperature and/or pressure. In fact, in the Ca_2Sn subarray, the stabilization of a TiSi structure (FeB type) is induced by the “*foreign*” Ca atom [3, 110].

An interesting observation that gives coherence to all these structures and phase transitions is the existence of the rocksalt carbide TiC [111]. The occurrence of this phase fits with the fact that TiSi, ZrSi and ZrGe are of the CrB type. Thus, the structures formed by heavier elements can be formed by the lighter ones under compression. Because the NaCl-type structure undergoes, under pressure, the transitions NaCl → CrB → CsCl, the rocksalt TiC would stabilize, by compression, any of these structures. Similarly, TiSi, ZrSi, ZrGe and even CaSn, SrSn and BaSn (all of them CrB type) could produce either by oxidation or compression, the CsCl-type structure.

This double transition has been observed in many compounds such as the pressure-induced CrB → CsCl transition in BaSn [1, 2], a point which will be discussed more extensively in the next sections.

Our conclusion is that the cation subarray in Ca_2SnO_4 is not a rare arrangement. Even if no isostructural alloy has been found so far, its interpretation in terms of the ***EZKC***, as well as its fitting into the general scheme of the related structures, indicates its strong relationship to the $ZrSi_2$ type.

The explanation of the Ca_2Sn subarray in terms of the ***EZKC*** can be extended to the Mn_2Ge subarray of Mn_2GeO_4. The compounds $Mn_{0.5}Co_{0.5}B$ [112], $Fe_{0.5}Mn_{0.5}B$ [113] and MnB [114] are of the FeB type. Now, if we write $Mn_{0.5}Co_{0.5}B$ as Mn (CoB_2) and postulate, following the ***EZKC***, that the Co atom transfers one electron to each B atom, the formula becomes $Mn(\Psi\text{-}MnC_2)$, equivalent to MnC and isoelectronic with the MnGe subarray of the oxide. The same result is obtained if we start from Mn_2Ge. The transfer of one electron from the Ge atom to one Mn atom would lead to the formula Ψ-Fe(MnAl), where the MnAl moiety is isoelectronic to MnB (also FeB type).

The conclusion is that in both Ca_2SnO_4 and Mn_2GeO_4, the insertion of an additional Ca (Mn) atom into a hypothetical CaSn (MnGe) subarray stabilizes the TiSi (FeB type) structures of their respective CaSn and MnGe moieties.

9 The Structure of Ba_2SnO_4

Ba_2SnO_4 and the isostructural Ca_2GeO_4 compounds are the final step in the long *journey* discussed in this work (Table 5). The aristotype is K_2NiF_4 (***I***4/mmm) and its structure is drawn in Fig. 27a. In this section, we will focus on Ba_2SnO_4 (Fig. 27a), leaving the description of the Ca_2GeO_4 polymorphs for a later section (Sect. 9.2).

The classical description of this structure consists of an intergrowth of perovskite-like blocks of composition $BaSnO_3$ and fragments of BaO (NaCl type). Both blocks composing the structure are drawn together in Fig. 27b, whereas the BaO fragment is outlined in a unit cell of the rocksalt BaO structure in Fig. 27c. These BaO fragments differ completely from the CaO fragments in Ca_2SnO_4 (Fig. 22). The other component of the structure, the $BaSnO_3$-blocks, are formed by slightly distorted cubes of Ba atoms (4.14 × 4.14 × 3.88 Å), centred by the Sn atoms. The O atoms form octahedra around the Sn atoms. This is, in fact, a distortion of the $BaSnO_3$ perovskite [115] and hence of the HP phase (CsCl type) of BaSn [1, 2] (Table 5).

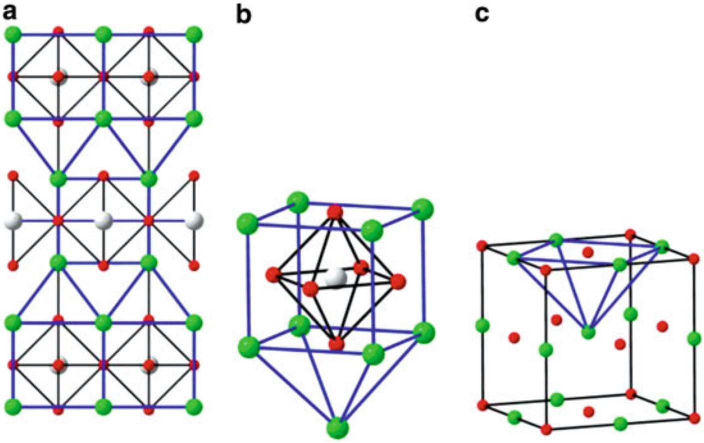

Fig. 27 (**a**) The structure of Ba_2SnO_4 (***I***4/mmm), viewed along the *a* axis, showing the perovskite-like blocks of composition $BaSnO_3$ alternating, along c, with fragments of the BaO (rocksalt) structure. The atoms are Ba (*green*), Sn (*grey*) and O (*red*). (**b**) A view of the two fragments. The *upper side* shows a $BaSnO_3$ perovskite-like fragment. The *lower part* is a fragment of the BaO represented in (**c**). (**c**) A unit cell of the rocksalt BaO structure. The *blue lines* remark the structural fragments forming part of Ba_2SnO_4. The Ba–Ba distances in the BaO fragment are 4 × 4.14 and 4 × 4.02 Å (mean 4.08 Å)

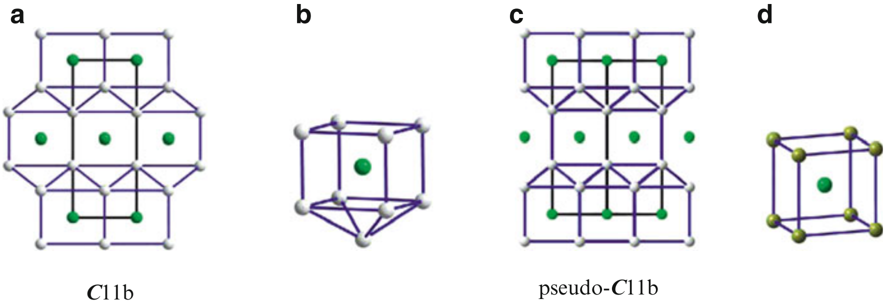

Fig. 28 (**a**) The tetragonal *C*11b structure (***I***4/mmm) of $MoSi_2$. The layers of tetragonal prisms centred by Mo atoms (*green spheres*) alternate with fragments of a similar Si bct net. Both fragments are outlined in (**b**). The structure (pseudo-*C*11b) of the $TiSi_2$ (***F***mmm) is projected in (**c**) where the body-centred tetragonal (bct) prisms become now almost cubic, as shown in (**d**)

From the data collected in Table 5, we can extract an important conclusion, i.e. the topology and distances of the basic units BaO and BaSn remain unaltered in the more complex compounds. Recall that this was reported for BaSn and $BaSnO_3$ [1] and can now be extended to Ba_2SnO_4. This means that in a given compound, both the structural and metric requirements of all its components are satisfied simultaneously. This assertion was evident in the Ca_2SnO_4 structure and enhances *the concept of multiple resonance structures* [33].

Unlike Ca_2SnO_4, whose Ca_2Sn subarray has no similarity with any alloy structure, the Ba_2Sn subarray of Ba_2SnO_4 is of the Mo_2Si type (***I***4/mmm), also isostructural to the related silicides $CrSi_2$ and WSi_2, among other compounds [116].

The Mo_2Si structure is projected in Fig. 28a. It consists of alternate layers of tetragonal prisms of Si, centred by Mo atoms, and fragments of body-centred tetragonal prisms of Si atoms. The fragment represented in Fig. 28b contains both structural elements to be compared with Fig. 27b. The dimensions of the $MoSi_8$ prisms are $a = 3.20$, $c = 2.67$ Å, a cell related to the cation array of the rutile-like oxides which, on the other hand, are formed by all the elements involved in these alloys (Cr, Mo, Si, etc.). As an example, we can cite the stishovite (SiO_2) (***P***4_2/mnm, $a = 4.10$, $c = 2.64$ Å) expanded in the *ab* plane by the insertion of oxygen.

Another interesting feature related to the $MoSi_2$ structure is the existence of a related polymorph of $TiSi_2$, denoted as pseudo-*C*11b. This phase is orthorhombic, S. G. ***F***mmm (a subgroup of ***I***4/mmm) and is represented in Fig. 28c. It is metastable [117] and has been isolated during the *C*49 to *C*54 transition of $TiSi_2$ [118]. Recall that the *C*49 structure was discussed on the occasion of the relationship between FeB and Mn_2Ge and corresponds to the $ZrSi_2$ type represented in Fig. 26c. This structure is also a metastable phase of $TiSi_2$, which has only been stabilized in thin layers [119]. Interestingly, this phase transforms later into the stable *C*54, *corresponding to the cation array of thenardite*, represented in Fig. 2. Note that in $TiSi_2$, the TiSi prisms are almost cubic (3.25 × 3.25 × 3.23 Å) (compare Fig. 28b, d).

An interesting property of the $MoSi_2$ structure (Fig. 28a) is that it remains stable up to 2,170 K, undergoing a transition to the $CrSi_2$-type structure, which is the

$CrSi_2$	←	C49	←	C11b	←	C54
Quartz	2123 K	CrB+Si		CsCl+Si		Thenardite
$\boldsymbol{P}6_222$		$\boldsymbol{C}$mcm		$\boldsymbol{I}$4/mmm		$\boldsymbol{F}$ddd

Scheme 3 Evolution of the $TiSi_2$ structures by increasing temperature. The central transition C49 ← C11b shows how the TiSi moiety undergoes the expected CsCl to CrB transformation

structure of the Si atoms in quartz [63]. This new relationship is, in our opinion, of greatest interest because it reflects, in the alloys, features that take place in the oxides. Thus, in the same manner that quartz transforms at high pressure into stishovite (rutile-like SiO_2) [120], the $MoSi_2$ structure (C11b) should recover, at very high temperatures (lower pressures), the quartz-like arrangement. And it occurs so! This transition [121] indicates that the quartz → rutile transition, occurring in SiO_2, GeO_2 and $GaAsO_4$, also takes place in the oxygen-free alloys.

In Scheme 3 are summarized the above transitions, which indicate that more structural types can be added to the "*structural walk*". Thus, if we take thenardite ($TiSi_2$) as the starting point, the atoms can follow an alternative way, forming the metastable C11b structure ($TiSi_2$) (Fig. 28c). This phase, which is an intergrowth of TiSi + Si in the forms of CsCl + *bcc*-Si, finally forms the C49 structure (Fig. 26c), which is also an intergrowth of TiSi + Si but in the forms of CrB + *bcc*-Si. *That is, in $TiSi_2$, the TiSi subnet undergoes its own CrB → CsCl transition.* It should be remarked that the CrB-type structure has not been found in the isolated phase TiSi. Instead, it forms the strongly related phase FeB type, discussed in connection with Ca_2SnO_4. Remember also that ZrSi exists in both polymorphs, i.e. CrB and FeB.

As already mentioned, the rutile → quartz transition occurs directly from C11b to $CrSi_2$. This feature should be connected with the transitions sequence zincblende → Quartz → NaCl → CrB (FeB) → CsCl, observed in some compounds, such as ZnTe [122]. Note the coincidence of these transitions with those quoted in Scheme 3.

The behaviour of the Si layers, intercalated between the TiSi-blocks, also merits discussion. In $TiSi_2$, the Si layers form $\mathbf{4^4}$ planar nets with Si–Si distances of 2.54 Å. If we assume they are part of a *fcc* cell, the unit cell parameter ($a = 3.61$ Å) would be comparable to that of *fcc*-Si, stable above 79 GPa. At 87 GPa, $a = 3.34$ Å and the Si–Si distances of 2.36 Å [123]. At the transition pressure, the values in $TiSi_2$ and *fcc*-Si would become closer.

9.1 The Ca_2SnO_4- and Ba_2SnO_4-Type Structures and the Decomposition Processes

In the light of the dissection of the structures of Ca_2SnO_4 and Ba_2SnO_4, and considering the experimental data on their decompositions at higher pressures (Tables 4 and 5), we can conclude that such decompositions seem to obey a mechanism that "is written" in the last steps of the *structural walk*.

Thus, the decomposition of Ba_2SnO_4 in the BaSnO3 perovskite and the rocksalt BaO is expectable in view of the structures drawn in Fig. 27, which means that the decomposition products “already existed” in Ba_2SnO_4. Moreover, the impression is that the process begins in the previous step (the Ca_2SnO_4 phase, Sr_2PbO_4 type).

We have seen (Figs. 21–23) that this structure admitted several descriptions. In one of them, we have outlined the similarity of the $CaSnO_3$-moiety with the isoelectronic C-In_2O_3 and how these fragments are mixed with fragments of the rocksalt CaO. The outcome we wish to emphasize here is that the CaSn prisms (Fig. 21d) are, in fact, fragments of a *fcc*-array like the one formed by cations in the C-In_2O_3 (Sc_2O_3). Stated differently, the Ca_8Sn prisms are, in fact, a fragment of a hypothetical CaSn alloy with the rocksalt structure.

Because the rocksalt structure undergoes the pressure-induced transitions NaCl → CrB → CsCl, this sequence is consistent with the phases observed in the binary alloys CaSn, BaSn, SrPb, etc. All these compounds, CrB type at ambient conditions, should convert into NaCl type at high temperature, but they transform to a CsCl type at high pressure. It should be remarked that unlike the CrB → CsCl transition, occurring in BaSn [2], the HT CrB → NaCl transition has never been reported. The main consequences of this behaviour are as follows:

1. The CaSn (*fcc*) array should convert into a *bcc* array when pressure increases. Although the data of Tables 4 and 5 do not include such a transition, the structural differences between Ca_2SnO_4 and Ba_2SnO_4 are consistent with this approach. It should be recalled that the heavier elements within a group of the Periodic Table stabilize the high-pressure phases of the lighter ones, so that the *fcc* sub-structure in CaSn should necessarily be of the CsCl type in the BaSn, as it really occurs!
2. Ca_2SnO_4 and Ba_2SnO_4 are previous stages to the real separation, which takes place at higher pressures. The moieties $BaSnO_3$ + BaO (perovskite + rocksalt) pre-exist in both structures and the compound is well prepared for this final separation.

Although we have already mentioned the experiments concerning the spinel → Sr_2PbO_4 transition at high pressure, a complete study concerning the spinel → Sr_2SnO_4 → Ba_2SnO_4 → decomposition has not been reported so far. On the contrary, the partial pressure-induced transitions Mn_2GeO_4 → Sr_2PbO_4 and Ca_2GeO_4 → Ba_2SnO_4 are known and will be discussed in the next subsection. An experimental or theoretical study of these processes should be desirable.

9.2 The Phases of CaGe, Ca_2Ge and the $CaGeO_3$ and Ca_2GeO_4 Oxides

In the Ca:Ge system, the phases CaGe and Ca_2Ge are of special interest in our discussion. CaGe is CrB type at ambient conditions [124]. Although it is expectable a CrB → CsCl transition at HP, as in BaSn [2], no HT/HP transition has been reported for CaGe. On the other hand, Ca_2Ge is, at ambient conditions, $PbCl_2$ type, like the related Ca_2Si and Ca_2Sn compounds [94].

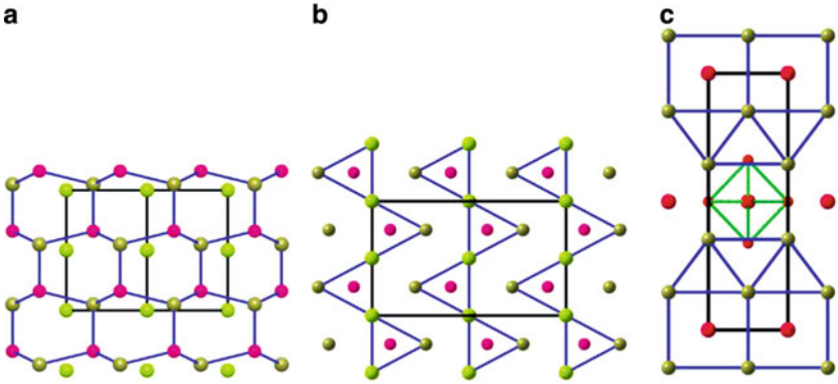

Fig. 29 The three polymorphs of Ca_2GeO_4. The stable phase at ambient conditions is the olivine-like structure represented in (**b**). Both *grey* and *green spheres* represent Ca atoms and *red spheres* are Ge atoms. When the olivine structure is heated above 1,726 K, the compound transforms to a stuffed wurtzite-like structure, represented in (**a**). Atoms colour as in (**b**). (**c**) The structure of Ca_2GeO_4 at high pressure. It is of the Ba_2SnO_4 type in which perovskite-like blocks $CaGeO_3$ co-exist with the CaO bilayers. The O atoms have been eliminated for clarity, except in the central part of the figure where a $CaGeO_3$ cube has been outlined. The GeO_6 octahedron is depicted with *green lines*. Compare Fig. 29a with Fig. 20c

If we analyse the structure of the oxides, we see that $CaGeO_3$ has two polymorphs at ambient pressure. One has the triclinic wollastonite-type structure. The other one is an orthorhombic perovskite of the $GdFeO_3$ type whose cation array is CsCl type. That is, the insertion of three O atoms provokes, in CaGe, the transition of the CrB → CsCl, as it occurs, under pressure, in the alloy.

Unlike Ca_2SiO_4, which has a cation array of the anti-$PbCl_2$ type [5] at ambient conditions, Ca_2GeO_4 is olivine type (Fig. 29b) and shows an interesting and uncommon behaviour. When heated, the olivine-like structure remains stable up to 1,726 K, transforming then into a Ca-filled wurtzite-like structure of formula Ca ($CaGeO_4$), which is represented in Fig. 29a [21]. The wurtzite-like skeleton is formed by the subarray $(CaGeO_4)^{2-}$, equivalent to the pseudo-formula Ca^{2+} [Ψ-$TiGeO_4$].

On the other hand, at 110 kbar and 900 K, the olivine-type structure transforms into the Ba_2SnO_4-type structure (***I***4/mmm) [125]. This phase is represented in Fig. 29c. Its comparison with that of Fig. 27a provides the unexpected result that the olivine structure transforms, at high pressure, directly to the Ba_2SnO_4-type structure, whereas it jumps directly into the Ca-filled tridymite at high temperature. Thus, in both transitions no intermediate phase (spinel or cotunnite) has been detected.

In the Ba_2SnO_4-like phase, we see that the CsCl-type fragments of composition $CaGeO_3$ are intercalated with the CaO bilayers. That is, the irregular CaGe cubes (CsCl type) observed in the perovskite-like phase of $CaGeO_3$ become completely regular in the HP phase of Ca_2GeO_4 which is of the Sr_2PbO_4 type.

10 The Question of the Charge Transfer Between Cations: Arguments Accounting for the Structures of the Group 14 Elements

The three phases of Ca_2GeO_4 (filled-wurtzite, olivine and Ba_2SnO_4 type), described above, might help to answer a crucial question, formulated in two previous works [14, 33], related to the ***EZKC***. This concept considers the possibility of a charge transfer between cations, even if they are of the same kind. Remember that this idea served to postulate the underlying zincblende resonance structures in antifluorites such as Li_2O, Li_2S, Na_2S or $(Li_3Al)N_2$, so that Li_2O could be regarded as Li^+(Ψ-BeO).

This explanation provides a rational understanding of many structures in terms of simple skeletons of the elements of Group 14, which underlie in many compounds [14]. Although the idea could be questioned on the basis of commonly accepted chemical arguments, it could find support in the structures of, for example, double alkali sulphates, chromates, etc., such as $LiKSO_4$. Remember that in these double sulphates, the two unlike alkali atoms are separated in two crystallographic different sites.

Thus, while in Li_2SO_4, which at HT adopts the anti-fluorite structure, all the Li atoms are located at tetrahedral S_4 voids, in the compounds Cs[$LiCrO_4$] and K [$LiMoO_4$] only the Li atoms are centering Mo_4 tetrahedra. Additionally, the Cs atoms are located at (1/2, 0, 0), forming a NaCl-type substructure with the Cr(Mo) atoms. The result is that an electron transfer from Cs to Li, the [Li^{1-}Mo] subarray, i.e. the [Ψ-BeMo] subnet, conforms to the zincblende-type structure. In this context, while the implicit existence of a zincblende network, in the HT-Li_2SO4 structure, could be questioned by the simultaneous existence of both Li^+ and Li^-, its occurrence seems doubtless in the chromates and molybdates.

The phase-transitions observed in Ca_2GeO_4 are, however, of great interest in the interpretation of this phenomenon. Even if the olivine → Ba_2SnO_4 transition, at HP, is important, probably the most relevant feature is the direct HT olivine → filled-wurtzite transition [20]. The three structures are represented in Fig. 29.

The crucial aspect here is that the final structure is the one adopted by the elements of Group 14, as well as by IV-IV, III-V and II-VI binary compounds. Among others, we can mention the hexagonal diamond (londsdaleite), CSi, AlP, BN, GaN, BeO, ZnO and wurtzite (ZnS) itself!

Thus, the wurtzite structure formed by the pair (CaGe) (Fig. 29a) can be explained in the light of the ***EZKC*** [14] if one Ca atom donates two electrons to the (CaGe) pair, becoming either [Ψ-TiGe] or [Ψ-ScAs], that is, a pseudo-(IV-IV) or a -(III-V) compound. In this respect, we must recall the wurtzite-like structure of GaN and the zincblende-type structure of ScP! This interpretation is consistent with the principle establishing the tendency of any structure to form four-connected networks [14].

We remarked above that in the case of anti-fluorites such as Li_2S and Na_2S, which undergo the reversible transition $Ni_2In \Leftrightarrow CaF_2$ at HP [6, 7], including also the high-temperature phase of Li_2SO_4 [32], this hypothesis could be seen as weakly founded, because the two resonance structures are identical. However, in the HT phase of Ca_2GeO_4, one Ca atom provokes the formation of a unique, four-connected [Ψ-TiGe] skeleton of the wurtzite type, which does not need the additional "*resonance concept*" to account for its structure.

The same occurs with the HT phase of $CsLi(CrO_4)$ [81], which is converted into (Ψ-Xe)[Ψ-$BeCrO_4$], where the Ψ-BeCr subarray is forming a blende-type structure. In the compound under discussion, the wurtzite-like network is formed, instead of the more common fluorite structure. Because in ZnS, the blende → wurtzite transition occurs at HT, the *walk* might commence from any of these two polymorphs.

Looking at Fig. 29a, b, it is noticeable that, in both phases, the Ca atoms (green) form $\mathbf{3^6}$ layers (*hcp*) which remain unaltered during the transition. On the contrary, the atom pair [CaGe] (grey and red, respectively) forms irregular $\mathbf{6^3}$ graphene layers in the olivine structure (Fig. 5), becoming puckered in the HT-Ca_2GeO_4, when the wurtzite-like structure is formed (Fig. 29a).

The distorted wurtzite-like structure of Ca_2GeO_4 is chemically meaningful when we see that in compounds such as $KLiBeF_4$ [58] and $KLiSO_4$ [59], the most electropositive atoms (K) transfer one electron to the Li atoms, converting them into K^+[Ψ-$BeBeF_4$] and K^+[Ψ-$BeSO_4$], respectively. In reality, they become K-stuffed tridymite-like structures, whose respective Be and BeS skeletons form, in turn, the londsdaleite and wurtzite structures.

This interpretation agrees with the fact that BeF_2, quartz type at ambient conditions [126], could transform into either cristobalite or tridymite, as it does SiO_2 itself. Moreover, real BeS is blende type and real $BeSO_4$ is cristobalite-like! Remember in this regard that the cristobalite-type structure is also implicit in the cubic Cs-filled blendes Cs[$LiCrO_4$] [81] and Cs[$LiMoO_4$] [78, 80] (see Scheme 1).

By examining the drawings of Fig. 20, one has the impression that when the two cations are of the same species, as in Ca_2GeO_4 and Ca_2SiO_4, the conversion of one Ca atom into a Ψ-Ti (Ψ-Ge) seems to be more difficult than in compounds with unlike cations. In this latter case, it seems that the difference in electronegativity favours the electron transfer. This could be a reason why in Ca_2GeO_4 (Fig. 20c), the wurtzite-like structure is more distorted (it is taking shape!), whereas in $KLiBeF_4$ and $KLiSO_4$ (Fig. 20a) the arrangement is closer to the ideal tridymite structure.

11 Conclusions

The results discussed in this chapter indicate that the structural transformations undergone by different compounds may be correlated in a rational manner. This correlation is reinforced by the observation that the same transitions occur in the oxides as well as in the corresponding alloys. These new relationships give additional support to the statement that the "cations subarrays govern the structures of oxides", an intuition first expressed by Wondratschek et al. [127, 128], later extended by O'Keeffe and Hyde [5] and Blatov et al. [11–13] and which has found physical meaning in the works of Vegas et al. [3, 4, 14, 33, 63, 64].

Although no compound has been identified which follows a transit along the complete series of structures described in our work, when the structures of the alloys and the oxides are considered simultaneously, one obtains a complete vision, "a movie", of how the initial structure is continuously transformed, producing a complete series of structures whose sequence is chemically meaningful. The identical behaviour of the alloys and the cation arrays helps the identification of the "*missing links*". When taken together the structures define a transition which is understandable and physically sound.

The whole series of transitions, collected in Scheme 1, can be thought of as resulting from small pieces (short steps) which connect to form a longer chain that we have named *Structural Journey*. These small pieces correspond to transitions which connect, for example, the olivine → thenardite → spinel structures in Na_2MoO_4 [15]. However, a change in the composition, e.g. in $LiCsCrO_4$ [81], makes the transition go in the opposite direction, i.e. a temperature-induced, transition olivine → cotunnite → Cs-filled zincblende takes place, whereas the double sulphate $KLiSO_4$ ($LiCaPO_4$ type), with a cation array of the Fe_2P type, transforms at HT into a stuffed-wurtzite. Both cation networks zincblende and wurtzite transform each other in the compounds $KLiMoO_4$ and $CsLiSO_4$. Thus, $KLiMoO_4$, wurtzite type ($\boldsymbol{P}6_3mc$) at ambient conditions, transforms into a cubic filled zincblende-type structure at 701 K [129].

Also interesting is the behaviour of K_2SO_4, which has a cotunnite-type structure at ambient conditions, which transforms into a Ni_2In at HT and goes, by decreasing the O content, up to the Ni_2Al-type structure in K_2SO_3 (isostructural to Na_2SO_3).

The manganese germanate Mn_2GeO_4 provides an illustrative example of the transition which connects the olivine-spinel pathway with the lower part of Scheme 1. It shows how spinels can transform under compression into the Sr_2PbO_4-type structure. Another germanate Ca_2GeO_4 shows us more drastic transitions, i.e. the room temperature, olivine-like phase transforms at elevated temperatures, into a Ca-filled wurtzite (the starting point of the walk), whereas, under pressure, the same compound takes up the Ba_2SnO_4-type structure, the last step before decomposition. The surprising behaviour of this compound is that both the olivine → wurtzite and the olivine → Ba_2SnO_4 transitions take place without the stabilization of the intermediate phases. The reason for these jumps could be that the intermediate structures could have a very narrow range of stability, a feature that could also occur for other expectable structures in the frame of Scheme 1, but which has never been observed. They could be described as "small stability range structures".

The above examples illustrate that all these pieces of structural information overlap completing the *walk for the Structural Journey*. It seems improbable that a single compound could adopt the complete set of structures of the *Structural Journey*. Ca_2GeO_4 comes closest. We have seen that to pass a step between two pieces, it is often necessary to change some of the atoms involved in the compounds. The equivalence between the effects of oxidation and pressure makes that transformations can also be achieved in the oxides. In this context, the joint comparison of oxides and alloys illuminates this concept, leading to the following set of transitions:

filled-ZnO → filled-ZnS → $CrSi_2$ → CaF_2 → Ni_2Al, Phenacite → Co_2Si → Ni_2In → $TiSi_2$ → Fe_2P → $MgCu_2$ → Ca_2Sn → $MoSi_2$ → decomposition

Some of these structural types, e.g. Ni_2Al, $TiSi_2$, Fe_2P, Ca_2Sn and $MoSi_2$, are, in fact, missing links which were not considered previously to be part of the chain. When all of them are taken into account, the complete *Structural Journey* becomes apparent. It should be added that the cation arrays, in many oxides, can be regarded at first glance as intermediate phases between two phases involved in a transition. The Na_2S subarray in the Na_2SO_3 structure provides a specific example which may be seen as a Ni_2In-type structure in the process of formation. Its similarity with a real structure type, i.e. the Ni_2Al structure, has also been noted.

Another interesting aspect is the bifurcated route between the olivine and the spinel structures. The first one passes through the $TiSi_2$-type structure. The second one is an intermediate for the Fe_2P-type structure. As it can be observed in Figs. 3 and 14, both structural types contain fragments of the spinel structure, and it could be speculated that the way followed by the compound ($TiSi_2$ or Fe_2P) might influence the type of spinel structure formed, that is, normal or inverse spinel.

This assertion needs a deeper study, but these figures give support to this hypothesis. If so, the inverse spinel should not be the result of cations looking for an appropriate void in an oxygen matrix, but the consequence of a previous cation arrangement. Thus, in the $TiSi_2$-type structure, the Ti atoms are forming the same adamantane structure found later in the spinels. So, it seems as if this requirement of the Ti atoms would result in the formation of the ...*ABCD*... stacking sequence of the graphene layers formed by the Si atoms.

The decomposition processes, followed by the structures of the Ba_2SnO_4 type, are also remarkable. Under pressure, the compound decomposes into $BaSnO_3$ and BaO. We must recall that, at ambient conditions, the corresponding Ba_2Sn alloy is cotunnite type ($PbCl_2$ type). Although, no high-pressure study has been reported so far on this alloy, it is expected that the alloy could also reach, at very high pressures, the $MoSi_2$-type structure (Fig. 28a) found in Ba_2SnO_4.

If this were so, our prediction about the Ba_2Sn alloy is that, in common with Ba_2SnO_4, further compression would lead to the decomposition to BaSn + Ba. This is consistent with the fact that the HP phase of BaSn is CsCl type [2], just one of the structures existing in the oxide. This hypothesis is supported by the behaviour of another series of isostructural compounds. Thus, the alloys Hg_2Mg, Au_2Ti and Ag_2Ho, like $TiSi_2$, are all of the *C*11b type (***I***mmm) (Fig. 28c). Surprisingly, there also exist the corresponding 1:1 compounds MgHg, AuTi and AgHo, and all of them have the CsCl-type structure!

This is one of the crucial points of our discussion, i.e. when the compounds Mn_2GeO_4 and Ca_2GeO_4 transform under pressure into structures of the Sr_2PbO_4 type and Ba_2SnO_4 type, respectively, the cations are not forming capricious structures, but they are preparing the partial substructures which remain after the decomposition. When the HP phase of Ca_2GeO_4 (Ba_2SnO_4 type) is formed, we are producing blocks of the perovskite $CaGeO_3$ which contains implicit the HP phase of the CaGe alloy (CsCl type), but simultaneously, fragments of the rocksalt CaO structure are also building up. Both components separate in an ordered manner when the pressure increases. Thus, the compounds of the Ba_2SnO_4-type structure can be contemplated as the intergrowth of phases which are just those in which the compounds decompose when the pressure increases. The decomposition products already existed!

We wish to finish this chapter mentioning the recent HP experiments on Na and K. Two new phases (*o*P8 and *h*P4) have been reported for these elements. In the case of Na, the *o*P8 phase (***P***nma), isolated at 117 GPa [130], transforms at 200 GPa into the hexagonal *h*P4 phase (***P***6_3/mmc) [131]. The same structures were observed for K [132, 133] in the range of 20–50 GPa. Interestingly, the work on *h*P4-K includes calculations of the electron localization function (ELF) at 25 GPa, showing maxima located at the 2*d* sites (1/3, 2/3, 1/4), of the space group P6_3/mmc. The ELF maxima contain approximately two electrons and have been interpreted as Lewis pairs (LPs) acting as pseudo-anions [133]. Note that the same sites are occupied by the S atoms in the HP phase of Na_2S (Fig. 1c) [7]. These results confirm that, at elevated pressures, the valence electrons can form LPs converting the metals into true ionic structures. This outcome confirms the validity of the AIMM model (Anions in Metallic Matrices Model) [134]. The model predicts that anions, like O^{2-}, S^{2-}, are formed when the O, S atoms (*foreign atoms*) locate in the vicinity of either bonding pairs or lone pairs of a metallic skeleton [63, 64, 134].

The stabilization of these high-pressure phases of Na and K also gives support to an intuitive hypothesis that considered the metallic subnets, in compound, as metastable structures of the parent metal [3, 110]. This idea was expressed as follows: *If high pressure gives rise to a redistribution of the electrons and hence to a phase transition, similar results could be obtained if electrons are redistributed by the presence of* ***foreign atoms***.

These predictions become a categorical statement after the work of Marqués et al. [133] where, for the first time, it is shown that, at very high pressures, the elemental K adopts the *h*P4 structure, a phase topologically identical to that of the K atoms in the HP K_2S and in the HT K_2SO_4. Thus, the structure of K remains in the series K → K_2S → K_2SO_4, indicating that a third *journey* seems to exist, i.e. that of the metals. The reader can find illustrative drawings in [135].

Along this chapter, we have remarked some of the most unusual features observed in crystal structures in last few years. In some cases we have referred to crucial aspects of these structures which have been hidden for almost one century. We could say more properly that our discussion has dealt with structural features which are rarely discussed in crystal chemical works. We are aware that many other insights are implicit in our work. They were not discussed in depth for the sake of space. We are convinced, however, that the reader will be able to deduce additional and unexpected relationships between all the structures dissected in this work. We have scattered ideas, with the hope that, like seeds, they may find fertile minds in which to sprout.

Acknowledgements I am gratefully indebted to Dr Alberto Solana for careful reading of the manuscript and also for his invaluable suggestions that helped to improve this chapter. I also wish to express my thanks to Dr Douglas V. Laurents for his valuable discussions.

References

1. Martínez-Cruz LA, Ramos-Gallardo A, Vegas A (1994) *M*Sn and *M*SnO$_3$ (M = Ca, Sr, Ba): new examples of oxygen-stuffed alloys. J Solid State Chem 110:397–398
2. Beck HP, Lederer G (1993) Thermische Dilatation und Hochdruckverhalten der Zintl-Phasen CaSn und BaSn. Z anorg allg Chem 619:897–900
3. Vegas A (2000) Cations in inorganic solids. Crystallogr Rev 7:189–286
4. Vegas A, Jansen M (2002) Structural relationships between cations and alloys; an equivalence between oxidation and pressure. Acta Crystallogr B58:38–53
5. O'Keeffe M, Hyde BG (1985) An alternative approach to non-molecular crystal structures: with emphasis on the arrangement of cations. Struct Bond 61:77–144
6. Grzechnik A, Vegas A, Syassen K, Loa I, Hanfland M, Jansen M (2000) Reversible antifluorite to anticotunnite phase transition in Li$_2$S at high pressures. J Solid State Chem 154:603–611
7. Vegas A, Grzechnik A, Syassen K, Loa I, Hanfland M, Jansen M (2001) Reversible phase transitions in Na$_2$S under pressure: a comparison with the cation array in Na$_2$SO$_4$. Acta Crystallogr B 57:151–156
8. Vegas A, Grzechnik A, Hanfland M, Mühle C, Jansen M (2002) Antifluorite to Ni$_2$In-type phase transition in K$_2$S at high pressure. Solid State Sci 4:1077–1081
9. Rasmussen SE, Jorgensen JE, Lundtoft B (1996) Structures and phase transitions of Na$_2$SO$_4$. J Appl Crystallogr 29:42–47
10. Léger JM, Haines J (1997) Crystal chemistry of the AX$_2$ compounds under pressure. Eur J Solid State Inorg Chem 34:785–796
11. Blatov VA, Peskov MV (2006) A comparative crystallochemical analysis of binary compounds and simple anhydrous salts containing pyramidal anions LO$_3$ (L = S, Se, Te, Cl, Br, I). Acta Crystallogr B 62:457–466
12. Blatov VA (2009) http://www.topos.ssu.samara.ru
13. Blatov VA (2011) Crystal structures of inorganic oxoacid salts perceived as cation arrays: a periodic-graph approach. Struct Bond. DOI: 10.1007/430_2010_34
14. Vegas A, García-Baonza V (2007) Pseudoatoms and preferred skeletons in crystals. Acta Crystallogr B 63:339–345
15. Bramnik KG, Ehrenberg H (2004) Study of the (Na$_2$O)-(MoO$_3$) system. Na$_6$Mo$_{11}$O$_{36}$-a new oxide with anatase-related structure and the crystal structures of Na$_2$MoO$_4$. Z anorg allg Chem 630:1336–1341
16. Liu L-G, Bassett WA (1986) Elements, oxides, silicates. High-pressure phases with implications for the earth's interior. In: Oxford monographs on geology and geophysics, vol 4. Clarendon press, Oxford, pp 168–172
17. Tarte P (1965) Olivine structure of cadmium ortho-germanate. J Inorg Nucl Chem 27:1933–1938
18. Wadsley AD, Reid AF, Ringwood AE (1968) The high pressure form of Mn$_2$GeO$_4$, a member of the olivine group. Acta Crystallogr B 24:740–742

19. Morimoto N, Tokonami M, Koto K, Nakajima S (1972) Crystal structures of the high pressure polymorphs of Mn_2GeO_4. Am Mineral 57:62–75
20. Eysel W, Hahn T (1970) Polymorphism and solid solution of Ca_2GeO_4 and Ca_2SiO_4. Z Kristallogr 131:322–341
21. Nishikawa M, Akimoto S (1971) Bridgman anvil with an internal heating system for phase transformation studies. High Temp High Press 3:161–176
22. Zintl E, Harder A, Dauth B (1934) The atomic structure of the oxides, sulfides, selenides and telluides of lithium, sodium and kalium. Z Elektrochem 40:588–593
23. Schön JC, Cancarevic Z, Jansen M (2004) Structure prediction of high-pressure phases for alkali metal sulfides. J Chem Phys 121:2289–2304
24. Zheng C, Hoffmann R (1989) Conjugation in the 3-connected net. The AlB_2 and $ThSi_2$ structures and their transition metal derivatives. Inorg Chem 28:1074–1080
25. Fang JH, Newnham RE (1965) Crystal structure of sinhalite. Mineral Mag 35:196–199
26. Capponi JJ (1973) Thesis. Université Scientifique et Médicale de Grenoble (France)
27. Zerr A, Miehe G, Serghiou G, Schwarz M, Kroke E, Riedel R, Fuess H, Kroll P, Boehler R (1999) Synthesis of cubic silicon nitride. Nature 400:340–342
28. Wang H, Chen Y, Kaneta Y, Iwata S (2006) First-principles investigation of the structural electronic and optical properties of olivine-Si_3N_4 and olivine-Ge_3N_4. J Phys Condens Matter 18:10663–10676
29. Fischmeister HF (1962) Röntgenkristallographische Ausdehnungsmessungen an einigen Alkalisulfaten. Ein Beitrag zur kenntniss der Anionenfehlordnung in I-Na_2SO_4. Monatsh Chem 93:420–434
30. Tomaszewski PE (2002) Golden book of phase transitions. Wroclaw 1:1–123
31. Haase A, Brauer G (1978) Hydratstufen und Kristallstrukturen von Bariumchlorid. Z anorg allg Chem 441:181–195
32. Nilsson L, Thomas JO, Tofield BC (1980) The structure of the high temperature solid electrolyte Li_2SO_4 at 908 K. J Phys C 13:6441–6451
33. Vegas A, Martin RL, Bevan DJM (2009) Compounds with a "stuffed" anti-bixbyite-type structure, analysed in terms of the Zintl-Klemm and coordination-defect concepts. Acta Crystallogr B 65:11–21
34. Parfitt DC, Keen DA, Hull S, Crichton WA, Mezouar M, Wilson M, Madden PA (2005) High pressure forms of lithium sulphate. Structural determination and computer simulation. Phys Rev B 72:054121(7)
35. Scherf C, Paulus W, Heger G, Hahn T (2000) Crystal structure analysis of the orthorhombic phase II of $KLiSO_4$. Physica B 276:247–249
36. Zachariasen WH, Buckley HE (1931) The crystal lattice of anhydrous sodium sulphite, Na_2SO_3. Phys Rev 37:1295–1305
37. Larsson LO, Kierkegard P (1969) The crystal structure of sodium sulphite. A refinement allowing for the effect of crystal twinning Acta Chem Scand 23:2253–2260
38. Oertel G (1961) Über die Struktur von Caesium-Wismut-Fotokathoden. Z anorg allg Chem 309:210–225
39. Schütte M, Wartchow R, Binnewies M (2003) Shape controlling synthesis. Formation of Fe_3Si by the reaction of iron with silicon tetrachloride and crystal structure refinement. Z anorg allg Chem 629:1846–1850
40. Santamaría-Pérez D, Nuss J, Haines J, Jansen M, Vegas A (2004) Iron silicides and their corresponding oxides: a high-pressure study of Fe_5Si_3. Solid State Sci 6:673–678
41. Reynaud F (1976) Use of electron-diffraction to demonstrate excess nickel atom ordering with respect to stoichiometry in nickel-rich β-NiAl alloys. Formation of Ni_2Al superstructure. J Appl Crystallogr 9:263–268
42. Fritz JN, Olinger B (1984) Equation of state of sodium. J Chem Phys 80:2864–2871
43. Ogg A (1916) The crystal structures of the isomorphic sulphates of K, NH_4, Rb and Cs. Phil Mag Serie 6(32):518–525
44. Sommer H, Hoppe R (1977) Crystal-structure of Cs_2S and a remark about Cs_2Se, Cs_2Te, Rb_2Se and Rb_2Te. Z anorg allg Chem 429:118–130

45. Zintl E, Harder A, Dauth B (1939) Gitterstruktur der Oxide, Sulfide, Selenide und Telluride des Lithiums, Natriums und Kaliums. Z anorg allg Chem 241:281–304
46. Andersen L, Stroemberg D (1986) The structure of potassium sulfite. Acta Chem Scand A 40:479–480
47. Robinson MT (1958) The crystal structures of β-K_2SO_4 and of β-K_2PO_3F. J Phys Chem 62:925–928
48. van den Berg AJ, Tuinstra F (1978) Space group and structure of α-K_2SO_4. Acta Crystallogr B 34:3177–3188
49. Errandonea D, Santamaría-Pérez D, Vegas A, Nuss J, Jansen M, Rodríguez-Hernández P, Muñoz A (2008) Structural stability of Fe_5Si_3 and Ni_2Si studied by high-pressure x-ray diffraction and ab initio total-energy calculations. Phys Rev B 77:094113
50. Kudielka H (1977) Crystal-structure of Fe_2Si, its relationship to ordered structures of α-(Fe, Si) mixed-crystal and to Fe_5Si_3 structure. Z Kristallogr 145:177–189
51. Hendricks SB, Kosting PR (1930) The crystal structure of Fe_2P, Fe_2N, Fe_3N and FeB. Z Kristallogr 74:511–533
52. Britvin SN, Rudashevsky NS, Krivovichev SV, Burns PC, Polekhovsky YuS (2002) Allabogdanite, $(Fe, Ni)_2P$, a new mineral from the Onello meteorite: the occurrence and crystal structure. Am Mineral 87:1245–1249
53. Chenevier B, Soubeyroux JL, Bacmann M, Fruchart D, Fruchart R (1987) The high-temperature orthorhombic-reversible-hexagonal phase-transformation of FeMnP. Solid State Comm 64:57–61
54. Brackett EB, Brackett TE (1963) Sass RL (1963) The crystal structures of barium chloride, barium bromide and barium iodide. J Phys Chem 67:2132–2135
55. Léger JM, Atouf A (1992) High-pressure phase transformation in cotunnite-type $BaCl_2$. J Phys Condens Matter 4:357–365
56. Léger JM, Haines J, Atouf A (1995) The post-cotunnite phase in $BaCl_2$, $BaBr_2$ and BaI_2 under high-pressure. J Appl Cryst 28:416–423
57. Hyde BG, Andersson S (1989) Inorganic Crystal Structures. Chapters III, VI, and VIII. Wiley, New York
58. Le Roy J, Aléonard S (1972) Structure des orthofluoroberyllates de lithium $MLiBeF_4$. Acta Crystallogr B 28:1383–1387
59. Solans X, Calvet MT, Martínez-Sarrión ML, Mestres L, Bakkali A, Bocanegra E, Mata J, Herraiz M (1999) Thermal analysis and X-ray diffraction study on $LiKSO_4$: a new phase transition. J Solid State Chem 148:316–324
60. Natta G, Corradini P, Allegra G (1961) The different crystalline modifications of $TiCl_3$, a catalyst component for the polymerization of α-olefins. I: α-, β-, γ-$TiCl_3$. II: δ-$TiCl_3$. J Polymer Sci 51:399–410
61. Tsai KR, Harris PM, Lassettre EN (1956) The crystal structure of tricesiun monoxide. J Phys Chem 60:345–347
62. Zachariasen WH (1948) Crystal chemical studies of the 5f-Series of elements. I. New structure types. Acta Crystallogr 1:265–268
63. Santamaría-Pérez D, Vegas A (2003) The Zintl-Klemm concept applied to cations in oxides. I. The structures of aluminates. Acta Crystallogr B 59:305–323
64. Santamaría-Pérez D, Vegas A, Liebau F (2005) The Zintl-Klemm concept applied to cations in oxides. II. The structures of silicates. Struct Bond 118:121–177
65. Jamieson JC (1963) Crystal structures of titanium, zirconium, and hafnium at high pressures. Science 140:72–73
66. Schönberg N (1954) An X-ray study of the tantalum-nitrogen system. Acta Chem Scand 8:213–220
67. Andersson S (1959) The Crystal structure of the so-called δ-titanium oxide and its structural relation to the ω-phases of some binary alloy systems of titanium. Acta Chem Scand 13:415–419
68. Vegas A, Mejía-López J, Romero AH, Kiwi M, Santamaría-Pérez D, García-Baonza V (2004) Structural similarities between Ti metal and titanium oxides: implications on the high-pressure behaviour of oxygen in metallic matrices. Solid State Sci 6:809–814

69. Czybulka A, Steinberg G, Schuster HU (1979) Darstellung und Struktur ternärer Silizide und Germanide des Lithiums mit den Seltenen Erden Y und Gd im Fe_2P-Typ. Z Naturforsch B 34:1057–1058
70. Carrillo-Cabrera W, Somer M, Peters EM, Peters K, von Schnering HG (1996) Crystal structure of sodium barium phosphide NaBaP. Z Kristallogr 211:191
71. Schönberg N (1954) The tungsten carbide and nickel arsenide structures. Acta Metall 2:427–432
72. Krypyakevych PI, Kuz'ma YB, Voroshilov YV, Shoemaker CB, Shoemaker D (1971) Crystal structure of NbCoB. Acta Crystallogr B 27:257–261
73. Toman K (1954) The structure of Ni_2Si. Acta Crystallogr 5:329–331
74. Morosin B, Smith DL (1967) The crystal structure of lithium sodium sulfate. Acta Crystallogr 22:906–910
75. Lightfoot P, Pienkowski MC, Bruce PG, Abrahams I (1991) Synthesis and structure of $LiCaPO_4$ by combined X-ray and neutron powder diffraction. J Mater Chem 1:1061–1063
76. Liang JK, Xu XT, Chai Z (1988) The phase-diagram of the system $LiNaSO_4$-$LiKSO_4$ and crystallographic parameters and ionic-conductivity of $Li_2NaK(SO_4)_2$. J Solid State Chem 76:270–275
77. Frueh AJ Jr (1961) The use of zone theory in problems of sulfide mineralogy, part III: polymorphism of Ag_2Te and Ag_2S. Am Mineral 46:654–660
78. Okada K, Osaka J (1980) Cesium lithium tungstate. A stuffed h-cristobalite structure. Acta Crystallogr B 36:657–659
79. Yong-Kwan D, DiSalvo FJ (2007) Synthesis and single crystal structures of ternary phosphides Li_4SrP_2 and A*Ae*P (A = Li, Na; *Ae* = Sr, Ba). J Solid State Chem 180:432–439
80. Klevtsova RF, Klevtsov PV, Alexandrov KS (1980) Synthesis and crystal-structure of $CsLiMoO_4$. Dokl Akad Nauk SSSR 255:1379–1382
81. Klevtsov PV, Perepelitsa AP, Ishchenko VN, Klevtsova RF, Glinskaya LA, Kruglik AI, Aleksandrov KS, Simonov MA (1989) Synthesis and crystal-structural investigations of $CsLiCrO_4$. Sov Phys Crystallogr 32:677–681
82. Ono S, Brodholt JP, Price GD (2008) First-priciples simulation of high pressure polymorphs in $MgAl_2O_4$. Phys Chem Miner 35:381–386
83. Levy D, Pavese A, Sani A, Pischedda V (2001) Structure and compressibility of synthetic $ZnAl_2O_4$ (gahnite) under high-pressure conditions, from synchrotron X-ray powder diffraction. Phys Chem Miner 28:612–618
84. Levy D, Pavese A, Hanfland M (2000) Phase transition of synthetic zinc ferrite spinel ($ZnFe_2O_4$) at high pressure, from synchrotron X-ray powder diffraction. Phys Chem Miner 27:638–644
85. Gerward L, Ziang JZ, Olsen JS, Recio JM, Waskowska W (2005) X-ray diffraction at high pressure and high or low temperature using synchrotron radiation. Selected applications in studies of spinel structures. J Alloys Compd 401:11–17
86. Errandonea D, Kumar RS, Manjón FJ, Ursaki VV, Rusu EV (2009) Post-spinel transformations and equation of state in $ZnGa_2O_4$: determination at high pressure by *in situ* x-ray diffraction. Phys Rev B 79:024103
87. Trömel M (1965) Zur Struktur der Verbindungen vom Sr_2PbO_4-Typ. Naturwiss 52:492–493
88. Trömel M (1969) Die Kristallstruktur der Verbindungen vom Sr_2PbO_4-Typ. Z anorg allg Chem 371:237–247
89. Weiss R, Faivre R (1959) Preparation et structure de plombates et stannates alcalinoterreux du type A_2BO_4. C R Acad Sci 248:106–108
90. Vegas A, Vallet-Regí M, González-Calbet JM, Alario-Franco MA (1986) The ASnO$_3$ (A = Ca, Sr) perovskites. Acta Crystallogr 42:167–172
91. Durand B, Diot M, Mollard P (1979) Preparation et characterisation de la varieté ilmenite des stannates de manganese $MnSnO_3$ et de calcium $CaSnO_3$. Annal Chim 4:559–607
92. Ramos-Gallardo A, Vegas A (1995) The cation array in the bixbyite-type structures. J Solid State Chem 119:131–133

93. Prewitt CT, Shannon RD, Rogers DB, Sleight WW (1969) The C rare earth oxide- corundum transition and crystal chemistry of oxides having the corundum structure. Inorg Chem 8:1985–1994
94. Eckerlin P, Leicht E, Wölfel E (1961) Die Kristallstruktur von Ca_2Sn und Ca_2Pb. Z anorg allg Chem 307:145–156
95. Andrusyak RI, Kotur BY (1991) Phase equilibriums in the Sc-Mn-Ge and Sc-Fe-Ge systems at 870 K. Russ Metall (Engl Transl) 4:204–208
96. Kuz'ma YV, Teslyuk MY, Gladyshevskii EI (1962) Ternary laves phases in the system Mn-Ni-Ge. J Struct Chem 3:143–145
97. Fujita Y (1974) Strong paramagnetism in ZrMnCo. J Phys Soc Jpn 37:273
98. Tsuzuki K, Ishikawa Y, Watanabe N, Akimoto S (1974) Neutron diffraction and paramagnetic scattering from a high pressure phase of $MnGeO_3$ (ilmenite). J Phys Soc Jpn 37:1242–1247
99. Hase W (1984) Neutronographische Bestimmung der Kristallstrukturparameter von Dy_2O_3, Tm_2O_3 und α-Mn_2O_3. Acta Crystallogr B 40:76–82
100. Moiseev VP, Popova OS (1959) X-ray study of electrolytic deposits of manganese. Russ J Phys Chem 33:344–348
101. Ohoyama T (1961) X-ray and magnetic studies of manganese-germanium system. J Phys Soc Jpn 16:1995–2002
102. Goldschmidt VM (1932) Die Rutilmodifikation der Germanium Dioxyds. Z Phys Chem B 17:172–176
103. Ott H (1926) Die Strukturen von MnO, MnS, AgF, NiS, SnI_4, $SrCl_2$, BaF_2, Praezisionsmessungen einiger Alkalihalogenide. Z Kristallogr 63:222–230
104. Haines J, Léger JM, Hoyau S (1995) 2nd-order rutile-type to $CaCl_2$-type phase-transition in β-MnO_2 at high-pressure. J Phys Chem Solids 56:965–973
105. Vegas A, Martínez-Ripoll M (1992) From crystal structure data towards reaction paths in the solid state. Acta Crystallogr B 48:747–752
106. Brukl C, Nowotny H, Schob O, Benesovsky F (1961) Die Kristallstrukturen von TiSi, $Ti(Al, Si)_2$ und $Mo(Al, Si)_2$. Monatsh Chem 92:781–788
107. Rossteutscher W, Schubert K (1965) Strukturuntersuchungen in einigen T(4-5)-B(4-5) Systemen. Z Metallkd 56:813–822
108. Karpinskii OG, Shamrai VF (1969) Crystal structure of CrB-type ZrSi compound. Russ Met:136–137
109. Schob O, Parthé E (1965) AB compounds with Sc, Y and rare earth metals. I. Scandium and Yttrium compounds with CrB and CsCl structure. Acta Crystallogr 19:214–224
110. Vegas A, Martínez-Cruz LA (1995) A study of the cation arrays in MB_2, MB_4 MB_6 borides. Part II. Cluster formation and bonding aspects. Z Kristallogr 210:581–584
111. Novotny H, Kieffer R (1947) Roentgenographische Untersuchungen von Karbidsystemen. Z Metallkd 38:257–265
112. Traore K, Kappler JP (1979) Study of the variation of the cristalline parameters of solid-solutions of manganese, cobalt, nickel and iron borides, as a function of their composition. Bull Soc Chim Fr 1:419–425
113. Kanaizuka T (1981) Invar like properties of transition-metal monoborides $Mn_{1-x}Cr_xB$ and $Mn_{1-x}Fe_xB$. Mater Res Bull 16:1601–1608
114. Kiessling R (1950) The borides of manganese. Acta Chem Scand 4:146–159
115. Megaw HD (1946) Crystal structure of double oxides of the perovskite type. Proc Phys Soc London (1946) 58:133–152
116. Zachariasen WH (1927) Über die Kristallstruktur von $MoSi_2$ und WSi_2. Z Phys Chem 128:39–48
117. Jongste JF, Loopstra OB, Janssen GCAM, Radelaar S (1993) Elastic-constants and thermal-expansion coefficient of metastable *C*49 $TiSi_2$. J Appl Phys 73:2816–2820
118. Smith PL, Ortega R, Brennan B (1998) Pseudo-*C*11b phase formation of titanium disilicide $TiSi_2$ (Fmmm) during the *C*49 to *C*54 transition. Mater Res Soc Symp Proc 481:605–610

119. Beyers R, Sinclair R (1985) Metastable phase formation in titanium-silicon thin-films. J Appl Phys 57:5240–5245
120. Stishov SM, Belov NV (1962) About the crystal structure of a new compact modification of SiO_2. Dokl Akad Nauk SSSR 143:951–954
121. Parthé E, Nowotny HN, Schmidt H (1955) Strukturuntersuchungen an Siliziden. Monatsh Chem 86:385–396
122. McMahon MI, Nelmes RJ, Wright NG, Allan DR (1994) Crystal structure studies of II-VI semiconductors using angle-dispersive diffraction techniques with an image-plate detector. AIP Conf Proc 309:633–636
123. Duclos SJ, Vohra YK, Ruoff AL (1987) hcp to fcc transition in silicon at 78 GPa and studies to 100 GPa. Phys Rev Lett 58:775–777
124. Eckerlin P, Meyer HJ, Wölfel E (1955) Die Kristallstruktur von CaSn and CaGe. Z anorg allg Chem 280:322–328
125. Reid AF, Ringwood AE (1970) The crystal chemistry of dense M_3O_4 polymorphs: high pressure Ca_2GeO_4 of K_2NiF_4 structure type. J Solid State Chem 1:557–565
126. Wright AF, Fitch AN, Wright AC (1988) The preparation and structure of the α- and β-quartz polymorphs of beryllium fluoride. J Solid State Chem 73:298–304
127. Wondratschek H, Merker L, Schubert K (1964) Beziehungen zwischen der Apatit-Struktur und der Struktur der Verbindungen vom Mn_5Si_3 ($D8_8$)Type. Z Kristallogr 120:393–395
128. Wondratschek H, Merker L, Schubert K (1964) Beziehungen zwischen der Apatit-Struktur und der Struktur der Verbindungen vom Mn_5Si_3 ($D8_8$)Type. Z Kristallogr 120:478 (erratum correction)
129. Okada K, Ossaka J (1981) Crystal data and phase transitions of $KLiWO_4$ and $KLiMoO_4$. J Solid State Chem 37:325–327
130. Gregoryanz E, Lundegaard LF, McMahon MI, Guillaume C, Nelmes RJ, Mezouar M (2008) Structural diversity of sodium. Science 320:1054–1057
131. Ma Y, Eremets M, Oganov AR, Xie Y, Trojan I, Lyakhov MS, AO VM, Prakapenka V (2009) Transparent dense sodium. Nature 458:182–183
132. Lundegaard LF, Marqués M, Stinton G, Ackland GJ, Nelmes RJ, McMahon MI (2009) Observation of the *o*P8 crystal structure in potassium at high pressure. Phys Rev B 80:020101
133. Marqués M, Ackland GJ, Lundegaard LF, Stinton G, Nelmes RJ, McMahon MI, Contreras-García J (2009) Potassium under pressure: a pseudobinary ionic compound. Phys Rev Lett 103: 115501(4)
134. Vegas A, Santamaría-Pérez D, Marqués M, Flórez M, García-Baonza V, Recio JM (2006) Anions in metallic matrices model: application to the aluminium crystal chemistry. Acta Crystallogr B 62:220–227
135. Vegas A, Mattesini M (2010) Towards a generalized vision of oxides: disclosing the role of cations and anions in determining unit-cell dimensions. Acta Crystallogr B 66:338–344

Index

A
Ag_3PO_4 105
$Al_6Ca_4O_{13}$ 112
Alloys 67, 133
  anion-stuffed 32
  real stuffed 3
Anatase 165
Antibixbyites 94, 123
Anticotunnite 136
Antifluorite 94
Aragonite 42

B
$BaCl_2$ 161
Ba_2SnO_4 183
Bärnighausen trees 93, 95
Barometer, internal 154
Bixbyite 93, 111, 178
Boracite 116
Bromates 51

C
Calcite 42
$CaPd_3O_4$ 102
Carbonates 41
Ca_2SnO_4 172, 179
Cation arrays 31, 41, 67, 133
$CdY_4Mo_3O_{16}$ 114
Cerussite 42
Cesium sulfate 57
Chlorates 51
Clathrasils 1
Clathrate hydrates 1, 4
Clathrates 1
  DDR-type 14
  intermetallic 21
Colusite 108
Cooperite 57
Coordination defect (CD) theory 94
Corundum 46, 56
CoSn 161
Cotunnite 53, 57, 138
Cristobalite 8, 11
Crystal chemistry 67, 93
Cu_3WO_4 122

D
Danalite 107
Dodecasil 12

E
Eulitite 55

F
Farringtonite 56
FeB 179
$FeGeV_2$ 103
Fe_2P 159
Fluorite 93
Forsterite 69

G
Germanates 190
Germanides 7
Germanite 108
Graphenes 85
Grey isomorphism 41
Group/subgroup relationships 93, 95

H
High pressure synthesis 78, 93, 133
Huttonite 53
Hydrates 1, 4

I
Inclusion compounds 5
Inorganic structures 93
Iodates 51
Ionic packings 31

K
$KLiMoO_4$ 190
Keatite 8

L
$LaCl_3$ 162
Larnite 32
Laves phases 154, 177
$LiNaSO_4$ 168
Lithium, elemental 76
Lithium nitrides 93
Lithium orthophosphate 56
$Li_7V^VN_4$ 118

M
Magnesite 42
Manganosite 179
Marokite 171
Melanophlogite 1, 10
Metals 133
Metavariscite 23
Mn_2GeO_4 176
Monazite 53

N
Neodymium phosphates 56
Ni_2Al 147, 150, 191
Nickel boracite 117
Ni_2In 42, 53, 71, 136
Nitrates 46
Nitrogen, molecular 93, 120

O
Octet rule 1
Olivine 53, 69, 136
Orthoarsenates 55
Orthoborates 45
Orthogermanates 53
Orthophosphates 55
Orthosilicates 53
OsO_2F_2 106
Oxidation–pressure relationship 138, 140, 156, 176
Oxides 133
Oxoacid salts 31, 41
Oxoanions 31, 33, 41, 51

P
Packing, sphere 32
  net 39, 62
PbO 84
Pearson's generalised octet rule 1
Perhalogenates 58
Periodic graph 31
Perovskite 135, 172, 183
Phase transitions 67, 133
Phenacite 155, 169
Point charges 32
Pressure, internal, estimating 152
  oxidation relationship 138, 140, 156, 176
Pseudo-magnesium 81
Pt_3O_4 103
Pyrite 50
Pyrolusite 178

Q
Quartz 11, 185

R
Resonance structures 67
RuO_4 106
Rutile 50, 53, 179

S
Scheelite 53
Selenates 56
Selenites 49
Silicon nitride 144
Sinhalite 69
Sodalite 93, 107
Sodium perchlorate sodalite, neon-stuffed 107
Sphalerite 56, 58, 111
Spinels 58, 69, 136, 137
  inverse 144
  post-spinel structures 170
Sr_2PbO_4 172
Strontianite 42
Sulfates 56, 136
Sulfides 32, 77, 136, 140
Sulfites 49, 136, 148

T
Tectoaluminosilicates 2
Tectosilicates 1
Tellurites 49
Thenardite 58, 68, 81, 136, 140, 184
Topology 34
Tricapped trigonal prisms (TCTPs) 147, 161

Tridymite 8
Triphylite 67, 70

V
Valence electron concentration 10

W
Witherite 42
Wollastonite 187
Wurtzite 56, 136, 169

Z
Zeolites 6, 21
Zintl–Klemm concept 1, 93
  extended (EZKC) 4, 67, 70, 94, 133, 161
Zintl phases 33, 67
  inverse 9
Zintl polyanions 4, 13
Zircon 53
Zirconia, tetragonal 128
ZnS sphalerite 110